



# Synthesis of BODIPY Dyads to Study Electronic Energy Transfer

A Dissertation Submitted to:  
School of Chemistry, Newcastle University  
*In Partial Fulfillment of the Requirements for the Degree of  
DOCTOR OF PHILOSOPHY*

Dan Bai

*October 2013*

## Contents

Cover page	
Acknowledgements	ii
Dedication	iii
Abstract	iv
Publications & Presentations	vi
Contents page	viii
List of Tables and Schemes	xiii
Compounds Nomenclature	xxii



## ***Acknowledgements***

Allow me to convey gratitude to Prof. Andrew C. Benniston and Prof. Anthony Harriman providing guidance at each and every stage; enable me to develop an understanding of the area. I am much obliged to the supervisors providing advice and pastoral care, their constant kindness very much appreciated. Many thanks to Ruth, Victoria, Dr Songjie Yang, Thomas and Sophie for kind support throughout the course of research work, also for the inspirational conversation at afternoon teatime, which were always *joie de vivre*.

Many thanks to Dr Ross Harrington, Dr Jerry Hagon, Dr Corinne Wills and Effat for collaborations and contributions on crystallography, molecular orbital calculation, NMR and fluorescence spectroscopy results. Many thanks to all at School of Chemistry create the research atmosphere that gave me a great pleasure to work within during this study and previous MSc program; it's been a marvellous journey.

## ***Dedication***

To dear parents Haiping Bai & Hong Deng  
for their unconditional love & wise support

## Abstract

Nature's efficiency of converting sunlight into chemically stored energy have inspired many scientists research into the field of "artificial photosynthesis." In order to produce renewable sustainable energy many chemists are looking for viable *modus operandi* to make carefully designed artificial analogues which could duplicate the essential features of natural photosynthesis. The mechanism of electronic excitation energy transfer between weakly coupled chromophores is well known as Förster resonance energy transfer (FRET). This thesis covers the work of the qualitatively and quantitative study the electro-energy transfer process within tailor-made boron dipyrromethene (Bodipy) systems.

Chapter 1 clarifies the research area and aims - an introduction to the field of artificial photosynthesis, covering recent aspects and the milestones. A mini chronicle of FRET theory development and its modern day applications is included, alongside a brief literature review of artificial fluorescent dyes - concentrated on the chemistry of fluorescent Bodipy compounds.

Chapter 2 presents the experimental data for molecular systems discussed in the following chapters, covering the specific synthesis methodology and in-depth characterization for each precursor and target compounds.

Chapter 3 reports the synthesis and characterization of metal chelated molecular rotors based on the ruthenium (II) tris-bipyridine and ruthenium(II) terpyridine linked Bodipy rotor system. The concept was the systems would perform as dual-mode temperature and viscosity probes. The  $^3\text{MLCT}$  luminescence decay and the metal centred energy transfer to the Bodipy rotor was recorded at 80 K. Fast pump probe experiments were performed to monitor excited state processes. A series Bodipy dyad systems were also presented.

Chapter 4 concentrates on the properties of multichromophoric dyads in which one of the Bodipy groups absorbs and emits at longer wavelength. The idea

was to alter the Förster overlap and try and produce more sensitive viscosity probes. The final part of the chapter focuses on a simple donor-acceptor Bodipy dyad for neural imaging applications.

Chapter 5 discusses the synthesis and characterization of an anthracenyl-Bodipy dyad containing a rigid triazole bridge, which acts as an electronic insulator. Efficient electronic energy transfer occurs from the anthracenyl-based unit to the Bodipy system and becomes faster in solvents of lower refractive index. The rate of electronic energy transfer is discussed in terms of Förster theory.

Chapter 6 concerns the synthesis and characterization of a multicomponent energy transfer cassette. A linear molecular dyad was synthesised comprising a pyrene-thiophene energy donor linked via a triazole unit to a borondipyrromethene (Bodipy) energy acceptor. Rates for energy transfer ( $k_{\text{EET}}$ ) were measured and correlated to calculated overlap integrals ( $J_F$ ). A solvent effect was also observed and is discussed.

Chapter 7 is the general conclusions and remarks chapter highlighting future work.

## Publications & Presentations

Results collected in Chapter 3 are presented in the articles:

E Bahaidarah, D. Bai, A C. Benniston, A. Harriman, S. Mitchell, S. Yang, H. Lemmetyinen and N. V. Tkachenko. A Hybrid Molecular Rotor Triplet Sensitizer Dyad based on Bodipy-Spacer-Ru(II)-Polypyridyl Components, *RSC Advances*, (in preparation)

Results collected in Chapter 4 are presented in the articles:

D Bai, Andrew C. Benniston, Sophie Clift, Jannetta Steyn, Nicola Everitt, and Peter Andrasb, Fluorescence-based Neural Imaging with Neutral Boron Dipyrromethene (Bodipy) Dyads. *Analyst*. **2013** (submitted)

D. Bai, A C. Benniston, V. L. Whittle, Helge Lemmetyinen and Nikolai V. Tkachenko. ROFRET: A molecular-scale fluorescence probe displaying viscosity enhanced intramolecular Förster energy transfer. *Chem.-Eur. J.* **2013**, (in preparation).

Results collected in Chapter 5 are presented in the article:

D. Bai, A C. Benniston, J Hagon, H Lemmetyinen, N V Tkachenko, R W Harrington. Tuning the Förster Overlap integral: Energy Transfer over 20 Ångstroms from a Pyrene-based Donor to Borondipyrromethene (Bodipy). *Phys. Chem. Chem. Phys.*, **2013**, 15(24): 9854-61.

Results collected in Chapter 6 are presented in the article:

D. Bai, A C. Benniston, J Hagon, H Lemmetyinen, N V Tkachenko, W Clegg, R W Harrington, Exploring Förster Electronic Energy Transfer in a Decoupled Anthracenyl-based Borondipyrromethene (Bodipy) Dyad. *Phys. Chem. Chem. Phys.* **2012**, 14(13): 4447-56.

## **Presentations:**

Post Graduate Solar Fuels Symposium of ISACS 12: Challenges in Chemical Renewable Energy, 3rd September, 2013, University of Cambridge (Poster presentation)

Materials Chemistry (MC11) RSC Conference, 8-11th July 2013, University of Warwick (Poster presentation)

SET for BRITAIN. 18th March 2013, House of Commons. (Invited poster presentation: “ Electronic Energy Transfer in BODIPY compounds ”)

Solar to Fuels Symposium. 18th Jan. 2012, RSC Chemistry Centre, London. (Poster presentation)

Faraday Discussion 155: Artificial Photosynthesis, 05-07th Sept. 2011. University of Edinburgh (Poster presentation: “Exploring Electronic Energy Transfer in BODIPY compounds ”)

Photochemistry and Photochemical Techniques, 16-18th May 2011. Trinity College Dublin (Invited oral presentation: “Exploring Förster Theory in BODIPY compounds ”)

## Contents

<b>Chapter 1 Research Aims &amp; General Introduction.....</b>	<b>1</b>
1.1 Nature Inspired Artificial Photosynthesis.....	2
1.1.1 Photoinduced Electronic Energy Transfer (EET) Process.....	2
1.1.1.1 Nature Regulated Light-Harvesting Antenna Systems.....	2
1.1.1.2 Study EET Process in Natural & Artificial Arrays.....	5
1.1.2 Mechanism of Förster Resonance Energy Transfer (FRET).....	7
1.1.2.1 The Chronicle of FRET.....	8
1.1.2.2 Terms & Conditions of FRET.....	13
1.1.2.2.1 The Parameters within FRET Equation.....	13
1.1.2.2.2 Excitation Energy Redistribution Pathways.....	14
1.1.2.2.3 The Critical Distance.....	16
1.1.2.2.4 The Orientation Factor.....	18
1.2 The Chemistry of BODIPY Compounds.....	20
1.2.1 Synthesis & Modification.....	20
1.2.1.1 The Scaffold.....	20
1.2.1.2 Modifications.....	25
1.2.1.2.1 Modification at Pyrrole Skeleton.....	26
1.2.1.2.2 Modification at Meso-Position.....	27
1.2.1.2.3 Modification via Electrophilic Substitution & Cross-coupling Reaction .....	29
1.2.1.2.4 Modification at Boron Atom.....	30
1.2.1.2.5 Aza-Bodipy.....	31
1.2.1.2.6 Build-in Water Solubility.....	31
1.2.1.2.7 Bio-Conjugate Systems.....	32
1.2.2 Applications & Development.....	33

1.3 Conclusion Remarks.....	34
1.4 References.....	35
<b>Chapter 2 Experimental Data &amp; Synthetic Protocols.....</b>	<b>40</b>
2.1 Instrumentation.....	41
2.1.1 Nuclear Magnetic Resonance.....	41
2.1.2 Mass Spectrometry.....	41
2.1.3 Melting Point.....	41
2.1.4 UV/visible and Emission Spectroscopy.....	41
2.1.5 Transient Absorption Measurements.....	42
2.1.6 Molecular Modeling.....	43
2.1.7 Electrochemistry.....	43
2.1.8 Infra-Red Spectroscopy.....	43
2.1.9 Crystallography.....	43
2.2 Chemicals.....	44
2.3 Solvent & Purification Methods.....	46
2.4 Synthetic Protocols.....	47
<b>Chapter 3 Multi-Mode Fluorescent Molecular Rotors.....</b>	<b>105</b>
3.1 Background and Molecular Design Principles.....	106
3.1.1 Molecular Rotors.....	106
3.1.1.1 Julolidine Aryl-Alkenyl Rotor Probe.....	106
3.1.1.2 Unhindered Bodipy System as Molecular Rotors.....	107
3.1.2 Molecular Design Principle.....	108
3.2 Results and Discussion.....	110
3.2.1 General Synthetic Strategy.....	110
3.2.1.1 Synthesis of Functionalised Rotor Precursors.....	110
3.2.1.2 Activated Complementary “Click-on” Segments.....	115



3.2.2 Synthesis of Target Rotor Connected Systems.....	115
3.2.2.1 Rotor Connected to Metal Complexes.....	118
3.2.2.2 Rotor & Hindrance - Dyads Connected via Alkyl Spacers.....	119
3.2.3 Molecular Orbital Calculations	
& Minimised Energy Diagrams.....	124
3.2.3.1 Computational Calculations for ROMC1 and ROMC2.....	125
3.2.3.2 Computer Calculations for ROBD1.....	127
3.2.4 Photophysical Measurements.....	128
3.2.4.1 Photophysical Properties	
of Ruthenium(II) Molecular Dyads.....	129
3.2.4.1.1 Properties of ROMC1.....	130
3.2.4.1.2 Properties of ROMC2.....	135
3.2.4.2 Properties of ROBD1 and ROBD2.....	137
3.3 Remarks and Conclusions.....	144
3.4 References.....	145
<b>Chapter 4 Modulated Multichromophoric Systems.....</b>	<b>148</b>
4.1 Background and Molecular Design Principle.....	149
4.1.1 Versatility of Bodipy Compounds.....	149
4.1.1.1 Literature Methods.....	149
4.1.1.2 Molecular Design Principle.....	155
4.2 Results and Discussion.....	157
4.2.1 Synthesis of Julolidine Donor Acceptor Probes.....	157
4.2.2 Synthesis of Multichromophoric Systems.....	158
4.2.2.1 Preparation of Activated Distyryl Bodipy Precursor.....	158
4.2.2.2 Synthesis of Alkyl Linked Dyad Systems.....	160
4.2.2.3 Towards Polyether-linked Dyad Systems.....	161
4.2.3 Molecular Structure and Orbital Calculations.....	165

4.2.3.1 Crystal Structure of MJULBD.....	165
4.2.3.2 Red & Blue BLRO.....	167
4.2.4 Results and Analysis of Photophysics Measurements.....	169
4.2.4.1 Electrochemical and Absorption/Fluorescence Properties of MJULBD.....	169
4.2.4.2 Neural Imaging with MJULBD.....	172
4.2.4.3 Absorption/Fluorescence Properties of BLRO.....	175
4.3 Conclusion.....	177
4.4 References.....	178
<b>Chapter 5 Energy Transfer in Closely Spaced Dyads</b>	
5.1 Background and Molecular Design Principle.....	181
5.1.1 Through-Bond & Through-Space Energy Transfer.....	181
5.1.2 The Alignment of Dipole Moments and FRET Efficiency.....	183
5.2 Results and Discussion.....	189
5.2.1 Synthesis of Precursor Compounds.....	189
5.2.1.1 Preparation of 8(4-Azidephenyl)-Bodipy (AZBOD).....	189
5.2.1.2 Preparation of azide activated anthracene compounds.....	192
5.2.2 Synthesis and Characterisation of Electronically Decoupled Dyad Systems.....	193
5.2.3 Preparation of reference compounds.....	198
5.2.4 Molecular Orbital Calculations & Electrochemistry.....	201
5.2.5 Photophysical Measurements.....	205
5.2.5.1 Absorption and Fluorescence.....	205
5.2.5.2 Time-Resolved Studies.....	208
5.2.5.3 Interpretation of Fast Spectroscopy Data.....	211
5.2.5.4 Electronic Energy Transfer (EET) Mechanism.....	213
5.2.5.5 Comparison with Förster Theory in Toluene.....	213
5.2.5.6 Comparison to ANTBD2.....	217
5.3 Remarks and Conclusions.....	218
5.4 References.....	219

<b>Chapter 6 Tuning Förster Resonance Energy Transfer Efficiency.....</b>	<b>221</b>
6.1 Background and Molecular Design Principles.....	222
6.1.1 Parameters for FRET Efficiency.....	222
6.1.2 Aim of Research and Molecular Design Principle.....	224
6.2 Results and Discussion.....	225
6.2.1 Synthesis of Bodipy Tethered Dyad Systems.....	225
6.2.1.1 Preparation of precursors and control compounds.....	225
6.2.1.2 Preparation of Dyad Systems PTTBD and NAPBD.....	226
6.2.2 Characterisation of of PTTBD and NAPBD.....	227
6.2.2.1 Crystal structure of PTTBD.....	227
6.2.2.2 Characterization of NAPBD.....	229
6.2.3 Molecular Orbital Calculation and Energy Diagrams.....	234
6.2.4 Photophysical Measurement and Analysis.....	235
6.3 Remarks and Conclusion.....	250
6.4 References.....	251

## List of Tables and Schemes

### Tables

1.1 Key terms in fluorescent spectroscopy measurements.....	12
1.2. Ab initial Bodipy compounds synthesised by Treibs and Kreuzer1.....	21
1.3 Applications of fluorescent molecule.....	34
2.1 Chemicals implemented in experimental work.....	45
2.2 Solvents implemented in experimental work.....	46
4.1 Literature recorded Bodipy systems and their structure alteration plus their optical data.....	151
4.2 Literature reported styryl-substituted Bodipy systems.....	151
5.1 Polycyclic aromatic hydrocarbons (PAH) compounds and their transition dipole moments.....	186
5.2 Selected photophysical properties of some key chromophores used in studies.....	187
6.1 Selected bond lengths and angles for PTTBD.....	228
6.2 Photophysical parameters for PT in a range of solvents and the calculated Förster overlap integral.....	238
6.3 Kinetic parameters measured for PTTBD in a range of solvents.....	242

### Schemes

1.1 Photosynthesis mechanism within membrane complexes.....	2
1.2 Electrophilic substitution of Bodipy synthesis by Treibs and Kreuzer.....	20
1,3 Base catalysed route of Bodipy synthesis by Treibs and Kreuzer.....	21
1.4 Resonance equivalents of Bodipy core.....	22
1.5 General Synthetic route of F-Bodipy platform.....	22
1.6 Prepare F-Bodipy platform via succinic anhydride.....	23
1.7 General synthetic route of asymmetric Bodipy platform.....	23
1.8 Synthesis of Bodipy platform via Vilsmeier-Haack reaction.....	24
1.9 Mechanism of POCl <sub>3</sub> catalysed Bodipy platform synthesis.....	24
1.10 Synthetic methods of Bodipy parent core.....	25
1.11 One-step synthesis of 1,7-substituted Bodipy.....	26
1.12 Primary phosphine incorpor Bodipy.....	27

1.13 Electrophilic substitution on Bodipy core.....	29
1.14. 2,6-position of F-Bodipy activated by cross-coupling reaction.....	30
2.1 Previously prepared acetylene compounds and their nomenclature.....	47
3.1 Preparation of ALCRO via the protected 4-(benzyloxy)benzaldehyde PHRO.....	111
3.2 Preparation of ALCRO via one-step condensation of 4-hydroxy benzaldehyde with pyrrole.....	112
3.3 Synthetic routes of ACETRO and AZRO.....	114
3.4 Basic mechanism for 'click' reaction.....	116
3.5 Preparation of the metal-based rotor compound ROMC1 starting from MCNAP and AZRO.....	118
3.6 Preparation of the ruthenium(II) bis-terpyridine complex based rotor compound.....	119
3.7 Preparation of ROBD1 from ACETRO and AZBOD .....	120
3.8 Preparation of ROBD2 starting from ACETBOD and AZRO.....	123
4.1 Preparation of julolidinecarboxaldehyde via the Vilsmeier–Haack reaction.....	157
4.2 Preparation of MJULBD and the attempted increase in p-conjugation via Knoevenagel condensation.....	158
4.3 Preparation of the precursor compounds with extended p-conjugation...	159
4.4 Preparation of BLRO via the “click” Reaction.....	160
4.5 Preparation of BLBD via “click” chemistry.....	161
4.6 Synthetic route of the polyether-based spacer derivative TSROT.....	162
4.7 Attempted synthesis of the polyether-based dyad ROTSEBD.....	163
4.8. Attempted synthetic route of polyether connected dyad compound of Bodipy rotor and distyryl condensed Bodipy.....	164
4.9 Attempted double “click” reaction to produce EBDSB.....	165
5.1 Reagents and conditions for the preparation of AZBOD.....	191
5.2 Method used in the preparation of the azide derivatives of anthracene from the amino derivatives.....	193
5.3 Synthetic route to the anthracene-based dyads via click chemistry to introduce the triazole group.....	194
5.4 Preparation of the control compound PHBD.....	199
5.5 Preparation of the control compounds PHANT and PHANT2.....	199

6.1 Preparation of PTTBD.....	226
6.2 Preparation of NAPBD.....	227

## Figures

1.1 Illustration of light-harvesting LHC-II system.....	4
1.2 Illustration of electronic energy transfer and energy migration routes in <i>Rhodopseudomonas acidophila</i> .....	5
1.3 Energy transfer mechanism within Fenna-Matthews-Olson (FMO) complex model.....	6
1.4 Illustration of artificial light-harvesting antenna-sensitizer solar cell.....	7
1.5 Perrin's measurement of fluorescent lifetime on fluorescein and erythrosine.....	9
1.6 Left: schematic illustration of Franck-Codon energy coordinates; Absorption Right: fluorescence transition states corresponding to the energy diagram.....	10
1.7 Jablonski diagram of excitation energy redistribution pathways.....	10
1.8 Jablonski diagram of excitation energy redistribution via Förster type energy transfer.....	11
1.9 Electron spin states of excitation energy redistribution pathways.....	14
1.10 Jablonski diagram of Förster resonance energy transfer between a donor-acceptor dyad.....	15
1.11 FRET dependency on separation distance between a donor and acceptor pair.....	17
1.12 Orientation factor in Hertzian dipole alignments.....	18
1.13 Illustration of critical angles in equation of orientation factor calculation.....	19
1.14 Conformational modification effects on spectroscopy properties of Bodipy core.....	26
1.15 Exemplary meso-modified Bodipy systems made by MPL members....	28
1.16 Energy transfer cassette of E-Bodipy system.....	30
1.17 B-O chelated Aza-Bodipy system.....	31
1.18 Water soluble tetra-styryl substituted Bodipy .....	32
1.19 Asymmetric Bodipy incorporated amino acid.....	33

3.1 The archetypical molecular rotor 9-(dicyano-vinyl)julolidine (DCVJ) and 9-(2-Carboxy-2-cyanovinyl)julolidine (CCVJ).....	107
3.2 Two prototype molecular rotors developed to probe viscosity of solvents (ROBOD) and the viscosity of cell membranes (BD-ROT).....	108
3.3 Metal chelating temperature sensitive lumophores ROMC1 and ROMC2 .....	109
3.4 Molecular dyads based on a rotor Bodipy and an internal standard capable of potential ratiometric sensing.....	109
3.5 Room temperature $^1\text{H}$ NMR spectrum for PHRO in $\text{CDCl}_3$ .....	111
3.6 Room temperature $^1\text{H}$ NMR spectrum for ALCRO in $\text{CDCl}_3$ .....	112
3.7 Room temperature $^1\text{H}$ NMR spectrum for ALCRO in $\text{CDCl}_3$ produced by the unprotected reaction.....	113
3.8 FTIR spectrum for AZRO showing the azide stretch marked with an asterisk and the fingerprint region.....	115
3.9 $^1\text{H}$ NMR spectrum of the test compound NPBD in $\text{CDCl}_3$ .....	117
3.10 Room temperature $^1\text{H}$ NMR spectrum for ROBD1 in $\text{CDCl}_3$ . ....	121
3.11 Partial room temperature $^1\text{H}$ NMR spectrum for ROBD1 in $\text{CDCl}_3$ .....	122
3.12 Room temperature $^1\text{H}$ NMR spectrum for ROBD2 in $\text{CDCl}_3$ .....	124
3.13 DFT (B3LYP, 3-21G) computer calculated energy-minimised structures for ROMC1 and ROMC2.....	125
3.14 Selected DFT calculated molecular orbitals for ROMC1.....	126
3.15 Selected energy-minimised structures for ROBD1 calculated using Gaussian 03 (B3LYP) and 3-21 G basis set.....	128
3.16 Room temperature absorption (black) and emission (red) spectra for MCNAP in MeCN.....	129
3.17 Room temperature absorption (black) and emission (red) spectra for ROMC1 in BuCN.....	131
3.18 Emission spectra recorded for ROMC1 in BuCN with a decrease in temperature.....	132
3.19 Plots showing the temperature dependence of quantum yields for the ruthenium-centered (RU) phosphorescence and rotor (ROTOR) fluorescence in BuCN.....	133
3.20 Calculated differential transient absorption profiles recorded after excitation of ROMC1 in MeCN with a 70 fs laser pulse delivered at 395 nm	

.....	134
3.21 Proposed mechanism picture of deactivation for ROMC1 showing the possible excited state decay routes to terminate at the triplet localised on the Bodipy.....	135
3.22 Room temperature absorption (black) and emission (red) spectra for ROMC2 in MeCN.....	136
3.23 Calculated differential transient absorption profiles recorded after excitation of ROMC2 in MeCN with a 70 fs laser pulse delivered at 395 nm.....	137
3.24 Room temperature normalised absorption spectra for ROBD1 (black) and a fully alkylated Bodipy (blue) and a rotor Bodipy (red) in MeOH.....	138
3.25 Increase in the fluorescence intensity for ROBD1 with change in selected alkanol solvents.....	140
3.26 Differential transient absorption spectra recorded at different time delays .....	141
3.27 Lifetime data collected for ROBD1 in OctOH using up-conversion spectroscopy following excitation at 395 nm with a 70 fs laser pulse.....	143
3.28 Fluorescence intensity versus no of carbon atoms in alkanol solvents for ROBD2.....	144
4.1 Water-soluble $\pi$ -extended energy transfer cassette systems.....	151
4.2 Porphyrin comprised distyryl Bodipy tweezer compound.....	154
4.3 Example of a pyrenyl distyryl-Bodipy photodynamic therapy sensitizer. ....	155
4.4 Illustration of the donor-acceptor Bodipy MJUBOD .....	156
4.5 Examples of Bodipy dyads containing a long-wavelength emitting chromophore.....	157
4.6 X-ray determined molecular structure for MJULBD (top) and the angle between planes created using the Bodipy unit and julolidine group (bottom). ....	166
4.7 Top: Computed structure for MJULBD showing the twisted julolidine unit. Bottom: The HOMO and LUMO for the dyad as calculated by DFT (B3LYP) 6-311G.....	167
4.8 Top: Computer calculated energy minimized structure for BLRO. Bottom: View of BLRO along the extended Bodipy unit.....	168



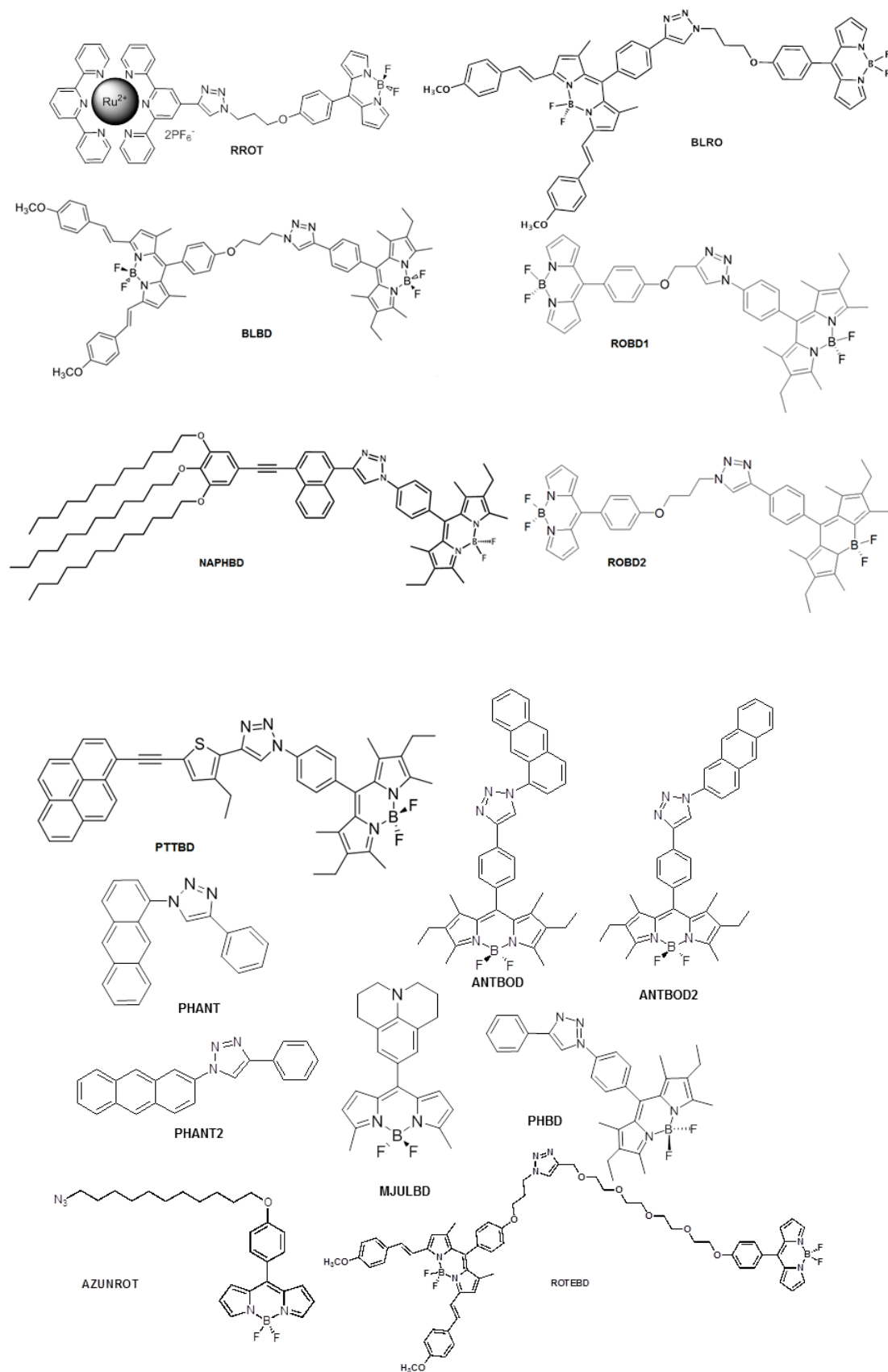
4.9 Selected HOMO/LUMOs for BLRO with arrows showing electronic transitions associated with Bodipy-based absorption.....	169
4.10 Cyclic voltammogram for MJULBD.....	170
4.11 Absorption spectra for MJULBD recorded in a range of solvents of different polarity.....	171
4.12 Absorption (black) and fluorescence (red) spectra for MJULBD in dilute cyclohexane.....	172
4.13 Top: Fluorescence image of the stomatogastric ganglion (STG) of <i>C. pagarus</i> after bathing with a MJULBD saline solution. Bottom: Extracellular and optical VSD recording using MJULBD of neural activities in the crab STG. ....	174
4.14 Room temperature absorption spectra for BLRO recorded in two alkanol solvents.....	175
4.15 Room temperature fluorescence spectra for BLRO recorded in two alkanol solvents.....	177
5.1 Summary of the energy transfer dynamics and time scales within the photosynthetic purple non-sulfur bacteria LHC II and the reaction center ....	181
5.2 Cartoon representation of a donor-acceptor assembly.....	182
5.3 A molecular rotaxane-based assembly where FRET is the mechanism for energy transfer.....	183
5.4 A molecular system for which through-bond energy transfer is the mechanism. ....	183
5.5 Example of a donor-acceptor Bodipy-anthracene dyad.....	184
5.6 A near orthogonally arranged donor-acceptor dyad.....	185
5.7 Picture showing the dual electron exchange mechanism and the role of the bridging orbitals in promoting the process.....	188
5.8 The two anthracene-Bodipy dyads designed to study Förster energy transfer.....	189
5.9 Molecular structure of AZBOD.....	191
5.10 X-ray determined molecular structure for ANTBD showing the atomic numbering scheme.....	195
5.11 Crystal packing diagram for ANTBD.....	196

5.12 Top: Prediction of proton chemical shifts for ANTBD2 using ChemDraw Ultra. Bottom: Room temperature $^1\text{H}$ NMR spectrum for ANTBD2 in $\text{CDCl}_3$ , showing the aromatic region only and partial assignments.....	197
5.13 Observed and theoretical mass spectrum for ANTBD2 revealing the $[\text{M-H}]^+$ molecular ion.....	198
5.14 Room temperature $^1\text{H}$ NMR spectrum for PHANT in $\text{CDCl}_3$ . ....	200
5.15 Room temperature $^{13}\text{C}$ NMR spectrum for PHANT in $\text{CDCl}_3$ .....	201
5.16 HOMO and LUMO molecular orbitals calculated for PHANT using Gaussian-03 at the Hartree-Fock level and using a 6-311G basis set. Energies are given in Hartrees.....	202
5.17 Representation of the HOMO and LUMO molecular orbitals for ANTBD and their corresponding energies calculated using DFT (B3LYP) level using the 6-311G basis set.....	203
5.18 Cyclic voltammogram recorded for PHBD in dry $\text{CH}_2\text{Cl}_2$ (0.2 M TBATFB) at a glassy carbon electrode.....	204
5.19 Cyclic voltammogram recorded for ANTBD in dry $\text{CH}_2\text{Cl}_2$ (0.2 M TBATFB) at a glassy carbon electrode.....	205
5.20 Absorption (black) and emission (red) spectra for PHANT in dilute toluene.....	206
5.21 Absorption/fluorescence spectra for ANTBD (black) and the absorption spectrum for an equimolar mixture of PHANT and PHBD (red) in toluene.....	207
5.22 Comparison of the corrected fluorescence excitation spectrum (red) with the absorption spectrum (black) for ANTBD in dry toluene.....	208
5.23 Differential transient absorption profiles recorded at 1.9 ps (black), 14.6 ps (red) and 206 ps (blue) after excitation of a sample of ANTBD in toluene at 400 nm with a 70 fs laser pulse.....	209
5.24 Femtosecond up-conversion profiles recorded at two different wavelengths following excitation of ANTBD in toluene at 380 nm with a 70 fs laser pulse.....	211
5.25 Left: calculated planes for the long-axis of the anthracenyl group (blue), Bodipy unit (red), and intramolecular axis (green) using the X-ray determined molecular structure for ANTBD. Right: cartoon representation of the bond angles and numbering/lettering scheme used in the discussion of Förster theory.....	214

5.26 Pictorial representation of pathways for EET and vibrational cooling. Note: $k_1$ and $k_2$ represent rates of EET into the $S_2$ and $S_1$ states from anthracene.	216
5.27 Top: Absorption (black) and emission (red) spectra for ANTBD2 in dilute toluene. Bottom: Comparison of absorption and corrected fluorescence excitation spectra for ANTBD2.	218
6.1 Example of using the change in FRET efficiency to produce a voltage sensitive probe system	223
6.2 Use of FRET to demonstrate the association of the two oligonucleotide chains.	224
6.3 Acetylene activated precursor compounds for carrying out 'click' reactions, alongside their reference control compounds.	225
6.4 Molecular structure for PTTBD as determined by X-ray analysis.	228
6.5 Partial numerical scheme of NAPBD.	229
6.6 $^1\text{H}$ NMR spectrum for NAPBD in $\text{CDCl}_3$ at room temperature with assignment of peaks for the aromatic and aliphatic region.	230
6.7 Partial $^1\text{H}$ - $^1\text{H}$ COSY spectrum for NAPBD in $\text{CDCl}_3$ showing selected correlations in the aromatic region.	231
6.8 Partial $^1\text{H}$ - $^1\text{H}$ COSY spectrum for NAPBD in $\text{CDCl}_3$ showing selected correlations in the aliphatic region.	231
6.9 Selected HMQC spectrum for NAPBD in $\text{CDCl}_3$ showing the alkyl region.	232
6.10 Selected HMQC spectrum for NAPBD in $\text{CDCl}_3$ showing the aromatic region.	233
6.11 Partial HMBC spectrum for NAPBD in $\text{CDCl}_3$ showing the aromatic region.	234
6.17 Component differential transient absorption spectra recorded for PTTBD in DMF following excitation with a 70 fs laser pulse at 400 nm.	243
6.12 Selection of HOMOs and LUMOs for PTTBD calculated by DFT (B3LYP) 6-311G basis set.	235

6.13 Ambient temperature normalised absorption (black) and fluorescence (red) spectra for PTTBD in dilute MeTHF.....	237
6.14 The spectral overlap regions from the normalised emission for PT and absorption for PHBD.....	239
6.15 Transient absorption profiles recorded after excitation of PT in toluene with a 70 fs laser pulse delivered at 400 nm.....	240
6.16 Transient absorption profiles recorded after excitation of PTTBD in MeTHF with a 70 fs laser pulse delivered at 400 nm.....	241
6.17 Component differential transient absorption spectra recorded for PTTBD in DMF following excitation with a 70 fs laser pulse at 400 nm.....	243
6.18 Basic model to show deactivation pathways following excitation of the pyrene unit in PTTBD.....	244
6.19 Relationship between the rate constant of energy transfer ( $k_{\text{EET}}$ ) and the Förster overlap integral ( $J_{\text{F}}$ ).....	245
6.20 Relationship between the rate constant of EET for PTTBD and the solvent polarity function (DF).....	247
6.21 Cyclic voltammogram for NAPBD .....	248
6.22 Absorption (black) and emission (red) spectra for NAPBD in MeTHF. ....	249
6.23 Collection of fluorescence up-conversion spectra for NAPBD in a range of solvents.....	250

## Compounds Nomenclature



# Chapter 1

## Research Aims & General Introduction



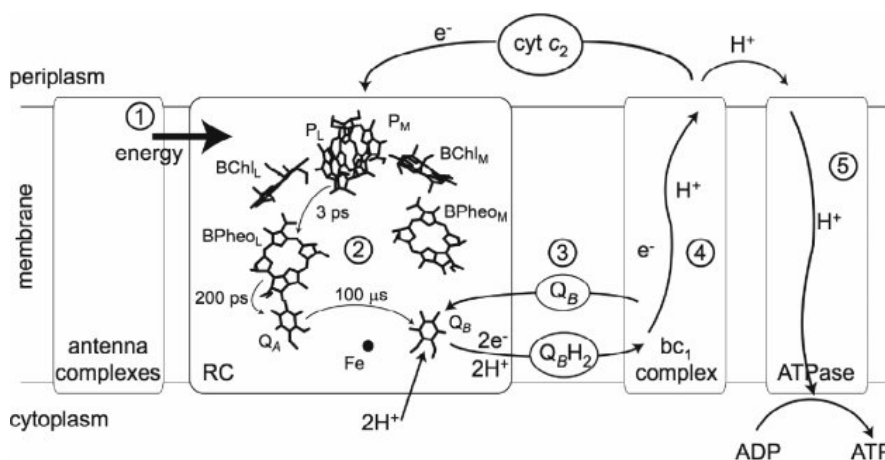
## 1.1 Nature Inspired Artificial Photosynthesis

### 1.1.1 Photoinduced Electronic Energy Transfer (EET) Process

#### 1.1.1.1 Nature Regulated Light-Harvesting Antenna Systems

Nature's efficiency of converting sunlight into chemically stored energy has inspired many scientists research efforts. The research field is commonly referred to as "artificial photosynthesis."<sup>1-4</sup> Via photosynthesis, natural systems collect, concentrate and convert light energy into electrochemical energy. The energy is converted into chemical potential energy, which can be stored in adenosine triphosphate and other compounds and utilized by carbohydrate based living organisms.

Photosynthetic species like most green plants and oceanic algae are capable of absorbing solar energy directly via their chlorophyll pigments. The porphyrin group is one of the molecules essential to complete the task of light-harvesting and photonic energy storage. The structure of chlorophyll pigments within the periplasmic space and cytoplasmic membrane alongside the energy transformation processes are illustrated in the following (Scheme 1.1).



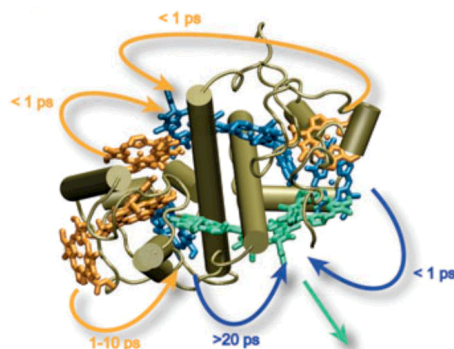
**Scheme 1.1.** The basic working of photosynthesis. 1: Excitation energy transfer to the reaction centre, 2: charge separation within the reaction centre, 3: Reduced hydroquinone QBH<sub>2</sub> released from the reaction centre, 4:

Oxidation of the hydroquinone and initiation of a proton gradient across the membrane, 5: Synthesis of ATP from ADP in ATPase which is driven by the proton gradient. Image courtesy to Lang & Köhler (2013).

Photons collected by chlorophyll molecules instigate resonance energy transfer, and energy is transferred throughout the chlorophyll molecule arrays. Within the energy transduction cascade the initially captured solar energy is stored at the reaction center protein complex via electron transport and photophosphorylation. Upon excitation, two electrons are lost from photosystem II and transferred to the mobile carrier molecule plastoquinone  $Q_B$ . Two protons from the stroma are picked up by  $Q_B$ , and this process is accompanied by the splitting of water molecules (which creates a gradient of hydrogen ions) and molecular oxygen. Electrons are then transferred to Photosystem I complex via the mobile carrier plastocyanin, where electrons are again energized by photons, and transferred to ferredoxin-NADP-reductase (FNR). Afterwards during the Calvin-Benson cycle (the photosynthetic dark reactions, which includes carbon dioxide fixation and reduction), two electrons and a hydrogen ion add to  $NADP^+$  to generate NADPH. The electron transport chain created hydrogen ion gradient assists ADP and  $P_i$  to generate ATP via ATP synthase. The mechanism is similar to the ATP synthesis route in mitochondria. The ATP and NADPH are part of the process for sugar production which acts as biological energy resource.<sup>5-6</sup>

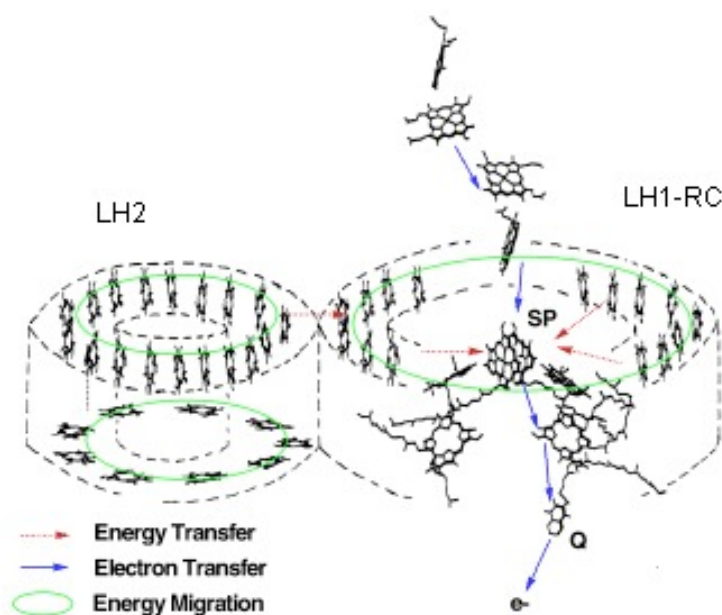
The crystal structures of the light-harvesting complex of plants and oceanic phototropic proteobacteria were determined in the 90's and on-wards.<sup>7-10</sup> The key components of photosynthesis system are the light harvesting antenna (LH2), the reaction centre (LH1-RC) and charge recombination site. The following is the schematic picture (Figure 1.1) of the plant light-harvesting pigment-protein complex of photosystem II (LHC-II).





**Figure 1.1.** Illustration of light-harvesting LHC-II system in the monomer. Energy transfer pathway and timescale are indicated in curly arrows. Green: energy acceptor Chl-a molecule; blue: other Chl-a molecule; orange: Chl-b molecule; brown: affiliated anchor protein. Image courtesy of Andrews, Curutchet and Scholes.<sup>11</sup>

Energy transfer is guided towards the reaction centre (LH1) from adjacent antenna complexes (LHII) with a high degree of efficiency. Each transfer stage is subject to an energy gradient, which ensures directed transportation of energy and prevents a random walk process that would otherwise greatly reduce the rate of delivering energy to the reaction centre. Electron transfer, resonance energy transfer and energy migration pathways within light-harvesting antenna and reaction centre in the oceanic phototrophic creature *Rhodospseudomonas acidophila* are illustrated in Figure 1.2.

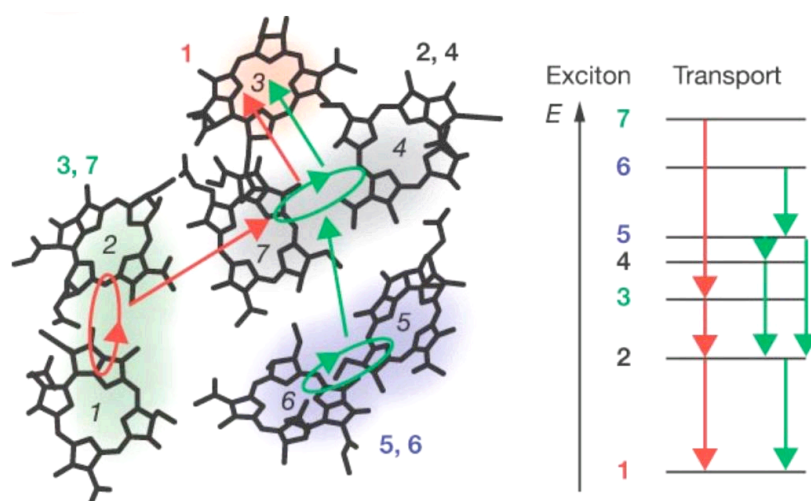


**Figure 1.2.** Illustration of electronic energy transfer and energy migration routes in *Rhodospseudomonas acidophila*. Image courtesy of Choi, Yamazaki, Yamazaki and Aida.<sup>12</sup>

Anchored by an affiliated pigment-protein, the porphyrin based chlorophyll molecules at the light harvesting arrays are arranged in a Stonehenge kind of fashion in order to collect photons. Once the photons are collected, it requires an electronic energy transfer (EET) process for them to be concentrated to the reaction centre. The charge separation reaction produces an electron, which is further transported to the charge recombination site at the photosynthetic membrane, where the chemical potential energy is created and stored.

#### 1.1.1.2 Study EET Process in Natural & Artificial Arrays

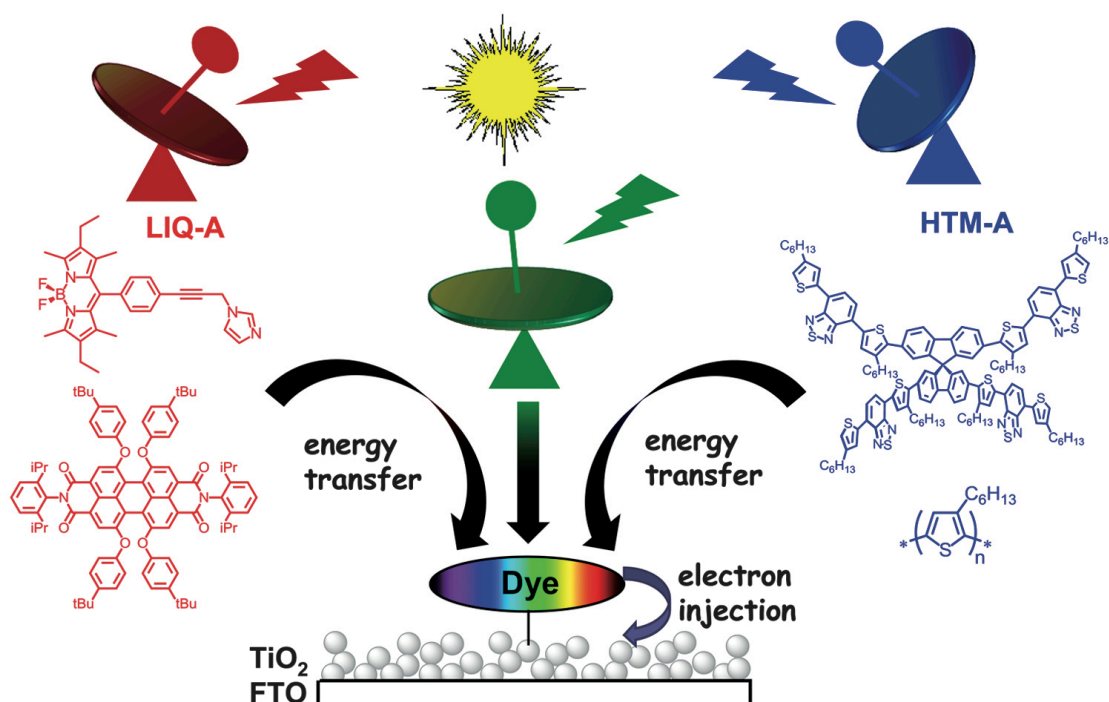
Mechanisms of electronic energy transfer have been researched for more than five decades with both natural and artificial molecular arrays. One of the well-understood mechanism models is the porphyrin-based green sulphur bacteria energy transfer channel, namely the Fenna-Matthews-Olson (FMO) complex. Monomers of FMO consist of seven Bacteriochlorophylls (BChl) embedded within protein scaffold (Figure 1.3).<sup>13</sup>



**Figure 1.3.** Energy transfer mechanism within Fenna-Matthews-Olson (FMO) complex model. Chlorophyll molecules are qualitatively overlaid, the reaction centre is labelled 3; light-harvesting antenna are labelled 1, 2, 5, 6, 4, 7. Exciton delocalization patterns are indicated in coloured shading.<sup>14</sup> Image courtesy of Fleming *et al.*

Hamiltonian and excitonic basis wavefunctions are determined at each chromophore, corresponding to energies and transition moments. Two main photoexcitation redistribution pathways are indicated by red and green arrows. Note that transfer process is not completely stepwise between closely spaced donor-acceptor pairs (e.g. BChl3 and BChl7), and intermediate transition moments (BChl5 and BChl6) are left out.

Many artificial photosynthetic systems have nature inspired design principles. Examination of electronic energy transfer processes can be conducted in solutions and in solid materials (e.g., crystalline materials, quantum dots, metal-organic frameworks and catalyst coated semiconductors).<sup>15-18</sup> One recent review article summarised key components of bio-inspired artificial light-harvesting antenna arrays, and electronic energy transfer processes within a solar cell system as represented in Figure 1.4.



**Figure 1.4.** Illustration of an artificial light-harvesting antenna-sensitizer solar cell. Image courtesy of F Odobel, Y Pellegrina and J Warnan. (2013).

Photon harvesting and energy transfer efficiency are optimised in the multichromophoric system. The device performance is recorded with a remarkable light-generated current density value ( $J_{sc}$ ) of  $20 \text{ mA}\cdot\text{cm}^{-2}$  to  $30 \text{ mA}\cdot\text{cm}^{-2}$ . The multiple sensitizers with complementary absorption spectra created an antenna effect to cover the broad region of 400–700 nm, and the whole system benefits from the high extinction coefficient.<sup>19</sup>

### 1.1.2 Mechanism of Förster Resonance Energy Transfer (FRET)

Regarding both natural photosynthetic systems and artificial assemblies, FRET – a theory that has many applications in bioengineering and medicinal chemistry - elucidates the mechanism of the excitation energy transfer between weakly coupled chromophores. FRET involves through-space interactions, and is complementary to the through-bond route where electron exchange interactions occur within strongly coupled chromophoric arrays. Photophysical measurements provide opportunity for the through-bond and

through-space mechanisms to be investigated separately, within carefully designed closely-coupled molecular dyad systems. In a donor-acceptor paired molecular system energy can be transferred through space, without the exchange of electrons. Resonance energy transfer is a non-radiative process, which does not require the collision of two atoms or two molecular systems, and is not mediated by the emission and re-absorption of a photon.<sup>20-21</sup>

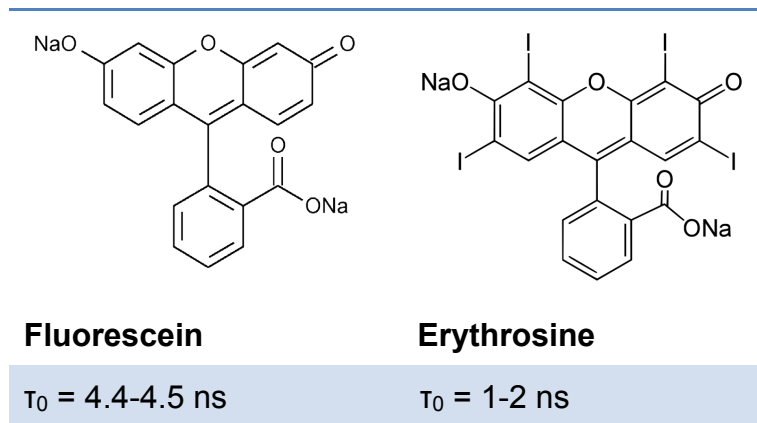
#### 1.1.2.1 The Chronicle of FRET

Ever since “the golden age of physics” onwards, the development of mechanistic research and practical application regarding electronic energy transfer (EET) has increased in popularity. The notion of resonance energy transfer study started very early on in the 20<sup>th</sup> century, and was accompanied by the appearance of new spectroscopic techniques, and followed the research development of electromagnetic (EM) field theory and quantum mechanics (QM).<sup>22</sup>

In 1918 Jean Baptiste Perrin managed to carry out fluorescence depolarization experiments within an activator-sensitizer system. Perrin was the pioneer to note that besides radiation and reabsorption, a transfer of energy - between the primarily excited molecule and its neighbours – “transfert d'activation” - could take place through a direct electrodynamic interaction. The exchange coupling mechanism - the “ resonance energy transfer ” - is via oscillating dipoles.

In 1920 the fluorescence polarization phenomenon was discovered by Weigert and Perrin (Jean Perrin's son), from the measurement of fluorescein, erythrosine, rhodamine and other dyes in solution (Figure 1.5). They derived an equation to note that the degree of fluorescence polarization is inversely proportional to the mobility of the emitting species, and proportional to the

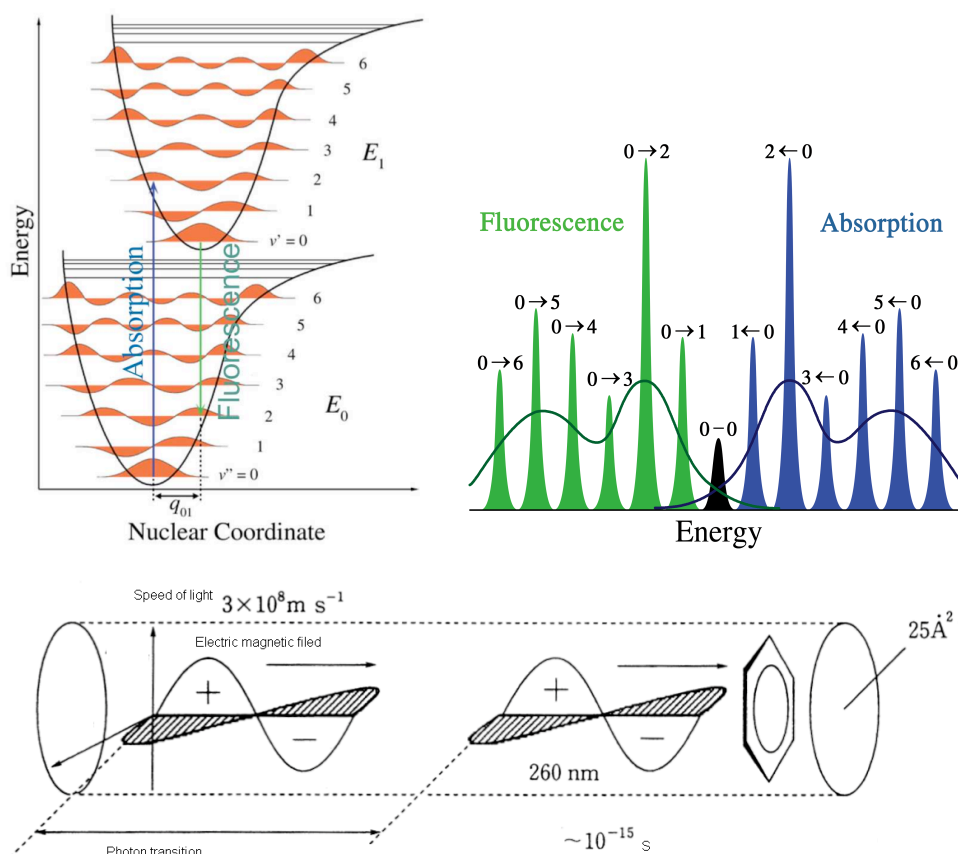
increase of medium viscosity and the increase of temperature.



**Figure 1.5.** Perrin's measurement of fluorescent lifetime on fluorescein and erythrosine.<sup>22</sup>

In 1923 the effect of fluorescence polarization was attributed to molecular rotation, and was later confirmed by Vavilov and Evshin through quantitative measurements. Later in 1926 Gaviola measured the excited state lifetime of fluorescein and erythrosine in H<sub>2</sub>O-glycerol with a phase-shift fluorometer. The results fit with Perrin's equation, even though the apparatus scale limit was only accurate to a nanosecond.

In 1925 Franck and in 1926 Condon analysed the absorption spectra and fluorescence emission spectra to predict possible electronic transition routes upon photon absorption between potential energy curves (Figure 1.6a left). The Franck-Condon principle for the electronic transition between potential energy states is described in terms of quantized nuclear vibrational modes. The excited electronic state redistribution is reflected in the angular distribution of the photon and electron energy.



**Figure 1.6.** (a) Left: schematic illustration of Franck-Condon energy coordinates; right: absorption and fluorescence transition states corresponding to the energy diagram. (b) Photon absorption event in organic molecule model. Image courtesy of Adolphs (2008) and Haruo (1999).<sup>23</sup>

In the view Figure 1.6 (b), upon absorption of a photon, benzene absorbs light at 254 nm wavelength, and the time required for one photon to pass through the molecule is calculated as:

$$t = 260 \text{ (nm)} / 3 \times 10^{17} \text{ (nm s}^{-1}\text{)} = 0.8 \times 10^{-15} \text{ s}$$

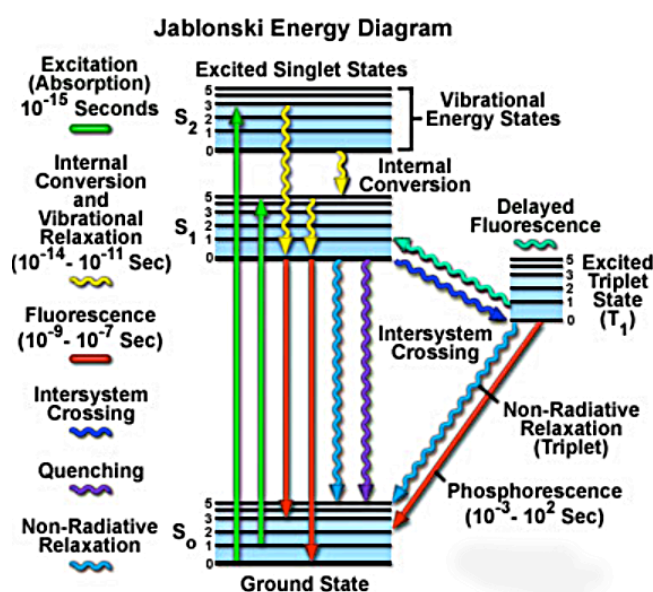
Because photon absorption happens within femtosecond timescale ( $10^{-15} \text{ s}$ ), and the vibrational movement of a nuclei along its oscillating electric field requires  $10^{-13} \text{ s}$ , it can be considered that during the transition the molecule's nuclei remain stationary. Thus, the electron transition takes place perpendicular to the nuclear coordinate. According to the Born-Oppenheimer approximation,<sup>23</sup> probability and intensity of electronic transitions are proportional to the squared integral of electronic transition moment times the

squared integral of vibrational overlap (Franck-Condon factor). The larger the energy gap separation and the more conformation difference results in better vibrational overlap integral during vertical transitions (Figure 1.6a right).

In 1927 Vavilov also defined the term quantum yield from the spectrum of fluorescein. In 1928 the term of dipole-dipole interaction was coined by Kallmann and London, and the parameter  $R_0$  was defined via applying quantum theory of resonance energy transfer between various atoms in the gas phase.

In 1932 Perrin published, inspired by Hallmann and London's theory, the qualitative discussion of the frequency-weighted spectral overlap of the donor fluorescence spectrum and the acceptor absorption spectrum. Quantum mechanical theory lead to the quantitative calculation of energy transfer between molecules in solution.

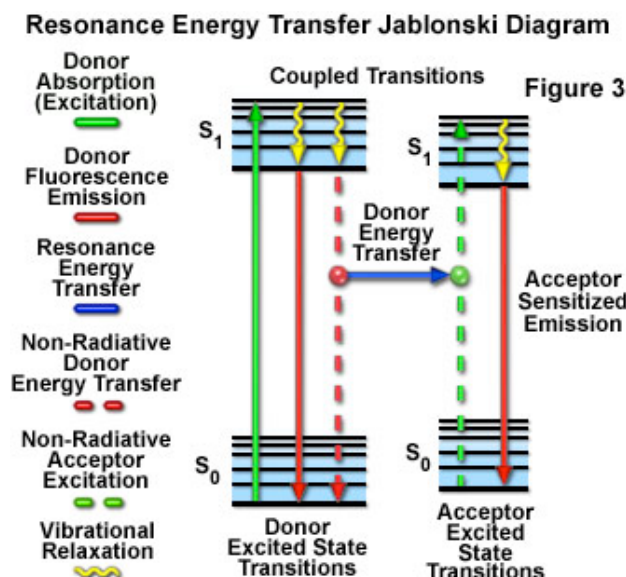
In 1935 the Aleksander Jablonski illustrated the energy diagram of possible redistribution pathways (Figure 1.7).



**Figure 1.7.** Jablonski diagram of excitation energy redistribution pathways. Image courtesy of Olympusmicro.<sup>24</sup>



In 1946, Theodor Förster stated the energy transfer process as being a non-radiative process (not associated with electromagnetic radiation) via inductive resonance transfer, which depends mainly on the Coulombic coupling (induced polarization) and dipole-dipole interactions within donor–acceptor dyads.<sup>25</sup>



**Figure 1.8.** Jablonski diagram of excitation energy redistribution via Förster type energy transfer. Image courtesy of Olympusmicro.<sup>24</sup>

The measurement of intrinsic fluorescence was performed later on in 1950 and standardized by the physical chemist and molecular spectroscopist Michael Kasha to form the Kasha–Vavilov rule. Put simply the measured luminescence quantum yield is independent of the wavelength of exciting radiation. The measurement also described that redistribution of excited state could be via photon emission or non-radiative processes :

$$\phi = k_r / (k_r + \Sigma k_{nr}) \text{ (Eq. 1)}$$

The calculation of fluorescence quantum yield  $\phi$  can be achieved via the equation of photons absorbed divided by photons emitted through fluorescence. It can also be represented by the radiative rate constant ( $k_r$ ) and non-radiative constant rate ( $k_{nr}$ ) as shown in Eq.1. In practice, the integrated

emission intensities of an unknown dye can be determined with respect to a reference compound (control fluorophore with known quantum yield).

The lifetime ( $\tau$ ) of the excited state is defined by the average time the molecule stays in its excited state. The lifetime can be determined by calculating the average time in the excited state by time-resolved measurements. Concepts regarding fluorescence property and spectroscopy measurements mentioned above are listed in Table 1.1.

Terms & Abbreviation	Concept Description	Unit	Measurement
<b>Molar extinction coefficient (<math>\epsilon</math>)</b>	Also called molar absorptivity, measures capacity of a fluorophore to absorb light at a given wavelength	$M^{-1}cm^{-1}$	<b>A given substance dissolved in a given solute the absorbance is constant and proportional to concentration.</b>
<b>Fluorescence quantum yield (<math>\Phi_f</math>)</b>	The ratio of photons absorbed to photons emitted through fluorescence. In other words the quantum yield gives the probability of the excited state being deactivated by fluorescence rather than by another non-radiative mechanism	NA	<b>The <math>\Phi_f</math> of a fluorophore is typically determined relative to a reference compound of known <math>\Phi_f</math> value</b>
<b>Fluorescence lifetime (<math>\tau</math>)</b>	The characteristic time that a molecule remains in an excited state before returning to the ground state	ns	<b>The time a molecule spends in the excited state determines by the sum of the kinetic constants of all deexcitation processes</b>

<b>Stokes shift</b>	The difference (usually in frequency units) between the spectral positions of the band maxima (or the band origin) of the lowest energy absorption and fluorescence /luminescence arising from the same electronic transition	cm <sup>-1</sup>	
<b>Brightness</b> ( $\epsilon\Phi_f$ )	The intensity of fluorescence signal at given excitation wavelength	NA	<b>Molar extinction coefficient multiplied by fluorescence quantum yield</b>
<b>FWHM</b>	The fluorescence full-width its half maximum histogram peak	nm	

**Table 1.1** Key terms in fluorescent spectroscopy measurements.<sup>20,21</sup>

Alongside the intrinsic parameter of molecular weight and the environmental factors of temperature and viscosity, other influencing factors on fluorescence emission have been studied by many researchers and include: polarity, hydrogen bonding, ion electric potential, quenchers, pressure and pH.

In early 90's the term smFRET (single-molecule FRET) was coined alongside the development of fluorescence microscopic imaging techniques.<sup>26-27</sup> Monitoring fluorescent dye labelled bio-molecular dynamics at single-molecule ultra fine resolution contributes greatly to the area of biomedical engineering research.

### 1.1.2.2 The Parameters within the FRET Equation

Förster theory states the rate for electronic energy transfer ( $k_{EET}$ ) is related to a number of parameters as shown in Equation 2:<sup>24</sup>

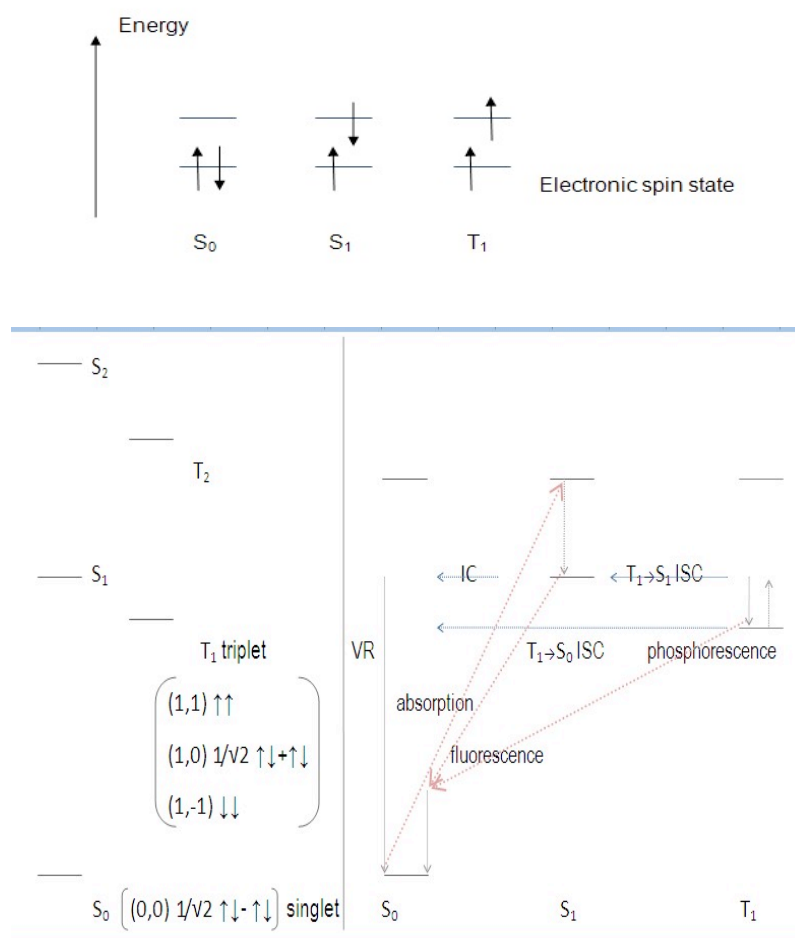
$$k_{EET} = \frac{8.8 \times 10^{-25} \kappa^2 \phi_D}{n^4 \tau_D R^6} J_F \quad (\text{Eq. 2})$$

Within the equation:  $\kappa^2$  is the orientation factor,  $\phi_D$  is the quantum yield of the

donor in absence of the acceptor,  $n$  is the refractive index of the solvent,  $\tau_D$  is the lifetime of the donor in absence of the acceptor,  $R$  is the donor-acceptor separation distance (in cm) and  $J_F$  represents the overlap integral (in  $\text{mmol}^{-1} \text{cm}^6$ ). The term  $\phi_A/\tau_A$  is immediately identified as the radiative rate ( $k_{\text{RAD}}$ ) for the donor alone.

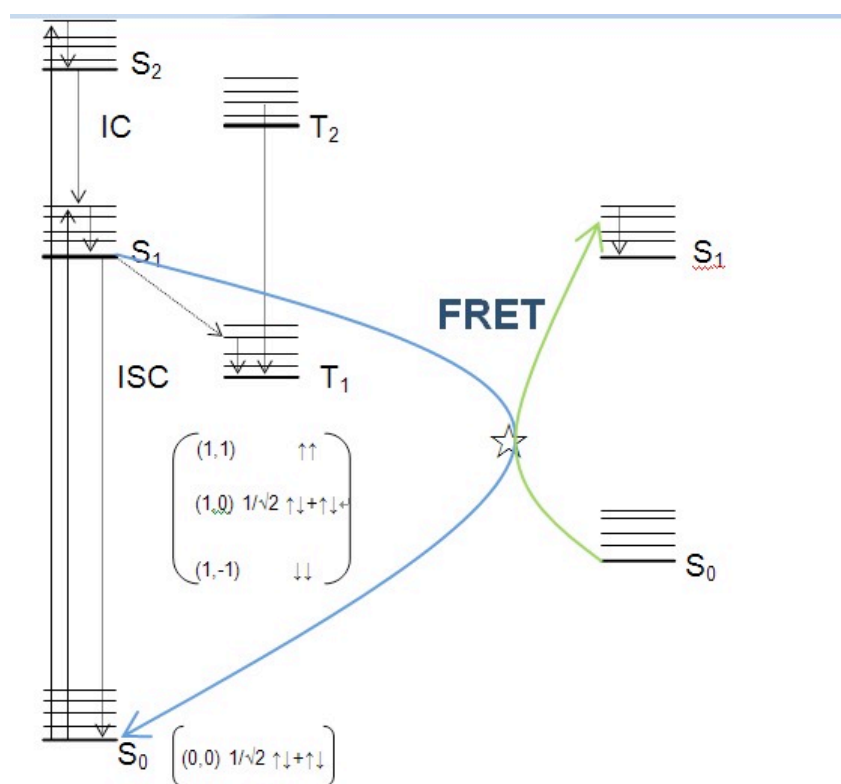
### 1.1.2.1 Terms & Conditions of FRET

Fluorophores (chromophores) live for around  $10^{-15}$ - $10^{-9}$  seconds in the electronic excited state, and can choose from fluorescence emission, non-radiative decay and excitation migration processes to return to the ground state (Figure 1.9). Electronic energy transfer happens within time/space scale of  $10^{-9}$  to  $10^{-6}$  m :  $10^{-12}$  to  $10^0$  s.



**Figure 1.9.** Electron spin states of excitation energy redistribution pathways.

The chromophore can return from the excited state to its ground state via electromagnetic radiation loss, which involves the emission of one quantum of light, and the acceptor reabsorbs the light. When radiation induces a transition electric dipole moment in the donor moiety the corresponding dipole moment in a neighboring acceptor moiety can be affected. Preliminary studies revealed that the Förster-type dipole-dipole energy transfer is associated with a  $S_1$ - $S_1$  electron transfer mechanism (Figure 1.10)<sup>20-21</sup>



**Figure 1.10.** Jablonski diagram of Förster resonance energy transfer between a donor-acceptor dyad. Blue line states the emission of donor moiety, green line states the absorbance of acceptor moiety. ISC: intersystem crossing; IC: internal conversion;  $S_1 \rightarrow S_0$ : fluorescence;  $T_1 \rightarrow S_0$ : phosphorescence.

Note that intersystem crossing (ISC) process between  $T_1 \rightarrow S_0$  or  $S_1 \rightarrow T_1$  requires spin-orbit coupling which facilitates the change of electron spin states. An internal conversion (IC) process depends on nuclear kinetic energy (vibrational relaxation). The energy gap between transition states are usually:

$S_1 \rightarrow T_1 < T_1 \rightarrow S_0 < S_2 \rightarrow S_1 \ll S_1 \rightarrow S_0$ ; efficient energy transfer between  $S_2 \rightarrow S_1$  state is of critical importance in photosynthesis.<sup>20-21</sup>

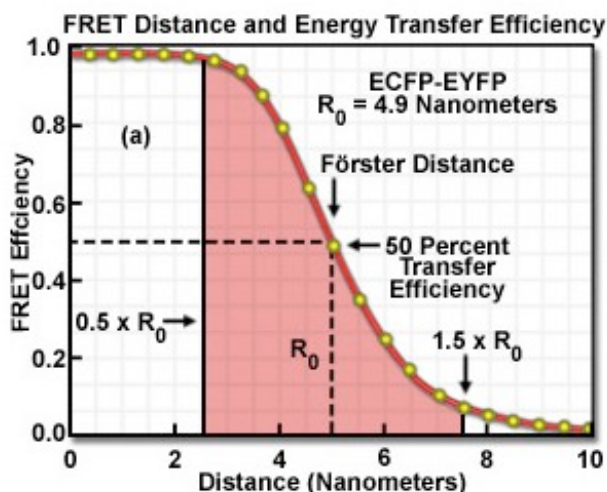
### The Förster Critical Distance

In case of a donor-acceptor molecule certain conditions for efficient Förster-type resonance energy transfer need to take place: the donor and acceptor moiety should be separated by a short distance (of the order of 0.5-10 nm). In typical case the  $R_0$  value is calculated from 20 to 100 Å. According to FRET theory, the energy transfer rate depends on the inverse sixth power (Förster) distance. Many literature reports that for a closely spaced donor-acceptor, the Förster distance ( $R_0$ ) is represented the separation distance where rate constant  $k_{EET} = 1/\tau_D$  ( $\tau_D$  is the donor lifetime)

$$k_{EET} = R^6 / (R^6 + R_0^6) \text{ (Eq. 3)}$$

$R$  = distance between of donor and acceptor;  $R_0$  = Förster critical distance

The FRET distance and energy transfer efficiency is illustrated in Figure 1.11.



**Fig. 1.11.** FRET dependency on separation distance between a donor and acceptor pair. Image courtesy of G J. Kremers (2006)<sup>28</sup>.

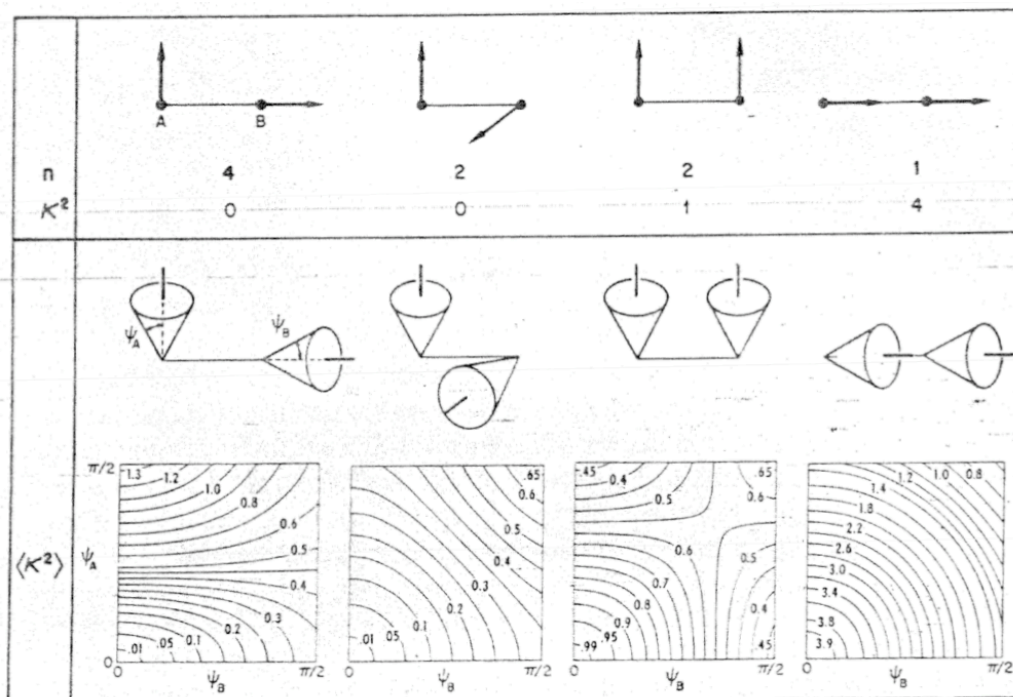
The Förster critical distance ( $R_0$ ) measured as the centre-to-centre distance between the donor and the acceptor is a parameter characteristic of a donor-acceptor pair, and represents the distance at which energy transfer efficiency is 50% of the maximum. This is related to several parameters as shown in the alternative version of the Förster equation below:

$$R_0^6 = \frac{(8.8 \times 10^{-25}) K^2 \Phi_D}{n^4} \int_0^\infty F_D(\nu) \epsilon_A(\nu) \frac{d(\nu)}{\nu^4} \quad (\text{Eq. 4})$$

( $n$ : refraction index;  $\Phi_D$ : quantum yield of fluorescence of the donor; the overlap integral are the final terms;  $\kappa^2$ : orientation factor)

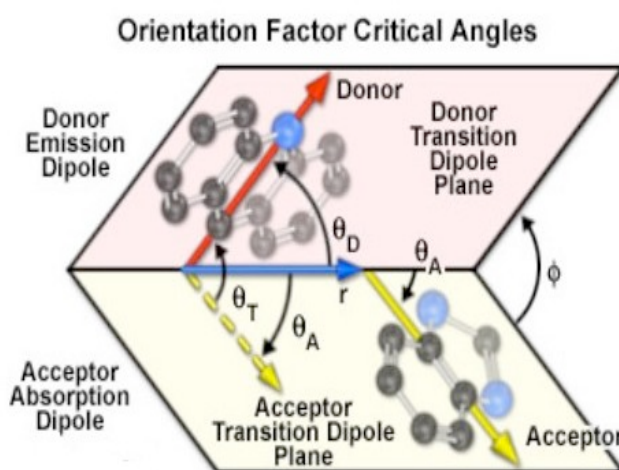
### The Orientation Factor

The angular alignment of the fluorescent dipoles and spatial arrangement of donor and acceptor moieties are represented by the orientation factor  $\kappa^2$ . The model of a classic electric near-field Hertzian dipole can also represent the quantum mechanical derived Hamiltonian of a FRET transition dipole pair. (Figure 1.12).



**Fig. 1.12.** (a) Orientation factor in Hertzian dipole alignments. Image courtesy of Eisinger (1970).<sup>29</sup>

Energy transfer efficiency depends on the relative intramolecular orientation of the transition moment vector dipoles between the donor and acceptor moieties (Figure 1.13).



**Figure 1.13.** Illustration of critical angles in equation of orientation factor calculation Image courtesy of Olympusmicro.<sup>24</sup>

Within the equation  $K^2$  can be calculated via:



$$\begin{aligned}\kappa^2 &= (\cos \theta_T - 3\cos \theta_D \cos \theta_A)^2 \\ &= (\sin \theta_D \sin \theta_A \cos \Phi - 2\cos \theta_D \cos \theta_A)^2 \text{ (Eq. 5)}\end{aligned}$$

In an average distribution dipole vector model  $\kappa^2 = 2/3$ .

### Overlap integral

The overlap integral  $J(\lambda)$  term is given by the equation below:

$$J(\lambda) = \frac{\int_0^\infty F_D(\lambda) \epsilon_A(\lambda) \lambda^4 d\lambda}{\int_0^\infty F_D(\lambda) d\lambda} \quad \text{(Eq. 6)}$$

$F_D(\lambda)$  : the integrated fluorescence spectrum of the donor

$\epsilon_A(\lambda)$  : the molar decadic absorption coefficient of the acceptor

Spectra overlap is critical to ensure that energy transfer is always forward (from donor to acceptor). Back-transfer is thus usually avoided because of the intramolecular vibrational redistribution (IVR) created by the Stokes shift. The value of the overlap integral for forward energy transfer is generally much larger than the corresponding overlap integral for back transfer, and the excited state of acceptor is always lower in energy than the donor excited state.<sup>20,21</sup>

## 1.2 The Chemistry of BODIPY Compounds

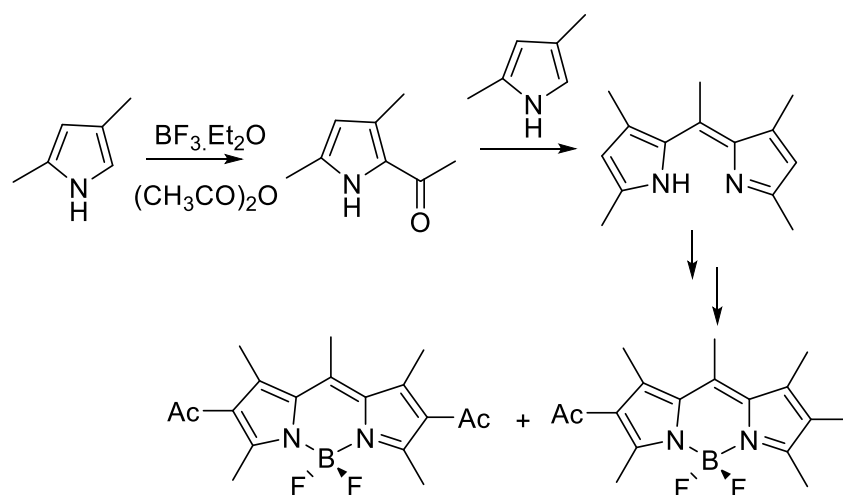
### 1.2.1 Synthesis & Modification

Many artificial photosynthetic systems consist of porphyrin-based chromophores. Known as “porphyrin’s little sister”, boradiazaindacene compound (IUPAC name 4,4-difluoro-4-borate-3a-azonia-4a-aza-s-indacene; trade mark BODIPY), is a new compound with tremendous application for its

unique chemistry practicality and versatility. Many modifications of Bodipy based systems have been carried out in the past few decades, and compounds continue to draw considerable research effort.<sup>30-31</sup>

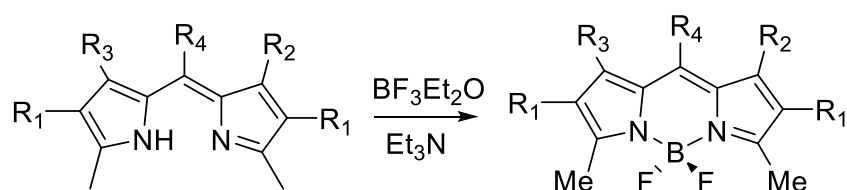
### 1.2.1.1 The Scaffold

In 1968, Treibs and Kreuzer managed to synthesise the pioneering compounds of boradiazaindacene fluorophores.<sup>32</sup> The synthetic method was described as proceeding via an electrophilic substitution of 2,4-dimethylpyrrole with acetic anhydride and catalyzed by  $\text{BF}_3 \cdot \text{Et}_2\text{O}$  as the Lewis acid. (Scheme 1.2).



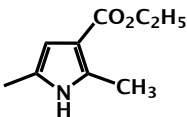
**Scheme 1.2.** Electrophilic substitution route of Bodipy synthesis developed by Treibs and Kreuzer.

An alternative reaction is to chelate boron trifluoroetherate to the intermediate dipyrromethene, and use an organic base like triethylamine to remove the proton on the pyrrole group. Using this method a series of F-BODIPY dyes in yields between 40% - 70%<sup>32</sup> were prepared (Scheme 1.3).



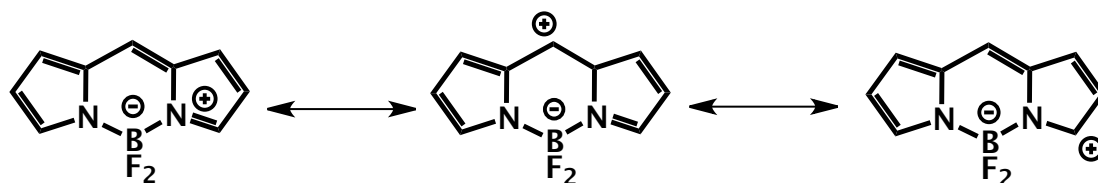
**Scheme 1.3.** Base catalysed route of Bodipy synthesis developed by Treibs and Kreuzer.

Various R groups could be incorporated in the Bodipy core which “tune” the dyes’ properties as illustrated in Table 1.2.

R <sub>1</sub>	R <sub>2</sub>	R <sub>3</sub>	R <sub>4</sub>
H	CH <sub>3</sub>	CH <sub>3</sub>	H
CO <sub>2</sub> C <sub>2</sub> H <sub>5</sub>	CH <sub>3</sub>	CH <sub>3</sub>	CH <sub>3</sub>
CO <sub>2</sub> C <sub>2</sub> H <sub>5</sub>	CH <sub>3</sub>	CH <sub>3</sub>	HO5
CO <sub>2</sub> C <sub>2</sub> H <sub>5</sub>	CH <sub>3</sub>	CH <sub>3</sub>	C <sub>2</sub> O <sub>5</sub>
CO <sub>2</sub> C <sub>2</sub> H <sub>5</sub>	H	H	H
CO <sub>2</sub> C <sub>2</sub> H <sub>5</sub>	H	H	
CO <sub>2</sub> C <sub>2</sub> H <sub>5</sub>	CH <sub>3</sub>	CH <sub>3</sub>	CN

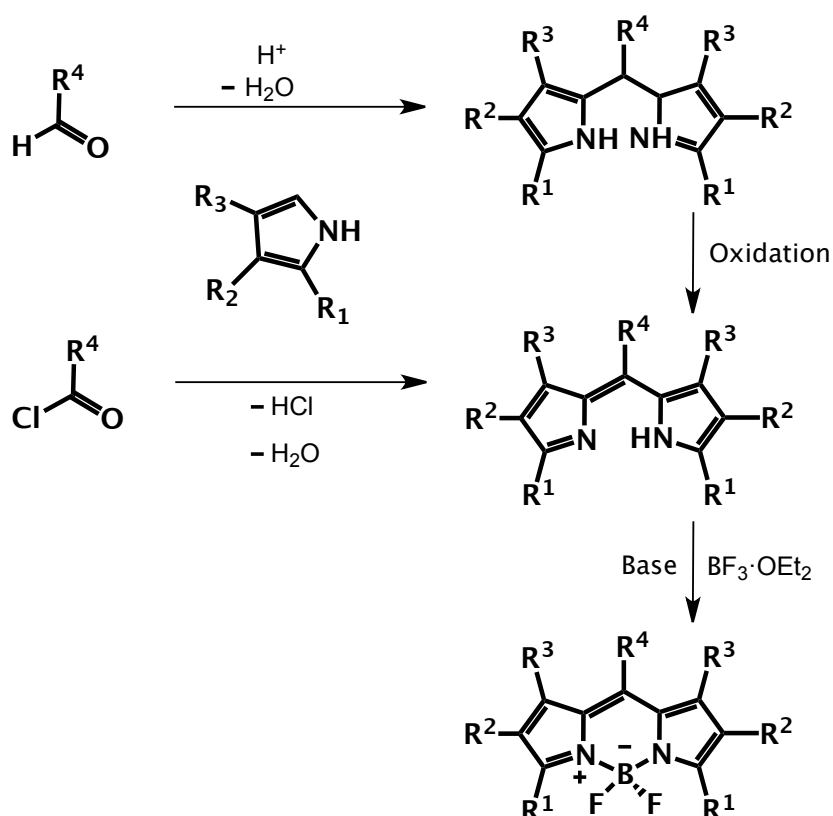
**Table 1.2.** Series of Bodipy compounds synthesised by Treibs and Kreuzer.

In drawing out the dipyrin segment a zwitterionic structure is often shown, where a negative charge is placed on the boron and the one nitrogen is positive. In coordination chemistry terms this bond is a simple dative covalent bond, but using the notation it is possible to draw out resonance structures (Scheme 1.4). Using the resonance notation it is possible to explain the reactivity of the dipyrin core.



**Scheme 1.4.** The resonance equivalents of the Bodipy core.

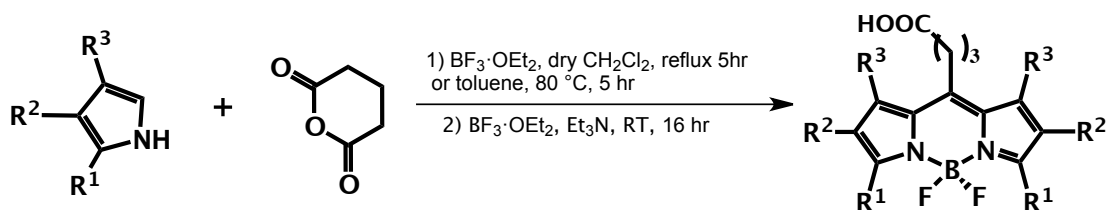
Other synthetic routes to the Bodipy platform are well established, the basic methods to the unit are presented in Scheme 1.5.<sup>30</sup> In the top case the starting material is the aldehyde and by this route the intermediate dipyrromethane is produced; this must be oxidised to the dipyrromethene before chelation. If one starts from the acid chloride the oxidation step is not required, since the meso carbon is already in the correct oxidation state.



$R^4$  = alkyl, aryl

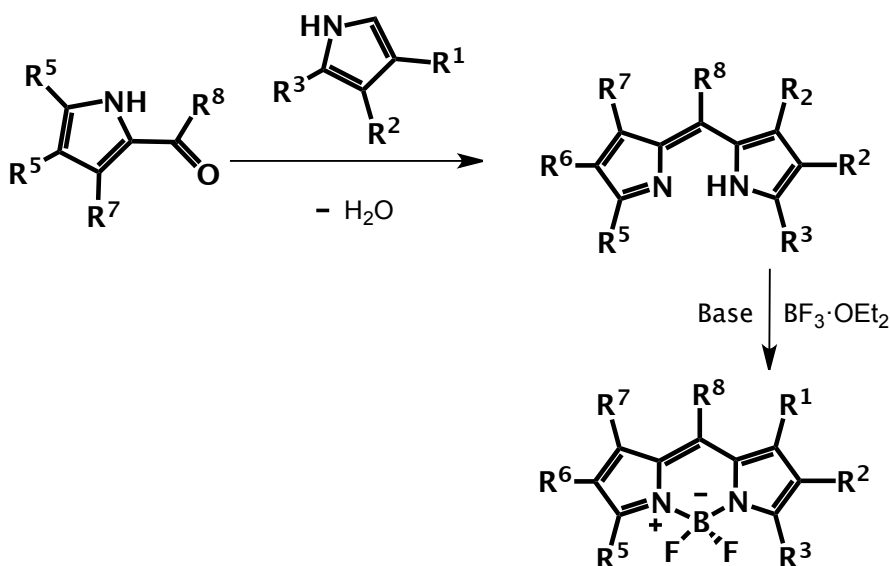
**Scheme 1.5.** General synthetic route of the F-Bodipy platform starting from either and aldehyde or acid chloride.

Preparation of the Bodipy platform can be achieved from an acid anhydride, like glutaric anhydride or succinic anhydride. The unique feature of this method is the generation of a free carboxylic acid moiety at the meso position, which is good for the creation of a further bioconjugate (Scheme 1.6).<sup>30</sup>



**Scheme 1.6.** Preparation of the F-Bodipy platform via succinic anhydride.

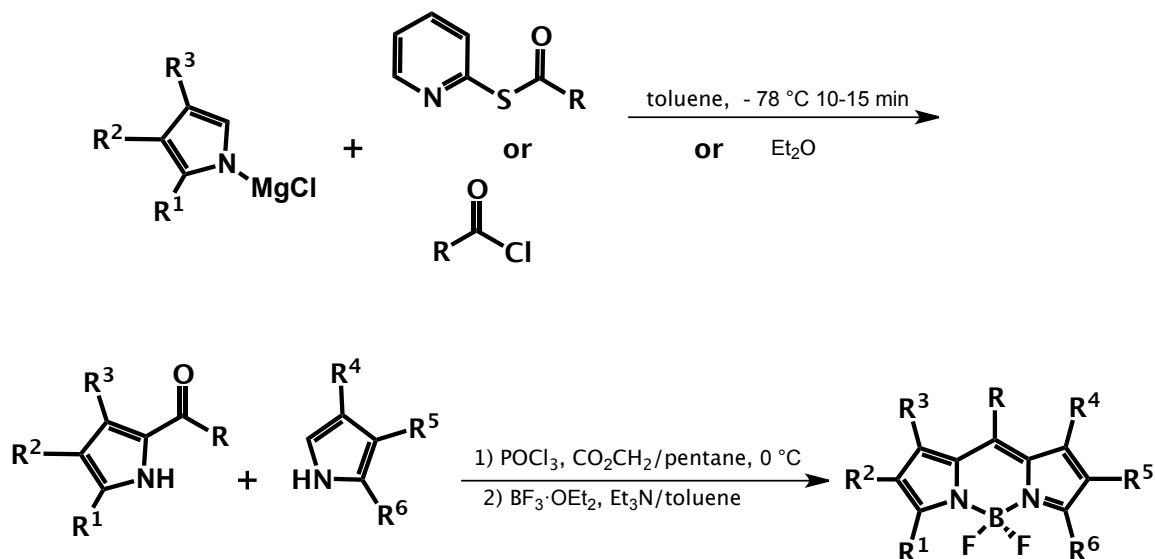
Many literature examples have reported the synthetic procedure for producing the asymmetric Bodipy platform (Scheme 1.7), which usually involves two different substituted pyrrole moieties.<sup>30</sup> In this method, however, one of the pyrrole groups must contain a carbonyl functional group. Thus, a downside of the procedure is the requirement in some cases to prepare the necessary carbonyl-based pyrrole.



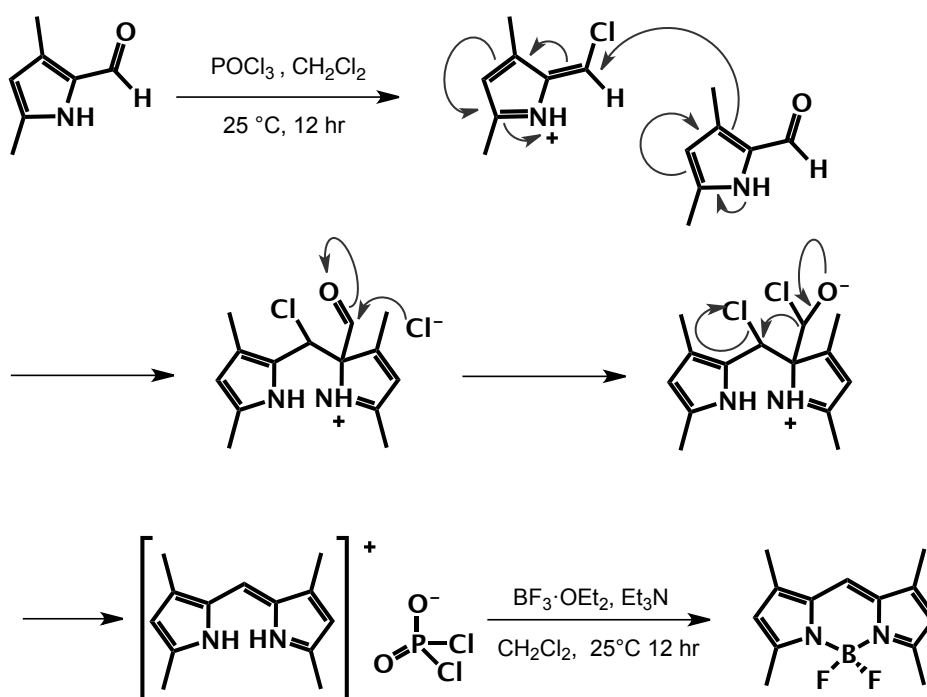
**Scheme 1.7.** General synthetic route to asymmetric Bodipy compounds.

Another vastly implemented synthetic route to condense pyrrole groups is via the Vilsmeier-Haack reaction (Scheme 1.8). The POCl<sub>3</sub> reacts with pyrrole-2-carbaldehyde to give a chlorovinyl reagent, and is then followed by

electrophilic attack from the carbon of another pyrrole-2-carbaldehyde. The intermediate cation then leads to formation of the dipyrromethene (Scheme 1.9).<sup>31</sup>



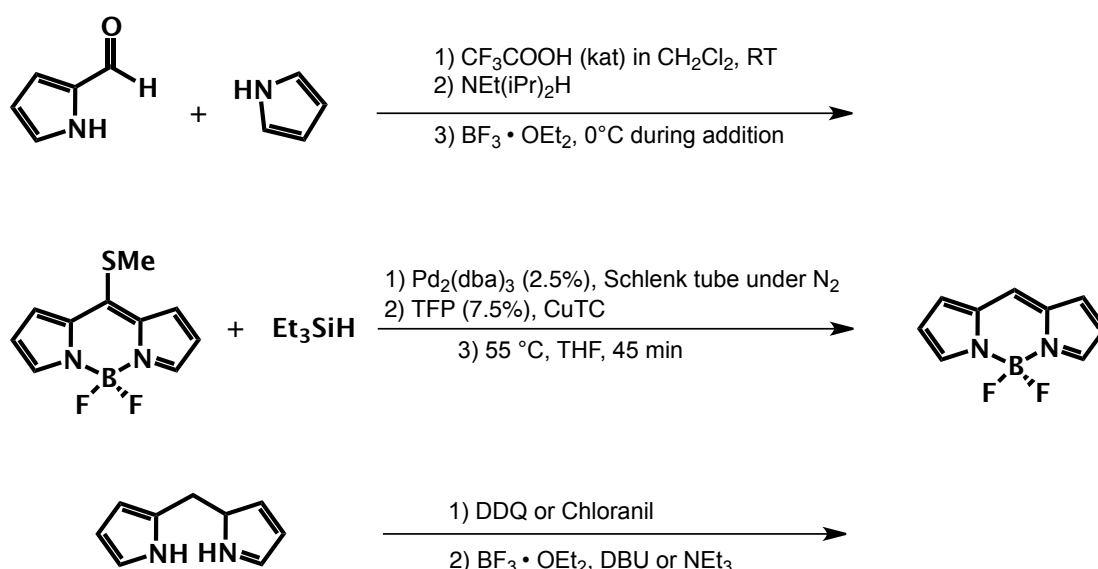
**Scheme 1.8.** Synthesis of Bodipy platform via Vilsmeier-Haack reaction.



**Scheme 1.9.** Mechanism of  $\text{POCl}_3$  catalysed Bodipy platform synthesis.

Alongside the vast majority of substituent-activated Bodipy dyes, it was not until 2009 that the synthesis of the parent

4,4-difluoro-4-bora-3a,4a-diaza-s-indacene core was reported. Jung and co-workers reported the MacDonald [2+2] condensation reaction, catalyzed by trifluoroacetic acid, to condense pyrrole (1 equiv.) with pyrrole-2-carbaldehyde (1.15 equiv.). The acquired unsubstituted dipyrin was then chelated to the boron trifluoroetherate in a low yield of 8%.<sup>32</sup> Tang and Peña-Cabrera's team synthesized the Bodipy core by reducing the thiomethyl Bodipy precursor; the measured fluorescence quantum yield in water is 90%.<sup>33</sup> It is not obvious why a purely organic molecule is soluble in water. Tram *et al.* carried out oxidation of dipyrromethane at  $-78^{\circ}\text{C}$ . The 5-10% yield of the desired compound was attributed to the instability of the dipyrin intermediate, which was reported stable only under temperatures of  $-40^{\circ}\text{C}$  (Scheme 1.10).<sup>34</sup>

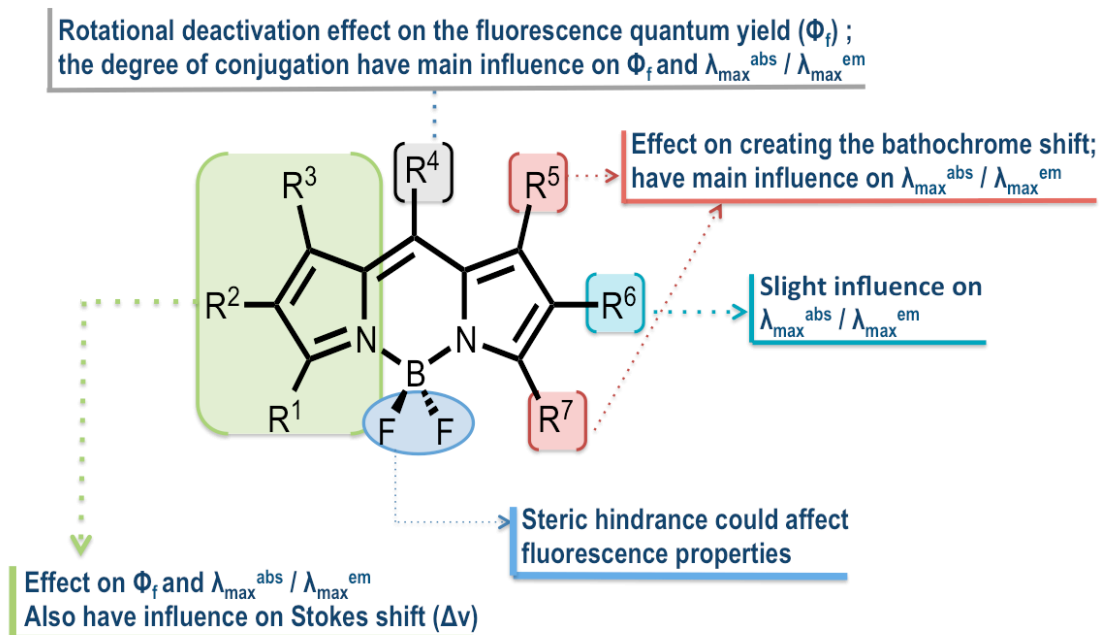


**Scheme 1.10.** Synthetic methods toward preparation of the Bodipy parent core.

### 1.2.1.1 Modifications

The fluorine atoms and the pyrrole skeleton of a parent Bodipy core can be substituted with many different functional moieties (Figure 1.14). As illustrated in Figure 1.14 these changes can have a major affect on the properties of the dye. It is very noticeable that a Bodipy unit without any substituents on the pyrrole groups, but an aromatic ring in the meso position, display low quantum

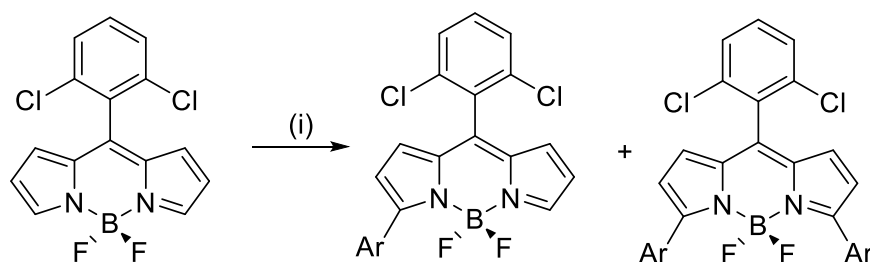
yields. This point will be discussed in later chapters.



**Figure 1.14.** Conformational modification effects on the spectroscopic properties of the Bodipy core. Content of image courtesy of Galangau (2012) and Krüger (2008).<sup>36-37</sup>

#### 1.2.1.1.1 Modification at the Pyrrole Skeleton

Boens' group recently reported the Pt(II) catalyzed C–H arylation reaction and added an aromatic moiety directly to the 1,7-position of the Bodipy core. (Scheme 1.11a).<sup>37</sup>

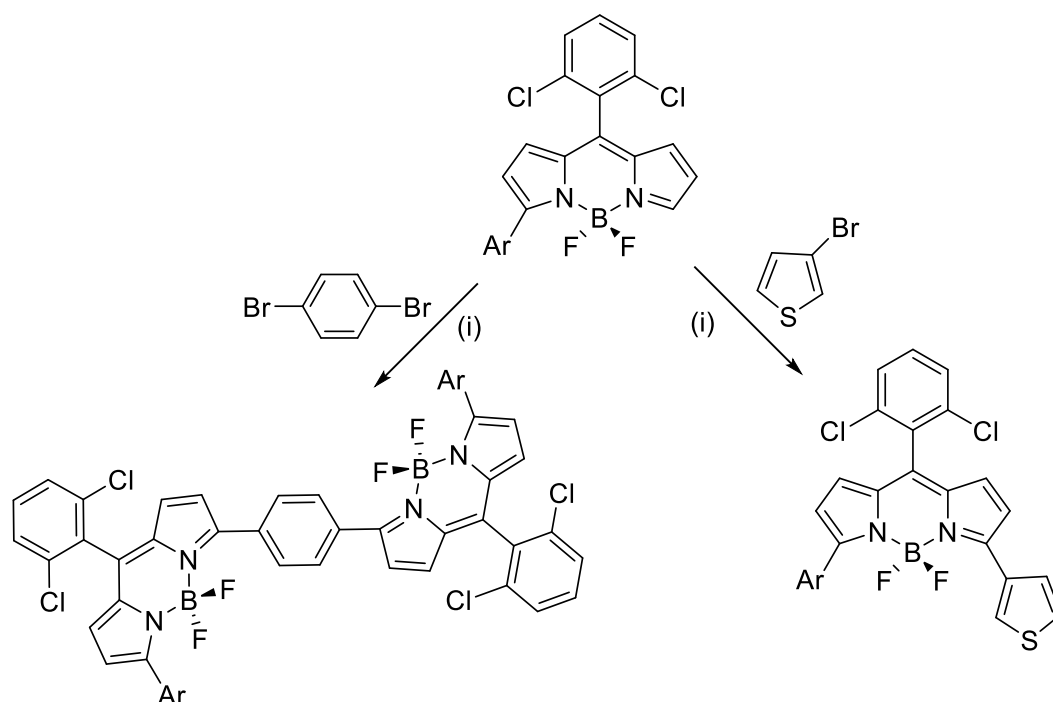


**Scheme 1.11a.** One-step synthesis of 1,7-substituted Bodipy compounds. Reaction conditions (i): Pd(OAc)<sub>2</sub> (5-10 mol %), HPCy<sub>3</sub>BF<sub>4</sub> (10 mol %), K<sub>2</sub>CO<sub>3</sub> (2-4 equiv), PivOH (catalytic amount) in toluene 100°C 4 days.

Aromatic substituents including phenyl, 4-anisyl, 4-(dimethylamino)-phenyl,



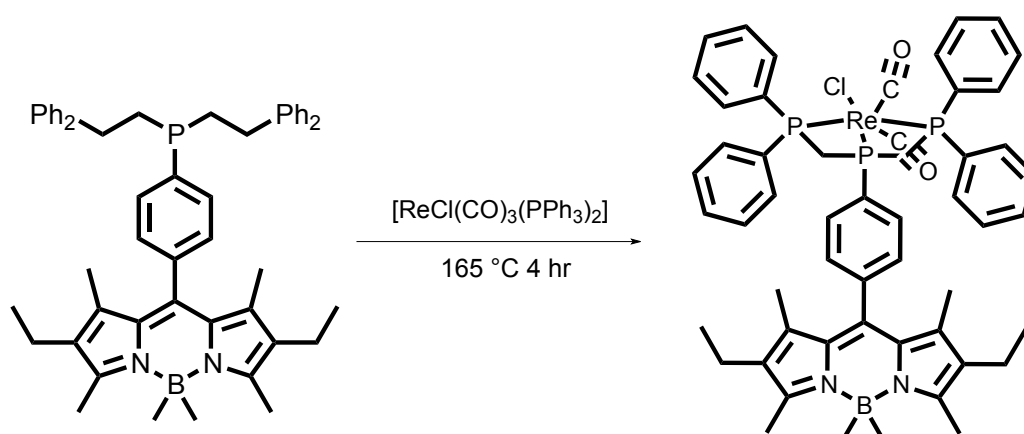
3-thienyl, 4-cyanophenyl mesityl, 1-naphthyl could be introduced easily into the Bodipy core. The novel synthetic method involved an unhindered Bodipy which was reacted in an apolar solvent with palladium(II) acetate and tricyclophosphine tetrafluoroborate and bromo-aromatic compounds. A catalytic amount of pivalic acid (2,2-dimethylpropanoic acid) was added to accelerate the reaction to completion. The mono-arylsubstituted derivative could be further activated to produce unsymmetrical systems. (Scheme 1.11b)



**Scheme 1.11b.** Asymmetric synthesis via C-H arylation. Reaction conditions (i): Pd(OAc)<sub>2</sub>, HPCy<sub>3</sub>BF<sub>4</sub>, K<sub>2</sub>CO<sub>3</sub>, PivOH (catalytic amount) in toluene 100°C 4 days.

#### 1.2.1.1.2 Modification at the Meso-Position

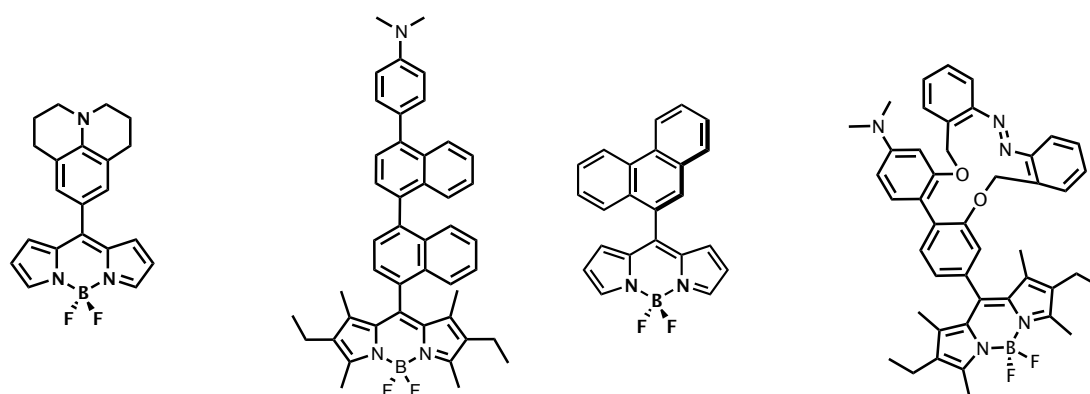
Higham's team recently reported the *ab initial* air-stable primary phosphino ligand, 1,4-bis(diphenylphosphino)butane (DPPB) with diethyl phosphite were applied, incorporating to the Bodipy fluorophore in an *ad hoc* manner. The reaction was catalyzed by palladium(II) acetate to convert the bromophenyl-moiety at meso-position of Bodipy into 4-diethylphosphonato)phenyl- moiety.<sup>38</sup>



**Scheme 1.12.** Example of a Bodipy incorporating a phosphine group and its rhenium complex.

The system could further be activated to chelate metal, meanwhile adding functionality via modification at methyl- / ethyl- units at the Bodipy skeleton.

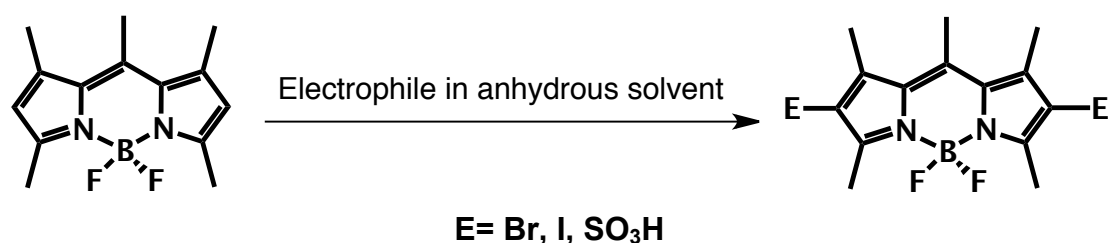
Molecular Photonic Laboratory members have reported a great many rationally designed meso-modified systems (Figure 1.15). The effect of molecular conformation on electronic and photophysical properties have been thoroughly examined, in order to investigate energy and charge transfer processes and application as viscosity probes and optical switches.<sup>39-42</sup>



**Figure 1.15.** Examples of meso-modified Bodipy systems made by MPL members.

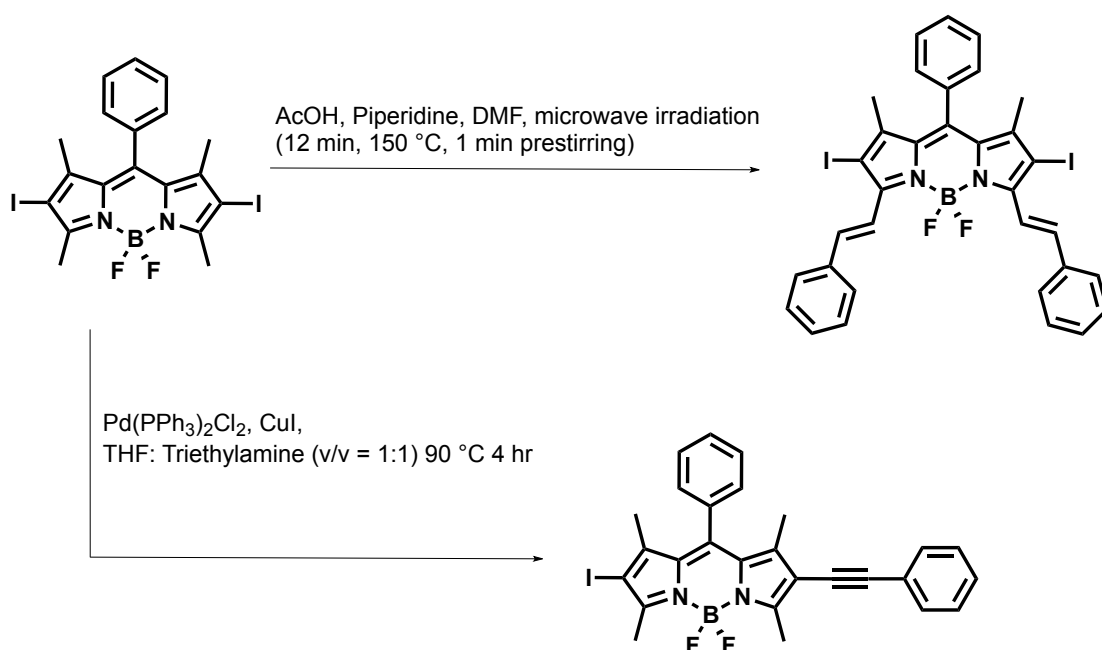
### 1.2.1.1.3 Electrophilic Substitution & Cross-coupling Reactions

Electrophilic substitution at the 2- and 6- positions (Scheme 1.13) is possible and adds substituents such as bromine, iodine or sulphonate groups directly to the chromophores. Heavy atoms introduce an enhancement in intersystem crossing efficiency ( $\Phi_{isc}$ ), from the lowest singlet excited state to the triplet state via the internal heavy-atom effect.<sup>30,31</sup>



**Scheme 1.13.** Electrophilic substitution on the Bodipy core.

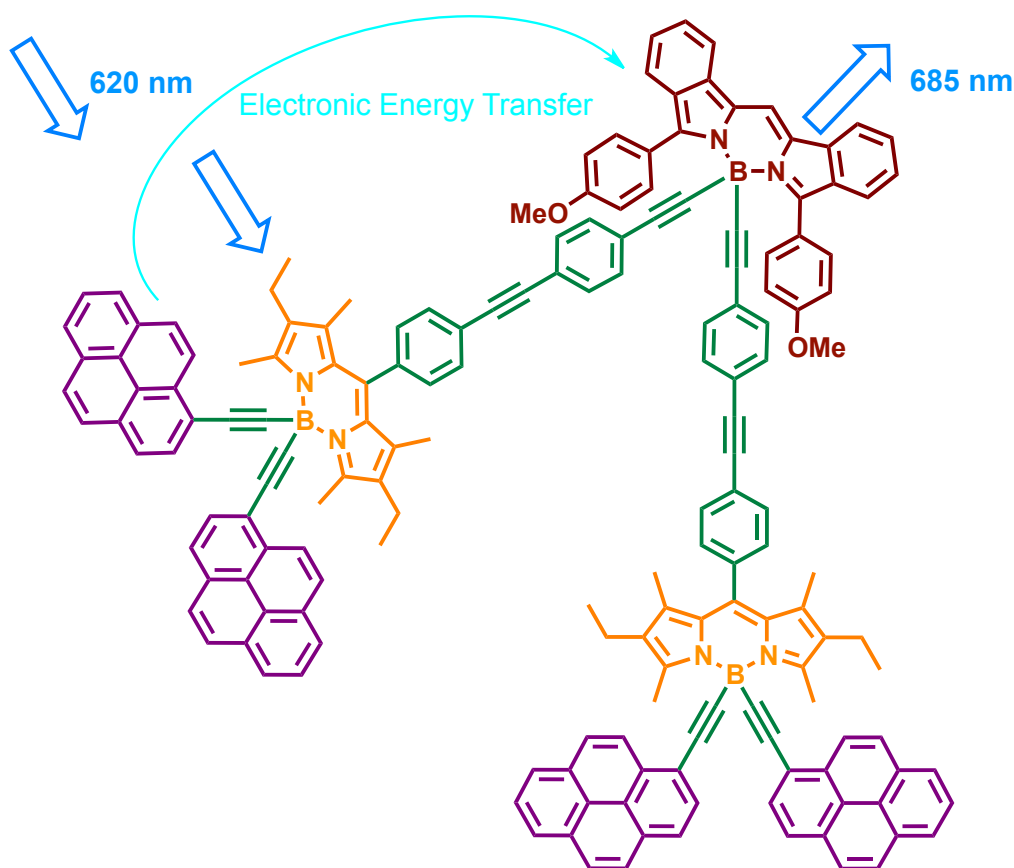
Metal catalyzed cross-coupling reactions are of great importance and can be used to connect substituent group onto the Bodipy group. A halogen atom in pyrrole skeleton can be exploited to make sophisticated scaffolds containing ethyne, ethene and aryl groups via a series of carbon-bond forming reactions. (Scheme 1.14).



**Scheme 1.14.** The 2,6-position of F-Bodipy activated by cross-coupling reactions.<sup>30</sup>

#### 1.2.1.1.4 Modification at the Boron Atom

A new scope of diversity-oriented Bodipy modification is to replace the two fluorine atoms using ethynyl-lithium reagents. Using this type of chemistry groups such as acetylene, tolyl, naphthyl, pyrenyl, fluorenyl and terpyridinyl moieties can be incorporated at the boron centre. By extensive extrapolation from the boron it is possible to construct a family of "E-Bodipy" systems. The reaction condition of alkyl-lithium Grignard reagents are mild and tolerate functional groups (e.g., phenylethynylpyrene, pyrene and 4'-terpyridine) at the meso-position of the Bodipy core. The B-F replacement product is very stable, thus making it an ideal synthetic protocol for constructing multi-chromophoric systems.<sup>43</sup>



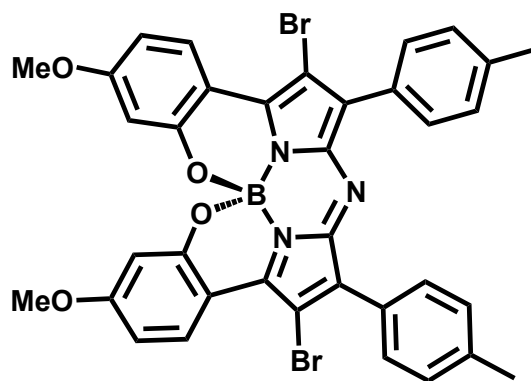
**Figure 1.16.** An energy transfer cassette based on an E-Bodipy system.

An energy transfer cassette system has been synthesized with functionalized 1,4-phenylene-diethynylene oligomer repeating units connecting the boron of

one Bodipy core, and the meso-position of an affiliated Bodipy; the affiliated Bodipy was also acetylene modified at the boron atom and connected to pyrene residues (Figure 1.16). A photophysics study validated the respective conjugation length dependence and bridge-mediated effect on intramolecular electronic energy transfer.

#### 1.2.1.1.5 Aza-Bodipy

Azadipyrromethene can be prepared via the addition of nitromethane to chalcones in the presence of cumene or isopropyl alcohol and are catalysed by ammonium acetate. Chelation of the  $\text{BF}_2$  unit and intramolecular phenolic oxygen-fluorine displacement results in the formation of a benzo{1,3,2}oxazaborinine condensed aza-Bodipy. (Figure 1.17). Emission is reported around 688-782 nm, which matches to the near-infrared (NIR) region (i.e., 700~1000 nm), and thus make B-O chelated aza-Bodipy compounds adequate as *in vivo* molecular imaging probes.<sup>44</sup>

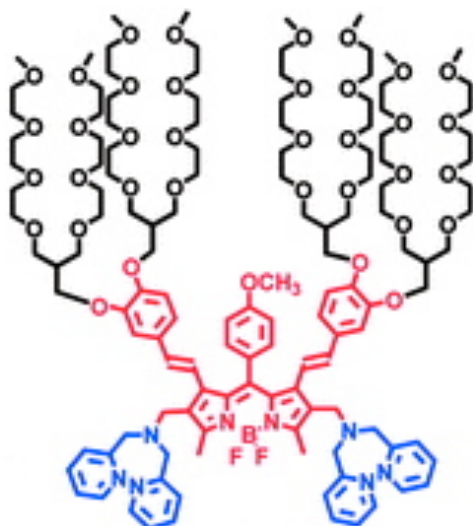


**Figure 1.17.** Example of a B-O chelated aza-Bodipy system.

#### 1.2.1.1.6 Build-in Water Solubility

Good water solubility of fluorophore systems is often required when operating in biological environments. Enhanced water-solubility can be achieved via substitution of a highly water soluble side chain. The water soluble Bodipy compound presented in Figure 1.18 contains a solubility-modified

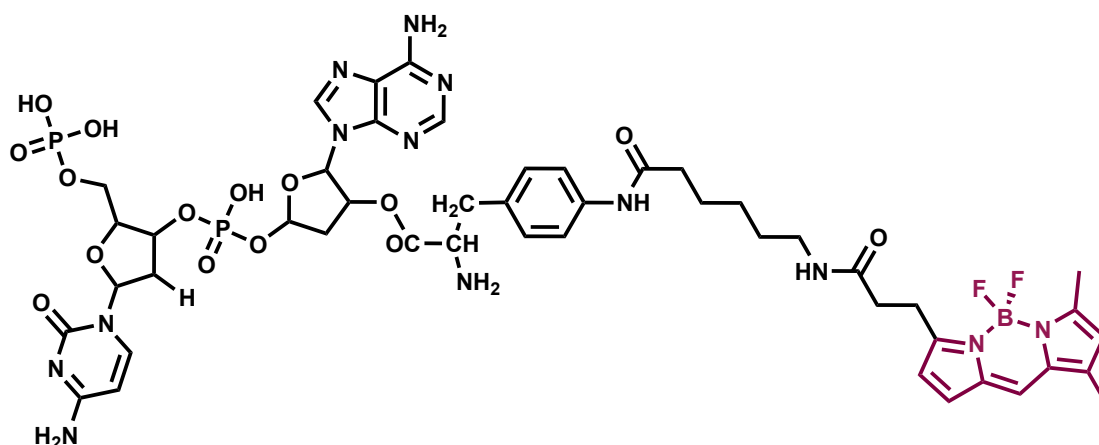
benzaldehyde at the Bodipy core, and was synthesized via reaction of a 3,4-dihydroxybenzaldehyde with a brominated branched oligo(ethylene glycol)methyl ether under basic conditions ( $K_2CO_3$ , DMF,  $80^\circ C$ ).<sup>45</sup>



**Figure 1.18.** A water soluble tetra-styryl substituted Bodipy. Image courtesy of H. Liu (2013).

#### 1.2.1.1.7 Bio-Conjugate Systems

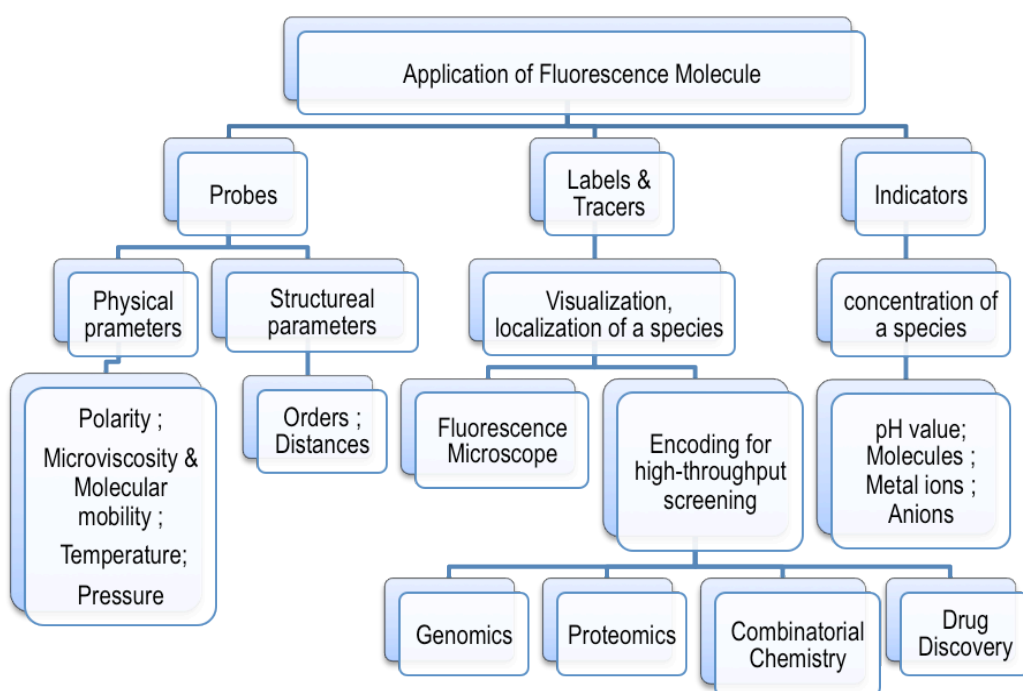
Specific recognition on the molecular level is aided by the development of fluorescence labelled high-contrast imaging probes. Bodipy dyes are among the most popular commercial fluorescent markers with applications ranging from *in-situ* cellular labelling, to *in-vivo* protein tagging, DNA labelling, sugar molecule labelling and to modification and functionalization of bionanoparticles and polymers.<sup>48</sup> The amino acid system presented in Figure 1.19, where an aromatic ring is bonded to a side chain of an amino acid, is labelled with an asymmetric Bodipy via an amide bond to the phenyl moiety. The amino acid can undergo a translation process to construct a fluorophore incorporated into a tRNA protein.<sup>46</sup>



**Figure 1.19.** An asymmetric Bodipy incorporated into an amino acid.

### 1.2.2 Applications & Development

Alongside photophysical mechanistic studies, FRET and fluorescent dyes have a broad range of applications covering, for example, protein dynamism and evolvability, immunoassay, protein folding, signal transduction, ion ( $\text{Ca}^+$ ) concentration measurements.<sup>47-48</sup> Conformational dynamics information and spatial proximities can be acquired in real-time and intra-operative monitoring can be achieved via analysis of spectroscopic data. In cooperation with the fast-laser technique of time-correlated single-proton counting and fluorescence lifetime imaging microscopy, resolution of FRET assisted microscopy can achieve femtolitre level monitoring in tissue and cellular environments. For brevity a broad range of molecular fluorescence applications are categorized in Table 1.3.<sup>48</sup>



**Table 1.3.** Applications of fluorescent molecules.

### 1.3 Concluding Remarks

Within the emerging research area of artificial photosynthesis, rational designed and tailor-made fluorophore systems based on the Bodipy platform has become extremely important. In this thesis will be discussed different aspects of Bodipy compounds with the aim to perform fundamental photophysical studies and develop novel molecular probes. Conditions for efficient Förster energy transfer will be discussed, tested and validated, through investigations of FRET efficiency and associated parameters. This part of the work is presented in chapters 5 & 6. Synthetic methods and the photophysical properties for a series of molecular rotor and dyad systems are covered in chapters 3 & 4, featuring metal complex linked molecular rotor ensemble act as a hybrid ratiometric agent and julolidine based voltage sensitive low-weight fluorescent dye as neuro-image probe.



## 1.4 References

1. A. C. Benniston and A. Harriman (2008) Artificial Photosynthesis. *Materials Today* 11(12): 26-34.
2. A. Listorti, J. Durrant and J. Barber (2009) Artificial Photosynthesis: Solar to Fuel. *Nature Materials* 8, 929 – 930.
3. I. McConnell, G. Li and G. W. Brudvig (2010) Energy conversion in natural and artificial photosynthesis. *Chem Biol.* 28, 17(5): 434-47.
4. (a) D. Gust, T. A. Moore and A. L. Moore (2012) Realizing artificial photosynthesis. *Faraday Discuss.* 155, 9-26; (b) E. Lang and J Köhler (2013) Experimental Physics IV, Universität Bayreuth.
5. J. Barber and J. B. Marder (1986) Photosynthesis and the application of molecular genetics. *Biotechnology and Genetic Engineering Reviews* Vol. 6. Springer. pp 355-97.
6. S. J. Anthony-Cahill, C. K. Mathews, D. R. Appling and K. E. van Holde (2013) *Biochemistry*. 4th Edition. Prentice Hall. pp 265-90.
7. C. H. Chang, O. El-Kabbani, D. Tiede, J. Norris and M. Schiffer (1991) Structure of the membrane-bound protein photosynthetic reaction center from *Rhodobacter sphaeroides*. *Biochemistry* 30, 5352–5360.
8. G. McDermott, S. M. Prince, A. A. Freer, A. M. Hawthornthwaite-Lawless, M Z. Papiz, R. J. Cogdell and N. W. Isaacs (1994) Crystal structure of an integral membrane light-harvesting complex from photosynthetic bacteria. *Nature* 374, 517-521.
9. Z. Liu, H. Yan, K. Wang, T. Kuang, J. Zhang, L. Gui, X. An and W. Chang (2004) Crystal structure of spinach major light-harvesting complex at 2.72 Å resolution. *Nature*. 428(6980): 287-92.
10. R. J. Cogdell, H. Hashimoto and A. T. Gardiner (2004) Purple bacterial light-harvesting complexes: from dreams to structures. *Photosynthesis Research*. 80,173-179.
11. D. L. Andrews, C. Curutchet and G. D. Scholes, (2011) Resonance Energy Transfer: Beyond the Limits, *Laser Photonics Rev.* 5(1): 114-23.
12. M.-S. Choi, T. Yamazaki, I. Yamazaki and T. Aida (2003) Bioinspired molecular design of light-harvesting multiporphyrin arrays. *Angew. Chem. Int. Ed.* 43,150-158.
13. T. Brixner, J. Stenger, H. M. Vaswani, M. Cho, R. E. Blankenship and G. R. Fleming (2005) Two-dimensional spectroscopy of electronic couplings in photosynthesis. *Nature* 434, 625-28.
14. H. Michel, Molecular Membrane Biology, Max-Planck-Institut für BioPhysik.

15. A. C. Benniston, G. Copley, A. Harriman A, D. B. Rewinska, R. W. Harrington and W. Clegg (2008) A donor-acceptor molecular dyad showing multiple electronic energy-transfer processes in crystalline and amorphous states. *J. Am. Chem. Soc.* 130 (**23**): 7174-75.
16. A. R. Clapp, I. L. Medintz and H. Mattoussi (2006) Förster resonance energy transfer investigations using quantum-dot fluorophores. *ChemPhysChem*. 7(**1**): 47-57.
17. C. Y. Lee, O. K. Farha, B. J. Hong, A. A. Sarjeant, S. T. Nguyen, J. T. Hupp (2011), Light-harvesting metal-organic frameworks (MOFs): efficient strut-to-strut energy transfer in bodipy and porphyrin-based MOFs. *J. Am. Chem. Soc.*, 133 (**40**): 15858–61.
18. F Wen and C Li (2013) Hybrid Artificial Photosynthetic Systems Comprising Semiconductors as Light Harvesters and Biomimetic Complexes as Molecular Cocatalysts. *Acc. Chem. Res.*, Article ASAP.
19. F. Odobel, Y. Pellegrina and J. Warnan. Bio-inspired artificial light-harvesting antennas for enhancement of solar energy capture in dye-sensitized solar cells *Energy Environ. Sci.*, **6**, 2041-52.
20. (a) C. E. Wayne and R. P. Wayne (1996) Photochemistry. Oxford Chemistry Primers. pp 40, 78-92; (b) B. Valeur, M. N. Berberan-Santos (2012) Molecular Fluorescence: Principles and Applications. Wiley VCH; 2nd Edition pp 20-45.
21. A. Gilbert, (1991) Essentials of Molecular Photochemistry. Blackwell Science Press. pp. 9, 145-184, 412-440, 502.
22. R. Clegg and E. Jares-Erijman (2013) FRET - Förster resonance energy transfer: from theory to applications. Wiley-VCH. vol. 1 pp 1-45.
23. (a) J. Adolphs. (2008) Theory of Excitation Energy Transfer in Pigment-Protein Complexes. Dissertation. Freie Universität Berlin. (b) I. Haruo, T. Katsuhiko, S. Masako and P. Tyonji (1999) Photochemistry. Maruzen Co., Ltd. Retrieved <http://ocw.nagoya-u.jp/files/263/seki.pdf> (c) S H. Lin (1988) Advances in Multi-Photon Processes and Spectroscopy: Vol. 4. World Scientific. pp. 77-135; (d) M. Tsubouchi (2013) Time-resolved photoelectron imaging study of ionization dynamic and intersystem crossing of pyrazine. Retrieved: <http://jairo.nii.ac.jp/0201/00000326>
24. (a) Th. Förster (1959) 10th Spiers Memorial Lecture. Transfer mechanisms of electronic excitation. *Discuss. Faraday Soc.*, **27**, 7-17 (b) Th. Förster (1946) Energiewanderung und Fluoreszenz, *Naturwissenschaften*. 33(**6**): 166-175.
25. Fluorescence Resonance Energy Transfer (FRET) Microscopy. (2013) Olympusmicro. <http://www.olympusmicro.com/primer/techniques/fluorescence/>
26. T. Ha, T. Enderle, D. F. Ogletree, D. S. Chemla, P. R. Selvin and S. Weiss (1996) Probing the interaction between two single molecules: fluorescence

- resonance energy transfer between a single donor and a single acceptor. *Proc Natl Acad Sci U S A.* 25; 93(**13**): 6264–68.
27. R. Roy R. S Hohng and T. Ha (2008) A practical guide to single-molecule FRET. *Nat Methods.* 5(**6**): 507-16.
28. G. J. Kremers, J. Goedhart, E. B. van Munster and T. W. Gadella Jr. (2006) Cyan and yellow super fluorescent proteins with improved brightness, protein folding, and FRET Förster Radius. *Biochemistry* **45**, 6570-80.
29. (a) J. Eisinger (1970) Biological Molecules in Their Excited States. *Nature.* **226**, 113-8.
30. G. Ulrich, R. Ziessel, A. Harriman (2008) The Chemistry of Fluorescent Bodipy Dyes: Versatility Unsurpassed *Angew. Chem. Int. Ed.*, 47(**7**): 1184-1201.
31. (a) A. C. Benniston and G. Copley (2009) Lighting the way ahead with boron dipyrromethene (Bodipy) dyes. *Phys.Chem.Chem.Phys.*, **11**, 4124-4131  
(b) L. Wu and K. Burgess (2008) A new synthesis of symmetric boraindacene (BODIPY) dyes, *Chem. Commun.* 4933-35.
32. A Treibs und F-H Kreuzer. Difluorboryl-Komplexe von Di- und Tripyrrylmethenen. *Justus Liebigs Annalen der Chemie* 1968, 718(**1**): 208-223.
33. A. Schmitt, B. Hinkeldey, M. Wild, G. Jung. (2009). Synthesis of the Core Compound of the BODIPY Dye Class: 4,4'-Difluoro-4-bora-(3a,4a)-diazas-indacene. *Journal of Fluorescence.* 19 (**4**): 755–759.
34. I. J. Arroyo, R. Hu, G. Merino, B. Z. Tang and E. Peña-Cabrera (2009). Efficient Preparation and Optical Description of the Parent Borondipyrromethene System. *J. Org. Chem.* 74 (**15**): 5719–22.
35. K. Tram, H. Yan, H. A. Jenkins, S. Vassiliev and D. Bruce (2009). The synthesis and crystal structure of unsubstituted 4,4-difluoro-4-bora-3a,4a-diazas-indacene (BODIPY). *Dyes and Pigments* 82 (**3**): 392–395.
36. (a) O. Galangau (2012) Synthèses et études de systèmes multichromophoriques à base de Bodipy. Laboratoire de Photophysique et de Photochimie Supramoléculaire et Macromoléculaires. Cachan. (b) R. A. Krüger (2008) Functional Dyes Studien zu hybridisierbaren Tetrapyrrol- Farbstoffen, Dissertation, vom Fachbereich Chemie der Philipps-Universität Marburg.
37. B. Verbelen, V. Leen, L. Wang, N. Boens and W. Dehaen (2012) Direct palladium-catalysed C–H arylation of BODIPY dyes at the 3- and 3,5-positions, *Chem. Commun.*, **48**, 9129–31.
38. L. H. Davies, B. Stewart, R. W. Harrington, W Clegg, and L. J. Higham (2012) Air-Stable, Highly Fluorescent Primary Phosphanes. *Angewandte Chemie International Edition.* 51(**20**): 4921–24.

39. A. C. Benniston, S. Clift and A. Harriman (2011) Intramolecular Charge-transfer Interactions in a Julolidine-Bodipy Molecular Dyad as Revealed by  $^{13}\text{C}$  NMR Chemical Shifts. *Journal of Molecular Structure*. 985 (2-3): 346-354.
40. A. C. Benniston, G. Copley, K. J. Elliott, R. W. Harrington and W. Clegg. (2005) Redox-controlled fluorescence modulation in a BODIPY-quinone dyad. *European Journal of Organic Chemistry*. **16**, 2705-2713.
41. A. C. Benniston, A. Harriman, V. L. Whittle and M Zelzer (2010) *European Journal of Organic Chemistry*. **3**, 523-530.
42. A. C. Benniston, S. Clift, J. Hagon, H. Lemmetyinen, N. V. Tkachenko, W. Clegg, R. W. Harrington (2012) Effect on Charge Transfer and Charge Recombination by Insertion of a Naphthalene-Based Bridge in Molecular Dyads Based on Borondipyrromethene (Bodipy). *ChemPhysChem*. 13(16): 3672-81.
43. A. Harriman, L. J. Mallon, K. Elliot, A. Haefele, G. Ulrich and R. Ziessel. (2009) Length Dependence for Intramolecular Energy Transfer in Three- and Four-Color Donor-Spacer-Acceptor Arrays. *J. Am. Chem. Soc.*, 131(37): 13375-86.
44. (a) A. Loudet, R. Bandichhor, K. Burgess, A. Palma, S. O. McDonnell, M. J. Hall and D. F. O'Shea (2008) B,O-Chelated Azadipyrromethenes as Near-IR Probes. *Organic Letters*. 10(21): 4771-74; (b) S. Shimizu, T. Iino, Y. Arakib and N. Kobayashi (2013) Pyrrolopyrrole aza-BODIPY analogues: a facile synthesis and intense fluorescence. *Chem. Commun.*, **49**, 1621-23.
45. S. Zhu, J. Zhang, J. Janjanama, G. Vegesnaa, F.-T. Luo, A. Tiwari and H. Liu (2013) Highly water-soluble BODIPY-based fluorescent probes for sensitive fluorescent sensing of zinc(II). *J. Mater. Chem. B*, **1**, 1722-28.
46. T. Hohsaka (2007) Non-natural labeled amino acid and method of constructing amino acid/trna complex. US Patent 20070117181 A1.
47. A. Miyawaki, J. Llopis, R. Heim, J. M. McCaffery, J. A. Adams, M. Ikura, R. Y. Tsien (1997) Fluorescent indicators for  $\text{Ca}^{2+}$  based on green fluorescent proteins and calmodulin. *Nature*, **388**, 882-87.
48. (a) E. Kim, S B. Park and A P. Demchenko (Ed.) (2010) Advanced Fluorescence Reporters in Chemistry and Biology I Fundamentals and Molecular Design. Springer. pp. 164-165; (b) B. Valeur and J.-C. Brochon (2001) New Trends in Fluorescence Spectroscopy: Applications to Chemical and Life Sciences. Springer Series on Fluorescence. pp 184-185, 297-299.

# Chapter 2

## Experimental Data & Synthetic Protocols



## **2.1 INSTRUMENTATION**

### **2.1.1 Nuclear Magnetic Resonance**

All one dimensional  $^1\text{H}$  NMR,  $^{13}\text{C}$ -NMR and the two dimensional  $^1\text{H}$ - $^1\text{H}$  COSY NMR were recorded on Bruker AVANCE 300 MHz, JEOL 400 MHz, or JEOL Lambda 500 MHz spectrometers;  $^1\text{H}$  - $^{13}\text{C}$  HMQC spectra,  $^{11}\text{B}$ - and  $^{19}\text{F}$ -NMR spectra were recorded using the 400 MHz spectrometer and analyzed via the software package MestReNova.<sup>1</sup> The chemical shifts for  $^1\text{H}$ - and  $^{13}\text{C}$ -NMR spectra are referenced internally to the residual protiated solvent. The  $^{11}\text{B}$ -NMR chemical shift is referenced relative to  $\text{BF}_3 \cdot \text{Et}_2\text{O}$  ( $\delta = 0$ ) and the  $^{19}\text{F}$ -NMR chemical shift to  $\text{CFCl}_3$  ( $\delta = 0$ ).

### **2.1.2 Mass Spectrometry**

Electron Impact (EI) mass spectra were obtained using a Micromass Autospec M high-resolution mass spectrometer coupled to a CARLO ERBA 8000 series gas chromatograph.

MALDI (Matrix assisted laser desorption ionization) mass spectra were obtained from the EPSRC mass Spectrometry Service at Swansea medical school using a Voyager DESTR MALDI-TOF mass spectrometer. The MALDI mass spectra were acquired, typically, using a DCTB, a dithianol or no matrix.

### **2.1.3 Melting Point**

Uncorrected melting points were measured using a Stuart® SMP11 apparatus and typically recorded twice to check for consistency in the readings.

### **2.1.4 UV/visible and Emission Spectroscopy**

Absorption spectra were recorded using a Hitachi U3310 spectrophotometer and corrected fluorescence spectra were recorded using a Hitachi F-4500 spectrometer. Fluorescence quantum yields were measured by the comparison method using a standard dye. Separate solutions of the sample and standard were made up in the appropriate solvent with optical densities (OD) of less than 0.05 at the identical excitation wavelength. Fluorescence

spectra were obtained and the areas calculated ( $A_{std}$  &  $A_{comp}$ ). The quantum yield of the unknown was calculated using the formula:

$$\varphi_{FL} = \varphi_{STD} \frac{A_{comp}}{A_{std}} \times \frac{OD_{std}}{OD_{comp}} \times \left( \frac{\eta_{comp}^2}{\eta_{std}^2} \right)$$

where  $\eta$  is the refractive index of the solvent.

### 2.1.5 Transient Absorption Measurements

Femto- to pico-second time-resolved absorption spectra were collected using a pump-probe technique described previously. The femtosecond pulses of a Ti-sapphire generator were amplified by using a multipass amplifier (CDP-Avesta, Moscow, Russia) pumped by a second harmonic of the Nd:YAG Q-switched laser (model LF114, Solar TII, Minsk, Belorussia). The amplified pulses were used to generate second harmonic (400 nm) for sample excitation (pump beam) and the white light continuum for a time-resolved spectrum detection (probe beam). The samples were placed in 1 mm rotating cuvettes, and averaging of 100 pulses at a 10 Hz repetition rate was used to improve the signal-to-noise ratio. The typical response time of the instrument was 150 fs (fwhm). Absorption spectra were recorded prior to and after all experiments to check for compound degradation.

Ultrafast fluorescence decays were measured by an up-conversion method as described previously. The instrument (FOG100, CDP, Moscow, Russia) utilizes the second harmonic (380 nm) of a 50 fs Ti:sapphire laser (TiF50, CDP, Moscow, Russia) pumped by an Nd laser (Verdi 6, Coherent). The samples were placed in a rotating disk-shaped 1 mm cuvette. A typical resolution for the instrument was 150 fs (fwhm).

### 2.1.6 Molecular Modeling

Molecular modeling was studied on various systems and metal complexes to illustrate the minimum energy conformation or to establish the sites of the molecular orbitals. The computational calculations were performed using a

32-bit version of Gaussian03 on a quadruple-core Intel Xeon system with 4GB RAM.

### 2.1.7 Electrochemistry

Cyclic voltammetry experiments were performed using a fully automated HCH Instruments Electrochemical Analyzer and a three-electrode set-up consisting of a glassy carbon working electrode, a platinum wire counter electrode and an Ag/AgCl reference electrode. Ferrocene was used as an internal standard. All studies were performed in deoxygenated  $\text{CH}_2\text{Cl}_2$  or butyronitrile containing tetra-n-butylammonium tetrafluoroborate ( $0.2 \text{ mol L}^{-1}$ ) as background electrolyte. Potentials were reproducible to within  $\pm 15 \text{ mV}$ .

### 2.1.8 Infra-Red Spectroscopy

FT-IR spectra (unpolarised) were recorded on solid samples where appropriate using a Varian Scimitar <sup>TM</sup> 800 FT-IR instrument and the diamond anvil cell device, the resolution was  $1 \text{ cm}^{-1}$  and 32 scans were summed and averaged.

### 2.1.9 Crystallography

All crystallographic measurements were performed by Dr Ross Harrington using the in-house facilities or the intense X-ray source at Diamond. Full structure determinations and details are attached in the Appendix.

## 2.2 CHEMICALS

All chemicals used in preparative work, their supplier and purity are listed in table 2.1

Chemical	Supplier	Purity
Acetic acid (Glacial)	Alfa Aesar	99.8%
Acetone	Riedel-de-Haën	
Acetonitrile	Riedel-de-Haën	
Acetonitrile- $\text{d}_3$	Alfa Aesar	99.8 atom % D
1-Aminoanthracene	Sigma-Aldrich	90%



2-Aminoanthracene	Sigma-Aldrich	96%
Basic alumina	Sigma-Aldrich	NA
Bromine	Sigma-Aldrich	99.5+%
1-Bromo-3-chloropropane	Sigma-Aldrich	99%
4-Bromobenzaldehyde	Sigma-Aldrich	99%
N-Bromosuccinimide	Sigma-Aldrich	99%
Boron trifluoride diethyl etherate	Alfa Aesar	Purified via redistillation
Calcium hydride	Sigma-Aldrich	95%
Chloroform-d <sub>3</sub>	Sigma-Aldrich	99.96 atom %
Copper	Aldrich	powder, ≥99.5%
Copper(II) sulfate pentahydrate	Aldrich	≥98.0%
2,3-Dichloro-5,6-dicyano- <i>p</i> -benzoquinone	Sigma-Aldrich	98%
2,4-Dimethyl-3-ethylpyrrole	Sigma-Aldrich	97%
2,4-Dimethylpyrrole	Sigma-Aldrich	97%
N,N-Diisopropylethylamine	Sigma-Aldrich	Purified via redistillation
Ethynyltrimethylsilane	Sigma-Aldrich	98%
Hydrochloric acid	Sigma-Aldrich	2M
Hydrogen	BOC Cylinder	Used as received
4-Hydroxybenzaldehyde	Sigma-Aldrich	98%
Julolidine	Sigma-Aldrich	97%
Magnesium sulphate	Sigma-Aldrich	99%
2-Methylpyrrole	Angene Chemical HK	98%
Palladium hydroxide on carbon / Pd(OH) <sub>2</sub> /C	Sigma-Aldrich	20 wt. % loading
Palladium on carbon Pd/C	Sigma-Aldrich	30 wt. % loading ≥ 99.99% trace metals basis
Phenylacetylene	Aldrich	98%

Phosphorus(V) oxychloride	Sigma-Aldrich	99%
Piperidine	Sigma-Aldrich	≥99.5%, purified via redistillation
Potassium fluoride	Sigma-Aldrich	anhydrous powder,
Potassium carbonate	Sigma-Aldrich	99.99%
Propargyl bromide	Aldrich	80 wt. % in toluene
Pyrrole	Alfa Aesar	Purified via redistillation
Sodium acetate	Sigma-Aldrich	99.99%
Sodium azide	Sigma-Aldrich	≥99.5%
Sodium bicarbonate	Sigma-Aldrich	>99.7%
Sodium carbonate	Sigma-Aldrich	99.995%
Sodium hydroxide	Sigma-Aldrich	pellets, 99.998%
Sodium nitrite	Sigma-Aldrich	>99.0%
Sodium sulphate	Sigma-Aldrich	>99.0%
Sulfuric acid	Sigma-Aldrich	99.99%
Tetraethylene glycol	Sigma-Aldrich	99%
Tetrakis(triphenylphosphine) palladium(0) / Pd(PPh <sub>3</sub> ) <sub>4</sub>	Sigma-Aldrich	99%
tert-Butyl nitrite	Sigma-Aldrich	≥90%
p-Toluenesulfonyl chloride	Sigma-Aldrich	>99%
Triethylamine	Sigma-Aldrich	>99.0%
Trifluoroacetic acid	Sigma-Aldrich	99%
Tris[(1-benzyl-1H-1,2,3-triazol-4-yl)methyl]amine (TBTA)	Sigma-Aldrich	97%

**Table 2.1** Chemicals implemented in experimental work.

### 2.3 Solvent and Purification Methods

Solvents and amines used in preparative work are listed in table 2.2 with respectively their purification methods.

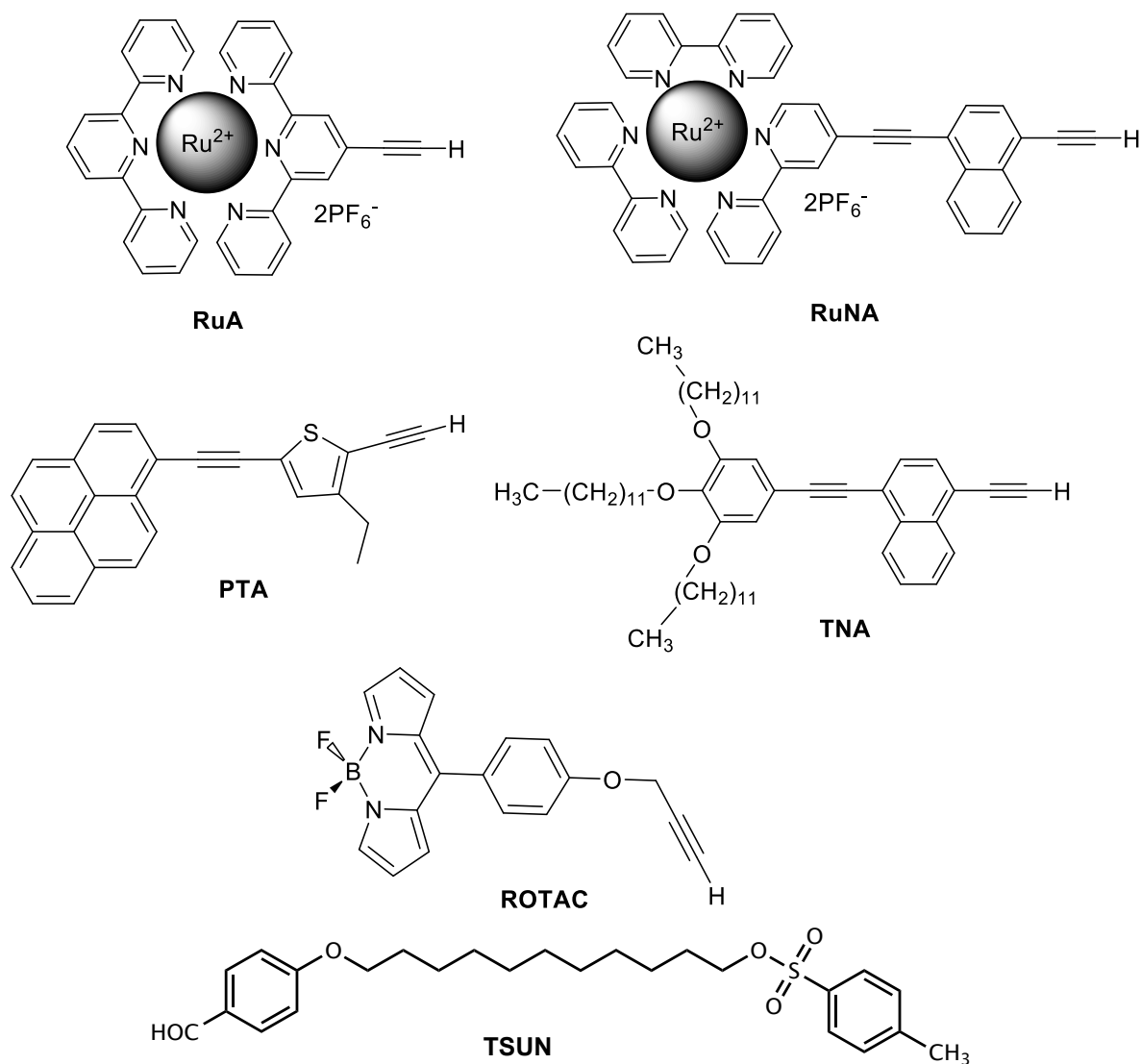
Solvent	Purification Method
Acetone	4Å molecular sieve dried, distilled from K <sub>2</sub> CO <sub>3</sub> under N <sub>2</sub>
Acetonitrile	4Å molecular sieve dried, distilled from CaH <sub>2</sub> under N <sub>2</sub>
Chloroform	Used as received
Dichloromethane	4Å molecular sieve dried, distilled from Na and CaH <sub>2</sub> under N <sub>2</sub>
Diethyl ether	Used as received
Diisopropylamine	4Å molecular sieve dried, distilled from CaH <sub>2</sub> under N <sub>2</sub>
Ethanol	4Å molecular sieve dried
Ethyl acetate	Used as received
Methanol	Used as received
N,N-Dimethylformamide	Used as received
Petroleum ether	Used as received
Tetrahydrofuran	Distilled from sodium/benzophenone under N <sub>2</sub>
Toluene	Distilled from Na under nitrogen
Triethylamine	Distilled from KOH under N <sub>2</sub>

**Table 2.2** Solvents implemented in experimental work.

### 2.4 SYNTHESIS

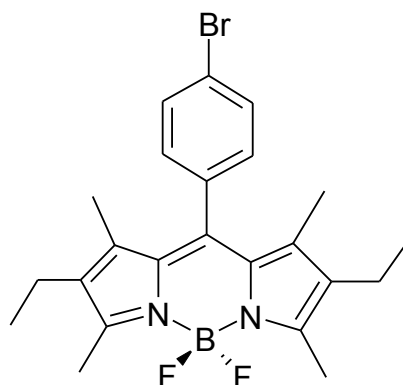
During the course of this research all preparation unless otherwise stated were carried out under an inert dry atmosphere of nitrogen. For known literature compounds only <sup>1</sup>H NMR spectra were recorded to authenticate their identity; all new compounds synthesized have been fully characterized, <sup>1</sup>H NMR and <sup>13</sup>C NMR spectra, IR spectra, mass spectra and melting points were recorded, supported by <sup>11</sup>B NMR and <sup>19</sup>F NMR and X-ray crystallography.

The following starting materials (Scheme 2.1) were available from previous work published by members of the group and used as received after checking their  $^1\text{H}$  NMR spectra.



**Scheme 2.1.** Previously prepared acetylene compounds and their nomenclature.

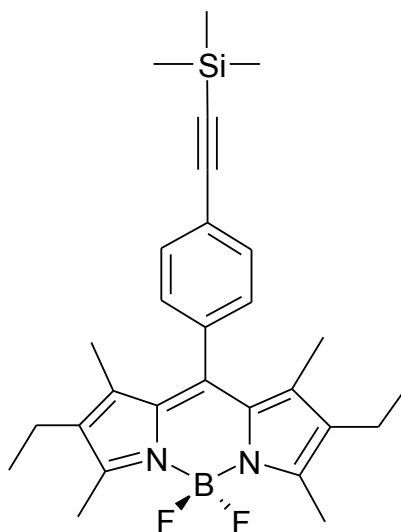
**4,4'-difluoro-8-(4-bromophenyl)-1,3,5,7-tetramethyl-  
2,6-diethyl-4-bora-3a,4a-diaza-s-indacene (BrBOD)**



Chemical Formula:  $C_{23}H_{26}BBrF_2N_2$  (rmm = 458.13)

To a stirred solution of 2,4-dimethyl-3-ethylpyrrole (2.70 mL, 16 mmol, 1 eq.) and 4-bromobenzaldehyde (1.850 g, 8 mmol, 0.5 eq.) in  $CH_2Cl_2$  (140 mL) was added dropwise trifluoroacetic acid (8 drops). The solution turned from green to deep red. The reaction was stirred at room temperature for 7 hours until the TLC showed complete consumption of the aldehyde ( $R_f$  = 0.31, deep red spot). 2,3-dichloro-5,6-dicyano-1,4-benzoquinone (1.82 g, 8 mmol, 0.5 eq.) was added and the reaction was stirred at room temperature for 18 hours. N,N-diisopropylethylamine (16.72 mL, 96 mmol,  $\geq 6$  eq.) and  $BF_3 \cdot Et_2O$  (16.22 mL, 128 mmol, 8 eq.) were then added, the reaction was stirred at room temperature for 6 hours, then washed with distilled  $H_2O$  ( $3 \times 100$  mL) and brine ( $3 \times 100$  mL). The extracted organic fractions were dried over  $MgSO_4$ , filtered and evaporated and vacuum dried to give the crude product as a plum coloured residue. Purification via column chromatography ( $SiO_2$ , eluant  $CH_2Cl_2$ :Petrol ether = 50%-80%,  $R_f$  = 0.27) and then recrystallization from  $CH_2Cl_2$ :petrol ether afforded the expected compound as plum red/ green tinted crystals (0.840 g, 1.83 mmol, 22.8 % yield). Mp. = 252-254 °C.  $^1H$  NMR ( $CDCl_3$ ):  $\delta$  0.97-1.02 (t, 6H,  $J$  = 7.5 Hz); 1.33 (s, 6H); 2.28-2.36 (q, 4H,  $J$  = 9 Hz); 2.55 (s, 6H); 7.18-7.21 (d, 2H,  $J$  = 9 Hz); 7.64-7.67 (d, 2H,  $J$  = 9 Hz).

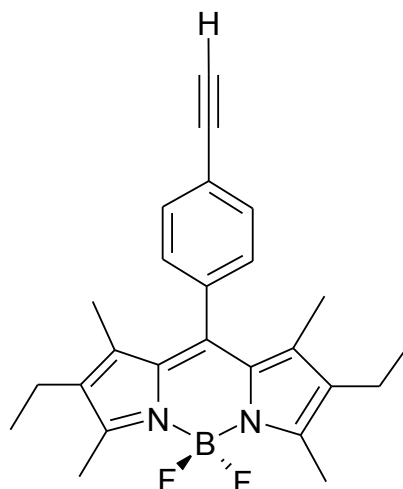
**4,4'-difluoro-8-(4-ethynyltrimethylsilane)-1,3,5,7-tetramethyl-2,6-diethyl-4-bora-3a,4a-diaza-s-indacene (SiBOD)**



Chemical Formula:  $C_{28}H_{35}BF_2N_2Si$  (rmm = 476.3)

To a stirred solution of **BrBOD** (742 mg, 1.60 mmol, 1 eq.) dissolved in anhydrous THF (40 mL) was added tetrakis(triphenylphosphine)palladium(0) (0.093 g, 0.080 mmol, 0.05 eq.) The reaction was purged under nitrogen (1 atmosphere) for 1 hour, then N.N-diisopropylethylamine (40 mL, freshly distilled from CaH) was added to the reaction along with ethynyltrimethylsilane (0.34 mL dropwise, 2.4 mmol, 1.5 eq.). The reaction were stirred at room temperature for 18 hours and monitored via TLC ( $SiO_2$ ,  $CH_2Cl_2$ :petrol ether, red spot,  $R_f$  = 0.50). The reaction were cooled to room temperature then quenched via HCl (1M, 50 mL) in ice (350 mL). The crude product was then washed with distilled  $H_2O$  (3 × 100 mL). The  $CH_2Cl_2$  extracted organic fractions were dried over  $MgSO_4$ , filtered and evaporated. Recrystallization from  $CH_2Cl_2$ :petrol ether afforded the expected compound as bright red crystals with a green tint (270 mg, 0.57 mmol, 36% yield). Mp. = 250-252 °C.  $^1H$  NMR (300 MHz,  $CDCl_3$ ):  $\delta$  = 0.20 (s, 9H); 0.87-0.92 (t, 6H,  $J$  = 9 Hz); 1.21 (s, 6H); 2.17-2.25 (q, 4H,  $J$  = 9 Hz); 2.44 (s, 6H); 7.14-7.17 (d, 2H,  $J$  = 9 Hz); 7.50-7.53 (d, 2H,  $J$  = 9 Hz).

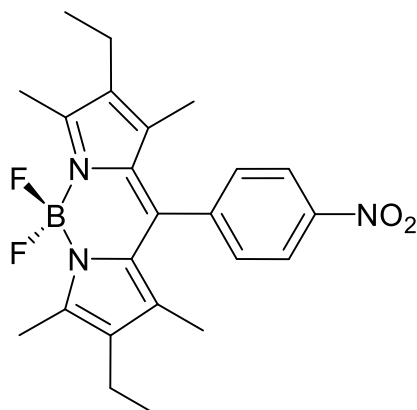
**4,4'-difluoro-8-(4-ethynylphenyl)-1,3,5,7-tetra  
methyl-2,6-diethyl-4-bora-3a,4a-diaza-s-indacene (ACETBD)**



Chemical Formula: C<sub>25</sub>H<sub>27</sub>BF<sub>2</sub>N<sub>2</sub> (rmm = 404.2)

Compound **SiBOD** (110 mg, 0.23 mmol, 1 eq.) was dissolved in anhydrous THF (40 mL), then added to a solution of methanol (40 mL, from molecular sieve sealed bottle storage). Potassium fluoride (40 mg, 0.69 mmol, 3 eq) was dissolved in anhydrous THF (5 mL) and added to the reaction mixture during 5 minutes. The reaction were stirred at room temperature for 72 hours, then concentrated by rotary evaporation. The crude product was then washed with distilled H<sub>2</sub>O (3 × 100 ml), extracted from dichloromethane and the organic fractions were dried over MgSO<sub>4</sub>, filtered and evaporated. Recrystallization from CH<sub>2</sub>Cl<sub>2</sub>:petrol ether afforded the expected compound as red crystals with a green yellow tint (85 mg, 0.21 mmol, 91% ) Mp. = 250-252 °C. <sup>1</sup>H NMR (300 MHz, CDCl<sub>3</sub>): δ = 0.88-0.93 (t, 6H, *J* = 7.5 Hz); 1.22 (s, 6H); 2.27-2.19 (q, 4H, *J* = 9 Hz); 2.46 (s, 6H); 3.11 (s, 1H), 7.19-7.21 (d, 2H, *J* = 9 Hz); 7.56-7.53 (d, 2H, *J* = 9 Hz).

**4,4'-difluoro-8-(4-nitrophenyl)-1,3,5,7-tetramethyl-  
2,6-diethyl-4-bora-3a,4a-diaza-s-indacene (NITBOD)**

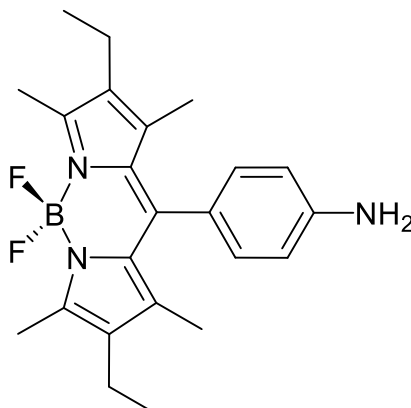


Chemical Formula:  $C_{23}H_{26}BF_2N_3O_2$  (rmm = 425.2)

To a stirred solution of 2,4-dimethyl-3-ethylpyrrole (2.11 ml, 16 mmol, 1 eq.) and 4-nitrobenzaldehyde (1.209 g, 8 mmol, 0.5 eq.) in DCM (400 ml) was added dropwise TFA (8 drops). The solution turned red from pale yellow. The reaction was stirred at room temperature until the TLC showed complete consumption of the aldehyde ( $R_f$  = 0.32, deep red spot and yellow fluorescence). DDQ (1.82 g, 8 mmol, 0.5 eq.) was added in a single portion, and the reaction was stirred at room temperature for 18 hours. N.N-diisopropylethylamine (16.72 ml, 96 mmol,  $\geq 6$  eq.) and  $BF_3 \cdot Et_2O$  (16.22 ml, 128 mmol, 8 eq.) were added, and the reaction was stirred at room temperature for 6 hours, then washed with water ( $3 \times 100$  ml) and brine ( $3 \times 100$  ml). The extracted organic fractions were dried over  $MgSO_4$ , filtered and evaporated and vacuum dried to give the crude product as a red residue with a chartreuse tint. The residue was purified via column chromatography ( $SiO_2$ , eluant: hexane: DCM = 4:3, red spot and yellow fluorescence,  $R_f$  = 0.37) to afford the expected compound as a red solid (1.105 g, 2.598 mmol, 32.5 % yield). Mp. = 201–204 °C.  $^1H$  NMR ( $CDCl_3$ ):  $\delta$  0.98 (t, 6H,  $J$  = 7.5 Hz); 1.26 (s, 6H); 2.30 (q, 4H,  $J$  = 7.5 Hz); 2.54 (s, 6H); 7.51-7.55 (d, 2H,  $J$  = 9 Hz); 8.36-8.39 (d, 2H,  $J$  = 9 Hz).



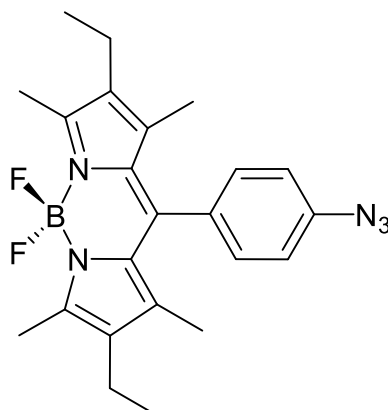
**4,4'-difluoro-8-(4-aminophenyl)-1,3,5,7-tetramethyl-2,6-diethyl-4-bora-3a,4a-diaza-s-indacene (AMBOD)**



Chemical Formula:  $C_{23}H_{28}BF_2N_3$  (rmm = 395.2)

To stirred solution of **NITBOD** (805 mg, 1.89 mmol, 1 eq.) in THF (40 ml) was added Pd/C (0.100 g, 0.094 mmol, 0.05 eq.) The reaction was evacuated and then sealed under hydrogen (1 atmosphere) and stirred at room temperature for 36 hours until complete consumption of the starting material was observed by TLC ( $SiO_2$ , DCM, red spot,  $R_f$  = 0.32). The solvent was evaporated and vacuum dried to afford the expected compound as a red solid (427 mg, 1.08 mmol, 57 % yield).  $^1H$  NMR (300 MHz,  $CDCl_3$ ):  $\delta$  = 0.98 (t, 6H,  $J$  = 7.5 Hz); 1.41 (s, 6H); 2.31 (q, 4H,  $J$  = 7.5 Hz); 2.52 (s, 6H); 3.70 (br s, 2H), 6.78-6.81 (d, 2H,  $J$  = 9 Hz); 7.01-7.04 (d, 2H,  $J$  = 9 Hz).

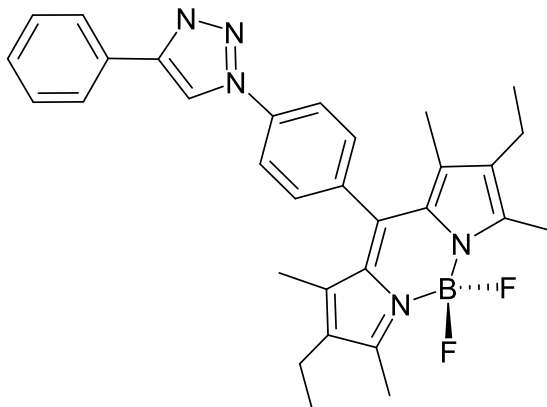
**4,4'-difluoro-8-(4-azidophenyl)-1,3,5,7-tetramethyl-2,6-diethyl-4-bora-3a,4a-diaza-s-indacene (AZBOD)**



Chemical Formula:  $C_{23}H_{26}BF_2N_5$  (rmm = 421.2)

A solution of **AMBOD** (598 mg, 1.95 mmol ) in anhydrous MeCN (40 mL, freshly distilled from  $CaH_2$ ) was cooled to  $-20\text{ }^{\circ}C$  (ThermoHaakel EK<sup>®</sup> 90, acetone bath).  $tBuNO_2$  (0.9 ml, 7.6 mmol, 5 eq) was added over 15 mins, and the solution was stirred at  $-20\text{ }^{\circ}C$  for 30 mins. Then  $TMSN_3$  (1.0 ml, 7.5 mmol, 5 eq) was added over a duration of 15 mins. The reaction mixture was stirred at  $-20\text{ }^{\circ}C$  for 18 hour and then for a further day at  $0\text{ }^{\circ}C$ . The solvent was removed and the crude product was purified via column chromatography ( $SiO_2$ , eluant: hexane: DCM = 4:1,  $R_f$  = 0.42). The product was vacuum dried and slow vapor diffusion crystallization used to afford the expected compound as a deep red solid (225 mg, 0.54 mmol, 27.5 % yield). Mp. =  $157\text{-}158\text{ }^{\circ}C$ .  $^1H$  NMR (300 MHz  $CDCl_3$ ):  $\delta$  = 0.99 (t, 6H,  $J$  = 7.5 Hz); 1.35 (s, 6H); 2.29-2.37 (q, 4H,  $J$  = 7.5 Hz); 2.55 (s, 6H); 7.16- 7.19 (d, 2H,  $J$  = 9 Hz), 7.28-7.31 (d, 2H,  $J$  = 9 Hz).  $^{13}C$  NMR (75 MHz,  $CDCl_3$ )  $\delta$  = 154.16, 141.06, 139.13, 138.14, 133.03, 132.65, 131.012, 130.172, 119.68, 17.10, 14.45, 12.47, 11.85. FTIR (solid) 2963, 2128 ( $N_3$ ), 1538, 1182, 975, 759  $cm^{-1}$ .

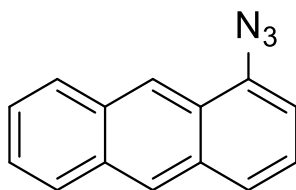
**2,8-diethyl-5,5-difluoro-1,3,7,9-tetramethyl-10-(4-(4-phenyl-1*H*-1,2,3-triazol-1-yl)phenyl)-5*H*-dipyrrolo[1,2-*c*:2',1'-*f*][1,3,2]diazaborinin-4-ium-5-uide(PHBOD)**



Chemical Formula: C<sub>31</sub>H<sub>33</sub>BF<sub>2</sub>N<sub>5</sub> (rmm = 524.3)

To a solution of **AZBOD** (65 mg, 0.15 mmol, 1 eq) in THF (40 mL anhydrous purged with N<sub>2</sub>) was added tris-[(1-benzyl-1*H*-1,2,3-triazol-4-yl)methyl]amine (TBTA) (8 mg, 0.015 mmol, 0.1 eq) and Cu (10 mg, 0.15 mmol, 1 eq). To the solution was added an aqueous solution of CuSO<sub>4</sub>·5H<sub>2</sub>O (4 mg, 0.015 mmol, 0.1 eq), followed by ethynylbenzene (0.017 ml, 16 mg, 0.15 mmol, 1 eq) in 1:1 H<sub>2</sub>O:THF (10 ml). The reaction was stirred at 37 °C for 18 hours. Purification of crude material via column chromatography (SiO<sub>2</sub>, eluant petrol:DCM = 1:1 then ethyl acetate 5%-80%, *R<sub>f</sub>* = 0.125) and recrystallization gave the product as a red solid (70 mg, 0.1337 mmol, 93.65 % yield). Mp. 238-241°C. <sup>1</sup>H NMR (300 MHz, CDCl<sub>3</sub>): δ = 0.97-1.02 (t, 6H, *J* = 7.5 Hz), 1.36 (s, 6H), 2.28-2.35 (q, 4H, *J* = 7.5 Hz), 2.55 (s, 6H), 7.39-7.42 (t, 1H, *J* = 7.2 Hz), 7.46-7.51 (m, 4H), 7.92-7.95 (d, 2H, *J* = 9 Hz), 7.97-8.00 (d, 2H, *J* = 9 Hz). <sup>13</sup>C NMR (75 MHz, CDCl<sub>3</sub>): δ = 154.38, 148.71, 138.00, 137.29, 136.37, 133.16, 130.55, 130.06, 129.97, 128.97, 128.60, 125.87, 120.66, 117.34, 17.04, 14.58, 12.54, 12.04. <sup>11</sup>B NMR (128 MHz CDCl<sub>3</sub>): δ = -0.1535 (t, *J* = 34.38 Hz). <sup>19</sup>F NMR (376 MHz CDCl<sub>3</sub>): δ = -145.55 (q, *J* = 34.6 Hz, *J* = 31.77 Hz). FTIR (solid) 2970, 1539, 1472, 1191, 972, 760 cm<sup>-1</sup>.

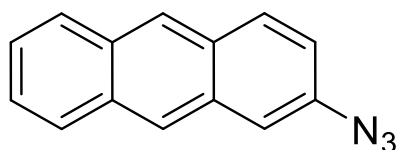
## Preparation of 1-Azidoanthracene



Chemical Formula:  $C_{14}H_9N_3$  (rmm = 219.1)

To 1-aminoanthracene (0.486 g, 2.5 mmol) placed in a 3-necked flask, fitted with a low-temperature thermometer and a dropping funnel, was added water (15 mL). To the suspension at room temperature and with stirring was added carefully conc.  $H_2SO_4$  (3 mL). The suspension was stirred for 1 hr at room temperature, and the reaction mixture was then cooled to 0 °C in an ice/salt bath. Maintaining a temperature of 0 °C at all times a solution of  $NaNO_2$  (235 mg, 3.4 mmol) in water (8 mL) was added dropwise to the stirred solution. The resultant red solution was stirred for 30 mins at 0 °C. To the stirred solution  $NaN_3$  (320 mg, 4.9 mmol) in water (5 mL) was then added dropwise over 10 mins. The ice/salt bath was removed and the mixture was left to stir at room temperature for 5 hrs. The black/brown precipitate formed was filtered off through a sintered funnel and washed with water (5 x 20 mL) and air dried for 1 hr. The solid was then washed with ice cold EtOH (5 mL) and air dried for 30 mins. The crude material was suspended in ethyl acetate and pipetted onto a silica gel column (ca. 3 cm x 20 cm) made up using petrol (40/60). (Note: a black deposit stays at the top of the column). The column was eluted using petrol (40/60) to afford as the first fraction the desired product as a brown solid (150 mg, 0.68 mmol, 27% yield). A second cruder fraction also eluted when the solvent was changed to ethyl acetate. This material was taken up into hot ethanol which was filtered and cooled in a freezer to afford a brown solid.  $^1H$  NMR (300 MHz,  $CDCl_3$ )  $\delta$  = 8.69 (s, 1H), 8.40 (s, 1H), 8.06-7.98 (m, 2H), 7.80 (d, 1H,  $J$  = 9 Hz), 7.52-7.42 (m, 3H), 7.23 (d, 1H,  $J$  = 6Hz).  $^{13}C$  NMR (75 MHz,  $CDCl_3$ )  $\delta$  = 137.3, 132.7, 132.1, 129.0, 128.3, 126.5, 126.4, 125.4, 125.0, 122.0, 113.1. FT-IR (neat): 2110 ( $N_3$ ), 1621, 1536, 1455, 1382, 1286, 1160, 1066, 951, 785  $cm^{-1}$ .

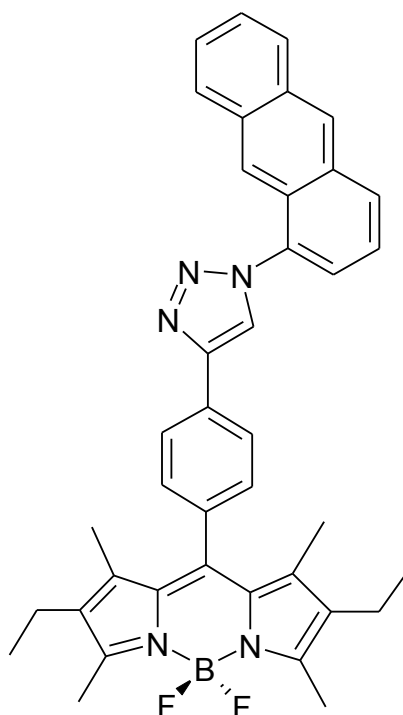
## Preparation of 2-Azidoanthracene



Chemical Formula:  $C_{14}H_9N_3$  (rmm = 219.1)

A 500-mL round-bottomed flask equipped with a PTFE-coated magnetic stir bar was charged with compound 2-aminoanthracene (0.168 g, 0.87mmol, 1 eq.) in  $H_2O$  (15 mL). To the brown coloured suspension at 25 °C was added carefully conc.  $H_2SO_4$  (3 mL) with stirring. The solution was kept at 20 °C for 1 hr and then the reaction was cooled to  $-4$  to 0 °C via an ice and NaCl bath. The reaction was monitored via thermometer maintaining the reaction mixture under 0 °C at all times. A solution of  $NaNO_2$  (150 mg, 2.17 mmol, 2.5 eq) in  $H_2O$  (10 mL) was added during 5 minutes. The reaction appeared brick-red colour. The solution was kept at  $-4$  to 0 °C and a solution of  $NaN_3$  (175 mg, 2.70 mmol, 3.1 eq in minimum amount of  $H_2O$ ) was added drop by drop under the solution surface during 10 minutes with stirring. The ice/water bath was removed and the reaction was stirred at 20 °C for 5 hours. The crude product was collected by filtration and washed with  $H_2O$  ( $5 \times 20$  mL), air dried and washed with ice cold EtOH (5 mL) then allowed to dry in air for 30 mins. The brown solid was purified by column chromatography ( $SiO_2$ , eluant ethyl acetate: petrol ether 10%-80%,  $R_f$  = 0.51) to afford the expected compound as an ochre coloured solid (140 mg, 0.63 mmol, 73 %)  $^1H$  NMR (300 MHz,  $CDCl_3$ ):  $\delta$  = 8.43 (s, 1H); 8.35 (s, 1H), 7.99-8.04 (m, 2H); 7.62 (s, 1H); 7.47-7.53 (m, 2H), 7.28 (s, 1H), 7.15-7.19 (d, 1H). FTIR (solid): 2112.698 (azide), 1627.276, 1578.958, 1456.645, 1342.589, 1247.322, 1115.078  $cm^{-1}$ .

## Preparation of ANTBD

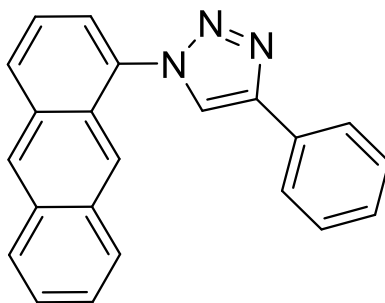


Chemical Formula:  $C_{39}H_{36}BF_2N_5$  (rmm = 623.3)

Compound **ACETBD** (85 mg, 0.21 mmol, 1 eq) was dissolved in THF (40 mL purged with  $N_2$ ) and to the solution was added tris-[(1-benzyl-1H-1,2,3-triazol-4-yl)methyl]amine (TBTA) (11 mg, 0.021 mmol, 0.1 eq) and Cu (14 mg, 0.21 mmol, 1 eq). To the solution was added an aqueous solution of  $CuSO_4 \cdot 5H_2O$  (2 mg, 0.021 mmol, 0.1 eq in 50 ml  $H_2O$ ) and 1-azidoanthracene (48 mg, 0.21 mol, 1 eq) in THF (10 ml) during 5 minutes. The reaction was stirred at 40 °C for 18 hours. After solvent removal the crude material was purified via column chromatography ( $SiO_2$ , eluant  $CH_2Cl_2$  : petrol ether = 10% - 80%,  $R_f$  = 0.16). Recrystallization from  $CH_2Cl_2$  and petrol ether afforded the expected compound as deep red crystals (95 mg, 0.15 mmol, 72.5% yield) Mp. = 305.1-307.0 °C  $^1H$  NMR (300 MHz,  $CDCl_3$ ):  $\delta$  = 8.53 (s, 1H, triazo-H) ; 8.27 (s, 1H); 8.18-8.15 (d, 1H), 8.07-8.10 (d, 2H, phenyl-H); 8.03-7.98 (m, 2H); 7.91-7.88 (d, 1H); 7.59-7.42 (m, 3H) ; 7.39-7.36 (d, 2H, phenyl-H), 7.12-7.09 (d, 1H); 2.49 (s, 6H) ; 2.30-2.22 (q, 6H) ; 1.35 (s, 4H); 0.96-0.91(t, 6H)  $^{13}C$  NMR (75 MHz,  $CDCl_3$ ):  $\delta$  = 11.9; 12.5; 14.6; 17.0; 121.4; 122.6; 123.1; 123.8; 126.4; 126.4; 126.5; 126.5; 127.2; 128.0; 128.5; 129.1; 130.8; 130.8; 131.0; 131.8; 132.1;

132.5; 132.8; 133.6; 135.4; 135.6; 135.9; 138.3; 139.5; 147.1; 153.8.  $^{11}\text{B}$  NMR (128 MHz  $\text{CDCl}_3$ ):  $\delta$  = -0.1209 (t,  $J$  = 34.29 Hz).  $^{19}\text{F}$  NMR (376 MHz  $\text{CDCl}_3$ ):  $\delta$  = -145.6845 (q,  $J$  = 29.63 Hz,  $J$  = 33.87 Hz). MALDI  $\text{C}_{39}\text{H}_{36}\text{BN}_5\text{F}_2$  calculated = 623.30 found  $[\text{M-H}]^+$ : 622.2.

## Preparation of PHANT

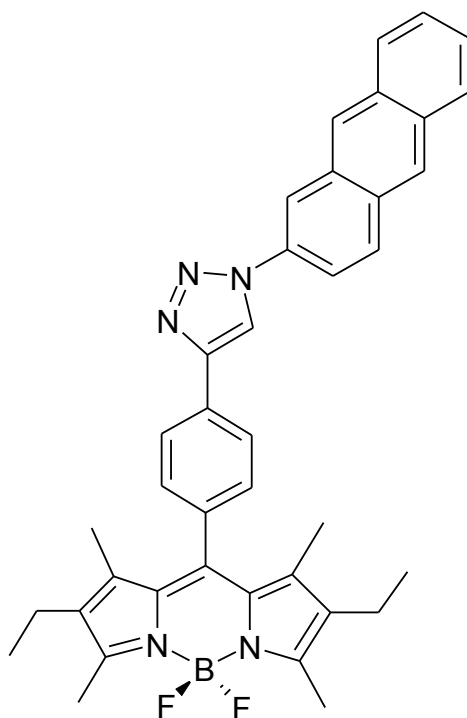


Chemical Formula:  $C_{22}H_{15}N_3$  (rmm = 321.1)

1-Azidoanthracene (72 mg, 0.328 mmol, 1 eq) was dissolved in THF (40 mL purged with  $N_2$ ) and to the solution was added tris-[(1-benzyl-1H-1,2,3-triazol-4-yl)methyl]amine (TBTA) (17 mg, 0.032 mmol, 0.1 eq) and Cu (20 mg, 0.31 mmol, 1 eq). Then during 5 minutes an aqueous solution of  $CuSO_4 \cdot 5H_2O$  (8 mg, 0.032 mmol, 0.1 eq in 50 ml  $H_2O$ ) was added. Phenylacetylene (0.12 mg, 0.13 mL, 1.17 mmol, 3.5 eq) was then added during 5 minutes. The reaction was stirred at 40 °C for 18 hours. After solvent removal the crude material was purified by column chromatography ( $SiO_2$ , eluant  $CH_2Cl_2$  : petrol ether = 10% - 80%,  $R_f$  = 0.08). Recrystallization from  $CH_2Cl_2$  and petrol ether afforded the expected compound as brown coloured crystals (97 mg, 0.304 mmol, 92.7% yield). Mp. = 76-78 °C.  $^1H$  NMR (300 MHz,  $CDCl_3$ ):  $\delta$  = 8.59 (s, 1H, triazo H); 8.30 (s, 1H); 8.24-8.21 (d, 1H); 8.26 (s, 1H, phenyl H), 8.08 (s, 1H); 8.03-8.05 (d, 2H, phenyl H); 7.96-7.94 (d, 1H); 7.67-7.65 (d, 1H) 7.56-7.41 (m, 3H); 7.54-7.51 (d, 2H, phenyl H) 7.28 (s, 1H).  $^{13}C$  NMR (125 MHz,  $CDCl_3$ ):  $\delta$  = 147.88, 133.91, 132.61, 132.20, 131.97, 131.01, 130.43, 129.11, 128.68, 128.56, 128.08, 127.21, 126.92, 126.61, 126.57, 126.01, 123.93, 123.20, 122.46, 121.63.



## Preparation of ANTBD2

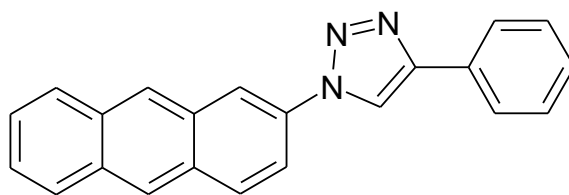


Chemical Formula:  $C_{39}H_{36}BF_2N_5$  (rmm = 623.3)

Compound **ACETBD** (70 mg, 0.17 mmol, 1 eq) was dissolved in THF (40 mL purged with  $N_2$ ) and to this was added tris-[(1-benzyl-1H-1,2,3-triazol-4-yl)methyl]amine (TBTA) (9 mg, 0.017 mmol, 0.1 eq) and Cu (11 mg, 0.17 mmol, 1 eq). Over 5 minutes an aqueous solution of  $CuSO_4 \cdot 5H_2O$  (4 mg, 0.021 mmol, 0.09 eq in 50 ml  $H_2O$ ) and 2-azidoanthracene (38 mg, 0.17 mol, 1 eq) dissolved in THF (10 ml) were added. The reaction was stirred at 40 °C for 18 hours. The crude material after solvent removal was purified by column chromatography ( $SiO_2$ , eluant  $CH_2Cl_2$ : petrol ether = 50%,  $R_f$  = 0.25). A freeze/thaw and vacuum-drying afforded the expected compound a red solid (60 mg, 0.17 mmol, 56% yield) Mp. = 230-231°C.  $^1H$  NMR (300 MHz,  $CDCl_3$ ):  $\delta$  = 8.52-8.50 (d, 1H) ; 8.46 (s, 1H, triazo H) ; 8.20-8.18 (d, 1H); 8.10-8.08 (d, 2H, phenyl H); 8.04-8.02 (m, 1H); 7.97-7.95 (dd, 1H); 7.53-7.51(m, 3H); 7.40-7.38 (d, 2H, phenyl H); 7.24 (s, 1H); 2.53 (s, 6H); 2.26-2.32 (q, 4H,  $J$  = 8 Hz); 1.36 (s, 6H); 0.95-0.99 (t, 6H,  $J$  = 8 Hz).  $^{13}C$  NMR (75 MHz,  $CDCl_3$ ):  $\delta$  = 153.88; 138.30; 147.81; 135.95; 133.74; 132.86; 132.53; 132.28; 130.78; 130.68; 130.60; 129.04; 128.30; 128.07; 127.09; 126.81; 126.441; 126.25; 118.82; 118.17; 118.08; 17.06; 14.63; 12.53; 11.92.  $^{11}B$  NMR (128 MHz

CDCl<sub>3</sub>):  $\delta$  = -0.1326 (t,  $J$  = 33.28 Hz). <sup>19</sup>F NMR (376 MHz CDCl<sub>3</sub>):  $\delta$  = -145.70 (q,  $J$  = 26.32 Hz,  $J$  = 33.84 Hz). MALDI C<sub>39</sub>H<sub>36</sub>BN<sub>5</sub>F<sub>2</sub> calculate. = 623.30 found found [M-H]<sup>+</sup>: 622.3.

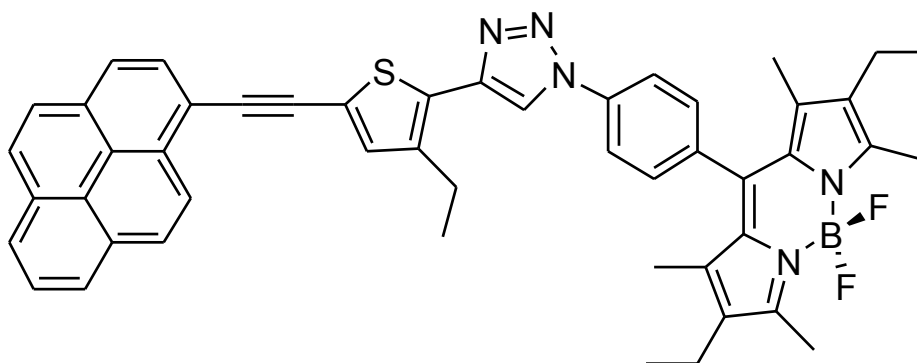
## Preparation PHANT2



Chemical Formula:  $C_{22}H_{15}N_3$  (rmm = 321.1)

2-Azidoanthracene (50 mg, 0.23 mmol, 1 eq) was dissolved in THF (40 mL purged with  $N_2$ ) and to this was added tris-[(1-benzyl-1H-1,2,3-triazol-4-yl)methyl]amine (TBTA) (12 mg, 0.023 mmol, 0.1 eq) and Cu (14 mg, 0.23 mmol, 1 eq). During 5 minutes an aqueous solution of  $CuSO_4 \cdot 5H_2O$  (6 mg, 0.023 mmol, 0.1 eq in 50 ml  $H_2O$ ) and phenylacetylene (0.08 mg, 0.09 mL, 0.79 mmol, 3.4 eq) were added. The reaction was stirred at 40 °C for 5 hours. After solvent removal the crude material was purified by column chromatography ( $SiO_2$ , eluant  $CH_2Cl_2$  : petrol ether = 50%,  $R_f$  = 0.07). Freeze/thaw and vacuum drying afforded the expected compound as a pale yellow solid (40 mg, 0.124 mmol, 54 % yield).  $^1H$  NMR (300 MHz,  $CDCl_3$ ):  $\delta$  = 8.47-8.45 (d, 1H); 8.42 (s, 1H); 8.32 (s, 1H, triazo H) ; 8.15-8.12 (d, 1H) ; 8.00-7.97 (m, 1H); 7.94-7.89 (m, 2H, phenyl H) ; 7.79(s, 1H, phenyl H), 7.58-7.55 (pentet, 1H) 7.49-7.33 (m, 3H) ; 7.26-7.24 (d, 2H, phenyl H) 6.86-6.82 (d, 1H).  $^{13}C$  NMR (125 MHz,  $CDCl_3$ ):  $\delta$  = 133.98, 132.77, 130.95, 129.26, 129.11, 128.77, 128.64, 128.42, 127.38, 127.08, 126.64, 126.48, 126.37, 126.10, 123.19 119.39, 118.45, 117.90, 115.47, 114.16.

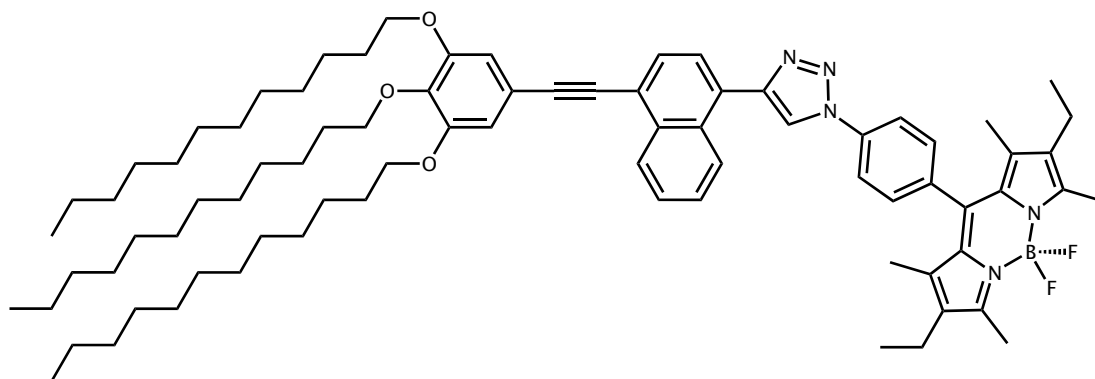
## Preparation of PTTBD



Chemical Formula:  $C_{49}H_{42}BF_2N_5S$  (rmm = 781.3)

To a solution of **AZBOD** (70 mg, 0.17 mmol, 1 eq) in THF (40 mL purged with  $N_2$ ) was added tris-[(1-benzyl-1H-1,2,3-triazol-4-yl)methyl]amine (TBTA) (9 mg, 0.016 mmol, 0.1 eq) and Cu (11 mg, 0.17 mmol, 1 eq). This was followed by an aqueous solution of  $CuSO_4 \cdot 5H_2O$  (4 mg, 0.016 mmol, 0.1 eq) and **PTA** (90 mg, 0.24 mol, 1.47 eq) dissolved in a 1:1 THF/  $H_2O$  (10 ml) mixture. The reaction was stirred at 37 °C for 36 hours and monitored via TLC. Removal of the solvents gave the crude mixture which was purified via column chromatography ( $SiO_2$ , eluant: petrol ether: DCM = 1:1,  $R_f$  = 0.37). The desired product was recrystallized by slow vapour diffusion using in  $CH_2Cl_2$  (95 mg, 0.1215 mmol, 72.93 % yield). Mp. = 266.4-267.2 °C.  $^1H$  NMR (300 MHz,  $CDCl_3$ ):  $\delta$  = 0.97-1.02 (t, 6H,  $J$  = 7.5 Hz), 1.38-1.42 (t, 3H,  $J$  = 7.5 Hz), 2.17 (s, 6H), 2.29-2.35 (q, 4H,  $J$  = 7.5 Hz), 2.56 (s, 6H), 2.89-2.97 (q, 2H,  $J$  = 7.5 Hz), 7.38 (s, 1H), 7.49-7.52 (d, 2H,  $J$  = 8.0 Hz); 7.98-8.14 (m, 5H); 8.19-8.25 (m, 6H), 8.59-8.63 (d, 1H,  $J$  = 9.0 Hz).  $^{13}C$  NMR (75 MHz,  $CDCl_3$ ):  $\delta$  = 154.87, 143.20, 142.56, 138.42, 137.51, 137.01, 134.55, 133.64, 132.19, 131.84, 131.66, 131.47, 130.99, 130.59, 129.79, 128.92, 128.74, 127.90, 127.66, 126.73, 126.17, 126.11, 125.82, 124.99, 124.88, 124.70, 122.95, 121.14, 118.18, 117.66, 94.02, 88.72, 31.37, 23.32, 17.51, 15.05, 14.93, 13.01, 12.53.  $^{11}B$  NMR (128 MHz,  $CDCl_3$ ):  $\delta$  -0.1535 (t,  $J$  = 31.9 Hz).  $^{19}F$  NMR (376 MHz,  $CDCl_3$ ):  $\delta$  -145.59 (q,  $J$  = 31.8 Hz,  $J$  = 34.7 Hz). FTIR (solid) 2973.22, 1066.69, 908.16  $cm^{-1}$ .

**2,8-diethyl-5,5-difluoro-1,3,7,9-tetramethyl-10-(4-(4-(4-((3,4,5-tris(dodecyloxy)phenyl)ethynyl)naphthalen-1-yl)-1*H*-1,2,3-triazol-1-yl)phenyl)-5*H*-dipyrrolo[1,2-*c*:2',1'-*f*][1,3,2]diazaborinin-4-ium-5-uide (NAPHBD)**

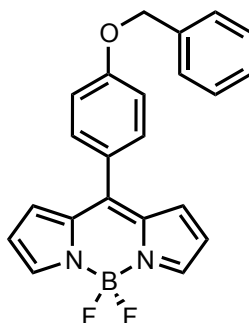


Chemical Formula: C<sub>79</sub>H<sub>110</sub>BF<sub>2</sub>N<sub>5</sub>O<sub>3</sub> (rmm = 1225.9)

To a solution of **AZBOD** (58 mg, 0.14 mmol, 1 eq) in THF (40 mL purged under N<sub>2</sub>) was added tris-[(1-benzyl-1*H*-1,2,3-triazol-4-yl)methyl]amine (TBTA) (7.3 mg, 0.014 mmol, 0.1 eq) and Cu (8.7 mg, 0.14 mmol, 1 eq). To the solution was added an aqueous solution of CuSO<sub>4</sub>·5H<sub>2</sub>O (3.4 mg, 0.014 mmol, 0.1 eq in 50 ml H<sub>2</sub>O) and then **TNA** (110 mg, 0.14 mol, 1 eq) in THF (10 ml). The reaction was stirred at 25 °C for 18 hour and then refluxed at 80 °C for 18 hour. The reaction was monitored via TLC and stopped after complete consumption of the starting materials. The solvents were removed and the crude mixture was purified by column chromatography (SiO<sub>2</sub>, eluant: toluene, R<sub>f</sub> = 0.20). The material obtained was further purified vial-in-a-vial vapor diffusion crystallization (CH<sub>2</sub>Cl<sub>2</sub> : Petro ether 2:8) to afford the expected compound as a red solid (41 mg, 33.4 mmol, 24 % yield) <sup>1</sup>H NMR (400 MHz, CDCl<sub>3</sub>): δ = 0.89 (t, 9H, *J* = 6 Hz), 1.01 (t, 6H, *J* = 7.5 Hz), 1.28 (m, 48H), 1.38 (s, 6H), 1.45-1.55 (m, 6H), 1.73-1.89 (m, 6H), 2.27-2.38 (q, 4H, *J* = 7.5 Hz), 2.56 (s, 6H), 4.00-4.06 (q, 6H, *J* = 6 Hz), 6.87 (s, 2H), 7.53-7.55 (d, 2H, *J* = 8.5 Hz), 7.60-7.70 (m, 2H, NapH), 7.79-7.86 (q, 2H, *J* = 6 Hz), 8.05-8.07 (d, 2H, *J* = 8.5 Hz), 8.41 (s, 1H), 8.54-8.57 (t, 2H, *J* = 8.5 Hz, NapH). <sup>13</sup>C NMR (75 MHz, CDCl<sub>3</sub>): δ = 154.45, 153.11, 147.62, 139.39, 137.97, 137.25, 136.56, 133.68, 133.26, 133.19, 130.96, 130.88, 130.57, 130.19, 129.75, 127.76,

127.29, 126.92, 126.76, 125.70, 122.24, 120.74, 120.47, 117.53, 110.24, 95.83, 86.14, 73.58, 69.21, 31.91, 30.32, 26.09, 22.67, 17.06, 14.59, 14.10, 12.56, 12.07. (Note: two aromatic carbon resonances and several alkyl carbon resonances are missing because of accidental equivalence).  $^{11}\text{B}$  NMR (128 MHz,  $\text{CDCl}_3$ ):  $\delta = -0.1535$  (t,  $J = 31.9$  MHz).  $^{19}\text{F}$  NMR (376 MHz  $\text{CDCl}_3$ ):  $\delta = -145.62$  (q,  $J = 30.3$  MHz).

**10-(4-(benzyloxy)phenyl)-5,5-difluoro-5*H*-dipyrrolo[1,2-*c*:2',1'-  
f][1,3,2]diazaborinin-4-ium-5-uide (PHROT).**



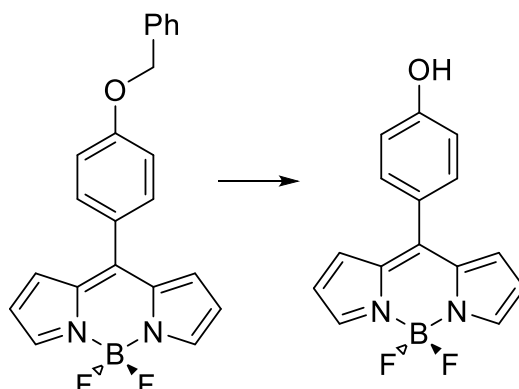
Chemical Formula: C<sub>22</sub>H<sub>17</sub>BF<sub>2</sub>N<sub>2</sub>O (rmm = 374.1)

To a two neck flask containing compound 4-(benzyloxy)benzaldehyde (4.24 g, 0.02 mol, 1 eq.) was added pyrrole (freshly distilled from CaH, 50 mL, 48.35 g, 0.58 mol, 36 eq.), followed by dropwise addition of trifluoroacetic acid (8 drops). The solution turned a deep brick red colour. The reaction was stirred at room temperature for 1 hour until the TLC showed complete consumption of the aldehyde (CH<sub>2</sub>Cl<sub>2</sub> : petrol ether 0%-50% R<sub>f</sub> = 0.52, brown spot). The reaction mixture was vacuum distilled to completely remove the pyrrole to afford a brown gluey crude compound. The crude material was purified via column chromatography (alumina, eluent ethyl acetate : petrol ether 0%-90%). This afforded the intermediate dipyrromethene after recrystallisation (cream crystals, 2.45 g, 0.008 mol, 27% yield). To the intermediate compound dissolved in CH<sub>2</sub>Cl<sub>2</sub> was added 2,3-dichloro-5,6-dicyano-1,4-benzoquinone (2.05 g, 0.009 mol, 1.125 eq.), and the reaction was stirred at room temperature for 4 hours (turned brown). In an ice bath the N,N-diisopropylethylamine (11.025 g, 15 mL, 0.108 mol, 12 eq.) and BF<sub>3</sub>·Et<sub>2</sub>O (19.330 g, 17 mL, 0.135 mol, 15 eq.) were then added and the reaction was stirred at ambient temperature for 18 hours. The solution was washed with distilled H<sub>2</sub>O (4 x 100 mL) and brine (4 x 100 mL). The extracted organic fractions were dried over MgSO<sub>4</sub>, filtered and evaporated and vacuum dried to give the crude product as a brown gluey solid. The residue was purified via column chromatography (SiO<sub>2</sub>, eluant: ethyl acetate : petrol ether = 0%-80%, R<sub>f</sub> = 0.10) and then recrystallization from petrol ether : CHCl<sub>3</sub> to afford the expected compound as an orange solid (1.06 g, 0.34 mmol, 16% yield). <sup>1</sup>H

NMR (CDCl<sub>3</sub>):  $\delta$  = 7.85 (s, 2H); 7.46-7.49 (d, 2H); 7.19-7.39 (m, 4H); 7.04-7.07 (d, 2H); 6.90-6.91 (d, 2H); 6.47-6.48 (d, 2H); 5.10 (s, 2H).



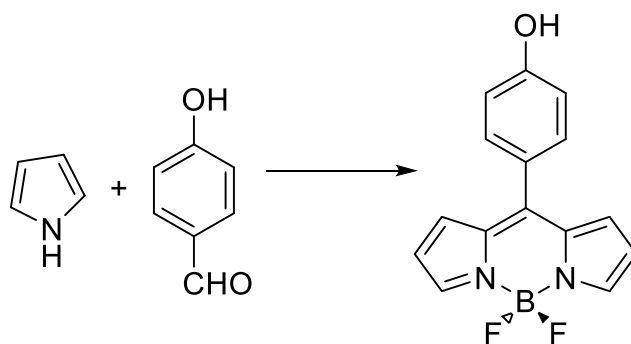
**5,5-difluoro-10-(4-hydroxyphenyl)-5*H*-dipyrrolo[1,2-*c*:2',1'-*f*][1,3,2]diazaborinin-4-ium-5-uide (ALCROT)**



Chemical Formula: C<sub>15</sub>H<sub>11</sub>BF<sub>2</sub>N<sub>2</sub>O (rmm = 284.1)

To a three neck flask equipped with a condenser and containing a magnetic stirrer were added **PHRO** (360 mg, 0.962 mmol, 1 eq), ethanol (80 ml) and 1,4-cyclohexadiene (0.36 mL, 3.8 mmol, 3.95 eq.). The orange suspension formed was stirred and thoroughly degassed by bubbling nitrogen through for 2 hours at ambient temperature. Under the flow of nitrogen, palladium hydroxide on carbon (7 mg, 0.05 eq.) was added and the solution was purged with nitrogen for a further 30 minutes. The temperature was raised to 70 °C and the reaction was stirred under nitrogen flow for 18 hours until the TLC indicated complete turnover of the starting material. The reaction mixture was cooled and filtered to remove the palladium residue which was washed with CH<sub>2</sub>Cl<sub>2</sub>. The combined solvents were taken off by a rotary evaporator. The orange coloured solid product was purified via column chromatography (silica gel, eluant: CH<sub>2</sub>Cl<sub>2</sub>: ethyl acetate = 9:1, R<sub>f</sub> = 0.32) to afford the expected compound (220 mg, 80.4% yield). <sup>1</sup>H NMR (300 MHz, CDCl<sub>3</sub>): δ = 7.94 (s, 2H); 7.50-7.53 (d, 2H); 6.99-7.02 (d, 2H); 6.56-6.57 (d, 2H); 5.49 (s, broad, aromatic C-OH).

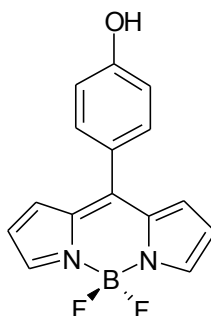
## Preparation of ALCROT



Chemical Formula:  $C_{15}H_{11}BF_2N_2O$  (rmm = 284.1)

4-Hydroxybenzaldehyde (3.70 g, 0.03 mol, 1 eq.) was added to pyrrole (freshly distilled from CaH, 40 mL, 38.68 g, 0.58 mol, 20 eq.) under nitrogen flow, followed by the dropwise addition of trifluoroacetic acid (8 drops). The solution turned from clear to red. The reaction was stirred at room temperature for 1 hour until the TLC showed complete consumption of the aldehyde (ethyl acetate : petrol ether 50%  $R_f$  = 0.26, brown spot). The reaction mixture was vacuum distilled to completely remove the pyrrole to afford a green brown crude compound. This material was purified by column chromatography (alumina, ethyl acetate : petrol ether 0%-90%). The intermediate dipyrromethene was attained by recrystallisation (white crystals, 1.9 g, 0.009 mol, 30.2% yield). The compound was dissolved in  $CH_2Cl_2$  and 2,3-dichloro-5,6-dicyano-1,4-benzoquinone (2.05 g, 0.009 mol, 1 eq.) was added, and the reaction was stirred at room temperature for 4 hours. The solution turned brown. In an ice bath N.N-diisopropylethylamine (11.025 g, 15 mL, 0.108 mol, 12 eq.) and  $BF_3 \cdot Et_2O$  (19.330 g, 17 mL, 0.135 mol, 15 eq.) were then added, and the reaction was stirred at ambient temperature for 18 hours, then washed with distilled  $H_2O$  (4 x 100 mL) and brine (4 x 100 mL). The extracted organic fractions were dried over  $MgSO_4$ , filtered and evaporated and vacuum dried to give the crude product as a brown gluey solid. The residue was purified via column chromatography ( $SiO_2$ , eluant: ethyl acetate: petrol ether = 0%-80%,  $R_f$  = 0.10) and then recrystallization from to petrol ether :  $CHCl_3$  to afford the expected compound an orange solid (3.95 g, 0.014 mol, 47% yield).  $^1H$  NMR ( $CDCl_3$ ):  $\delta$  = 7.85 (s, 2H); 7.41-7.42 (d, 2H); 6.91-6.93 (d, 2H); 6.48-6.49 (d, 2H); 5.23 (s, broad, aromatic C-OH).

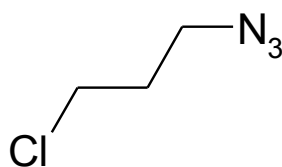
**5,5-difluoro-10-(4-hydroxyphenyl)-5*H*-dipyrrolo[1,2-*c*:2',1'-*f*][1,3,2]diazaborinin-4-ium-5-uide (ALCROT)**



Chemical Formula: C<sub>15</sub>H<sub>11</sub>BF<sub>2</sub>N<sub>2</sub>O (rmm = 284.1)

4-Hydroxybenzaldehyde (1.220 g, 0.01 mol, 1 eq.) was dissolved in anhydrous CH<sub>2</sub>Cl<sub>2</sub> (80 ml) and to the solution was added pyrrole (freshly distilled from CaH, 1.56 mL, 1.50 g, 2.25 eq.) followed by dropwise addition of trifluoroacetic acid (8 drops). The solution turned deep red. The reaction was stirred at room temperature for 4 hours until the TLC showed complete consumption of the aldehyde (*R*<sub>f</sub> = 0.30, deep red spot). 2,3-dichloro-5,6-dicyano-1,4-benzoquinone (2.27 g, 0.01 mol, 1 eq.) was added, and the reaction was stirred at room temperature for 18 hours. In ice bath N,N-diisopropylethylamine (15.51 g, 20.90 mL, 0.12 mol, 12 eq.) and BF<sub>3</sub>·Et<sub>2</sub>O (21.28 g, 18.51 mL, 0.15 mol, 15 eq.) were then added, and the reaction was stirred at 25 °C for 18 hours, and then washed with distilled H<sub>2</sub>O (4 x 100 mL) and brine (4 x 100 mL). The extracted organic fractions were dried over MgSO<sub>4</sub>, filtered and evaporated and vacuum dried to give the crude product as a brown gluey solid. The residue was purified via column chromatography (alumina, eluant: CH<sub>2</sub>Cl<sub>2</sub> : petrol ether = 50%-80%, *R*<sub>f</sub> = 0.15) and then recrystallization from to CHCl<sub>3</sub> to afford the expected compound as a red solid (0.41 g, 1.5 mmol, 15 % yield). <sup>1</sup>H NMR (CDCl<sub>3</sub>): δ = 7.85 (s, 2H); 7.41-7.42 (d, 2H); 6.91-6.93 (d, 2H); 6.48-6.49 (d, 2H); 5.60 (s, broad, aromatic C-OH).

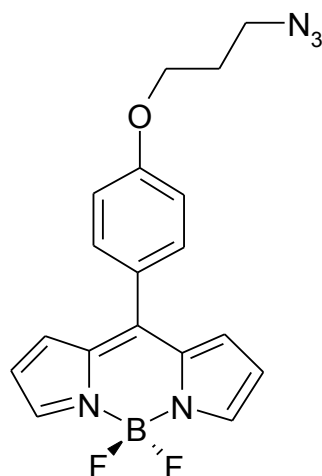
### Preparation of 1-azido-3-chloropropane



Chemical Formula: C<sub>3</sub>H<sub>6</sub>ClN<sub>3</sub> (rmm = 119.0)

NaN<sub>3</sub> (10 g, 0.15 mol, 1 equiv) was added to a solution of 1-bromo-3-chloropropane (23.80 g, 15 mL, 0.15 mol, 1 equiv) dissolved in DMSO (20 mL). The reaction was stirred at 40°C for 18 hours. The clear solution was concentrated and the crude product was washed with distilled H<sub>2</sub>O (4 x 50 mL) and extracted into hexane. The organic layer was separated and dried (MgSO<sub>4</sub>) and removed to give the expected product as a clear oil (17.04 g, 95 %). <sup>1</sup>H NMR (300 MHz, CDCl<sub>3</sub>) δ = 3.53-3.58 (t, 2H); 3.46-3.50 (t, 2H); 2.24-2.29 (t, 2H). FT-IR: 2089.881(alkyl azide), 1651.092, 1592.786, 1350.207, 1240.952 cm<sup>-1</sup>.

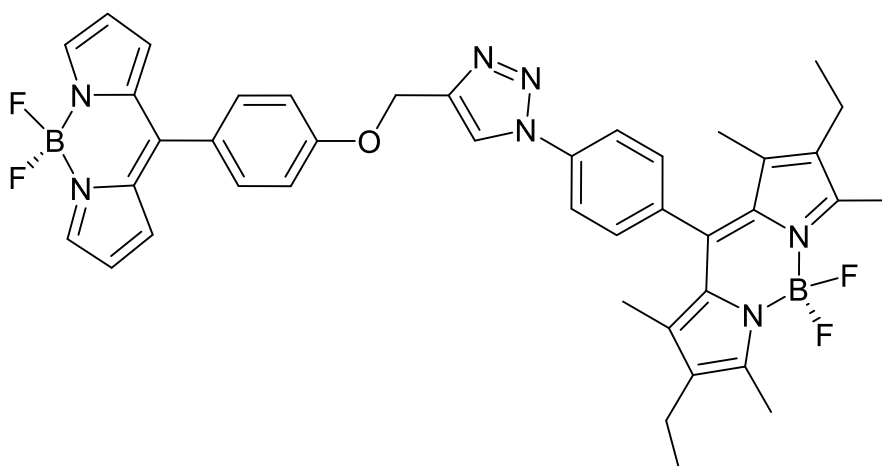
**10-(4-(3-azidopropoxy)phenyl)-5,5-difluoro-5H-dipyrrolo[1,2-c:2',1'-f][1,3,2]diazaborinin-4-ium-5-uide (AZROT)**



Chemical Formula:  $C_{18}H_{16}BF_2N_5O$  (rmm = 367.1)

1-Azido-3-chloropropane (96 mg, 0.80 mol, 4.7 equiv.) in DMF (4 mL) was added to a DMF (20 mL) solution of **ALCROT** (50 mg, 0.179 mol, 1 equiv.), followed by  $K_2CO_3$  (74 mg, 2 equiv. suspended in 5 mL DMF). The reaction was kept at 90°C for 5 hours with stirring. After cooling, the solution was washed with distilled  $H_2O$  (4 x 50 mL), extracted into toluene which was dried over  $MgSO_4$  and concentrated on a rotory evaporator. Purification via the prep-TLC method ( $SiO_2$ , eluant: toluene,  $R_f$  = 0.34) afford the expected compound as a deep red solid (20 mg, 0.054 mol, 30 %)  $^1H$  NMR (300 MHz,  $CDCl_3$ )  $\delta$  = 7.85 (s, 2H); 7.49-7.46 (d, 2H); 6.99-6.96 (d, 2H); 6.91-6.89 (d, 2H), 6.48-6.47 (d, 2H), 4.07-4.11 (t, 2H); 3.48-3.53 (t, 2H); 2.01-2.09 (t, 2H).  $^{13}C$  NMR (300 MHz,  $CDCl_3$ )  $\delta$  = 161.2; 143.5; 134.8; 132.5; 131.4; 126.6; 118.4; 114.5; 64.8; 48.1; 29.7; 28.7 FT-IR (solid) = 1249.1; 1385.0; 1538.9; 1602.1; 2095.0 (azide); 2360.7  $cm^{-1}$ .

## Preparation of ROBD1

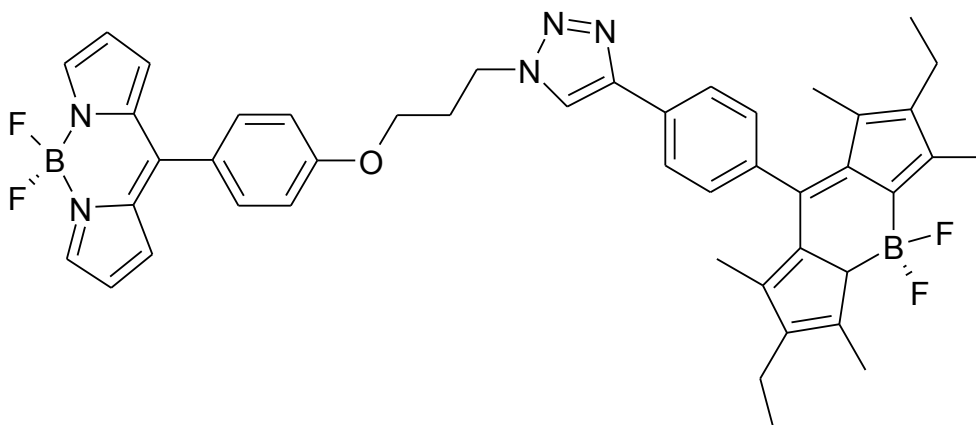


Chemical Formula:  $C_{41}H_{39}B_2F_4N_7O$  (rmm = 743.3)

**ROTAC** (20 mg, 0.054 mmol, 1 eq) was dissolved in THF (40 mL purged with  $N_2$ ) and to this was added tris-[(1-benzyl-1H-1,2,3-triazol-4-yl)methyl]amine (TBTA) (6 mg, 0.011 mmol, 0.2 eq) and Cu (3 mg, 0.047 mmol, 1 eq). The reaction was stirred at 28 °C for 1 hour, then over 10 minutes an aqueous solution of  $CuSO_4 \cdot 5H_2O$  (2 mg, 0.021 mmol, 0.4 equiv in 50 ml  $H_2O$ ) was added. To the reaction mixture was added **AZBOD** (25 mg, 0.062 mmol, 1 eq) in THF (10 ml) during 10 minutes. The reaction was stirred at 40 °C for 5 hours. The aqueous portion was separated and extracted with dichloromethane and the combined organics were removed on a rotary evaporator. The crude material was purified by column chromatography ( $SiO_2$ , eluant  $CH_2Cl_2$  : petrol ether = 50%; ethyl acetate was then added 50%-90% for collection of the last fraction). The compound was frozen under liquid nitrogen before applying a vacuum (x 4) to remove trapped impurities to afford the expected compound as a deep red solid (35 mg, 0.047 mmol, 87% yield)  $^1H$  NMR (300 MHz,  $CDCl_3$ ):  $\delta$  = 0.89-0.94 (t, 6H,  $J$  = 7.5 Hz), 1.27 (s, 6H) ; 2.20-2.28 (q, 4H,  $J$  = 7.5 Hz) ; 2.48 (s, 6H) ; 5.36 (s, 1H) ; 6.48-6.49 (d, 2H); 6.90 (d, 2H); 7.13-7.16 (d, 2H); 7.42-7.45(d, 2H); 7.50-7.53 (d, 2H); 7.86-7.87(d, 2H); 7.90 (s, 2H); 8.20 (s, 1H, triazo-H).  $^{13}C$  NMR (75 MHz,  $CDCl_3$ ) (25 Carbon):  $\delta$  = 11.02, 11.56, 13.46, 16.13, 28.71, 29.70, 61.39, 114.06, 117.29, 119.92, 126.32, 129.45, 129.77, 130.32, 131.37, 131.51, 132.38, 134.05, 136.01, 136.43, 136.91, 142.76, 143.84, 153.71, 159.79  $^{11}B$  NMR (128 MHz  $CDCl_3$ ):  $\delta$  = 0.0959; 0.1864; -0.4570; -0.6822; -0.9073 (pentet,  $J$  =

34.56, 28.58 Hz).  $^{19}\text{F}$  NMR (376 MHz  $\text{CDCl}_3$ ):  $\delta$  = -144.8861; -144.9544; -145.0283; -145.1023 (q,  $J$  = 28.20 Hz);  $\delta$  = -145.5460; -145.6143; -145.6996; -145.7850 (q,  $J$  = 30.08 Hz). Mass Spectrum  $\text{C}_{41}\text{H}_{39}\text{B}_2\text{N}_7\text{F}_4\text{O}$  calculated = 743.41 observed  $[\text{M-H}]^+ = 742$ .

## Preparation of ROBD2



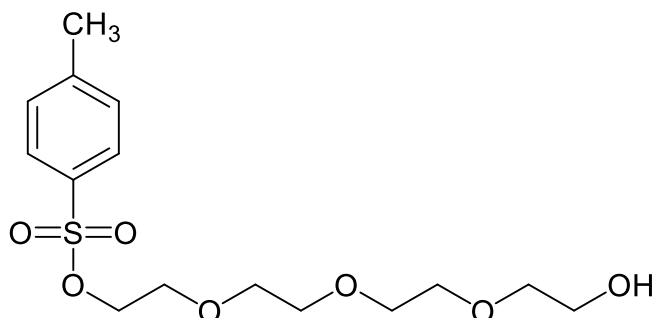
Chemical Formula:  $C_{43}H_{43}B_2F_4N_7O$  (rmm = 771.4)

**ACETBD** (25 mg, 0.062 mmol, 1 eq.) was dissolved in anhydrous THF (40 mL purged with  $N_2$ ) and to this was added tris-[(1-benzyl-1H-1,2,3-triazol-4-yl)methyl]amine (TBTA) (6 mg, 0.011 mmol, 0.18 eq) and Cu (4 mg, 0.062 mmol, 1 eq). Then during 5 minutes an aqueous solution of  $CuSO_4 \cdot 5H_2O$  (3 mg, 0.012 mmol, 0.18 eq in 50 ml  $H_2O$ ) was added. To the solution during 5 minutes was added **AZROT** (20 mg, 0.054 mmol, 0.87 eq). The reaction was stirred at 40 °C for 18 hours. The aqueous portion was separated and extracted with dichloromethane, rotary evaporate to concentrate. Purification of crude material via column chromatography ( $SiO_2$ , eluant  $CH_2Cl_2$  : petrol ether, 50%-90%,  $R_f$  = 0.07) to afford the expected compound a red solid (30 mg, 0.038 mmol, 70.4 % yield)  $^1H$  NMR (300 MHz,  $CDCl_3$ ):  $\delta$  = 7.91-7.88 (d, 2H); 7.85 (s, 1H, triazo H); 7.46-7.49 (d, 2H); 7.27-7.30 (d, 2H); 6.99-6.96 (d, 2H); 6.90-6.88 (d, 2H); 6.48-6.47 (d, 2H); 4.67-4.63 (t, 2H); 4.11-4.07 (t, 2H); 2.46 (s, 6H); 2.26-2.19 (q, 2H); 1.26 (s, 6H); 0.90-0.81 (t, 6H)  $^{13}C$  NMR (400 MHz,  $CDCl_3$ ):  $\delta$  = 161.26; 154.36; 147.67; 147.47; 144.03; 140.01; 138.56; 136.25; 135.32; 133.25; 131.55; 131.19; 129.51; 127.40; 126.58; 120.54; 118.60; 115.00; 65.12; 60.57; 47.58; 30.31; 21.17; 17.40; 14.75; 14.48; 12.77; 12.15  $^{11}B$  NMR (128 MHz  $CDCl_3$ ):  $\delta$  = 0.10612; -0.16301; -0.45008; -0.70126; -0.91657 (pentet,  $J$  = 32.00 Hz).  $^{19}F$  NMR (376 MHz  $CDCl_3$ ):  $\delta$  = -144.8201; -144.8935; -144.9626; -145.0361 (q,  $J$  = 26.32 Hz);  $\delta$  = -145.5156; -145.5804;



-145.6625; -145.7446 (q,  $J = 29.14$  Hz). Mass Spectrum  $C_{43}H_{43}B_2N_7F_4O$   
calculate. = 771.46 observed  $[M-H]^+ = 770.3$ .

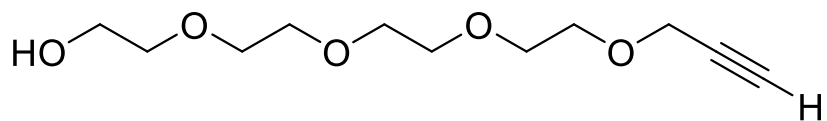
**2-(2-(2-(2-hydroxyethoxy)ethoxy)ethoxy)ethyl 4-methylbenzenesulfonate  
(TSETH)**



Chemical Formula:  $C_{15}H_{24}O_7S$  (rmm = 348.1)

Triethylamine (23.0 g, 16 mL, 0.23 mol, 1 equiv) was added to tetraethylene glycol (45.0 g, 40 mL, 0.23 mol), which was dissolved in  $CH_2Cl_2$  (40 mL). p-Toluenesulfonic chloride (4.42 g, 0.023 mol, 0.1 equiv) dissolved in  $CH_2Cl_2$  (20 mL) was dropwise added to the reaction mixture over 10 minutes. The reaction was stirred at 25 °C for 28 hours. The clear solution was concentrated. The crude product was washed with distilled  $H_2O$  (4 x 50 mL) and extracted with  $CH_2Cl_2$  which was separated and dried over magnesium sulfate. Removal of the organic portion afforded the expected product as a pale yellow oil (70 g, 0.2 mol, 87%).  $^1H$  NMR (300 MHz,  $CDCl_3$ )  $\delta$  = 7.73 (s, 2H); 7.30 (s, 2H); 4.09 (t, 2H), 3.52-3.64 (m, 12H); 2.38 (t, 2H).

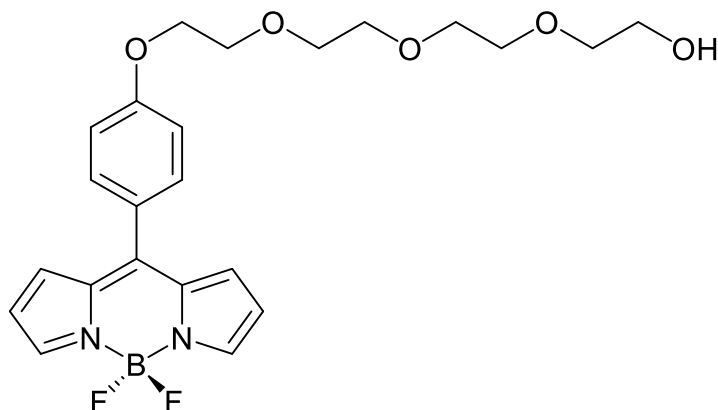
**2-(2-(2-(pent-4-yn-1-yloxy)ethoxy)ethoxy)ethanol (PEE)**



Chemical Formula: C<sub>11</sub>H<sub>20</sub>O<sub>4</sub> (rmm = 216.3)

To a THF solution of tetra-ethyleneglycol (1.94 g, 0.01 mol, 1 equiv) and 1-azido-3-chloropropane (0.178 g, 0.0015 mol, 0.15 equiv.) was added NaH (0.36 g, 0.015 mol, 1.5 equiv.). The reaction was kept at 0 °C in an ice-salt bath for 2 hours then ambient temperature for 4 hours. After solvent removal the residue was extracted with CH<sub>2</sub>Cl<sub>2</sub> : H<sub>2</sub>O and the organic layer was separated and removed to afford the target compound as a gel-like solid (257 mg, 0.47 mmol, 86%) <sup>1</sup>H NMR (300 MHz, CDCl<sub>3</sub>) δ = 4.50 (s, 1H); 4.04 (s, 10H); 3.90-3.87 (m, 6H); 3.39-3.28 (t, 1H); 2.31-2.28 (m, 2H).

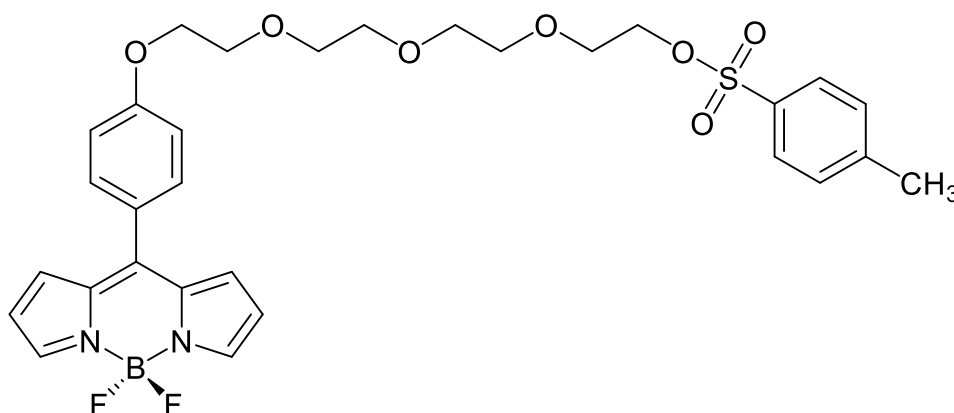
**5,5-difluoro-10-(4-(2-(2-(2-(2-hydroxyethoxy)ethoxy)ethoxy)ethoxy)phenyl)-5*H*-dipyrrolo[1,2-*c*:2',1'-*f*][1,3,2]diazaborinin-4-ium-5-uide (ETROT)**



Chemical Formula: C<sub>23</sub>H<sub>27</sub>BF<sub>2</sub>N<sub>2</sub>O<sub>5</sub> (460.20)

To a solution of compound **ALCROT** (400 mg, 1.4 mmol, 1 eq.) dissolved in DMF (80 mL) was added **TSETH** (2.35 g, 6.7 mmol, 4.7 eq.) in DMF (20 mL) followed by K<sub>2</sub>CO<sub>3</sub> (0.2 g, 1.4 mmol, 1 eq.). The reaction was stirred, under N<sub>2</sub> atmosphere at 90 °C for 5 hrs, then was concentrated and extracted with CH<sub>2</sub>Cl<sub>2</sub> and washed with H<sub>2</sub>O. The organics were dried over MgSO<sub>4</sub> and then taken off on a rotary evaporator. Purification of the crude material via column chromatography (SiO<sub>2</sub>, eluent Ethyl acetate : petrol ether = 0 – 50%) afforded the desired compound (255 mg, 0.55 mmol, 40 %) as a red oily solid. <sup>1</sup>H NMR (300 MHz, CDCl<sub>3</sub>) δ = 2.31 (s, broad, 1H); 3.61-3.79 (m, 12H); 3.91-3.94 (t, 2H); 4.23-4.27 (t, 2H); 6.56-6.57 (d, 2H); 6.97-6.99 (d, 2H); 7.06-7.09 (d, 2H); 7.53-7.55 (d, 2H); 7.93 (s, 2H). <sup>13</sup>C NMR (400 MHz, CDCl<sub>3</sub>) δ = 61.66; 70.20; 70.59; 70.78; 72.55; 114.59; 118.26; 126.44; 127.94; 129.80; 131.33; 132.35; 134.76; 143.37; 147.70; 161.19.

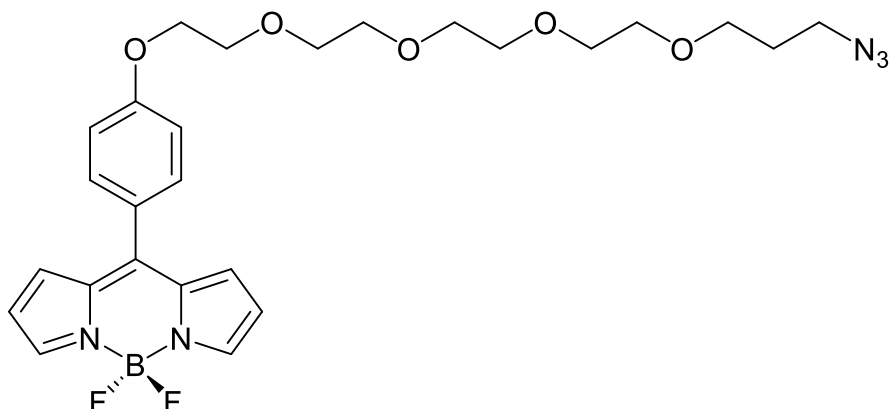
**5,5-difluoro-10-(4-(2-(2-(2-(2-(tosyloxy)ethoxy)ethoxy)ethoxy)ethoxy)phenyl)-5H-dipyrrolo[1,2-c:2',1'-f][1,3,2]diazaborinin-4-ium-5-uide (TSROT)**



Chemical Formula:  $C_{30}H_{33}BF_2N_2O_7S$  (rmm = 614.2)

To the solution of **ETROT** (230 mg, 0.5 mmol) in  $CH_2Cl_2$  was added triethylamine (50 mg, 0.07 mL, 0.5 mmol, 1 equiv). p-Toluenesulfonic chloride (142 mg, 0.75 mmol, 1.5 equiv) dissolved in  $CH_2Cl_2$  (20 mL) was added dropwise to the reaction mixture during 10 minutes. The reaction was allowed to stir at 10°C - 25 °C for 18 hours and was monitoring by TLC. The reaction was concentrated. The crude product was then washed with distilled  $H_2O$  (50 4 x mL) and extracted up into  $CH_2Cl_2$  which was dried over magnesium sulfate and concentrated *in vacuo* to give the target compound a brick-red gel-like solid (205 mg, 0.3 mol, 67%).  $^1H$  NMR (300 MHz,  $CDCl_3$ )  $\delta$  = 8.02(s, 1H); 7.85(s, 1H); 7.72-7.71(d, 2H); 7.48-7.45(d, 2H); 7.28-7.26(d, 2H); 7.19 (s, 1H); 7.01-6.98(d, 2H); 6.91-6.89 (d, 1H); 6.48(s, 1H); 4.26-4.24(t, 2H); 4.15-4.11(t, 2H); 4.10-4.07(t, 2H); 3.87-3.83(t, 2H); 3.62-3.46 (m, 8H); 2.37(s, 3H).

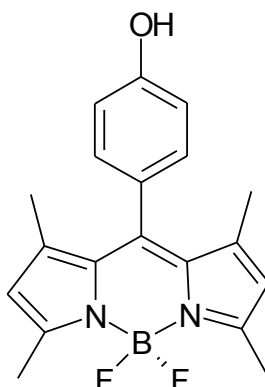
**10-(4-((15-azido-3,6,9,12-tetraoxapentadecyl)oxy)phenyl)-5,5-difluoro-5H-dipyrrolo[1,2-c:2',1'-f][1,3,2]diazaborinin-4-ium-5-uide (AZEROT)**



Chemical Formula:  $C_{26}H_{32}BF_2N_5O_5$  (rmm = 543.3)

To the THF solution of **ETROT** (255 mg, 0.55 mmol) and 1-azido-3-chloropropane (98 mg, 0.82 mmol, 1.5 equiv.) was added NaH (20 mg, 0.82 mmol, 1.5 equiv.). The reaction was stirred in an ice-salt bath at 0 °C for 2 hours then ambient temperature for 4 hours. Purification via extraction with  $CH_2Cl_2$  :  $H_2O$  gave the target compound as a brick-red gel-like solid (257 mg, 0.47 mmol, 86%).  $^1H$  NMR (300 MHz,  $CDCl_3$ )  $\delta$  = 0.89 (t, 2H); 1.27 (s, 4H); 3.62-3.77 (m, 12H); 3.93-3.95 (t, 2H); 4.24-4.25 (t, 2H); 6.56-6.56 (d, 2H); 6.98-6.99 (d, 2H); 7.07-7.10 (d, 2H); 7.53-7.56 (d, 2H); 7.93 (s, 2H)  $^{14}C$  NMR (400 MHz,  $CDCl_3$ )  $\delta$  = FTIR (solid) = 1043.5; 1111.8; 1252.3; 1386.2; 1541.4; 1602.6; 1671.2; 1717.5; 2099.1 (azide); 2873.7  $cm^{-1}$ .

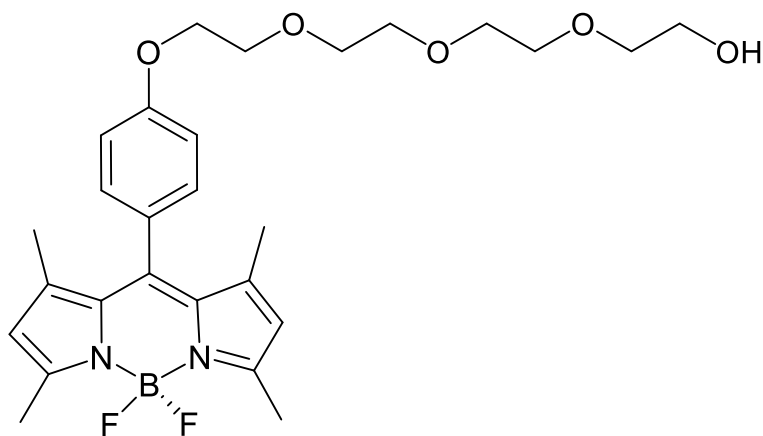
**5,5-difluoro-10-(4-hydroxyphenyl)-1,3,7,9-tetramethyl-5H-dipyrrolo[1,2-c:2',1'-f][1,3,2]diazaborinin-4-ium-5-uide (ALCMBD)**



Chemical Formula: C<sub>19</sub>H<sub>19</sub>BF<sub>2</sub>N<sub>2</sub>O (rmm = 340.2)

To a solution of 4-hydroxylbenzaldehyde (2.440 g, 0.02 mol, 1 eq.) in anhydrous CH<sub>2</sub>Cl<sub>2</sub> (80 ml) was added 2,4-dimethylpyrrole (freshly distilled from CaH, 4.60 mL, 4.28 g, 2.25 eq.) followed by dropwise addition of trifluoroacetic acid (8 drops). The clear reaction turned pale ochre (0.5 hour) then deep brick red (4.5 hours). The reaction was stirred at room temperature and monitored by TLC until it showed complete consumption of the aldehyde (R<sub>f</sub> = 0.70, in CH<sub>2</sub>Cl<sub>2</sub>, brick red spot). 2,3-Dichloro-5,6-dicyano-1,4-benzoquinone (4.54 g, 0.02 mol, 1 eq.) was added and the reaction was stirred at room temperature for 4 hours. In an ice bath N,N-diisopropylethylamine (30.42 g, 41 mL, 0.24 mol, 11.7 eq.) and BF<sub>3</sub>·Et<sub>2</sub>O (cooled in ice bath 42.7 g, 37 mL, 0.30 mol, 15 eq.) were then added and the reaction was stirred at ambient temperature for 18 hours, then washed with distilled H<sub>2</sub>O (4 x 100 mL) and brine (4 x 100 mL). The extracted organic fractions were dried over MgSO<sub>4</sub>, filtered and evaporated and vacuum dried to give the crude product as a brick red solid. The residue was purified via column chromatography (SiO<sub>2</sub>, eluant: CH<sub>2</sub>Cl<sub>2</sub>:petrol ether = 50%-80%, R<sub>f</sub> = 0.50) and then recrystallization from CHCl<sub>3</sub> to afford the expected compound as a brick red solid (1.27 g, 3.7 mmol, 18 % yield). <sup>1</sup>H NMR (CDCl<sub>3</sub>): δ = 7.04-7.07 (d, 2H); 6.85-6.87 (d, 2H); 5.91 (s, 2H); 5.12 (s, br, 1H); 2.48 (s, 6H); 1.37 (s, 6H) <sup>14</sup>C NMR (CDCl<sub>3</sub>) 14.77; 116.48; 121.50; 127.85; 129.94; 132.27; 142.11; 143.44; 155.78; 156.73. <sup>11</sup>B NMR (128 MHz CDCl<sub>3</sub>): δ = 0.0767 ; -0.1727 ; -0.4413 (t, J = 34.38).

**10-(4-((15-azido-3,6,9,12-tetraoxapentadecyl)oxy)phenyl)-5,5-difluoro-1,3,7,9-tetramethyl-5*H*-dipyrrolo[1,2-*c*:2',1'-*f*][1,3,2]diazaborinin-4-ium-5-uide (EMBD)**

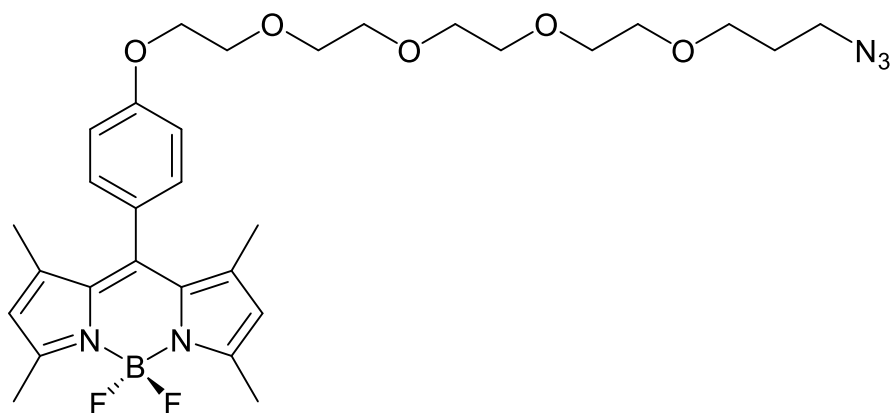


Chemical Formula:  $C_{27}H_{35}BF_2N_2O_5$  (rmm = 516.3)

To a solution of compound **ALCMBD** (340 mg, 1 mmol, 1 eq.) dissolved in DMF (80 mL) was added **TSETH** (0.5 g, 1.4 mmol, 1.4 eq.) in DMF 920 mL), followed by  $K_2CO_3$  (0.4 g, 2.8 eq.). The reaction was stirred under  $N_2$  at 90 °C for 8 hr and then was concentrated and extracted with  $CH_2Cl_2$  and washed with  $H_2O$  and brine. The organic layer was separated and dried over  $MgSO_4$  and then taken off on a rotary evaporator. The crude material was purified by column chromatography ( $SiO_2$ , eluent EtOAc : petro ether = 0 – 50%) to afford the desired compound as a brick-red solid (360 mg, 0.7 mmol, 70 %).  $^1H$  NMR (300 MHz  $CDCl_3$ ):  $\delta$  = 1.39 (s, 6H); 2.51 (s, 6H); 3.66-3.70 (m, 12H); 3.88-3.90 (t, 2H); 4.14-4.16 (t, 2H); 5.94 (s, 2H); 6.98-7.00 (d, 2H); 7.11-7.13 (d, 2H)  $^{14}C$  NMR (400 MHz  $CDCl_3$ ):  $\delta$  = 159.26; 155.17; 143.10; 141.74; 131.75; 130.13; 129.08; 127.14; 121.03; 115.10; 72.46; 70.81; 70.61; 70.54; 70.27; 69.68; 67.38; 61.70; 14.53.  $^{11}B$  NMR (128 MHz  $CDCl_3$ ):  $\delta$  = -146.02; -146.10; -146.25; -146.35 (q,  $J$  = 10.24 Hz).



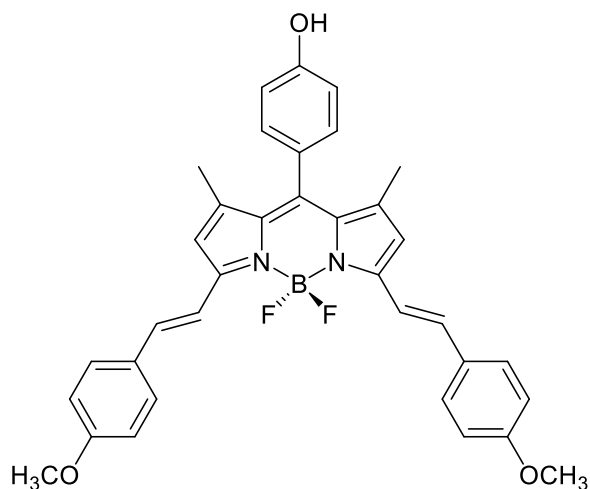
**10-(4-((15-azido-3,6,9,12-tetraoxapentadecyl)oxy)phenyl)-5,5-difluoro-1,3,7,9-tetramethyl-5*H*-dipyrrolo[1,2-*c*:2',1'-*f*][1,3,2]diazaborinin-4-ium-5-uide (AZEMBD)**



Chemical Formula:  $C_{30}H_{40}BF_2N_5O_5$  (rmm = 599.3)

To a THF solution of **EMBD** (360 mg, 0.69 mmol) and 1-azido-3-chloropropane (124 mg, 1.04 mmol, 1.5 equiv.) was added NaH (25 mg, 1.04 mmol, 1.5 equiv.) and the reaction was kept in an ice-salt bath at 0 °C for 2 hours then ambient temperature for 2 hours. Purification via extraction with  $CH_2Cl_2$ :  $H_2O$  gave the target compound a brick-red solid.  $^1H$  NMR (300 MHz  $CDCl_3$ ):  $\delta$  = 1.18 (s, 2H); 1.35 (s, 6H); 2.48 (s, 6H); 3.57-3.54 (m, 4H); 3.69-3.65 (m, 12H); 3.86-3.82 (t, 2H); 4.14-4.11 (t, 2H); 5.23 (s, ) 5.90 (s, 2H); 6.97-6.94 (d, 2H); 7.10-7.08 (d, 2H) FTIR (solid) = 1045.6; 1240.6; 1558.8; 1735.8; 2092.4 (azide); 2200.5  $cm^{-1}$ .

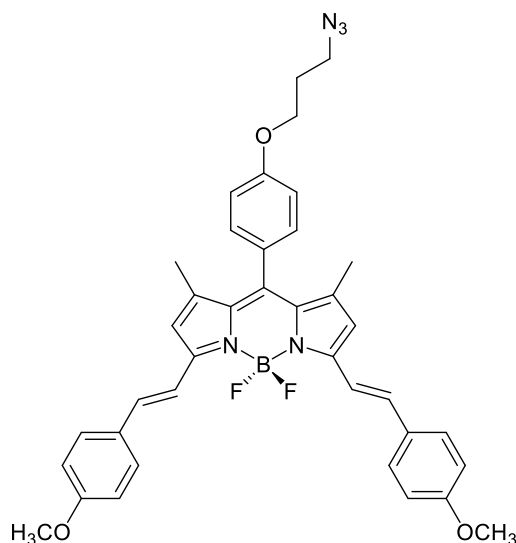
**5,5-difluoro-10-(4-hydroxyphenyl)-3,7-bis((*E*)-4-methoxystyryl)-1,9-dimethyl-5*H*-dipyrrolo[1,2-*c*:2',1'-*f*][1,3,2]diazaborinin-4-ium-5-uide (EBOD)**



Chemical Formula:  $C_{35}H_{31}BF_2N_2O_3$  (rmm = 576.2)

Compound **ALCMBD** (40.43 mg, 0.1 mmol) and 4-methoxybenzaldehyde (14.92 mg, 0.1 mmol) were dissolved in toluene (40 mL, freshly distilled), glacial acetic acid (0.08 mL, 13.97 eq.) and piperidine (0.09 mL, 9.12 eq.) under nitrogen flow in a Dean-Stark apparatus. The reaction mixture was refluxed at 120 °C for 56 hours. Any H<sub>2</sub>O formed during the reaction was removed azeotropically by the silica gel equipped in the burette of a Dean-Stark apparatus. During the reaction the sample were checked by TLC to confirm the consumption of all the starting material. The solvent was removed via a rotary evaporator and purified by column chromatography (silica gel, eluent ethyl acetate : hexane, 1:4). The iris blue coloured fraction ( $R_f$  = 0.27) was collected and the solvent was removed under reduced pressure to yield the distyryl dye (22 mg, 0.038 mmol, 38 %). <sup>1</sup>H NMR (CDCl<sub>3</sub>):  $\delta$  = 1.43 (s, 6H); 1.98 (s, 4H); 3.79 (s, 6H); 6.54 (s, 2H); 6.85-6.91 (m, 4H); 7.09-7.19 (d, 4H); 7.50-7.53 (d, 4H) <sup>13</sup>C NMR (CDCl<sub>3</sub>):  $\delta$  = 14.11; 14.76; 21.01; 30.89; 55.29; 60.46; 114.18; 115.96; 117.33; 128.93; 129.48; 129.69; 135.54; 141.87; 153.10; 157.00; 160.26 <sup>11</sup>B NMR (128 MHz CDCl<sub>3</sub>):  $\delta$  = 0.498; 0.230; -0.019 (t,  $J$  = 27.00 Hz).

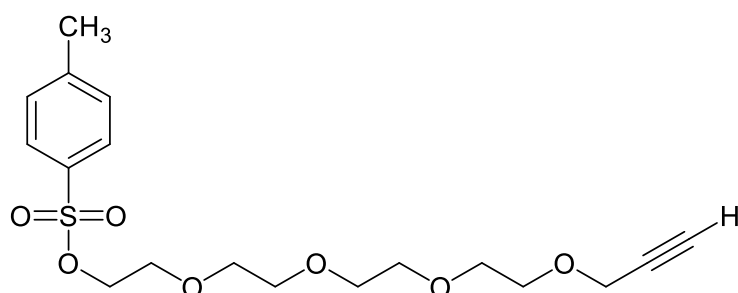
**10-(4-(3-azidopropoxy)phenyl)-5,5-difluoro-3,7-bis((*E*)-4-methoxystyryl)-1,9-dimethyl-5*H*-dipyrrolo[1,2-*c*:2',1'-*f*][1,3,2]diazaborinin-4-ium-5-uide (AZPEBD)**



Chemical Formula:  $C_{38}H_{36}BF_2N_5O_3$  (rmm = 659.3)

Compounds **EBOD** (0.130 g, 0.23 mmol, 1 equiv.) and  $K_2CO_3$  (0.062 g, 0.45 mmol, 2 equiv.) in DMF (40 mL) were stirred for 15 mins at ambient temperature under nitrogen. 1-Azido-3-chloropropane (0.040 g, 0.33 mmol, 1.45 equiv.) was then added and the reaction was stirred at room temperature for 4 h. After completion (TLC check eluent petrol ether :  $CH_2Cl_2$  50%) the reaction was diluted with  $H_2O$  (80 mL) and the product was extracted with dichloromethane (40 mL). The organic layer was washed with  $H_2O$  (10 mL) and dried ( $Na_2SO_4$ ) and concentrated to afford the expected compound (0.14 g, 0.20 mmol, 86 %).  $^1H$  NMR (300 HMz,  $CDCl_3$ ):  $\delta$  = 1.18 (s, 6H); 1.42 (s, 4H); 2.02-2.07 (t, 2H); 3.49-3.53 (t, 2H); 3.83 (s, 6H); 4.03-4.07 (t, 2H); 6.54 (s, 2H); 6.85-6.88 (d, 2H); 6.93-6.96 (d, 2H); 7.14-7.17 (d, 4H); 7.50-7.53 (d, 4H) FTIR (solid) = 1166.1; 1297.3; 1367.1; 2118.1 (azide); 2866.7  $cm^{-1}$ .

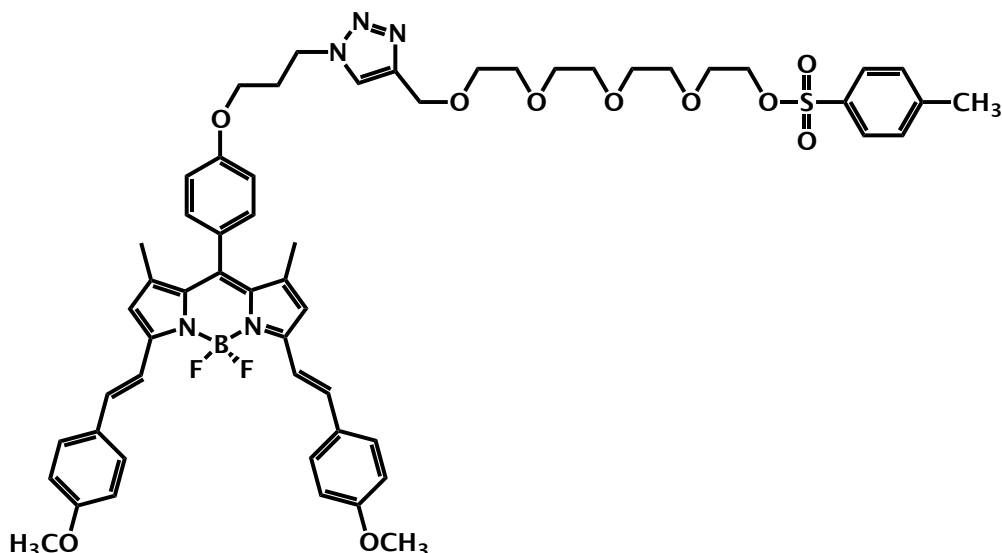
**3,6,9,12-tetraoxapentadec-14-yn-1-yl 4-methylbenzenesulfonate (TSEA)**



Chemical Formula: C<sub>18</sub>H<sub>26</sub>O<sub>7</sub>S (rmm = 386.1)

Triethylamine (117 mg, 0.1 mL, 1.16 mmol, 1 equiv.) was added to a solution of 2-(2-(2-(pent-4-yn-1-yloxy)ethoxy)ethoxy)ethanol (250 mg, 1.16 mmol, 1 equiv.) in CH<sub>2</sub>Cl<sub>2</sub> (20 mL). p-Toluenesulfonic chloride (22 mg, 0.116 mol, 0.1 equiv) dissolved in CH<sub>2</sub>Cl<sub>2</sub> (20 mL) and was added dropwise to the reaction mixture over 10 minutes. The reaction was allowed to stir at 25 °C for 18 hours and monitored via TLC. Purification by column chromatography (SiO<sub>2</sub>, eluent CH<sub>2</sub>Cl<sub>2</sub> : petrol ether = 0 – 50%) afforded the desired compound as a clear gel (290 mg, 0.75 mmol, 65%). <sup>1</sup>H NMR (300 MHz, CDCl<sub>3</sub>) δ = 7.63-7.61 (d, 2H); 7.60-7.59 (d, 2H); 4.02-3.87 (m, 4H); 3.56-3.52 (m, 14H); 3.37-3.35 (t, 1H, acetylene); 2.27 (s, 3H).

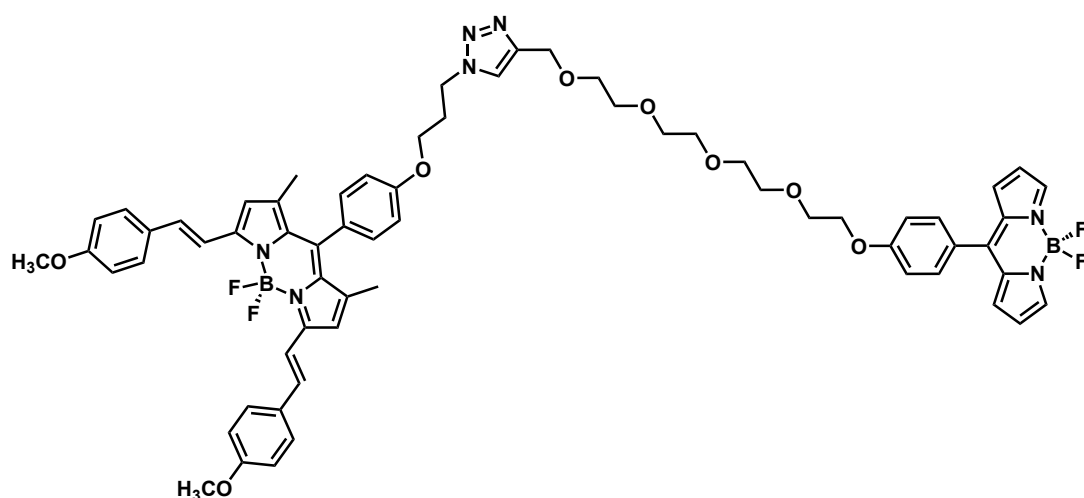
**5,5-difluoro-3,7-bis((E)-4-methoxystyryl)-1,9-dimethyl-10-(4-(3 (4-(13-(tosyloxy)-2,5,8,11-tetraoxatridecyl)-1H-1,2,3-triazol-1-yl)propoxy)phenyl)-5H-dipyrrolo[1,2-c:2',1'-f][1,3,2]diazaborinin-4-ium-5-uide (TSEEBD)**



Chemical Formula: C<sub>56</sub>H<sub>62</sub>BF<sub>2</sub>N<sub>5</sub>O<sub>10</sub>S (1045.4)

3,6,9,12-tetraoxapentadec-14-yn-1-yl 4-methylbenzenesulfonate (0.14 g, 0.36 mmol, 1.8 eq.) was dissolved in anhydrous THF (40 mL purged with N<sub>2</sub>) and to this was added tris-[(1-benzyl-1H-1,2,3-triazol-4-yl)methyl]amine (TBTA) (10 mg, 0.02 mmol, 0.18 eq) and Cu (12 mg, 0.20 mmol, 1 eq). Added to the solution over 5 minutes was an aqueous solution of CuSO<sub>4</sub>·5H<sub>2</sub>O (9 mg, 0.036 mmol, 0.18 eq in 50 ml H<sub>2</sub>O) followed by **AZPEBD** (0.14 g, 0.20 mmol, 1.0 equiv.) The reaction was stirred at 40 °C for 18 hours. The aqueous portion was separated and extracted with CH<sub>2</sub>Cl<sub>2</sub>. The organioc layer was separated dried (MgSO<sub>4</sub>) and removed on a rotary evaporator. Purification of the crude material via column chromatography (SiO<sub>2</sub>, eluant CH<sub>2</sub>Cl<sub>2</sub> : petrol ether, 10%-90%, *R<sub>f</sub>* = 0.05) afforded the expected compound as a blue solid (84 mg, 0.08 mmol, 40 % yield). <sup>1</sup>H NMR (300 MHz, CDCl<sub>3</sub>): δ = 7.74-7.72 (d, 4H); 7.61-7.59 (d, 4H); 7.52 (s, 1H, triazo); 7.50-7.49 (d, 4H); 7.42-7.40 (d, 2H); 7.24-7.22 (d, 2H); 7.21-7.19 (d, 1H); 6.91-6.89 (d, 1H); 6.83-6.81 (d, 2H); 4.66-4.64 (d, 2H); 4.11 (s, 4H); 3.99-3.97 (t, 2H); 3.79 (s, 6H); 3.65-3.61 (m, 16H); 2.34 (s, 3H); 1.50 (s, 3H); 1.38 (s, 3H); 1.34-1.32 (t, 2H).

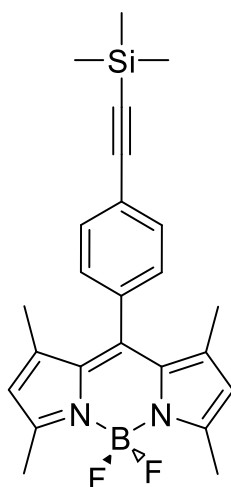
**10-(4-(3-(4-(13-(4-(5,5-difluoro-5*H*-dipyrrolo[1,2-*c*:2',1'-  
 $\Lambda$ [1,3,2]diazaborinin-4-ium-5-uid-10-yl)phenoxy)-2,5,8,11-  
tetraoxatridecyl)-1*H*-1,2,3-triazol-1-yl)propoxy)phenyl)-5,5-difluoro-3,7-  
bis((*E*-4-methoxystyryl)-1,9-dimethyl-5*H*-dipyrrolo[1,2-*c*:2',1'-  
 $\Lambda$ [1,3,2]diazaborinin-4-ium-5-uide (ROTEBD)**



Chemical Formula: C<sub>64</sub>H<sub>65</sub>B<sub>2</sub>F<sub>4</sub>N<sub>7</sub>O<sub>8</sub> (1157.5)

**TSEEBD** (81 mg, 0.076 mmol, 1 eq.) and **ALCROT** (40, 0.140 mmol, 1.8 eq.) were dissolved in anhydrous CH<sub>2</sub>Cl<sub>2</sub> (20 mL). Triethylamine (90 mg, 0.06 mL, 0.08 mmol, 1.2 equiv.) in CH<sub>2</sub>Cl<sub>2</sub> (20 mL) was added to the solution. The reaction was stirred at 25 °C for 18 hours and monitored via TLC. Purification via column chromatography (SiO<sub>2</sub>, eluent CH<sub>2</sub>Cl<sub>2</sub> : PetEt = 1:2) afforded the target compound a deep green solid (14 mg, 0.012 mmol, 16%). <sup>1</sup>H NMR (300 MHz, CDCl<sub>3</sub>) δ = 7.86 (s, 2H); 7.73-7.71 (d, 4H); 7.62 (s, 1H, triazo); 7.61-7.59 (d, 4H); 7.51-7.49 (d, 2H); 7.50-7.48 (d, 4H); 7.46-7.44 (d, 2H); 7.24-7.22 (d, 2H); 7.13-7.11 (d, 1H); 7.08-7.06 (d, 2H); 6.91-6.89 (d, 1H); 6.87-6.86 (d, 2H); 6.83-6.81 (d, 2H); 6.51-6.50 (d, 2H); 4.11 (s, 4H); 3.32-3.30 (t, 2H); 3.64-3.61 (m, 16H); 3.60 (s, 6H); 1.34-1.32 (t, 2H).

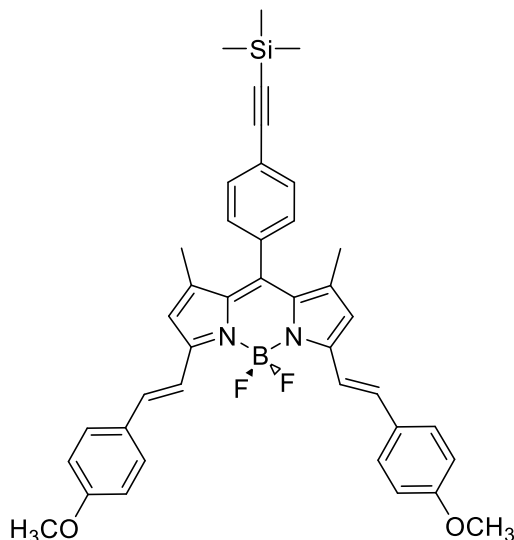
**5,5-difluoro-1,3,7,9-tetramethyl-10-(4-((trimethylsilyl)ethynyl)phenyl)-5H-dipyrrolo[1,2-c:2',1'-f][1,3,2]diazaborinin-4-ium-5-uide (SiMBOD)**



Chemical Formula:  $C_{24}H_{27}BF_2N_2Si$  (420.2)

To a stirred solution of **BrBOD** (678 mg, 1.68 mmol, 1 eq.) in anhydrous THF (80 mL) was added tetrakis(triphenylphosphine)palladium(0) (0.01 g, 0.008 mmol, 0.004 eq.) The reaction was purged under nitrogen (1 atmosphere) for 1.5 hour and to the reaction was added N,N-diisopropylethylamine (40 mL, freshly distilled from  $CaH_2$ ) and ethynyltrimethylsilane (0.45 mL dropwise, 3 mmol, 1.78 eq.). The reaction was stirred at room temperature for 18 hours and monitored by TLC ( $SiO_2$ ,  $CH_2Cl_2$  : petrol ether 0%-20%, red spot,  $R_f$  = 0.36). The reaction was cooled to room temperature then quenched with HCl (1M, 50 mL) in ice (350 mL). The crude product was then washed with distilled  $H_2O$  (3 x 100 mL). The  $CH_2Cl_2$  extracted organic fractions were dried over  $MgSO_4$ , filtered and evaporated. Recrystallization from  $CH_2Cl_2$  : petrol ether to afford expected compound bright red crystals. (252 mg, 0.06 mmol, 35%).  $^1H$  NMR (300 MHz,  $CDCl_3$ ):  $\delta$  = 7.46-7.43 (d, 2H), 7.10-7.07 (d, 2H); 5.82 (s, 2H); 2.39 (s, 6H); 1.24 (s, 6H); 0.12 (s, 9H).  $^{13}C$  NMR (300 MHz,  $CDCl_3$ ):  $\delta$  = 155.83; 143.07; 140.81; 135.28; 132.96; 132.80; 131.22; 128.28; 128.15; 123.98; 121.43; 104.26; 95.90; 14.70.  $^{11}B$  NMR (128 MHz  $CDCl_3$ ):  $\delta$  = 0.042; 0.222; 0.473 ( $J$  = 32.12 Hz).

**5,5-difluoro-3,7-bis((E)-4-methoxystyryl)-1,9-dimethyl-10-(4-  
((trimethylsilyl)ethynyl)phenyl)-5H-dipyrrolo[1,2-c:2',1'-  
f][1,3,2]diazaborinin-4-ium-5-uide (SiEBD)**

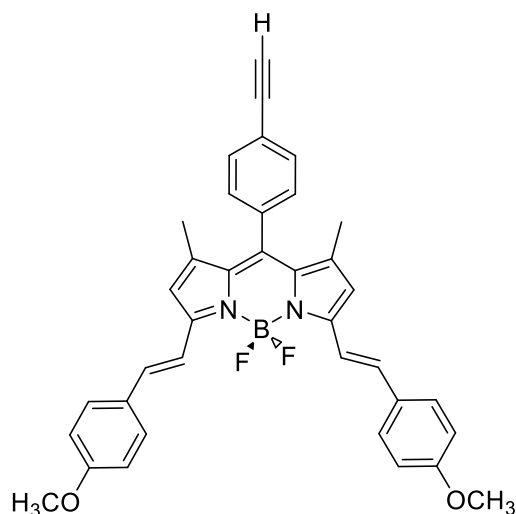


Chemical Formula:  $C_{40}H_{39}BF_2N_2O_2Si$  (rmm = 656.3)

Compound **SiMBOD** (154 mg, 0.36 mmol, 1 eq.) and 4-methoxybenzaldehyde (14 mg, 1 mmol, 2.7 eq.) were dissolved in toluene (40 mL, freshly distilled), containing glacial acetic acid (0.77 mL, 0.8 g, 13 mmol, 35 eq.) and piperidine (0.87 mL, 0.75 g, 8 mmol, 22 eq.). The reaction mixture was refluxed at 120 °C for 108 hours. The  $H_2O$  formed during the reaction was removed azeotropically by silica gel equipped in the burette of a Dean-Stark apparatus. During the reaction the sample were checked by TLC to confirm the consumption of the starting material. The solvent was removed via a rotary evaporator and purified via column chromatography (silica gel, eluent ethyl acetate : petrol ether, 1:4). The iris blue coloured fraction ( $R_f = 0.20$ ) was collected and the solvent was removed under reduced pressure to yield the expected compound (60 mg, 0.09 mmol, 25 %).  $^1H$  NMR ( $CDCl_3$ ):  $\delta$  = 7.88-7.85 (d, 2H); 7.65-7.63 (d, 2H); 7.59-7.57 (d, 4H); 7.33-7.31 (d, 2H); 7.05-7.02 (d, 2H); 6.97-6.94 (d, 4H); 6.63 (s, 1H); 3.92 (s, 1H); 3.88 (s, 6H); 2.59 (s, 3H); 1.48 (s, 3H); 0.31 (s, 9H).



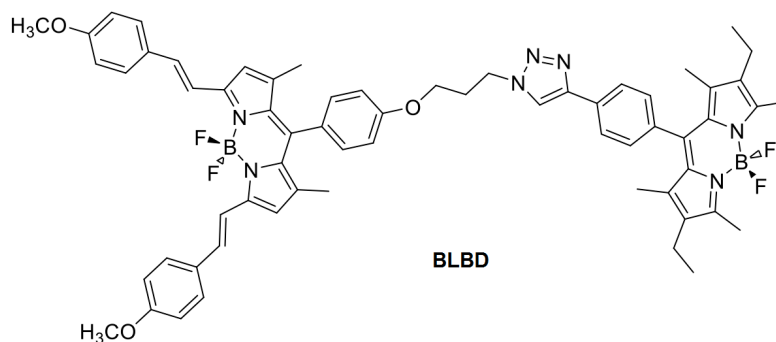
**10-(4-ethynylphenyl)-5,5-difluoro-3,7-bis((E)-4-methoxystyryl)-1,9-dimethyl-5H-dipyrrolo[1,2-c:2',1'-f][1,3,2]diazaborinin-4-ium-5-uide  
(ACEBD)**



Chemical Formula:  $C_{37}H_{31}BF_2N_2O_2$  (rmm = 584.2)

Compound **SiEBD** (60 mg, 0.091 mmol, 1 eq.) was dissolved in anhydrous THF (20 mL), followed by the addition of methanol (20 mL, from molecular sieved sealed bottle). KF (57 mg, 0.32 mmol, 3.5 eq) was dissolved in anhydrous THF (5 mL) and added to the reaction during 5 minutes. The reaction were stirred at room temperature for 18 hours, then concentrated by rotary evaporation. The crude product was washed with distilled  $H_2O$  (3 x 100 ml), extracted from dichloromethane and the organic fractions were dried over  $MgSO_4$ , filtered and evaporated. Purification via column chromatography (silica gel, eluent  $CH_2Cl_2$ : Petrol 1:1) afforded the target compound as a blue solid (48 mg, 0.08 mmol, 90% ).  $^1H$  NMR ( $CDCl_3$ ):  $\delta$  = 7.79-7.77 (d, 2H); 7.56-7.53 (d, 2H); 7.51-7.49 (d, 4H); 7.53-7.51 (d, 2H); 6.96-6.93 (d, 2H); 6.88-6.85 (d, 4H); 6.55 (s, 1H); 3.82 (s, 1H); 3.79 (s, 6H); 3.12 (s, 1H acetylene); 1.48 (s, 3H); 1.39 (s, 3H).

**10-(4-(1-(3-(4-(5,5-difluoro-3,7-bis((*E*)-4-methoxystyryl)-1,9-dimethyl-5*H*-dipyrrolo[1,2-*c*:2',1'-*f*][1,3,2]diazaborinin-4-ium-5-uid-10-yl)phenoxy)propyl)-1*H*-1,2,3-triazol-4-yl)phenyl)-2,8-diethyl-5,5-difluoro-1,3,7,9-tetramethyl-5*H*-dipyrrolo[1,2-*c*:2',1'-*f*][1,3,2]diazaborinin-4-ium-5-uide (BLBD)**

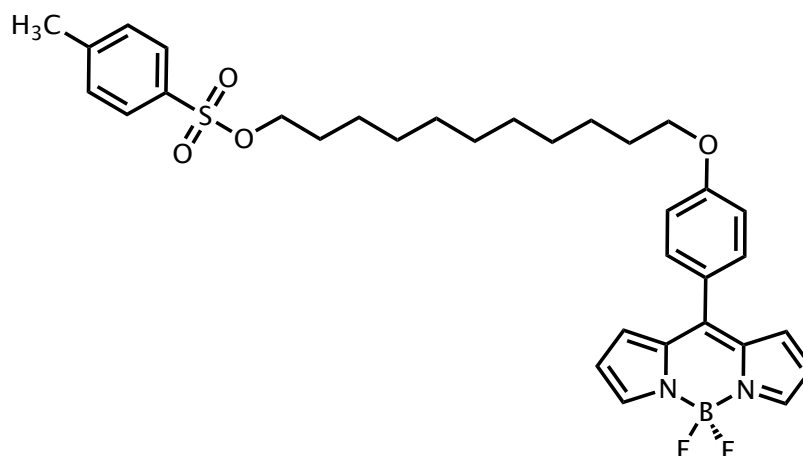


Chemical Formula: C<sub>64</sub>H<sub>67</sub>B<sub>2</sub>F<sub>4</sub>N<sub>7</sub>O<sub>3</sub> (rmm = 1079.5)

**ACETBD** (37 mg, 0.092 mmol, 1 eq.) was dissolved in anhydrous THF (40 mL purged with N<sub>2</sub>) and to this was added tris-[(1-benzyl-1*H*-1,2,3-triazol-4-yl)methyl]amine (TBTA) (5 mg, 0.009 mmol, 0.1 eq) and Cu (5 mg, 0.078 mmol, 0.85 eq). Then during 5 minutes an aqueous solution of CuSO<sub>4</sub>·5H<sub>2</sub>O (3 mg, 0.012 mmol, 0.13 eq in 50 ml H<sub>2</sub>O) was added. To the solution during 5 minutes compound **AZPEBD** (60 mg, 0.091 mmol, 0.98 eq) was added. The reaction was stirred at 40 °C for 18 hours. The aqueous portion was separated and extracted with dichloromethane. The combined organics were dried (MgSO<sub>4</sub>) and removed on a rotary evaporator. Purification of the crude material via column chromatography (SiO<sub>2</sub>, eluant CH<sub>2</sub>Cl<sub>2</sub> : petrol ether, 50%-90% removed the orange coloured fraction starting material, then ethyl acetate 50%-90% *R<sub>f</sub>* = 0.09) afforded the expected compound as a navy coloured solid (30 mg, 38 mmol, 63 % yield). <sup>1</sup>H NMR (300 MHz, CDCl<sub>3</sub>): δ = 7.90-7.87 (d, 2H); 7.82 (s, 1H, triazo H); 7.57 (s, 2H); 7.53-7.50 (d, 2H); 7.30-7.28 (d, 2H); 7.15-7.16 (d, 2H); 6.97 (s, 2H); 6.88-6.85 (d, 2H); 4.65-4.69 (t, 2H); 4.03-4.09 (t, 2H); 2.47 (s, 6H); 2.32-2.16(q, 2H); 1.19(s, 6H); 0.93-0.88(t, 6H) <sup>13</sup>C NMR (400 MHz, CDCl<sub>3</sub>): δ = 206.9; 160.3; 153.9; 152.7; 147.1; 141.5; 139.4; 138.2; 135.7; 133.4; 132.8; 131.6; 131.0; 130.7; 129.9; 129.5; 129.0; 128.9; 126.1; 120.3; 117.4; 117.1; 114.8; 114.2; 113.7 <sup>11</sup>B NMR (128

MHz CDCl<sub>3</sub>):  $\delta$  = 0.47007; 0.19998; 0.11896; -0.14212; -0.40320 (pentatet,  $J$  = 34.57 Hz;  $J$  = 33.42 Hz). <sup>19</sup>F NMR (376 MHz CDCl<sub>3</sub>):  $\delta$  = -138.2747; -138.3445; -138.4142; -138.5138 (q,  $J$  = 26.24 Hz);  $\delta$  = -145.5582; -145.6279; -145.6977; -145.7873 (q,  $J$  = 26.24 Hz). UV-Vis Absorption (CH<sub>2</sub>Cl<sub>2</sub>) = 520nm and 645 nm; MALDI C<sub>63</sub>H<sub>63</sub>B<sub>2</sub>F<sub>4</sub>N<sub>7</sub>O<sub>3</sub> = calculated  $M$  = 1063.84 observed [ $M$ -H<sup>+</sup>] = 1062.50.

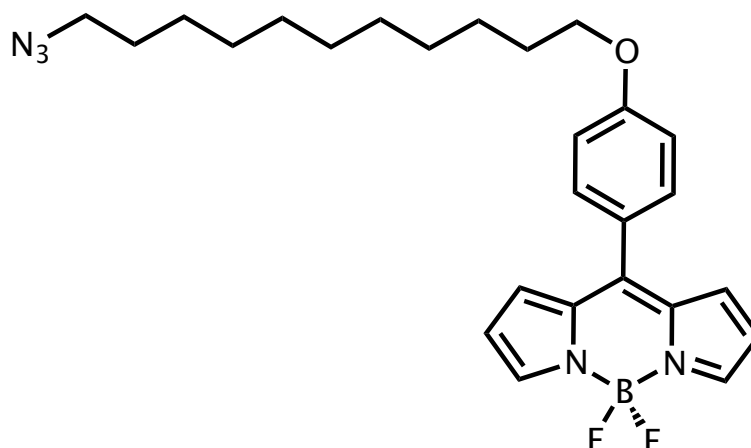
**5,5-difluoro-10-(4-((11-(tosyloxy)undecyl)oxy)phenyl)-5H-dipyrrolo[1,2-c:2',1'- $\eta$ ][1,3,2]diazaborinin-4-ium-5-uide (TSUNROT)**



C<sub>33</sub>H<sub>39</sub>BF<sub>2</sub>N<sub>2</sub>O<sub>4</sub>S 608.27

11-(4-formylphenoxy)undecyl 4-methylbenzenesulfonate (75 mg, 0.21 mmol, 1 equiv) without solution was added to pyrrole (freshly distilled from CaH, 36 mL, 35.22 g, 5.25 mmol, 25 eq.) under nitrogen flow, followed by drop wise trifluoroacetic acid (8 drops). The solution turned from clear to brick red. The reaction was stirred at room temperature for 2 hour until the TLC showed complete consumption of the aldehyde. The reaction mixture was vacuum distilled to remove pyrrole completely, afforded red gel-like crude compound, Purification via neutral aluminum column (EA : Petrol ether 0%-90%). The collected intermediate was then dissolved into CH<sub>2</sub>Cl<sub>2</sub>, 2,3-dichloro-5,6-dicyano-1,4-benzoquinone (0.48 g, 0.21 mmol, 1 eq.) was added, the reaction was stirred at room temperature for 8 hours, then in ice bath were added N,N-diisopropylethylamine (0.32, 4 mL, 2.52 mmol, 12 eq.) and BF<sub>3</sub>·Et<sub>2</sub>O (0.44 g, 3 mL, 3.15 mmol, 15 eq.), the reaction kept stirred at ambient temperature for 18 hours, then washed with distilled H<sub>2</sub>O (4 × 100 mL) and brine (4 × 100 mL). The extracted organic fractions were dried over MgSO<sub>4</sub>, filtered and evaporated and vacuum dried to give crude product as a red solid. The residue was purified via column chromatography (SiO<sub>2</sub>, eluant: ethyl acetate : hexane = 0%-80%) to afford the expected compound an orange solid (90 mg, 0.094 mmol, 45% yield). <sup>1</sup>H NMR (300 MHz, CDCl<sub>3</sub>): δ = 7.82 (s, 1H); 7.71-7.69 (d, 2H); 7.62-7.60 (d, 2H); 7.44-7.42 (d, 2H); 7.26-7.25 (d, 2H); 7.20 (s, 1H); 6.99-6.97 (d, 2H); 6.90-6.89 (d, 2H); 6.49-6.50 (d, 2H); 4.93-4.05 (m, 4H); 2.38 (s, 3H); 1.79-1.77 (t, 4H); 1.74-1.72 (t, 2H); 1.63-1.52 (m, 10H)

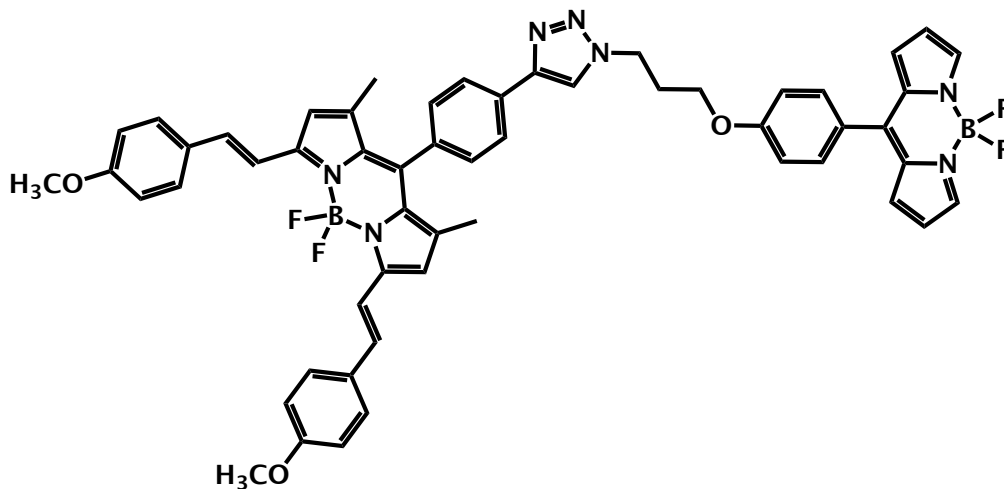
**10-(4-((11-azidoundecyl)oxy)phenyl)-5,5-difluoro-5H-dipyrrolo[1,2-*c*:2',1'-*f*][1,3,2]diazaborinin-4-ium-5-uide (AZUNROT)**



$C_{26}H_{32}BF_2N_5O$  479.27

To the solution of compound **TSUNROT** (90 mg, 0.094 mmol, 1 equiv.) in 20 mL DMF was added  $NaN_3$  (10 mg, 0.14 mmol, 1.5 equiv.) The reaction was kept under nitrogen atmosphere stirring at 90°C for 5 hour, then was concentrated, washed with  $H_2O$ , dried over  $MgSO_4$ , the organic portion extracted from  $CH_2Cl_2$ . Purification via column chromatography ( $SiO_2$ , eluant: ethyl acetate : hexane = 0%-50%) to afford the expected compound an red solid (38 mg, 0.082 mmol, 87% yield)  $^1H$  NMR (300 MHz,  $CDCl_3$ ):  $\delta$  = 7.15 (s, 1H); 7.01-6.99 (d, 2H); 6.76-6.74 (d, 2H); 4.00-3.98 (t, 2H); 6.60 (d, 2H); 6.05 (d, 1H); 5.82 (s, 1H); 5.35 (s, 1H); 1.74-1.72 (p, 2H); 1.69-1.67 (t, 2H); 1.34-1.32 (t, 2H); 1.20 (s, 14H) FT-IR (solid): 2338.8 (azide); 1638.7; 1227.0; 1054.5; 957.0; 831.8

**10-(4-(1-(3-(4-(5,5-difluoro-5H-dipyrrolo[1,2-c:2',1'-f][1,3,2]diazaborinin-4-ium-5-uid -10-yl)phenoxy)propyl)-1H-1,2,3-triazol-4-yl)phenyl)-5,5-difluoro-3,7-bis((E)-4-methoxystyryl)-1,9-dimethyl-5H-dipyrrolo[1,2-c:2',1'-f][1,3,2]diazaborinin-4-ium-5-uide (BLRO)**

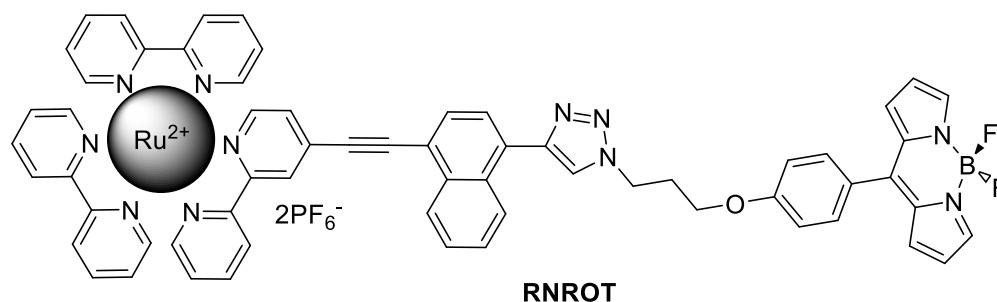


Chemical Formula:  $C_{55}H_{47}B_2F_4N_7O_3$  (rmm = 951.4)

**ACEBD** (48 mg, 0.08 mmol, 1 eq.) was dissolved in anhydrous THF (40 mL purged with  $N_2$ ) and to this was added tris-[(1-benzyl-1H-1,2,3-triazol-4-yl)methyl]amine (TBTA) (8 mg, 0.016 mmol, 0.2 eq) and Cu (5 mg, 0.08 mmol, 1 eq). Then was added during 5 minutes an aqueous solution of  $CuSO_4 \cdot 5H_2O$  (4 mg, 0.016 mmol, 0.2 eq in 50 ml  $H_2O$ ), followed by a solution of **AZROT** (37 mg, 0.10 mmol, 1.25 eq). The reaction was stirred at 8-15 °C for 18 hours. The aqueous portion was separated and extracted with dichloromethane, then concentrated via rotary evaporation. The crude material was purified by column chromatography ( $SiO_2$ , eluant  $CH_2Cl_2$  : petrol ether, 0%-80%) to afford the expected compound as a red solid (34 mg, 0.04 mmol, 45 % yield).  $^1H$  NMR (300 MHz,  $CDCl_3$ ):  $\delta$  = 7.90-7.87 (d, 2H); 7.82 (s, 1H, triazo H); 7.57 (s, 2H); 7.53-7.50 (d, 2H); 7.30-7.28 (d, 2H); 7.15-7.16 (d, 2H); 6.97 (s, 2H); 6.88-6.85 (d, 2H); 4.65-4.69 (t, 2H); 4.03-4.09 (t, 2H); 2.47 (s, 6H); 2.32-2.16 (q, 2H); 1.19 (s, 6H); 0.93-0.88 (t, 6H).  $^{13}C$  NMR (400 MHz,  $CDCl_3$ ):  $\delta$  = 206.9; 160.3; 153.9; 152.7; 147.1; 141.5; 139.4; 138.2; 135.7; 133.4; 132.8; 131.6; 131.0; 130.7; 129.9; 129.5; 129.0; 128.9; 126.1; 120.3; 117.4; 117.1; 114.8; 114.2; 113.7.  $^{11}B$  NMR (128 MHz  $CDCl_3$ ):  $\delta$  = 0.4989; 0.2494; 0.0384; -0.4413; -0.6716; -0.9018 ( $J$  = 29.44 Hz).  $^{19}F$  NMR (376 MHz  $CDCl_3$ ):  $\delta$  = -145.08; -145.01; -144.94; -144.89 (q,  $J$  = 26.32 Hz);  $\delta$  = -138.40; -138.42; -138.25 (q,  $J$

= 26.32 Hz) UV-Vis Absorption ( $\text{CH}_2\text{Cl}_2$ ) = 505 nm and 645 nm;  
 $\text{C}_{55}\text{H}_{47}\text{B}_2\text{F}_4\text{N}_7\text{O}_3$  calculated M = 951.39 MALDI observed  $[\text{M}+\text{H}^+]$  = 952.39.

## Preparation of ROMC1



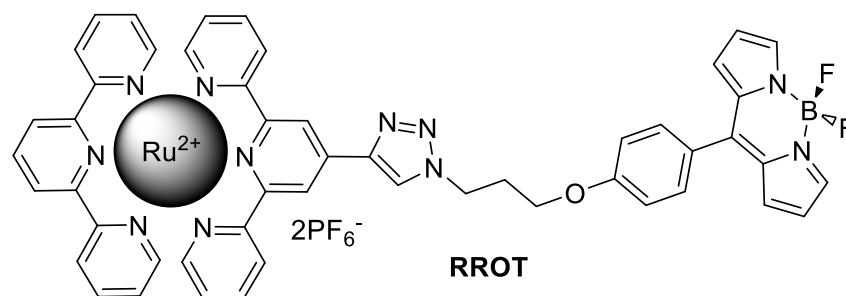
Chemical Formula:  $C_{62}H_{46}BF_{14}N_{11}OP_2Ru$  (rmm = 1401.1)

To a two-necked, round-bottomed 500 mL flask equipped with a magnetic stirrer was added **RuNA** (32 mg, 0.042 mmol, 1 eq.) dissolved in anhydrous THF (120 mL purged with  $N_2$ ). The catalyst tris-[(1-benzyl-1H-1,2,3-triazol-4-yl)methyl]amine (TBTA) (5 mg, 0.009 mmol, 0.2 eq) and Cu (4 mg, 0.042 mmol, 1 eq) were added. During 5 minutes an aqueous solution of  $CuSO_4 \cdot 5H_2O$  (3 mg, 0.009 mmol, 0.2 eq in 80 ml  $H_2O$ ) was added to the solution and stirred for 1.5 hrs, followed by the addition of **AZROT** (20 mg, 0.054 mmol, 1.28 eq). The reaction was stirred at 40 °C for 12 hours, and monitored by TLC. The aqueous portion was separated and extracted with dichloromethane, which was separated and dried ( $MgSO_4$ ) and removed on a rotary evaporator. Purification of the crude material was carried out by column chromatography ( $Al_2O_3$ , eluant acetonitrile : petrol ether, 10%-80%,  $R_f$  = 0.02). The compound collected was flash-frozen under liquid nitrogen by application of a vacuum (x 4) to allow any trapped solvent to escape. The desired compound was obtained as a red solid (15 mg, 0.014 mmol, 32 % yield).  $^1H$  NMR (300 MHz,  $CDCl_3$ ):  $\delta$  = 8.76 (s, H); 8.62-8.65 (t, 1H); 8.52-8.55 (d, 2H); 8.07-8.13 (m, H); 7.93 (s, H); 7.85-7.87(d, H); 7.76-7.80 (m, H); 7.59-7.61 (m, H); 7.44-7.48 (m, H); 7.10-7.12 (d, 2H); 7.00-7.01(d, 2H); 6.62-6.63 (d, 2H); 4.76-4.80 (t, 2H); 4.21-4.25 (t, 2H); 2.53-2.57 (t, 2H).  $^{13}C$  NMR (75 MHz,  $CDCl_3$ )  $\delta$  = 151.84; 151.79; 143.45; 137.99; 132.87; 132.57; 131.21; 129.17; 128.57; 127.71; 124.38; 114.69; 67.48; 38.52; 32.04; 30.34; 29.32; 28.64; 10.24.  $^{11}B$  NMR (128 MHz  $CDCl_3$ ):  $\delta$  = -0.59; -0.81; -1.18 (triplet,  $J$  = 28.16 Hz).  $^{19}F$  NMR (376 MHz  $CDCl_3$ ):  $\delta$  = -71.70, -71.83 (d,  $J$  = 48.88). Mass



Spectrum  $\text{C}_{62}\text{H}_{46}\text{BF}_{14}\text{N}_{11}\text{OP}_2\text{Ru}$  calculated = 1401.1 MALDI observed  $[\text{M-PF}_6]^+ = 1256.2$ .

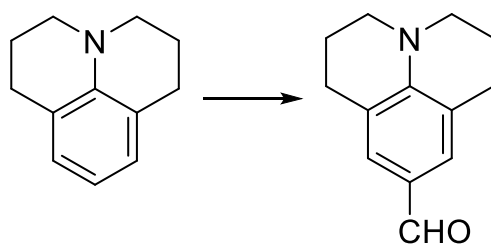
## Preparation of ROMC2



Chemical Formula:  $C_{50}H_{38}BF_{14}N_{11}OP_2Ru$  (rmm = 1249.2)

To a two-necked round-bottomed 500 mL flask equipped with a magnetic stirrer was added **AZROT** (70 mg, 0.17 mmol, 1 eq) and THF (120 mL purged with  $N_2$ ). The catalyst tris-[(1-benzyl-1H-1,2,3-triazol-4-yl)methyl]amine (TBTA) (9 mg, 0.016 mmol, 0.1 eq) and Cu (11 mg, 0.17 mmol, 1 eq) were added to the solution. The compound **RuA** (95 mg, 0.16 mmol, 1 eq.) was added, followed by an aqueous solution of  $CuSO_4 \cdot 5H_2O$  (4 mg, 0.016 mmol, 0.1 eq), (90 mg, 0.24 mol, 1.47 eq) dissolved in a 1:1 THF/  $H_2O$  (10 ml) mixture. The reaction was stirred at 40 °C for 36 hours and the reaction was monitored via TLC. Removal of the solvents gave the crude mixture which was purified via column chromatography (aluminum oxide, eluant acetonitrile:  $CH_2Cl_2$  = 0 % - 80 %,  $R_f$  = 0.2). The desired compound was recrystallized via slow vapour diffusion in  $CHCl_3$  : petrol ether (98 mg, 0.102 mmol, 60 % yield).  $^1H$  NMR (300 MHz,  $CDCl_3$ ):  $\delta$  = 9.18(s, 2H); 8.76-8.79(d, 4H); 8.59-8.62(d, 4H); 8.49-8.52(d, 2H); 8.40-8.45 (t, 1H); 7.89-7.95(m, 4H), 7.94 (s, 1H); 7.63-7.66 (d, 2H); 7.41-7.43 (d, 4H); 7.35-7.37 (d, 4H); 7.15-7.17(m, 2H); 7.04-7.14 (d, 1H); 6.53-6.54 (d, 1H); 4.85-4.89 (t, 2H); 4.26-4.30 (t, 2H); 2.58-2.62 (t, 2H).  $^{13}C$  NMR (300 MHz,  $CDCl_3$ ):  $\delta$  = 211.69; 163.34; 161.00; 160.74; 157.71; 157.62; 148.75; 143.37; 138.00; 132.84; 132.72; 129.81; 129.69; 129.00; 124.76; 120.14; 35.05  $^{11}B$  NMR (128 MHz,  $CDCl_3$ ):  $\delta$  = - 1.03, -0.81, -0.59 (t,  $J$  = 28)  $^{19}F$  NMR (376 MHz,  $CDCl_3$ ):  $\delta$  = -71.74, -71.62 (d,  $J$  = 48.00) Mass Spectrum  $C_{50}H_{38}BF_2N_{11}ORu$  calculated = 959.23 MALDI observed  $[M]^+$  = 959.35.

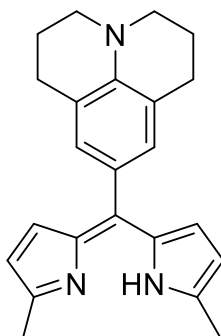
### Preparation of Julolidinecarboxaldehyde



Chemical Formula:  $C_{13}H_{15}NO$  (rmm = 201.3)

A 250 mL round flask equipped with a magnetic stirrer was charged with a solution of julolidine (1.0 g, 5.76 mmol, 1 eq.) and N,N-dimethylformamide (0.54 mL, 6.92 mmol, 1.2 eq.) in dichloromethane (20 mL). To the solution was added dropwise phosphorus(V) oxychloride (0.58 mL, 6.34 mmol, 1.1 eq.) and the reaction was stirred at 25°C for 8 hr. The reaction was treated with an aqueous solution of 2 M NaOH (2 g in 25 mL) and the mixture was stirred at 0 °C for 4 h, and monitored via TLC until complete consumption of the starting material. The organic layer was extracted by diethyl ether (10~50 ml), dried over  $MgSO_4$  and removed on a rotary evaporator. The crude residue was purified via column chromatography (silica gel, eluent diethyl ether: petrol ether 20%  $R_f$  = 0.15). Recrystallisation twice from diethyl ether: petrol ether (10%) afforded the target compound as a yellow solid (0.52 g, 2.58 mmol, 45 %).  $^1H$  NMR (300 MHz,  $CDCl_3$ ) 9.54 (s, 1 H, aldehyde), 7.25 (s, 2H), 3.27-3.24 (m, 4H), 2.74-2.70 (m, 4H), 1.96-1.88 (m, 4H).  $^{13}C$  NMR (300 MHz,  $CDCl_3$ ): 189.77 (aromatic aldehyde); 129.29; 120.34; 50.00; 27.62; 21.00.

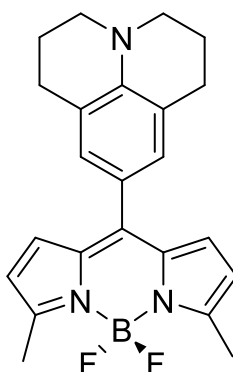
**(Z)-9-((5-methyl-1*H*-pyrrol-2-yl)(5-methyl-2*H*-pyrrol-2-ylidene)methyl-2,3,6,7-tetrahydro-1*H*,5*H*-pyrido[3,2,1-*ij*]quinolone (MJUL)**



Chemical Formula: C<sub>23</sub>H<sub>25</sub>N<sub>3</sub> (rmm = 343.2)

To a two-necked, round-bottomed 1L flask equipped with a magnetic stirrer and degassed CH<sub>2</sub>Cl<sub>2</sub> (400 mL) was added p-julolidinealdehyde (0.75 g, 3.7 mmol, 1 eq.) and 2-methylpyrrole (0.67 mL, 7.9 mmol, 2.14 eq.) A catalytic quantity (8 drops) of trifluoroacetic acid was then added. The yellow solution turned to deep red in 20 minutes. The flask was covered with aluminum foil to protect from light and the reaction were kept at 10-18 °C for 8 hours, and monitored via TLC until the complete consumption of the starting material. A solution of 2,3-dichloro-5,6-dicyano-1,4-benzoquinone (0.84 g, 3.7 mmol, 1 eq.) was then added and the reaction kept at 10-15 °C for 8 hours. The reaction was quenched with H<sub>2</sub>O and the organic layer was separated by adding CH<sub>2</sub>Cl<sub>2</sub> (200 mL), which was then washed with saturated brine (2 × 200 mL) and water (4 × 100 mL). The organics was dried over magnesium sulfate and filtered. Removal of the solvent under reduced pressure afforded a brick-red gel-like residue, which was then purified by column chromatography on neutral alumina (eluent petrol ether: CH<sub>2</sub>Cl<sub>2</sub> (2:1), then CH<sub>2</sub>Cl<sub>2</sub> : ethyl acetate 2:1). Recrystallization via CH<sub>2</sub>Cl<sub>2</sub>: petrol ether (1:4) afforded a brick red crystalline solid (0.51 g, 40% yield). Mp. = 114-118 °C. <sup>1</sup>H NMR (CDCl<sub>3</sub>, 300 MHz) δ (ppm) = 7.53-7.51(d, *J* = 0.31 Hz, 2H); 7.00 (s, 2H); 6.86-6.85 (d, *J* = 0.94, 1H); 6.24-6.23 (d, *J* = 0.95, 2H); 5.00 (s, 1H); 3.27-3.25 (t, *J* = 1.9 Hz, 4H); 2.78-2.75 (t, *J* = 1.9 Hz, 4H); 2.63 (s, 3H); 2.16 (s, 3H); 2.00-1.97 (m, 4H).

## Preparation of MJULBD



Chemical Formula:  $C_{23}H_{24}BF_2N_3$  (rmm = 391.2)

**MJUL** (0.51 g, 1.48 mmol, 1 eq.) was transferred to a two-necked, round-bottomed 1L flask equipped with a magnetic stirrer and nitrogen purged  $CH_2Cl_2$  (400 mL). *N,N*-diisopropylethylamine (4.12 mL, 3.06 g, 24.0 mmol, 16 eq.) was added dropwise during 15 minute and ice cooled  $BF_3 \cdot OEt_2$  (3.64 mL, 29.6 mmol, 20 eq.) was then added dropwise during 20 minutes. The reaction were stirred at 10-18 °C for 8 hours and monitored via TLC, then washed with distilled  $H_2O$  (5 x 200 mL) and brine (2 x 200 mL). The collected organic fractions were dried over  $MgSO_4$ , filtered and evaporated then vacuum dried to give the crude product as a purple colored residue. Purification via column chromatography ( $SiO_2$ , eluant  $CH_2Cl_2$ :petrol ether = 50%-80%,  $R_f$  = 0.20) and then recrystallization via  $CH_2Cl_2$ :petrol ether afforded the desired compound as deep plum coloured crystals (0.076 g, 0.92 mmol, 62.1 % yield).  $^1H$  NMR ( $CDCl_3$ , 300 MHz)  $\delta$  (ppm) = 6.99(s, 2H); 6.87-6.86(d, 4H); 6.24-6.23(d, 2H); 5.28-5.27(d, 2H); 3.26-3.23(t, 4H); 2.78-2.75 (t, 4H); 2.62 (s, 3H); 1.99-1.96 (m, 4H).  $^{13}C$  NMR (300 MHz,  $CDCl_3$ )  $\delta$  (ppm) = 154.95; 145.09; 144.36; 134.19; 130.43; 129.92; 121.22; 120.69; 118.29; 50.01; 27.82; 21.63; 14.88;  $^{11}B$  NMR (160 MHz,  $CDCl_3$ )  $\delta$  = +0.21; -0.02; -0.29 (t,  $J_{av}$  = 30.72 Hz).  $^{19}F$  NMR (470 MHz,  $CDCl_3$ )  $\delta$  = -145.07 (q,  $J_{av}$  = 36.6 Hz).

### Reference

1 Mestrelab Research Chemistry Software for NMR and LC GC MS  
<http://mestrelab.com/> (Retrieved on 12th-11-13)

## Chapter 3

# Multi-Mode Fluorescent Molecular Rotors



## 3.1 Background and Molecular Design Principles

### 3.1.1 Molecular Rotors

The concept of “molecular rotors” descends from the family of multi-chromophoric fluorescent molecules which are able to form the twisted intramolecular charge transfer (TICT) state upon photoexcitation.<sup>1-2</sup> The redistribution of the excited TICT state energy via a non-radiative process is an alternative to fluorescence emission, and competes as one of the main pathways of photoexcitation decay.<sup>3-4</sup> The formation of the TICT requires fairly large-amplitude of molecular motion, and a modulation of conformational change within the system, and is the origin of the dependence on solvent polarity.<sup>5-6</sup> Within molecular rotor systems, the fluorescent quantum yield and the environment viscosity are related by the analytically derived and experimentally validated Förster-Hoffmann equation:<sup>7</sup>

$$\log(\Phi_F) = C + x \text{Log}(\eta)$$

$\Phi_F$  : quantum yield of the rotor

x : molecule-dependent constant

C: temperature-dependent constant

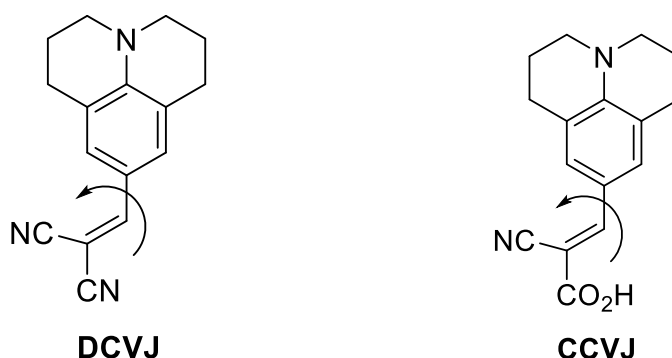
$\eta$  : viscosity dependent parameter

It is proven that the measurement of the rotationally quenched fluorescence emission intensity could indicate the solvent's viscosity.<sup>8</sup>

#### 3.1.1.1 Julolidine Aryl-Alkenyl Rotor Probe

The most well known molecular rotors are the molecules **DCVJ** and **CCVJ**, which are based on the julolidine donor and the cyano-vinyl rotor segment. Electron-transfer occurs from the julolidine nitrogen to the nitrile group upon photoexcitation (Figure 3.1).<sup>9-10</sup> This process is known to produce the intramolecular TICT state which acts as an efficient non-radiative decay pathway. Any process which leads to restricted

rotation of the cyanovinyl unit enhances the emission. Hence, local viscosity in the rotor vicinity is important and the origin of the fluorescence-viscosity effect.



**Figure 3.1.** The archetypical molecular rotor 9-(dicyano-vinyl)julolidine (**DCVJ**) and 9-(2-Carboxy-2-cyanovinyl)julolidine (**CCVJ**) with the arrow indicating motion of the julolidine-vinyl bond rotation.

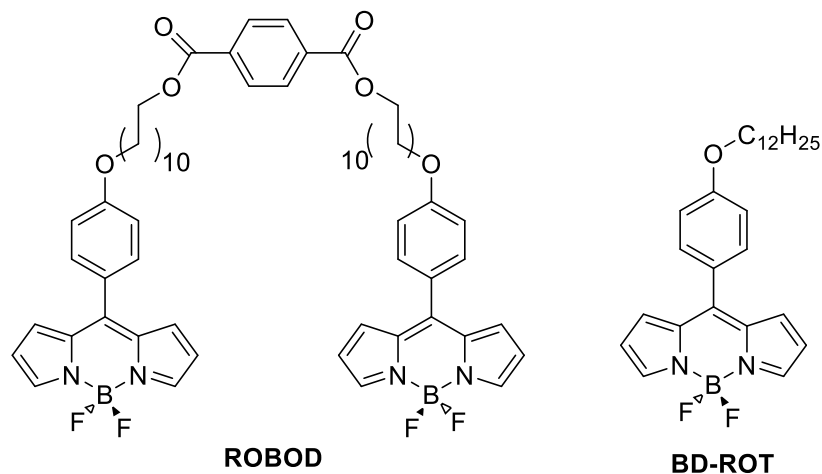
These molecular rotors of **DCVJ** and **CCVJ** are known for their unique application in immunofluorescent-antibody assay (IFA), where they are able to recognize and monitor the formulation and structural change of antigen-binding fragments via steady-state fluorescence measurements.<sup>11</sup> The compounds can also be used for other applications including lipid viscosity measurements.<sup>12</sup>

### 3.1.1.2 Unhindered Bodipy System as Molecular Rotors

Generally the fluorescence quantum yield of a fully alkylated Bodipy derivative containing an aryl meso group is relatively high. By comparison, the opposite is noticed for derivatives where the dipyrromethene backbone is devoid of groups. It is suggested that rotation of the meso aryl unit is linked to efficient non-radiative deactivation, and that restriction of its motion would result in fluorescence enhancement.<sup>13</sup> The first type of molecular systems<sup>14, 15</sup> to test this type of idea are shown in Figure 3.2. In the case of **ROBOD**, the fluorescence response was monitored by varying the solvent viscosity, and by keeping the solvent constant but varying the applied pressure.<sup>14</sup> For the related molecule, **BD-ROT**, lifetime



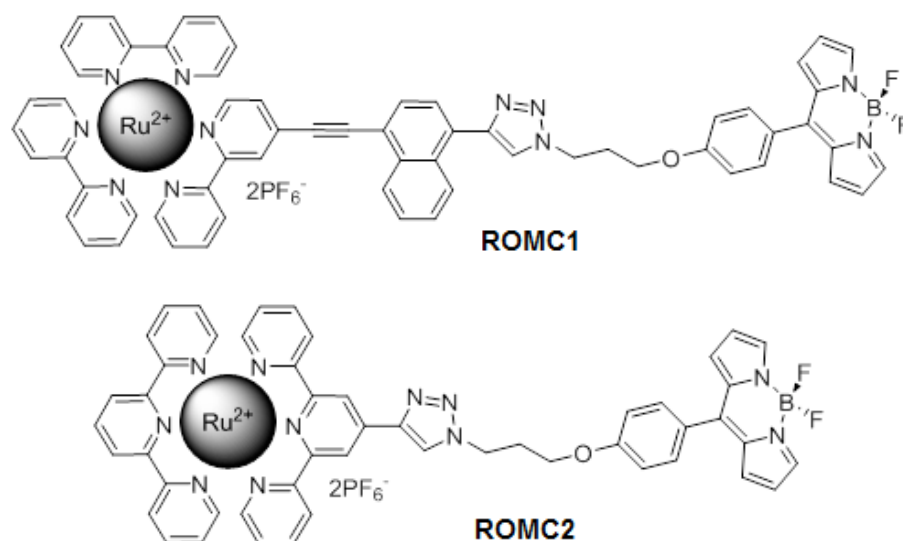
measurements were used to measure the local viscosity of cells.<sup>15</sup> It is noticeable that in both the compounds the Bodipy unit is the same, and it is the rotation of the phenol-based unit which affects the fluorescence yield.



**Figure 3.2.** Two prototype molecular rotors developed to probe viscosity of solvents (**ROBOD**) and the viscosity of cell membranes (**BD-ROT**).

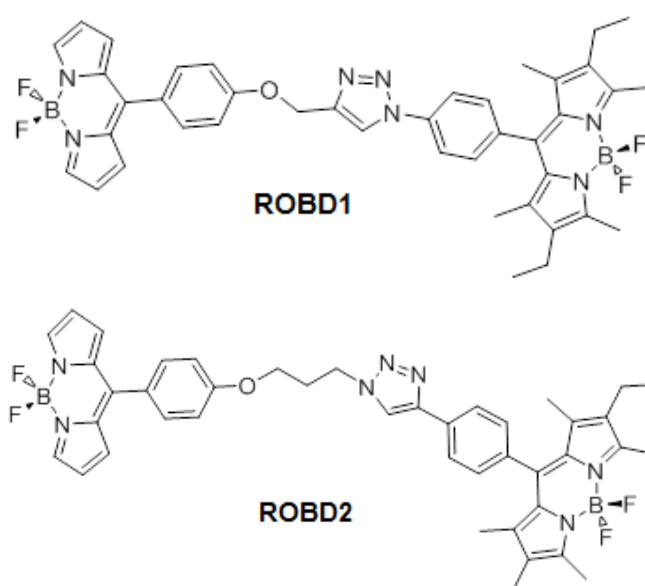
### 3.1.2 Molecular Design Principle

In view of the previous studies it was decided to survey for a multifunctional system containing the Bodipy rotor. Alongside the viscosity-sensitive functionality of the Bodipy rotor moiety, additional functionality could be achieved via coupling the rotor unit to a reporter unit(s) that perform a secondary specific function. Each part of the assembly could be activated, thus the entire system would be capable of responding to multiple parameters. Illustrated in Figure 3.3 are two examples of two molecular systems prepared with this idea in mind. As discussed later in the Chapter the workings of these molecular systems were more complicated.



**Figure 3.3.** Metal chelating temperature sensitive lumophores **ROMC1** and **ROMC2** that may act as a viscosity-thermometer probe.

An alternative strategy is to have a reporter on site which does not change but provides a steady fluorescence response. In this case, the idea would be to use a ratiometric approach and compare two well separated signals. Two simple prototypes are the derivatives **ROBD1** and **ROBD2** which contain the fully alkylated Bodipy derivative (Figure 3.4). As discussed later on the feasibility of this approach remain skeptical, but did afford an alternative way to improve sensitivity of the viscosity probe.



**Figure 3.4.** Molecular dyads based on a rotor Bodipy and an internal standard

capable of potential ratiometric sensing.

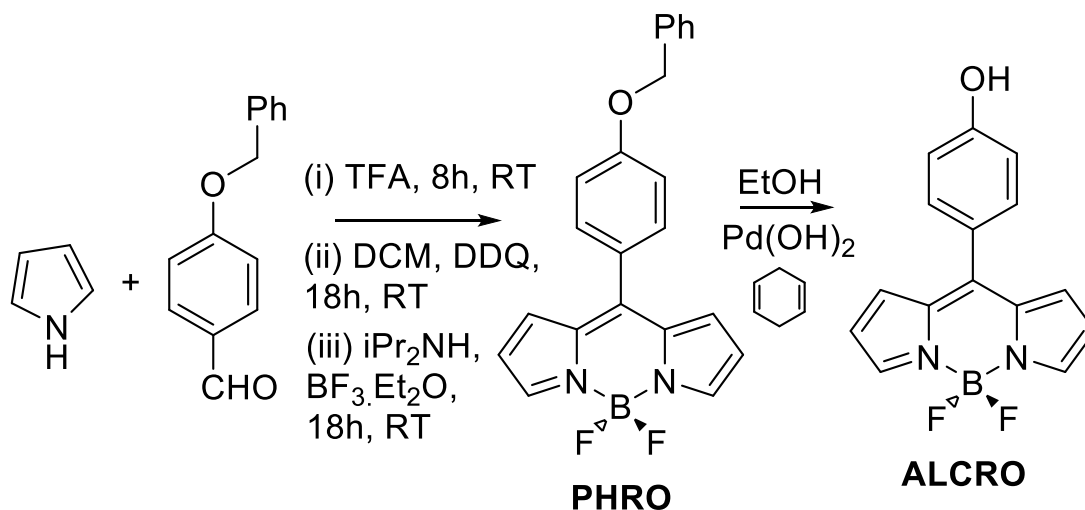
## 3.2 Results and Discussion

### 3.2.1 General Synthetic Strategy

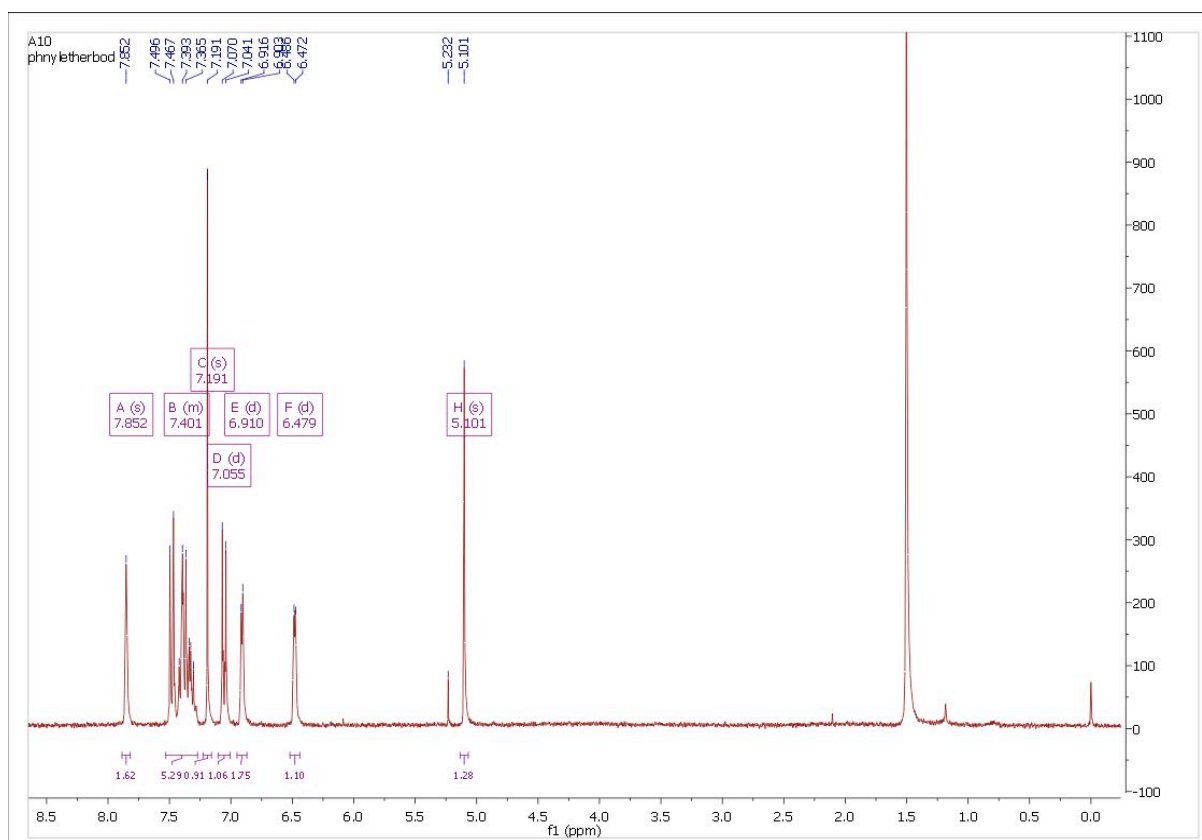
In designing the multifunctional molecular rotor systems we aimed to link manufactured components together in an efficient manner. The “click” reaction was chosen for its well-known reliability.<sup>16</sup> “Click” chemistry is an operator-friendly and fast version of triazole formation, which involves non-aldol type carbonyl chemistry and azide addition to C-C multi-bonds. The reaction requires only an internal or terminal alkyne (acetylene) derivative reacting with an azide precursor. Compounds containing either one of the units can be coupled readily together, thus a library of compounds can be efficiently prepared.

#### 3.2.1.1 Synthesis of Functionalised Rotor Precursors

The constituents of the basic rotor Bodipy are the dipyrromethene unit and a phenoxy group at the meso position. The synthesis of the alcohol activated rotor unit, **ALCRO**, is shown in Scheme 3.1, starting from pyrrole and the protected 4-(benzyloxy)benzaldehyde. The condensation of freshly distilled pyrrole with 4-(benzyloxy)benzaldehyde in the presence of a small amount of trifluoroacetic acid (TFA) produced the dipyrromethene adduct which was *in-situ* oxidised to the protected Bodipy **PHRO** (orange crystals 16% yield). The <sup>1</sup>H NMR spectrum for **PHRO** is shown in Figure 3.5. As well as the clear signals at 6.5, 6.9 and 7.8 ppm for the pyrrole protons, two doublets are observed corresponding to the para-substituted phenylene group. The singlet at 5.1 ppm is assigned to the OCH<sub>2</sub> unit of the protecting group.



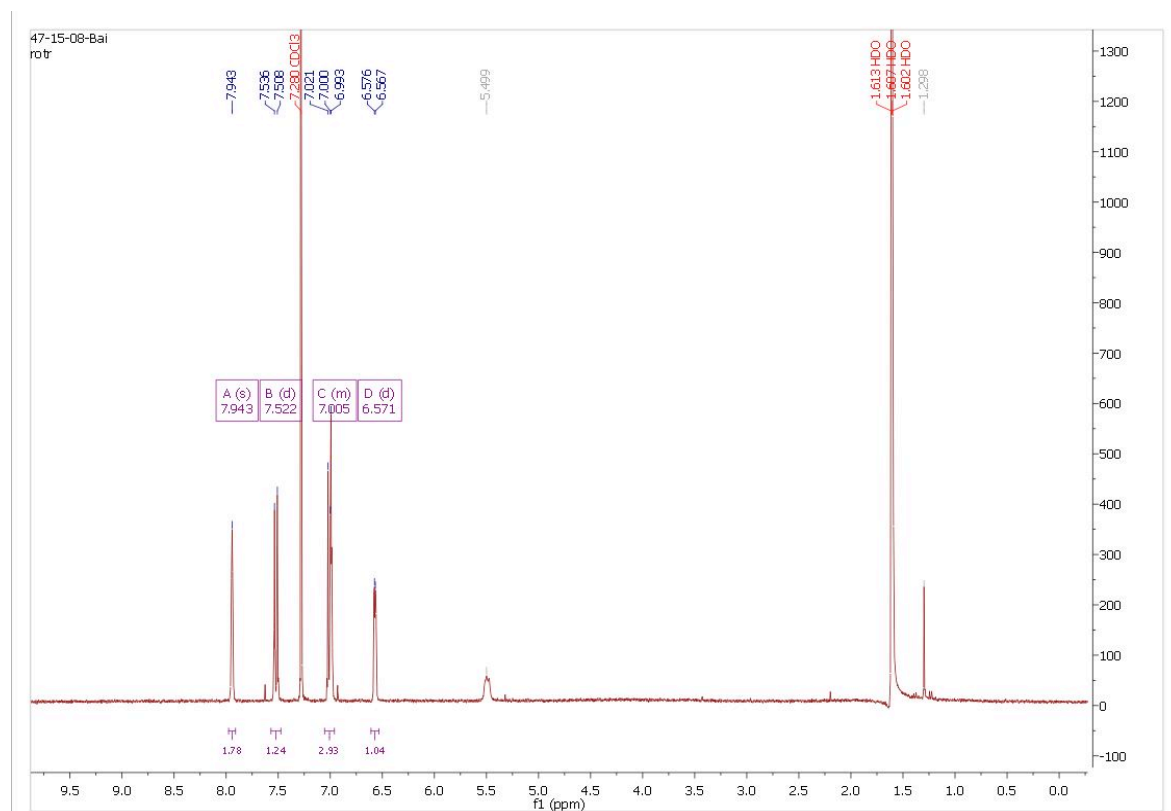
**Scheme 3.1.** Preparation of **ALCRO** via the protected 4-(benzyloxy)benzaldehyde **PHRO**.



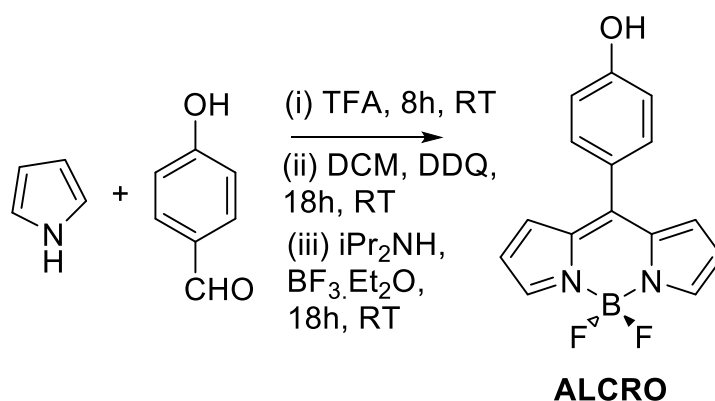
**Figure 3.5.** Room temperature  $^1\text{H}$  NMR spectrum for **PHRO** in  $\text{CDCl}_3$ .

The removal of the benzyl protecting group can be carried out under hydrogenation conditions, but we found that the H-atom transfer method was relatively easier in operation. The  $^1\text{H}$  NMR spectrum (Figure 3.6) indicates the removal of protecting

group according to the disappearance of the resonances for both the phenylene and methylene groups. Although the deprotection reaction of **PHRO** in cyclohexa-diene/ethanol with Pearlman's catalyst  $\text{Pd}(\text{OH})_2/\text{C}$  is efficient (red solid, 80% yield), care must be taken to obtain the intermediate.



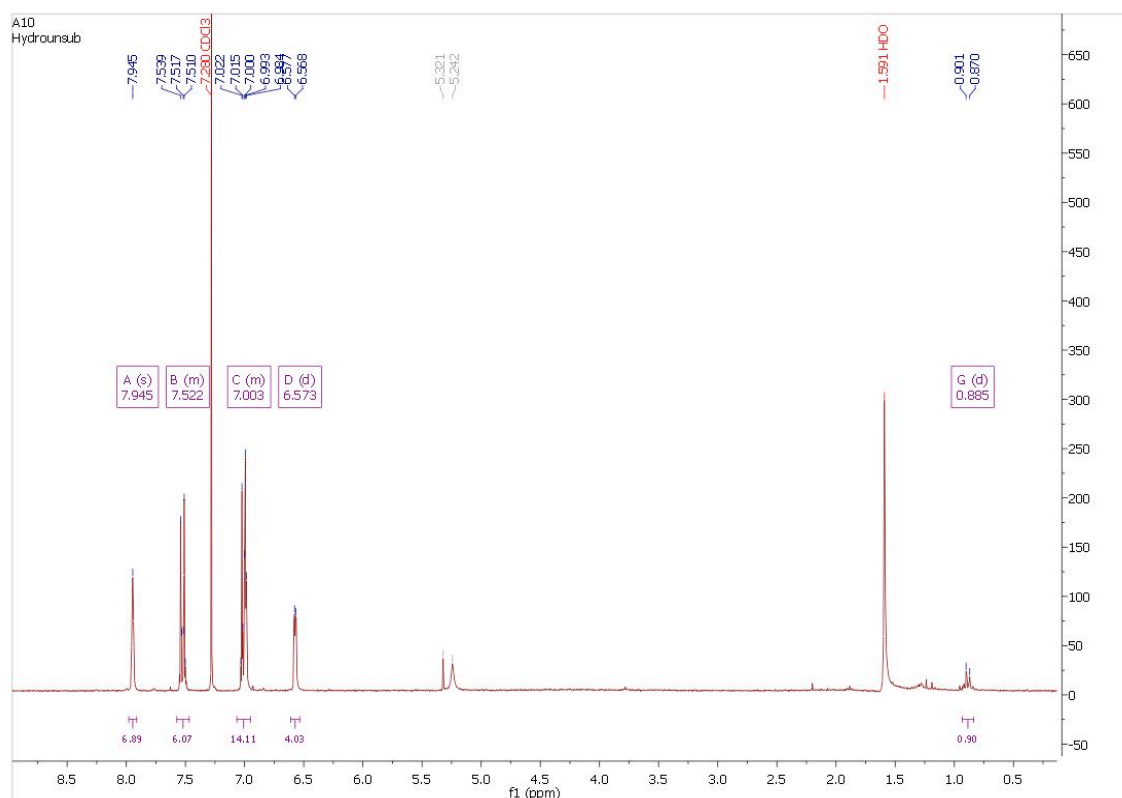
**Figure 3.6.** Room temperature  $^1\text{H}$  NMR spectrum for **ALCRO** in  $\text{CDCl}_3$ . The peak at ca. 1.5 is residual water.



**Scheme 3.2.** Preparation of **ALCRO** via one-step condensation of 4-hydroxybenzaldehyde with pyrrole.

The necessity of having the protecting group in place from the start was tested via the

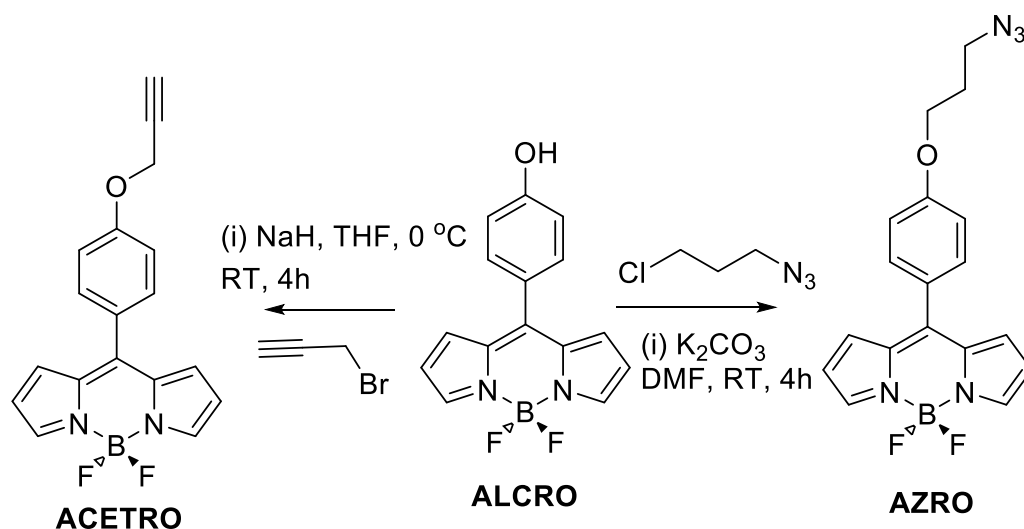
one step condensation of pyrrole and 4-hydroxybenzaldehyde (Scheme 3.2). The 4-hydroxybenzaldehyde route worked quite well to obtain pure **ALCRO** as a red crystalline solid (15% yield when starting with 1.22g, none purified intermediate; 47% yield when starting with 3.7g of recrystallized intermediate). The reaction is not affected by the presence of the hydroxyl group which remains intact after the reaction. As shown in Figure 3.7 the  $^1\text{H}$  NMR spectrum of the reaction product was identical to that shown in Figure 3.6.



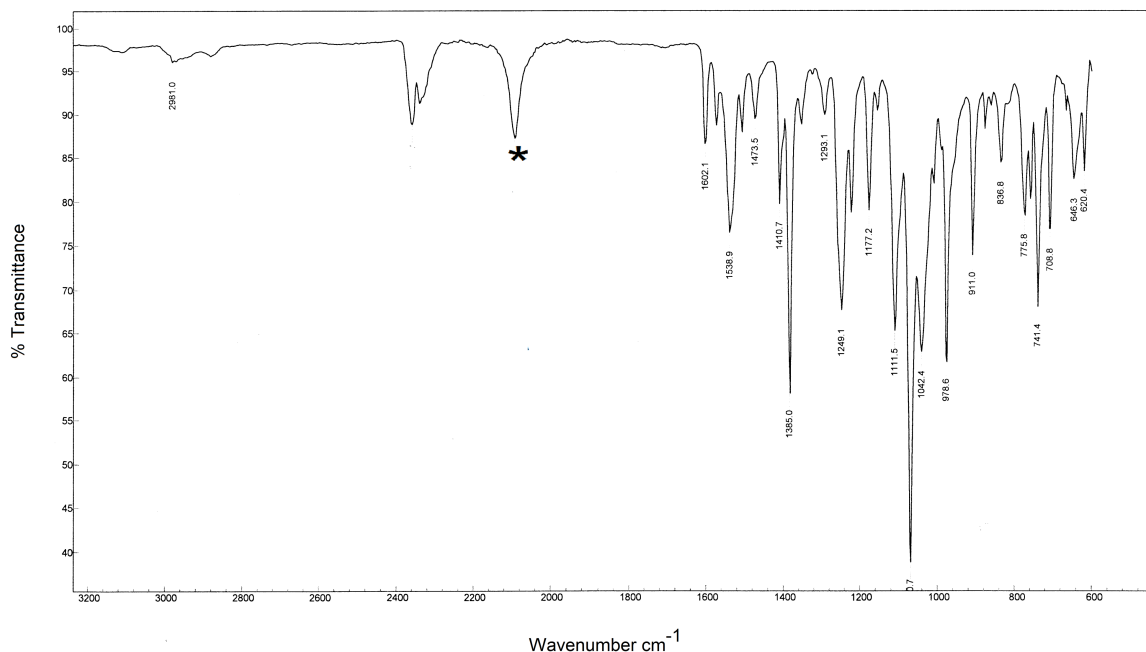
**Figure 3.7.** Room temperature  $^1\text{H}$  NMR spectrum for **ALCRO** in  $\text{CDCl}_3$  produced by the unprotected reaction. The peak at ca. 1.5 is residual water.

Note that in this reaction an excess amount of pyrrole must be used, but can be removed by distillation and recycled. Before proceeding to make the Bodipy derivative it is essential to isolate the 4-hydroxydipyrromethane intermediate compound (white crystals, 30% yield). The phenol unit in the rotor compound **ALCRO** can be readily deprotonated for the nucleophilic substitution with alkyl halides (Scheme 3.3). In order to connect an alkyl spacer compound **ALCRO** was reacted with

1-azido-3-chloropropane using  $\text{K}_2\text{CO}_3$  as the base to deprotonate the phenol group. The reaction appeared to proceed regioselectively by loss of the chloride preferentially to the azide in the nucleophilic attack. The I.R. spectrum of **2** (Figure 3.8) confirmed the presence of the azido since a strong band is observed at  $2095\text{ cm}^{-1}$ . In addition, the distinctive resonances for the propyl group were observed in the  $^1\text{H}$  NMR spectrum. The role of compound **AZRO** is to “click” with a suitable acetylene derivative. Reaction of compound **ALCRO** with propargyl bromide prepared the precursor **ACETRO**. In order to introduce an alkyl spacer the precursor **ACETRO** was prepared, which in this case contains the acetylene functional unit. The activated rotor compounds **ACETRO** and **AZRO** will appear again in chapter 6.



**Scheme 3.3.** Synthetic routes to the two acetylene- and azide- activated precursor rotor compounds **ACETRO** and **AZRO** implemented for the “click” reactions.



**Figure 3.8.** FTIR spectrum for **AZRO** showing the azide stretch marked with an asterisk and the fingerprint region. Note: the stretch at around  $2400\text{ cm}^{-1}$  is an artefact from poor background subtraction.

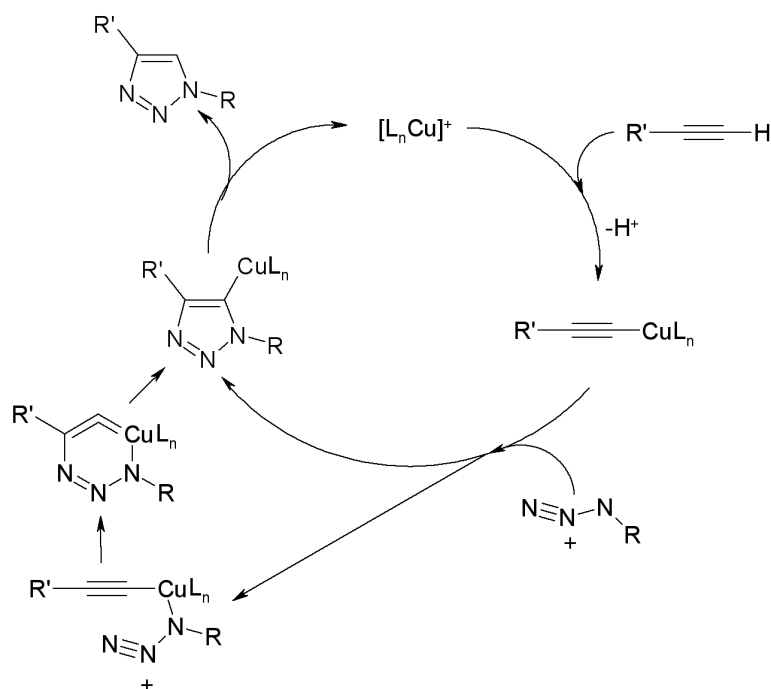
### 3.2.1.2 Activated Complementary “Click-on” Segments

To synthesise the metal-based reporter compounds (Figure 3.3) “click” chemistry was used and the synthetic procedure is shown in Scheme 3.5. From previous studies within the group the ruthenium (II) tris-bipyridine derivative **MCNAP** was also available.<sup>16</sup> The  $^1\text{H}$  NMR spectrum for **MCNAP** was checked before proceeding to ensure that no degradation of the material had occurred, and to prove the existence of the acetylene proton. The naphthalene group is necessary to try and separate the two halves of the final molecular dyad.

### 3.2.2 Synthesis of Target Rotor Connected Systems

“Click” chemistry was implemented to afford the target triazole unit, and the basic mechanism is shown in Scheme 3.4.

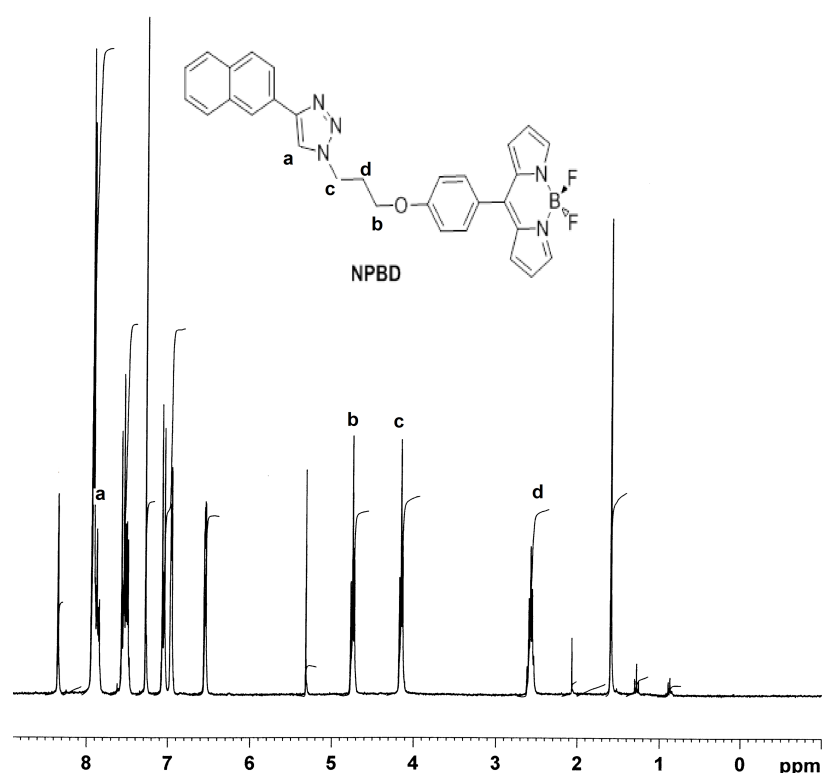




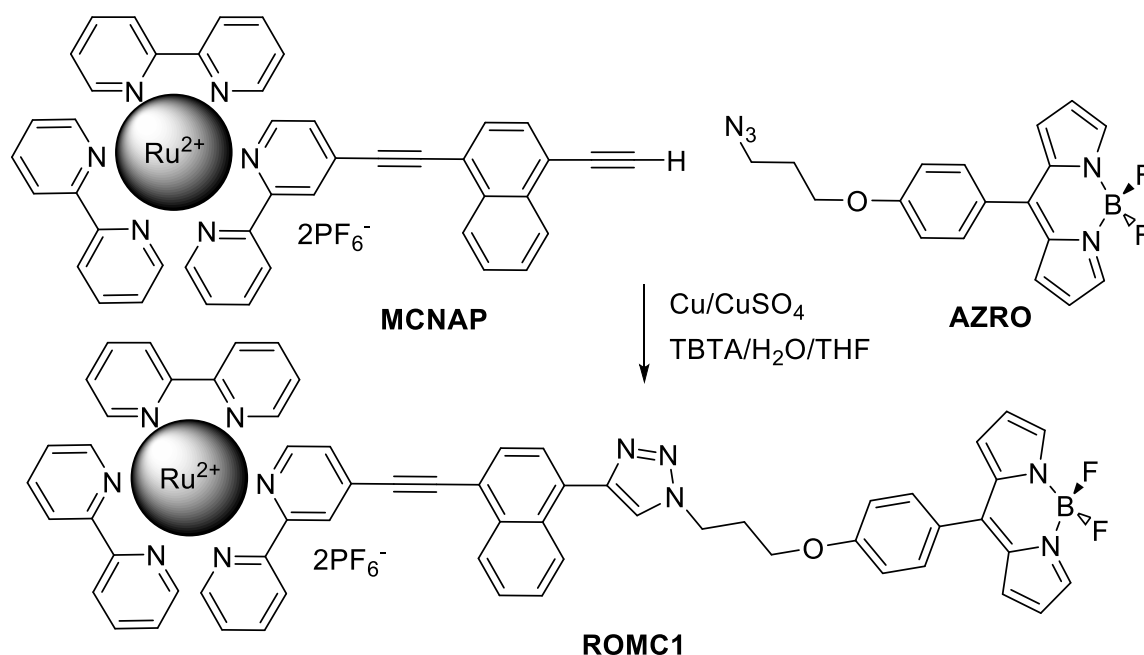
**Scheme 3.4.** Basic mechanism for 'click' reaction (courtesy of <http://www.organic-chemistry.org/namedreactions/huisgen-1,3-dipolar-cycloadditions.htm>).

Literature reported the catalytic active Cu(I) can be generated from Cu(I) salts with a reducing agent like sodium ascorbate. One of the possible mechanism is represented in Scheme 3.4. The catalyst CuI attacks the terminal alkyne to form the  $\pi$  complexation, CuL<sub>n</sub> inserted to the alkyne, which then transforms to a Cu-acetylide, and then [3 + 2] cycloaddition occurs to form the six-membered metalocycle, after deprotonation of the terminal hydrogen forms the triazo ring. As reported in literature, The pK<sub>a</sub> value of the terminal alkyne could be lowered by the  $\pi$  complexation of CuI of the terminal alkyne, allowing deprotonation to occur in an aqueous solvent without the addition of a base. Recent literature also reported the assistance of 2,6-lutidine, tris(2-pyridylmethyl)amine (TPMA) and N,N'-diisopropylethylamine (DIPEA) in non-basic solvents like acetonitrile or DMSO<sup>17-18</sup>. In practice, we found this method is quite air-sensitive. The alkyne-azide cycloaddition reaction is known to be exothermic in water, thus as reported in the literature the ligand tris-(benzyltriazolylmethyl) amine (TBTA) added is able to protect the Cu(I) catalyst from oxidation whilst enhancing its

catalytic activity. The tetradentate ligand completely envelopes the Cu(I) centre providing additional electron density to the metal center. Addition of water greatly accelerates the reaction and ensures the product precipitates. In order to optimise conditions for the click reaction we performed a simple test reaction in which ethynynaphthalene was coupled to compound **AZRO** to produce **NPBD**. The  $^1\text{H}$  NMR spectrum for **NPBD** is shown in Figure 3.9 and clearly shows that the naphthalene and rotor are coupled together. The optimized conditions employed in the preparation of **NPBD** were used in all subsequent “click” reactions.



**Figure 3.9.**  $^1\text{H}$  NMR spectrum of the test compound **NPBD** in  $\text{CDCl}_3$  showing selected resonance assignments.



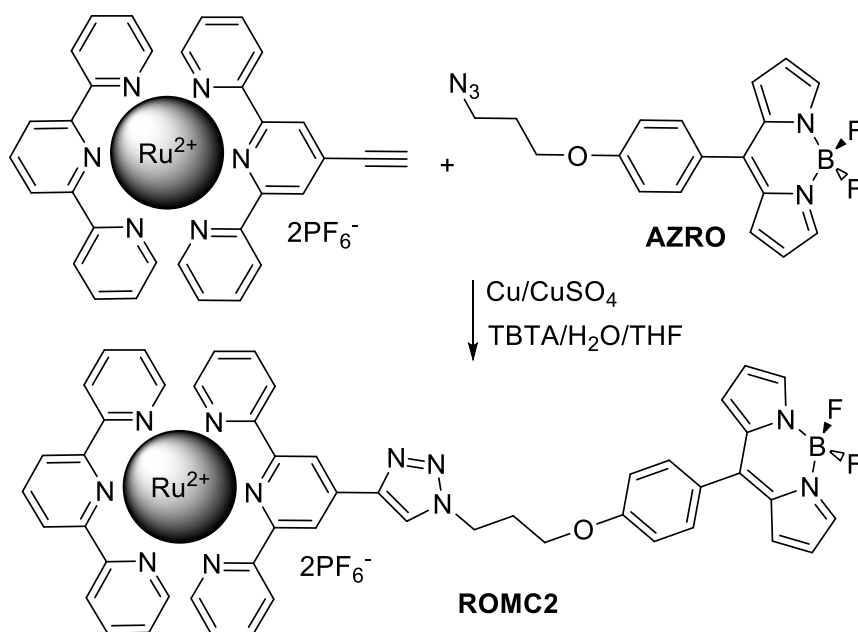
**Scheme 3.5.** Preparation of the metal-based rotor compound **ROMC1** starting from **MCNAP** and **AZRO**.

### 3.2.2.1 Rotor Connected to Metal Complexes

The preparation of **ROMC1** is shown in Scheme 3.5 and couples together the ruthenium-based chromophore **MCNAP** with the rotor **AZRO**. The only complication in this case was the solubility restriction imposed by using a salt as one of the starting materials. Since **MCNAP** as the hexfluorophosphate salt was insoluble in non-polar solvents we had to use the highly polar DMF instead. Despite this drawback the reaction proceeded smoothly to afford a red solid after careful column chromatography. The <sup>1</sup>H NMR spectrum for **ROMC1** is slightly more complicated because of the additional resonances associated with the aromatic groups (i.e., bipyridine and naphthalene). Even so it is still possible to identify key resonances especially for the propyl spacer which have characteristic chemical shifts and splitting patterns. More diagnostic is the MALDI mass spectrum which displayed a cluster of peaks at  $m/z = 1256.2$  corresponding to the  $[M-PF_6]^+$  ion. The theoretical and found isotope patterns fit extremely well for the molecular ion; the mass distribution is a

result of the several isotopes for ruthenium.

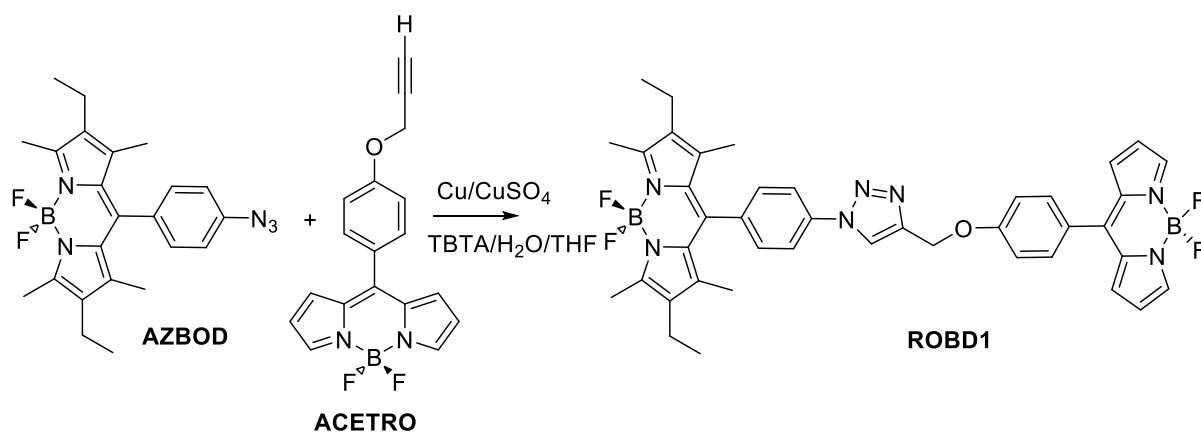
Again using the optimised “click” conditions the complex **ROMC2** (Scheme 3.6) was produced, which in this case incorporates the ruthenium(II) bis-terpyridine complex and there is no spacer unit. The triazole is connected directly to one of the terpyridine ligands.



**Scheme 3.6.** Preparation of the ruthenium(II) bis-terpyridine complex based rotor compound.

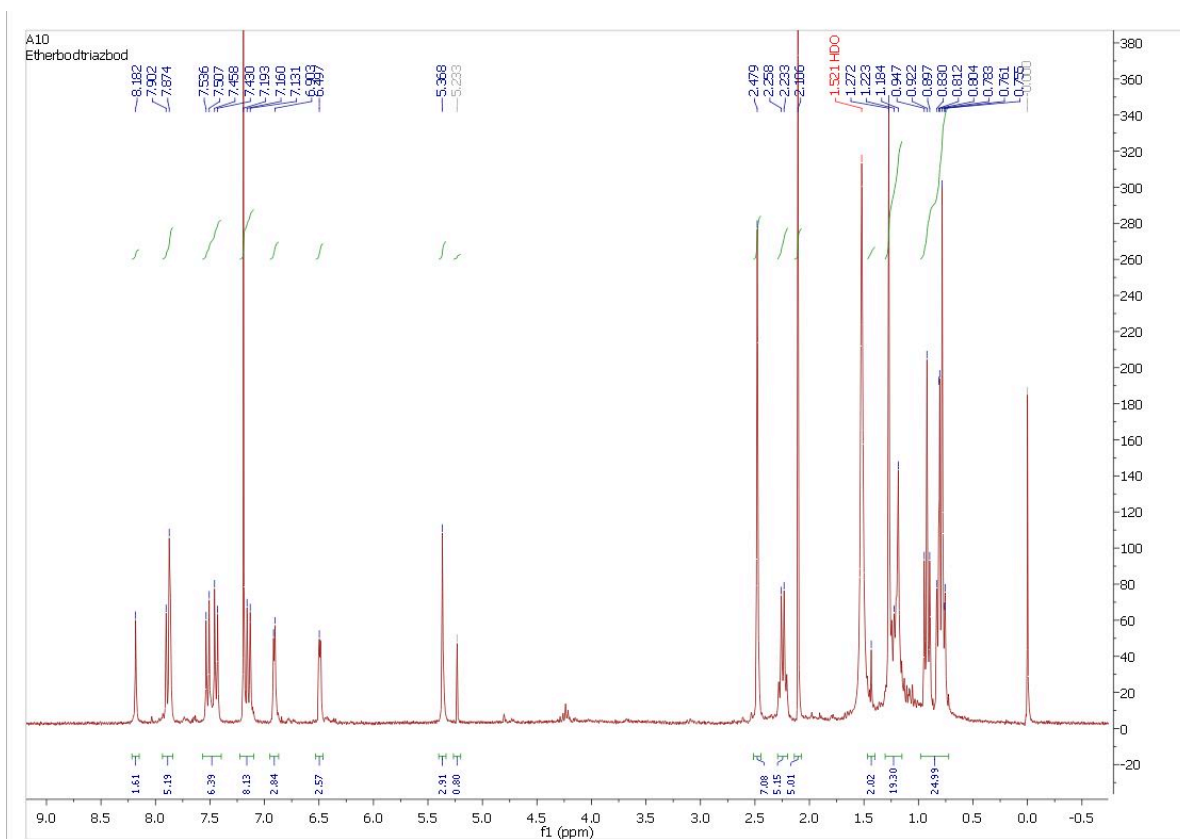
#### 3.2.2.2 Rotor & Hindrance - Dyads Connected via Alkyl Spacers

The set of compounds, **ROBD1** & **ROBD2**, were aimed to link together the rotor Bodipy to the fully alkylated Bodipy derivative. The simplest compound is the click product from the reaction of **ACETRO** and **AZBOD** (Scheme 3.7). Having learnt lessons on the “click” process, once again the same conditions were employed as discussed previously. The desired compound **ROBD1** was obtained in 32% yield as a red solid.

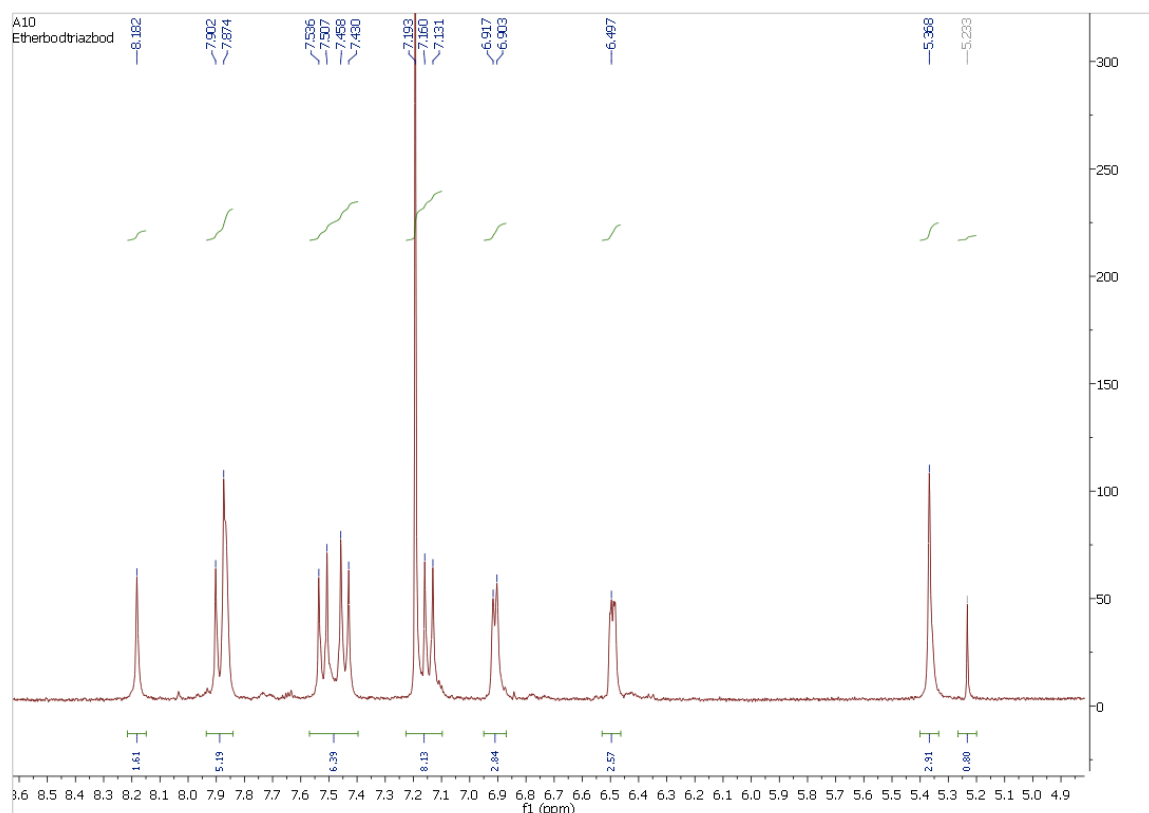


**Scheme 3.7.** Preparation of **ROBD1** starting from **ACETRO** and **AZBOD** via the “click” chemistry.

The  $^1\text{H}$  NMR spectrum for **ROBD1** is illustrated in Figure 3.10 and an expansion of the aromatic region is shown in Figure 3.11. Observation of a quartet and a triplet at 2.3 ppm and 0.9 ppm, respectively, are consistent with the incorporation of the non-rotor Bodipy. In addition, the signal at 5.4 ppm is assigned to the connector  $\text{OCH}_2$  group. The two doublet signals at 6.5 ppm and 6.9 ppm are characteristic of the rotor Bodipy (Figure 3.11). The singlet at 7.9 ppm is associated with the single proton for the triazole group.



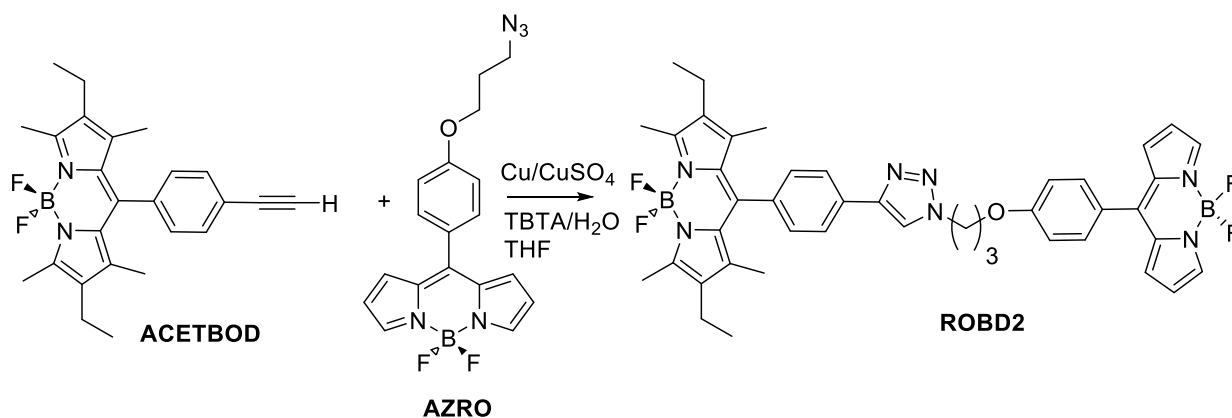
**Figure 3.10.** Room temperature  $^1\text{H}$  NMR spectrum for **ROBD1** in  $\text{CDCl}_3$ . Note: additional peaks are from solvent molecules.



**Figure 3.11.** Partial room temperature  $^1\text{H}$  NMR spectrum for **ROBD1** in  $\text{CDCl}_3$  showing the aromatic signals.

The MALDI mass spectrum for **ROMC1** displayed a peak at  $m/z = 742$  which is assigned to the  $[\text{M-H}]^+$  ion.

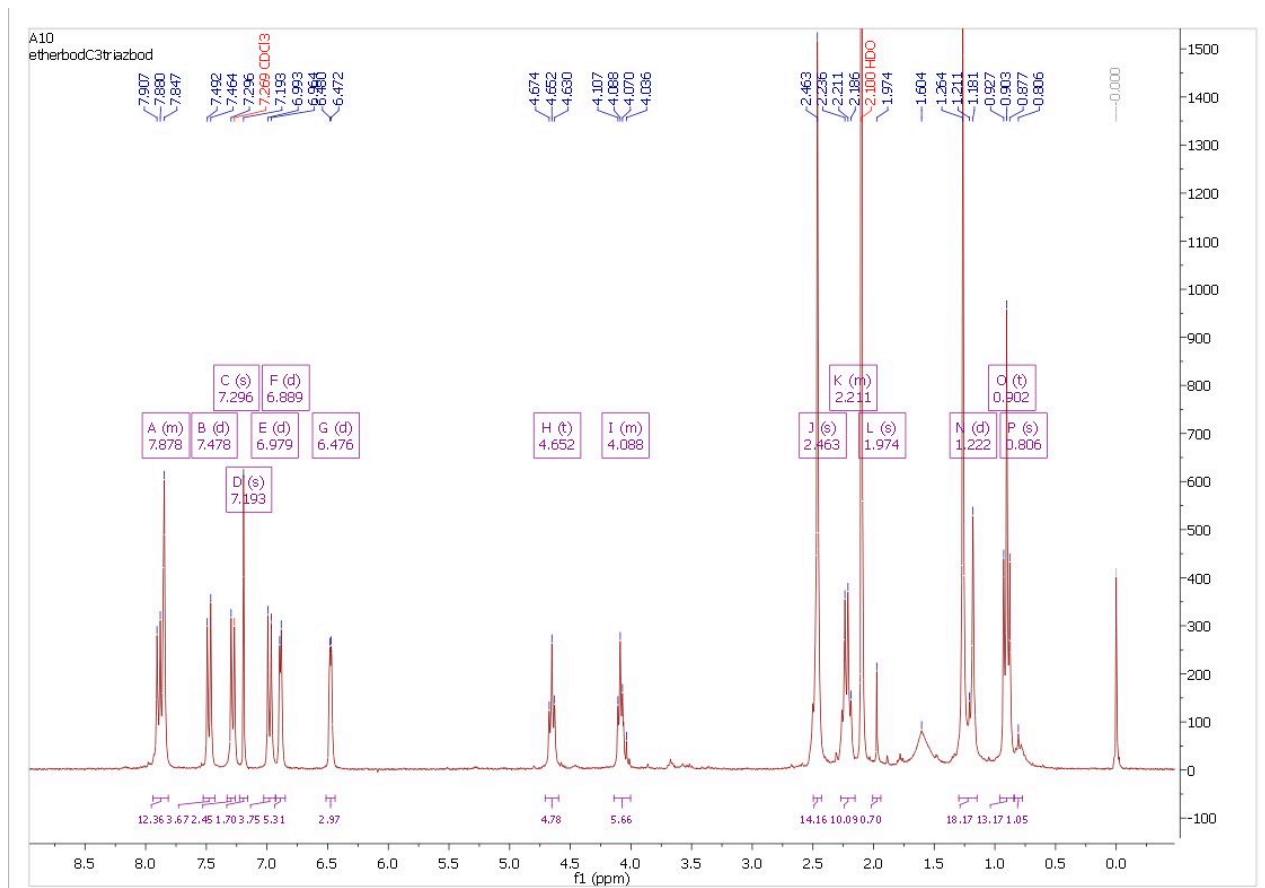
In order to increase the spacer length between the two Bodipy groups the synthetic methodology was altered slightly. Scheme 3.8 shows the azide containing Bodipy was now the rotor unit **AZRO** and the acetylene bearing Bodipy was fully alkylated. The compound **ACETBOD** (which appear again in Chapter 4) was prepared as the TMS protected derivative which was removed under hydrolysis conditions. Again the coupling of the two components using the method developed for compound **ROBD2** worked well (Yield = 70%)



**Scheme 3.8.** Preparation of **ROBD2** starting from **ACETBOD** and **AZRO** and using “click” chemistry.

There are many similar characteristics in the  $^1\text{H}$  NMR spectrum for **ROBD2** compared to the shorter spacer analogue (Figure 3.12). The most obvious difference though is the two additional triplets at 4.7 ppm and 4.1 ppm which are assigned to the  $\text{OCH}_2$  and  $\text{NCH}_2$  groups, respectively. The difference in chemical shifts is because of the difference in electronegativity between oxygen and nitrogen. The triplet patterns are caused by coupling to the central  $\text{CH}_2$  group of the propyl spacer. The MALDI mass spectrum collected for **ROBD2** was consistent with the structure and displayed a peak at  $m/z = 770$  refers to the  $[\text{M}-\text{H}]^+$





**Figure 3.12.** Room temperature  $^1\text{H}$  NMR spectrum for **ROBD2** in  $\text{CDCl}_3$ . Note: additional peaks are from solvent molecules

Both  $^{11}\text{B}$  and  $^{19}\text{F}$  NMR spectra revealed the presence of the two slightly different Bodipy units. The chemical shifts for the boron and fluorines for the rotor part are slightly shifted with respect to the fully alkylated Bodipy. The clear singlet at 7.8 ppm in the  $^1\text{H}$  NMR spectrum is readily assigned to the triazole group.

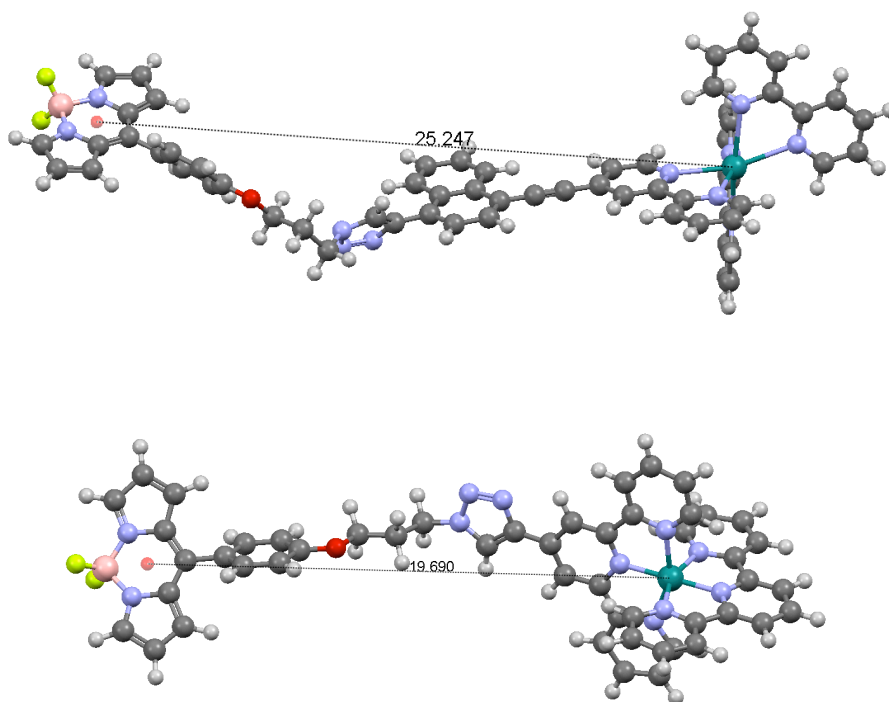
### 3.2.3 Molecular Orbital Calculations and Minimised Energy Diagrams

In order to gain a little more insight into the molecular systems, selected molecular modelling calculations were carried out using the programme Gaussian 03. Calculations were generally carried out by producing simple structures using MM<sup>+</sup> and importing them into the Gaussian 03 package. The structures were then refined by starting at semi-empirical (or Hartree-Fock) level and further minimising the structures. The final calculations were carried out using DFT (B3LYP) and increasing the basis

set. For purely organic compounds the 6-311G basis set was used and for ruthenium(II) complexes the basis set used was 3-21G.

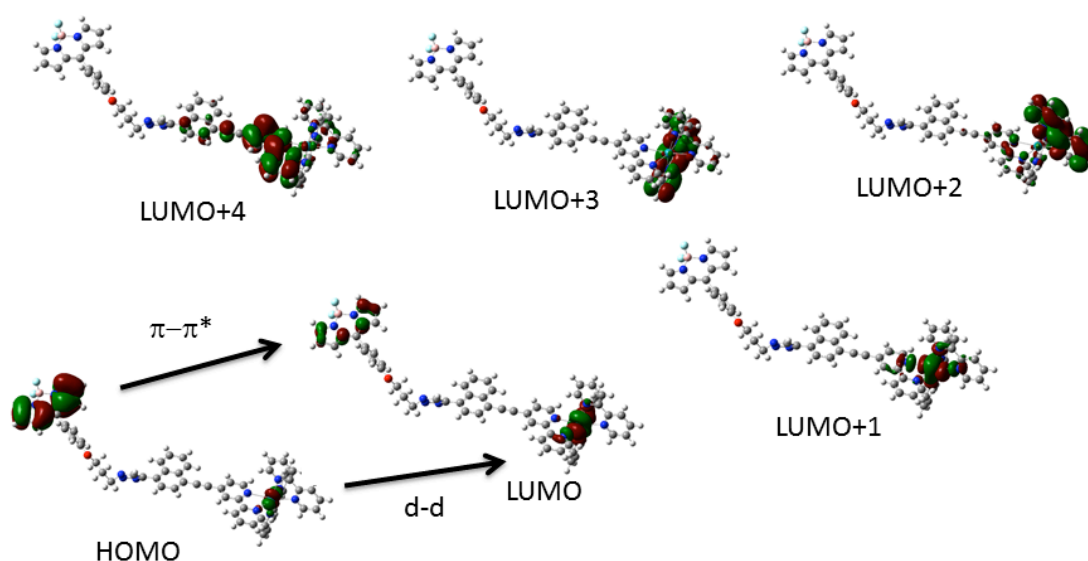
### 3.2.3.1 Computational Calculations for ROMC1 and ROMC2

The energy-minimised structure for **ROMC1** (Figure 3.13) places the rotor and ruthenium(II) bipy centres relatively far apart (ca. 25 Å). Clearly the extended structure represents only one conformation in which the propyl space is nearly fully extended. The spacer group is flexible and rotations about the N-CH<sub>2</sub> unit adjacent to the triazole are possible. Such molecular motions would reduce the distance between the two centres. We did not perform any molecular dynamics simulations to obtain a more comprehensive picture of the fluctuation in separation distance. It is noted that the enthyryl-naphthalene group is more rigid and may act to hinder the rotor from fully reaching the ruthenium(II)-bipy centre. For **ROMC2** the energy-minimised structure (Figure 3.13) the centre-to-centre distance is shorter (ca. 20Å).



**Figure 3.13.** DFT (B3LYP, 3-21G) computer calculated energy-minimised structures for **ROMC1** and **ROMC2**. The centre-to-centre distance is given in Ångstroms.

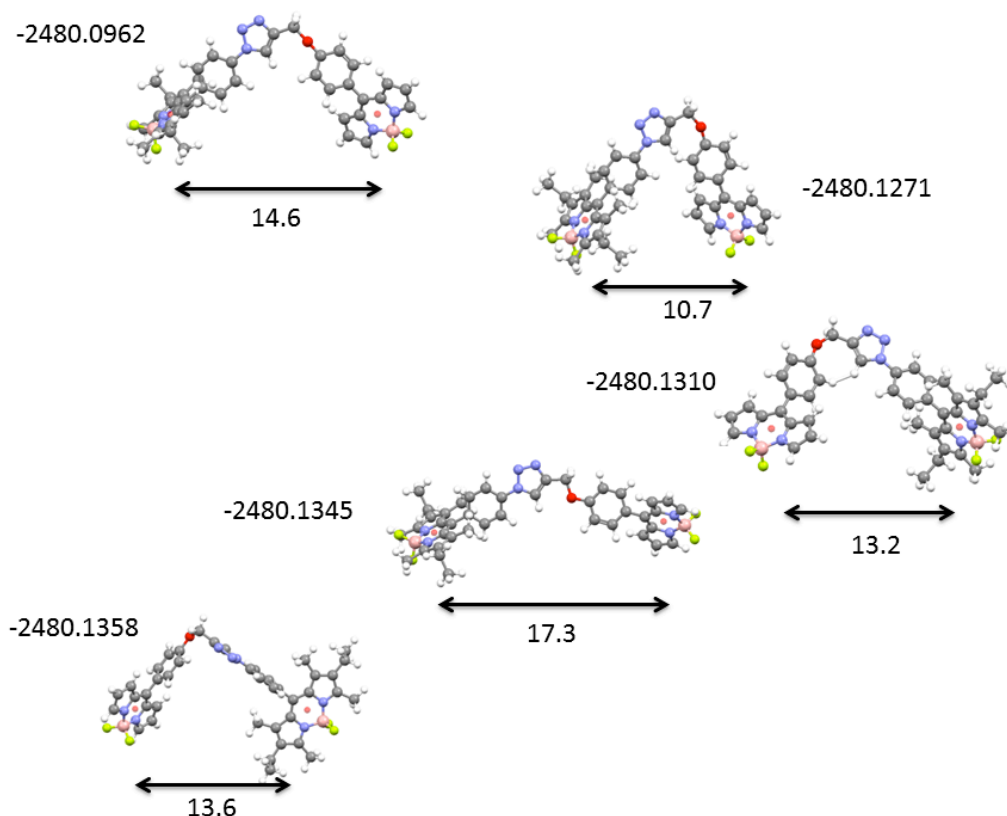
A simplified molecular orbital picture for **ROMC1** is shown in Figure 3.14 and basically shows that the most significant orbitals are localised on each segment (i.e., rotor, metal complex) of the dyad. It is noticeable that the HOMO and LUMO appear to have contributions from both the Bodipy and ruthenium(II)-bipy complex. It is possible that a d-d transition and a Bodipy localised  $\pi-\pi^*$  transition overlap. The HOMO for the complex is d-centred and electronic transitions to LUMO+2, LUMO+3 and LUMO+4 are the well known MLCT.



**Figure 3.14.** Selected DFT calculated molecular orbitals for **ROMC1**. Arrows show possible electronic transitions.

### 3.2.3.2 Computer Calculations for ROBD1

From inspection of **ROBD1** it is evident that the rotor Bodipy is susceptible to free rotation about the methylene connector. A basic precession cone is expected which will bring the rotor into close proximity to the second Bodipy. An energy-minimised structure calculated places the two subunits ca. 17 Å apart. A more insightful picture into molecular conformations was obtained by commencing with the energy-minimised structure, and through a series of scan steps, altering the dihedral angle at the oxygen atom. To reduce computer run time the basis set was reduced to 3-21G (B3LYP). Further refinement involved minimising the energy of the structure at each dihedral angle. In this way a profile was constructed containing a series of structures for which the intramolecular separation distance varied (Figure 3.15). The energy difference between, for example, two conformations where the separation distances are 10.7 Å and 17.3 Å is only 5 kcal mol<sup>-1</sup>. We infer from the calculations that **ROBD1** is flexible enough to permit the rotor and second Bodipy to easily sample numerous separation distances in fluid solution.



**Figure 3.15.** Selected energy-minimised structures for **ROBD1** calculated using Gaussian 03 (B3LYP) and 3-21 G basis set. Energies are given in Hartrees and separation distances in Ångströms.

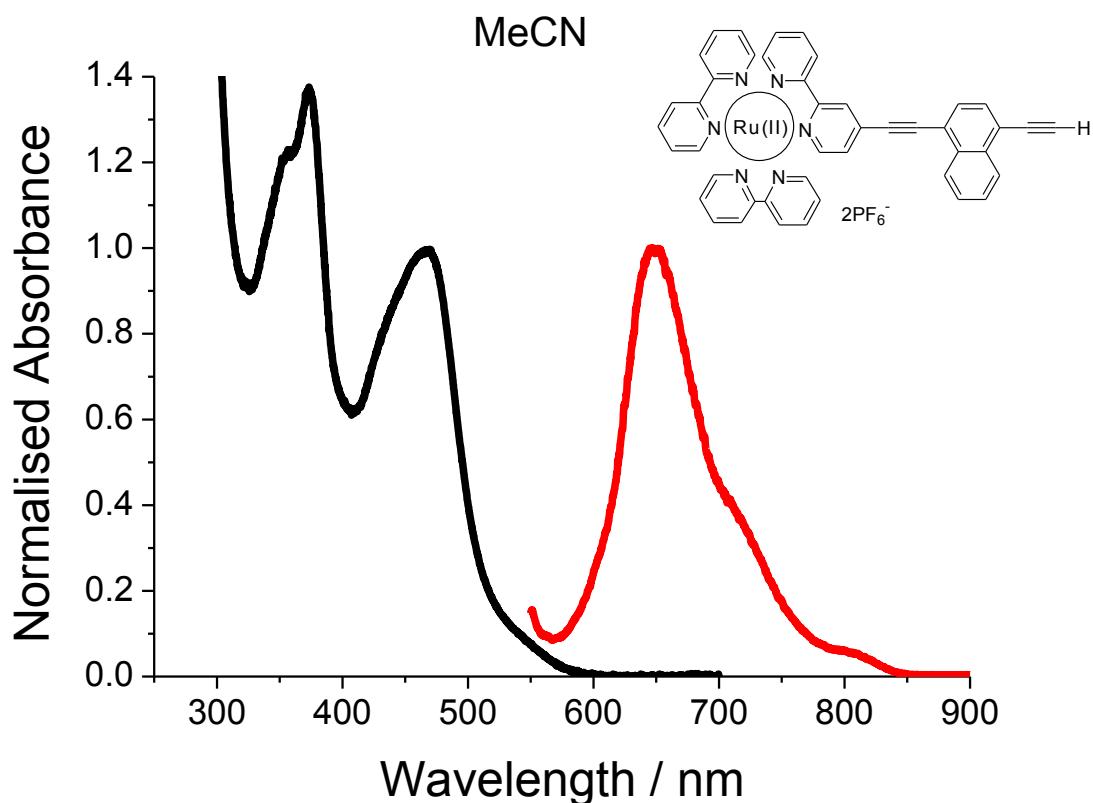
Considering that the spacer is more flexible in **ROBD2** the same type of behaviour was expected for the compound, it was not necessary to perform calculations again.

### 3.2.4 Photophysical Measurements

Different levels of photophysical studies were carried out on the discussed molecular systems, and cover steady-state measurements performed within the group in the Molecular Photonics Laboratory and fast spectroscopic measurements carried out in Tampere, Finland. The following discussion consists of two parts: the ruthenium-based assemblies, and the bis-Bodipy dyads.

### 3.2.4.1 Photophysical Properties of Ruthenium(II) Molecular Dyads

In order to try and understand the basis working of the two assemblies **ROMC1** and **ROMC2** we must review the photophysical properties of the basic units. It is known that the luminescence lifetime of  $[\text{Ru(II)(bipy)}_3]^{2+}$ , where bipy is 2,2'-bipyridine, in fluid solution is relatively long ( $\tau = 0.5 \mu\text{s}$ ).<sup>19</sup> Emission is from a triplet metal-to-ligand charge-transfer ( $^3\text{MLCT}$ ) state which is formed extremely quickly from the  $^1\text{MLCT}$  because of the heavy atom effect. Whereas the lifetime for  $[\text{Ru(II)(bipy)}_3]^{2+}$  is long the opposite is true for  $[\text{Ru(II)(terpy)}_2]^{2+}$ , and  $\tau$  is around 250 ps.<sup>20</sup> Already we can see a slight problem of working with  $[\text{Ru(II)(terpy)}_2]^{2+}$  since phosphorescence will be weak. However, with lowering temperatures the phosphorescence gets stronger since the thermally activated deactivation route becomes less important. As discussed previously, the lowest energy state associated with the Bodipy group is the triplet state. Even though intersystem crossing is inefficient in Bodipy the triplet can be populated by energy transfer from a local sensitiser.<sup>21</sup> The  $^3\text{MLCT}$  states for both the ruthenium(II) polypyridyl complexes are higher in energy than the Bodipy triplet state and it is very feasible that the two units in the dyads do not act independently, especially if they get into close contact.

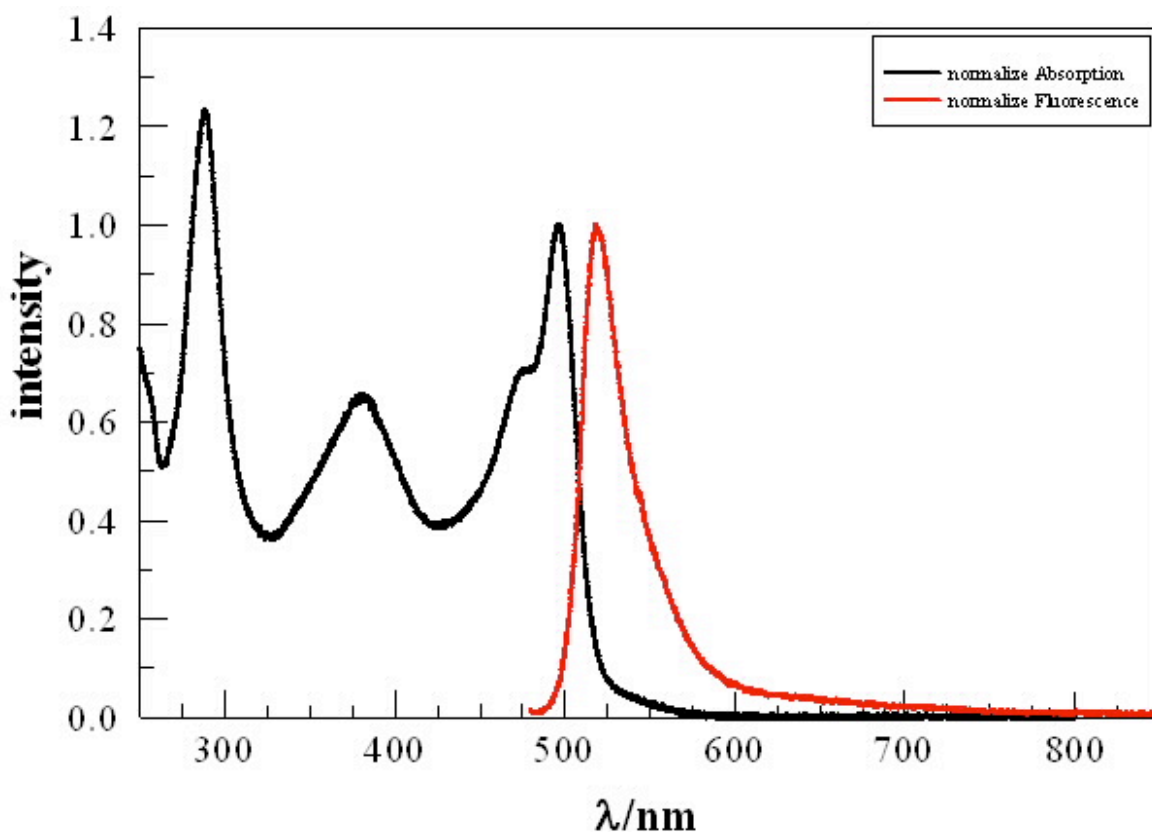


**Figure 3.16.** Room temperature absorption (black) and emission (red) spectra for **MCNAP** in MeCN.

#### 3.2.4.1.1 Properties of ROMC1

For comparison purposes the absorption and emission spectra for the precursor **MCNAP** are shown in Figure 3.16. The corresponding room temperature absorption/fluorescence spectra for **ROMC1** in BuCN are shown in Figure 3.17. The intense profile at around 290 nm is assigned to  $\pi-\pi^*$  electronic transitions of the 2,2'-bipyridine ligands. The further band at *ca.* 375 nm is due to the naphthalene group. The most interesting part of the spectrum is the long wavelength region where a sharp band is located at 520 nm which also contains a shoulder on the short wavelength side. Also quite prominent is a tail to the low-energy side of the main peak. It is possible to assign the sharp main peak to the rotor Bodipy and the shoulder partly

to the  $^1\text{MLCT}$  band of the ruthenium(II) polypyridyl complex. The tail is the spin-forbidden ground-state to  $^3\text{MCLT}$  absorption for the complex. The emission is dominated by a sharp band located at 520 nm which is fluorescence from the Bodipy group. Stretching from around 600 nm to 800 nm is an additional feature which is not typical for a Bodipy derivative. At the outset the emission is assigned to the ruthenium(II)-bipy complex. One point to note from inspection of Figure 3.17 is emission from the Bodipy overlaps fairly well with ruthenium(II) complex  $^3\text{MLCT}$  band. Thus, singlet (Bodipy) to triplet (ruthenium complex) energy transfer is feasible by a Förster-type mechanism. Any Dexter-type energy transfer would require close proximity of the two units to facilitate orbital overlap.

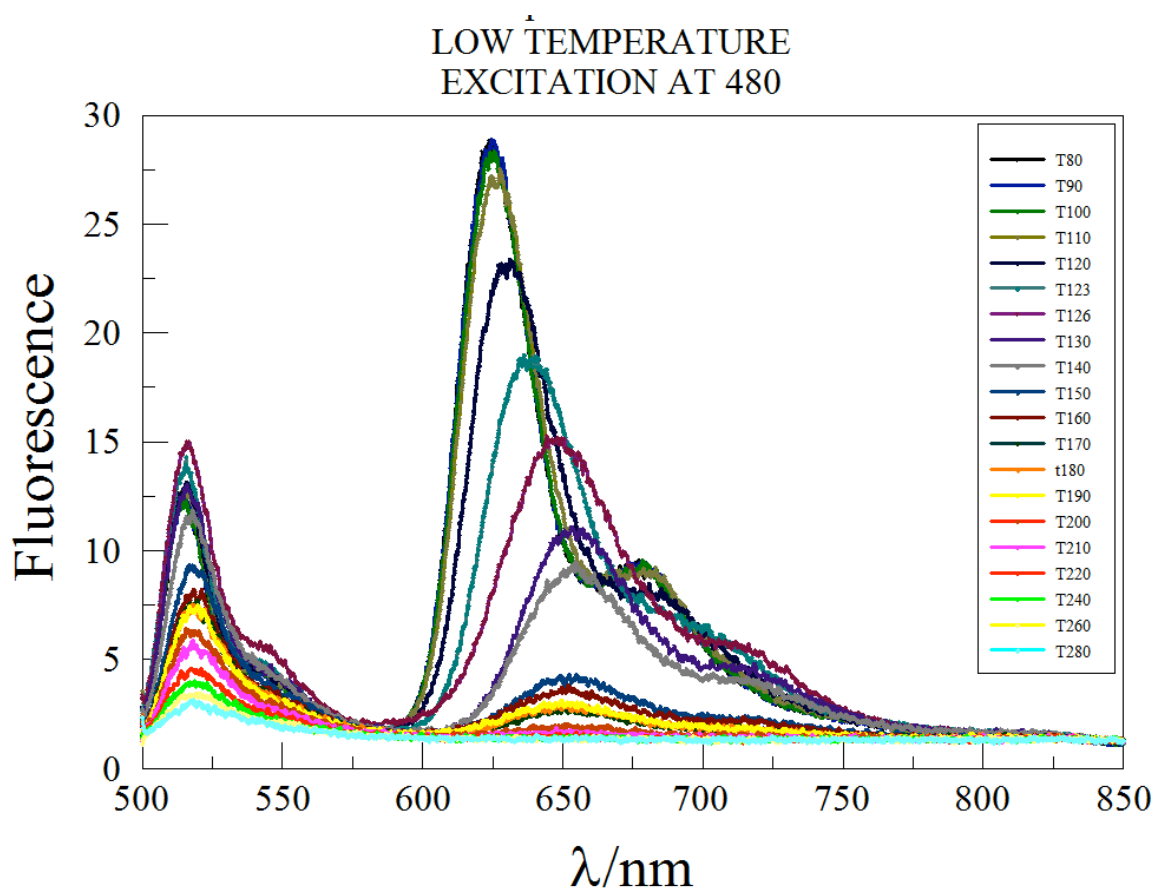


**Figure 3.17.** Room temperature absorption (black) and emission (red) spectra for **ROMC1** in BuCN

A more comprehensive insight into the emissive properties of **ROMC1** was obtained by variable temperature studies conducted in BuCN. Starting at room temperature emission spectra were recorded with decreasing temperature as shown in Figure 3.18.



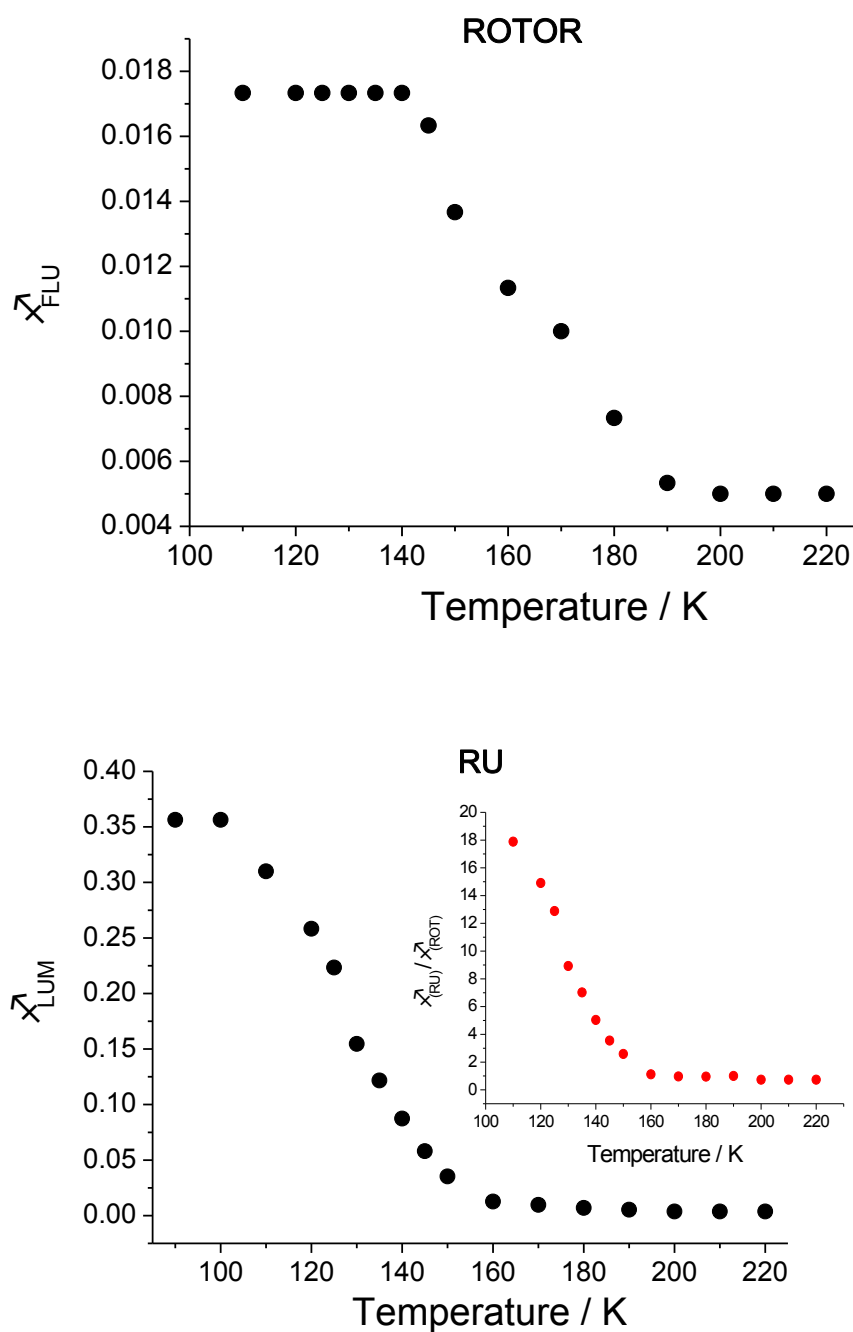
The most obvious change is the appearance of a broad profile centered around 620 nm, which gradually increases in intensity to around 150 K. After this point there is a major increase in the peak intensity and is accompanied by a blue-shift in the emission maximum. At 80K the emission profile is structured and typical of phosphorescence from a ruthenium(II)-bipy complex. The fluorescence from the Bodipy is also seen to increase slightly with a decrease in temperature to about 190K and again increase sharply to a plateau value.



**Figure 3.18.** Emission spectra recorded for **ROMC1** in BuCN with a decrease in temperature.

The temperature dependence data is in the optimum manner viewed in terms of quantum yield changes as shown in Figure 3.19. The sharp alteration in the quantum yields at around 160 K is identified with the glass transition temperature of the solvent. At around 140 K the solvent freezes and molecules are likely “frozen” in their lowest energy conformation. From the molecular structure calculations the separation distance should be around 25Å. It is possible that this separation distance is on par

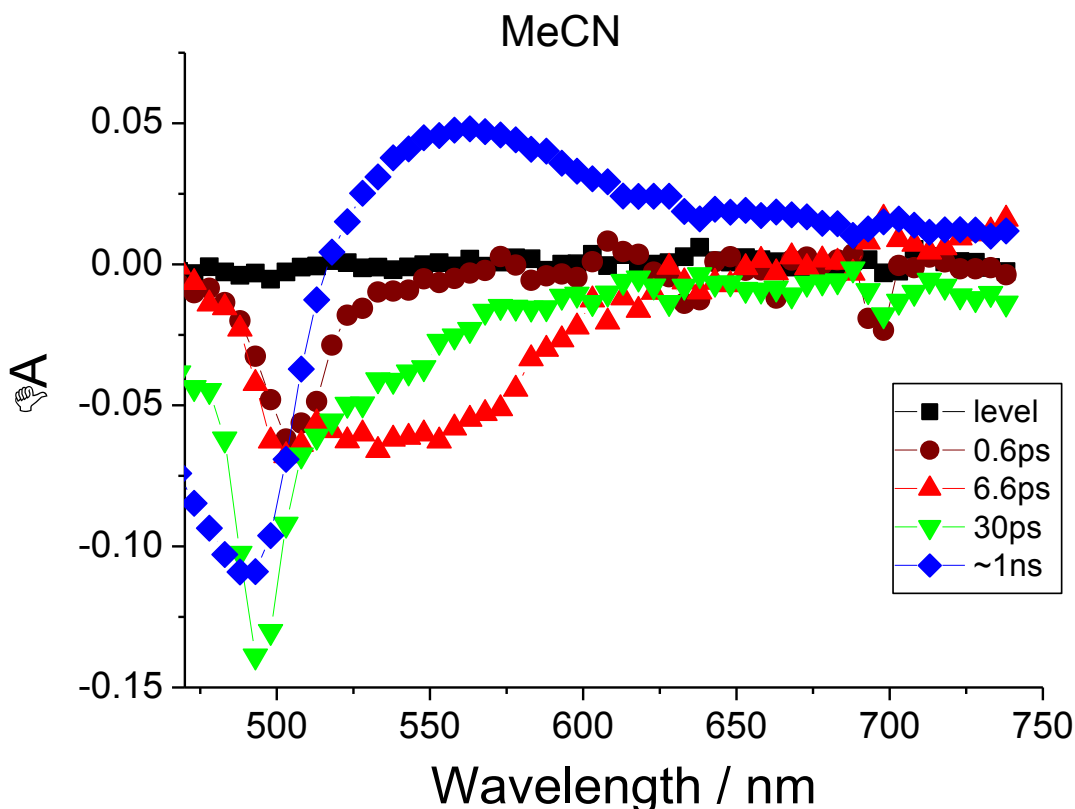
with, or greater than, the Förster critical distance ( $R_0$ ).



**Figure 3.19.** Plots showing the temperature dependence of quantum yields for the ruthenium-centered (**RU**) phosphorescence and rotor (**ROTOR**) fluorescence in BuCN.

We could delve a little more into the room temperature excited state behaviour of **ROMC1** using femtosecond pump-probe absorption spectroscopy. The calculated

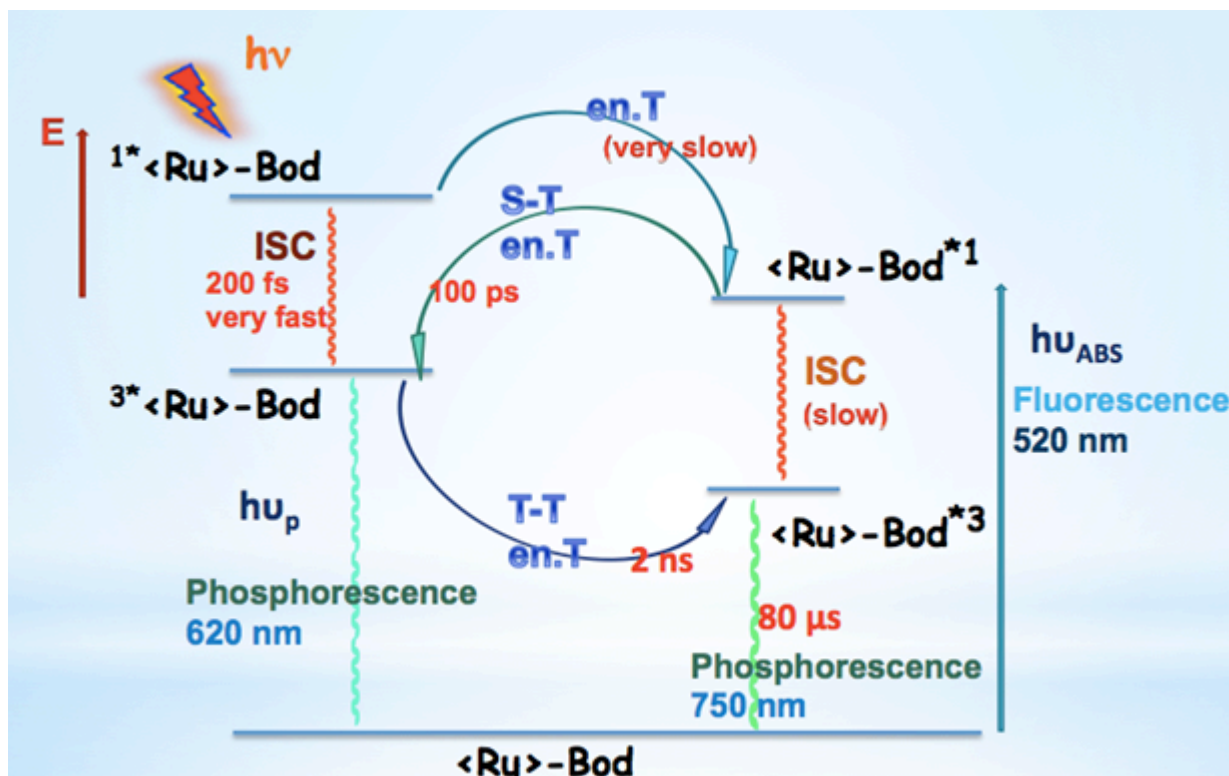
differential profiles from a global fit of the data are shown in Figure 3.20. The very short-lived transient is likely related to a fast relaxation process within the dyad. The most prominent feature is the long-lived transient which resembles the  $^3\text{MLCT}$   $[\text{Ru(III)}(\text{bipy})_2(\text{bipy}^-)]^{2+}$  state. The transient with a lifetime of around 30ps is associated with the Bodipy unit.



**Figure 3.20.** Calculated differential transient absorption profiles recorded after excitation of **ROMC1** in MeCN with a 70 fs laser pulse delivered at 395 nm.

Using all the collected data it is possible to construct a simplified diagram (Figure 3.21) to show the decay routes open to the dyad **ROMC1** in fluid solution. We can see that photons collected by the Bodipy unit get rapidly transferred to the ruthenium(II)-bipy centre by singlet-triplet energy transfer. This is a result of the good spectral overlap. Because of the extremely fast intersystem crossing  $^1\text{MLCT}$  to  $^3\text{MLCT}$ , energy transfer from the ruthenium(II)

complex to the Bodipy is unimportant. Once photons are collected at the metal centre they are transferred relatively slowly to the Bodipy group by triplet-triplet energy transfer. Thus energy collected in the molecular dyad percolates to the Bodipy unit and is often the reason for observed long-lived species in Bodipy-based assemblies.<sup>16,19</sup>

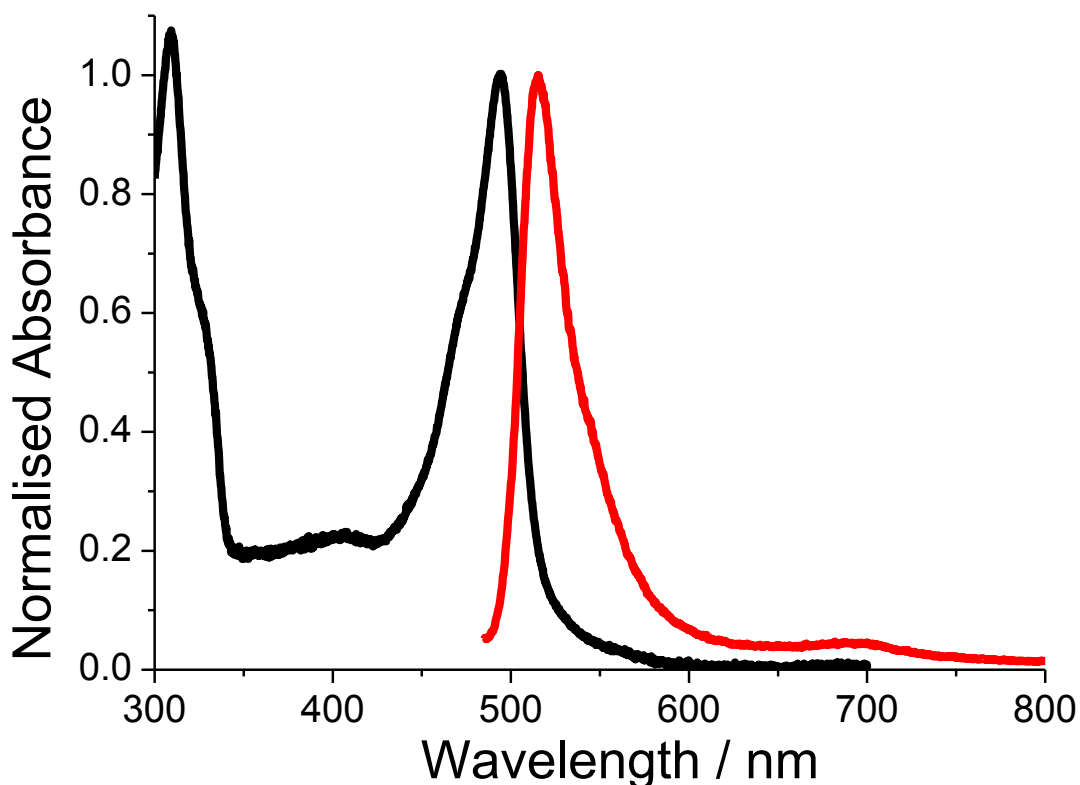


**Figure 3.21.** Proposed mechanism picture of deactivation for **ROMC1** showing the possible excited state decay routes to terminate at the triplet localised on the Bodipy.

### 3.2.4.1.2 Properties of ROMC2

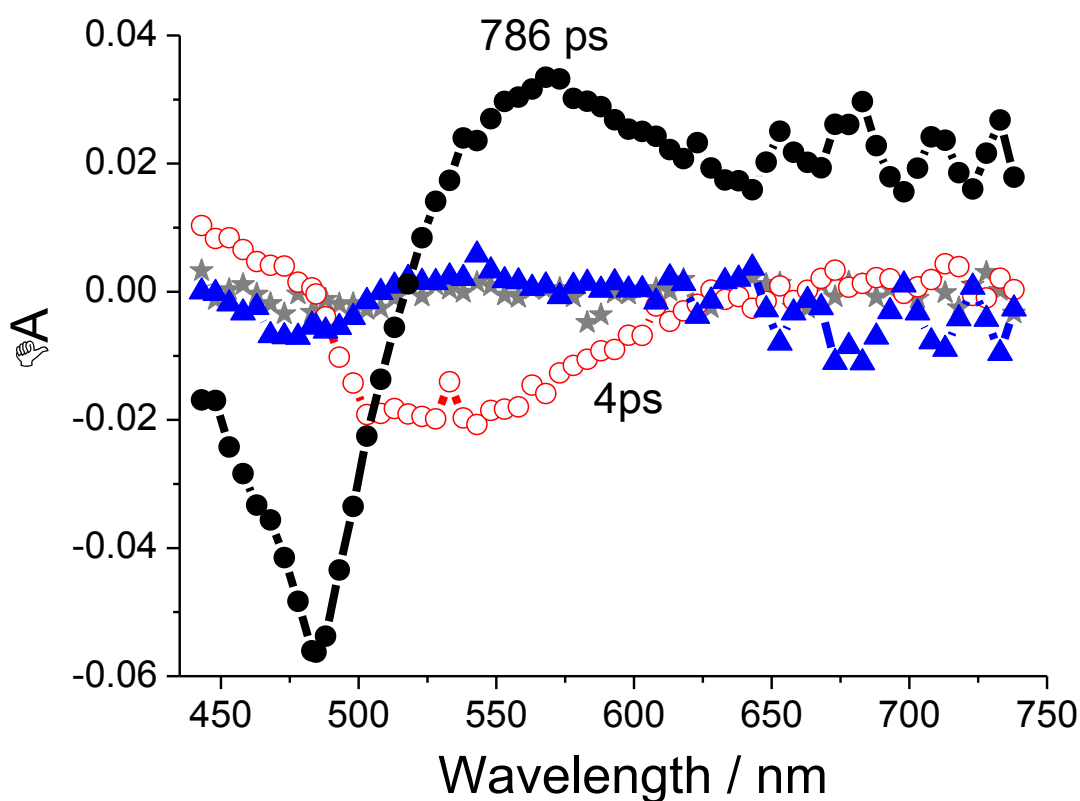
Considering the results collected for **ROMC1** the basic photophysical properties of **ROMC2** were easy to predict. We therefore did not perform such in-depth experiments as those for the other dyad. The electronic absorption spectrum for **ROMC2** in MeCN is shown in Figure 3.22. Unlike for the previous example the profiles for the Bodipy and ruthenium(II)-terpy groups overlap more, and clearly there is no absorption at around 400 nm since the naphthalene unit is missing. Again the spin-forbidden <sup>3</sup>MLCT band is observed as the low-energy tail. The Bodipy group dominates emission (Figure 3.22), but unlike in the case for **ROMC1** the long

wavelength profile is more evident.



**Figure 3.22.** Room temperature absorption (black) and emission (red) spectra for **ROMC2** in MeCN.

Although the data collected from fast pump-probe spectroscopic study were not sufficient, the general excited state behaviour could be elucidated. The final spectrum is in fitting with the  $^3\text{MLCT}$   $[\text{Ru}(\text{II})\text{terpy}(\text{terpy}^-)]^{2+}$ , but is shorter lived when compared to the analogous state for **ROMC1**. Again there is a fast decaying species which we take to be the singlet-to-triplet energy transfer between the Bodipy and the ruthenium(II)-terpy group (Figure 3.23).



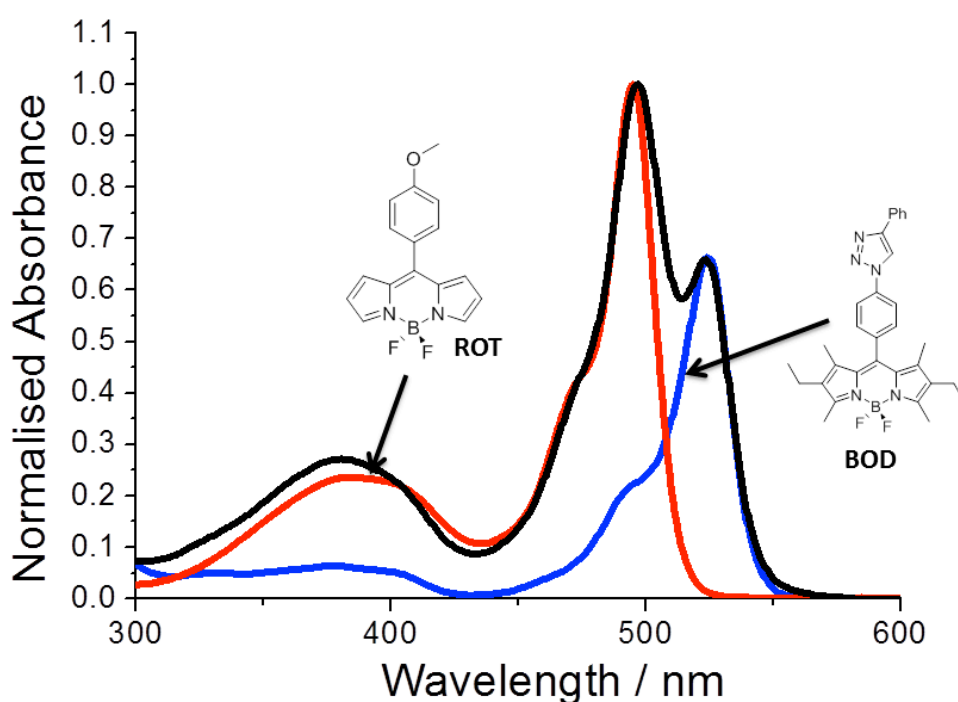
**Figure 3.23.** Calculated differential transient absorption profiles recorded after excitation of **ROMC2** in MeCN with a 70 fs laser pulse delivered at 395 nm.

#### 3.2.4.2 Properties of ROBD1 and ROBD2

The one problem with the prototype so-called Bodipy molecular rotor was the low starting point fluorescence output. We were especially interested to see if the original signal could be enhanced, with no detrimental effect on the overall fluorescence viscosity response. It is documented that the absorption maximum for non-alkylated Bodipy derivatives (i.e., rotor) occurs at higher energy compared to the alkylated version. Thus emission from the rotor overlaps particularly well with the absorption profile for fully alkylated Bodipy. From the basic theory, efficient electronic energy transfer (EET) is expected between the two groups at separation distances less than the Förster radius ( $R < R_0$ ). In the designed dyad, **ROBD1**, the triazole-alkyl spacer

separates the two Bodipy groups by ca. 17 Å, and electronically decouples the groups. The rotor Bodipy was anticipated to sensitise emission for the alkylated Bodipy so that the more fluorescent dye is now the reporter.

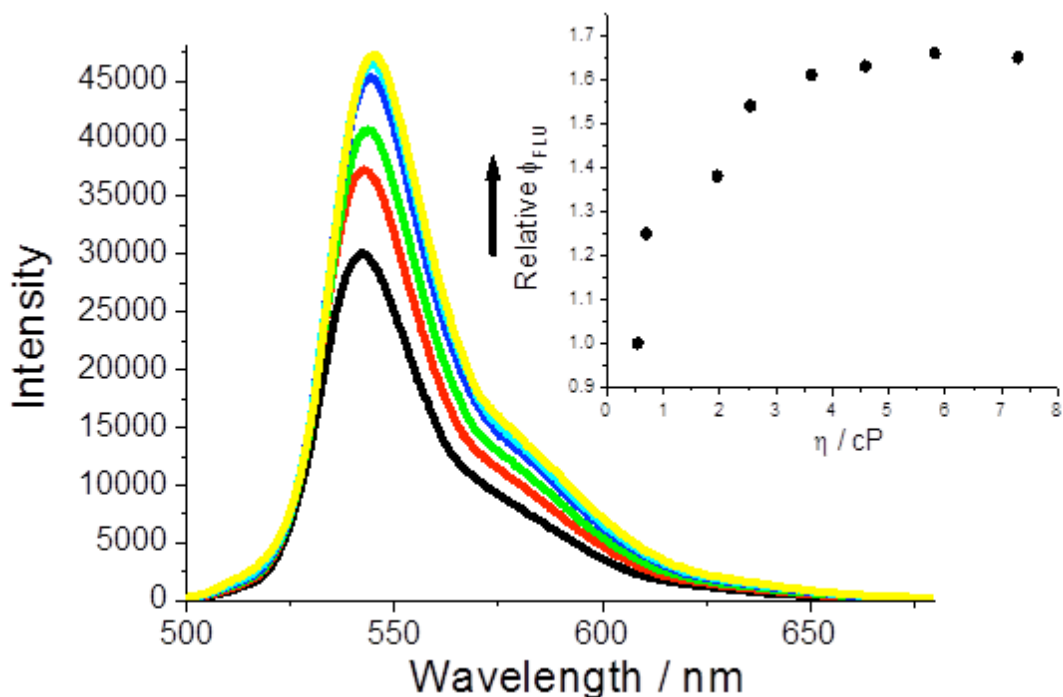
The electronic absorption spectrum for **ROBD1** in MeOH is shown in Figure 3.24. The overall profile is a convincing superimposition of the absorption spectra for two control compounds under identical conditions. The two main intense peaks at low-energy are the  $S_0$ - $S_1$  electronic transitions for the Bodipy. The peak maxima ( $\lambda_{\text{ABS}}$ ) are 497 nm and 524 nm, respectively. As seen previously, the HOMO-LUMO gap is affected by substitution of alkyl groups on the dipyrromethene backbone. The energy gap is reduced by ca.  $1000\text{ cm}^{-1}$  so that two clear maxima are observed for the two components. There is still appreciable overlap of bands (450 nm-500 nm) from both components to render selective excitation of a single chromophore problematic.



**Figure 3.24.** Room temperature normalised absorption spectra for **ROBD1** (black) and a fully alkylated Bodipy (blue) and a rotor Bodipy (red) in MeOH.

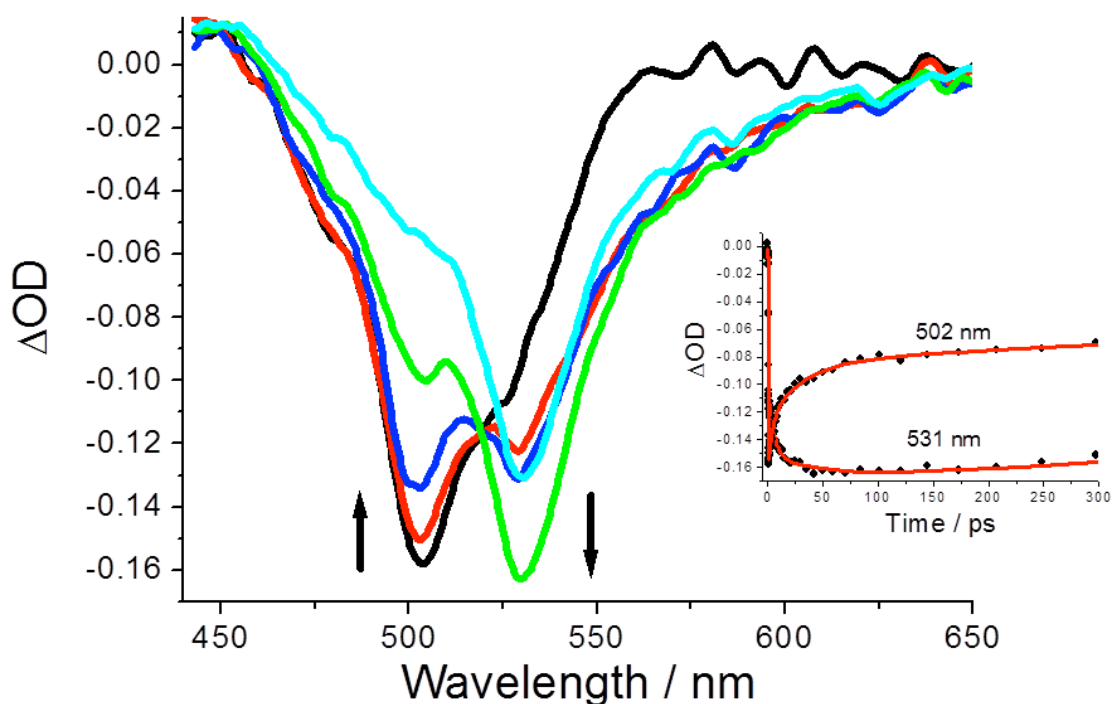
The fluorescence spectrum collected for a 1:1 mixture of **BD** and **ROT** in dilute MeOH, excited at 470 nm, is dominated by a profile centred at  $\lambda_{\text{EM}} = 542$  nm. A small shoulder is also seen situated at around 515 nm. The long wavelength band is assigned to emission from **BD**, while the shoulder is from **ROT**. The fully corrected fluorescence excitation spectrum is a poor match of the absorption profile. The spectrum resembles that observed for **BD** alone. The quantum yield of fluorescence ( $\phi_{\text{FLU}}$ ) for isolated **BD** is about 16 times larger than **ROT** in dilute MeOH at room temperature. At the excitation wavelength **BD** absorbs only ca. 25% of the photons. Therefore, the fluorescence intensity for **BD** should be about 4 times larger than for **ROT** assuming the two components are non-interacting. The observed difference is somewhat similar, which suggest that intermolecular energy transfer between **BD** and **ROT** is negligible. The emission spectrum for **ROBD1** is again dominated by a sharp band at 542 nm, but the possible shoulder at 515 nm is a little more difficult to judge. In contrast, the peak is more discernible in OctOH (n-octanol), especially when compared to **BD** in the same solvent. Contrary to the 1:1 mixture case, the fully corrected fluorescence excitation spectrum in MeOH (and OctOH) matches well with the absorption profile over a wide spectral range. The measured  $\phi_{\text{FLU}}$  is 0.17 and fluorescence lifetime ( $\tau_{\text{s}}$ ) in MeOH is 1.5 ns. The radiative rate constant ( $k_{\text{RAD}} = \phi_{\text{FLU}}/\tau_{\text{s}}$ ) of  $1.1 \times 10^8 \text{ s}^{-1}$  is consistent with values reported for Bodipy derivatives. The cumulative evidence supports the notion of efficient intramolecular energy transfer from **ROT** to **BD**.





**Figure 3.25.** Increase in the fluorescence intensity for **ROBD1** with change in selected alkanol solvents (black-CH<sub>3</sub>OH, red-C<sub>2</sub>H<sub>5</sub>OH, green-C<sub>3</sub>H<sub>7</sub>OH, blue-C<sub>4</sub>H<sub>9</sub>OH, cyano-C<sub>5</sub>H<sub>11</sub>OH, yellow-C<sub>8</sub>H<sub>17</sub>OH). Insert shows the change in  $\phi_{\text{FLU}}$  relative to methanol and corrected for refractive index changes for the solvents.

Absorption and fluorescence spectra recorded for **ROBD1** in other alkanol solvents were similar to the MeOH case. Any small shifts observed in both  $\lambda_{\text{ABS}}$  and  $\lambda_{\text{EM}}$  are accounted for by changes in polarizability of the solvents. Again, fluorescence excitation spectra matched extremely well with the absorption spectra, in line with the view of efficient intramolecular energy transfer. A distinct increase in  $\phi_{\text{FLU}}$  (Figure 3.25) is noticed for optically matched solutions of **ROBD1** in linear alkanols. Correcting for small changes in the refractive index of the solvents across the series, the relative  $\phi_{\text{FLU}}$  increases and reaches a plateau at around pentanol. The same data re-plotted against viscosity shows that levelling off occurs at around 6 cP. The limiting  $\phi_{\text{FLU}}$  is ca. 0.28. The dyad **ROBD1** would only appear to respond to a narrow viscosity window. On a positive note the output signal is more discernible than for simple **ROT** alone, since the starting quantum yield is around 4.5 times greater.

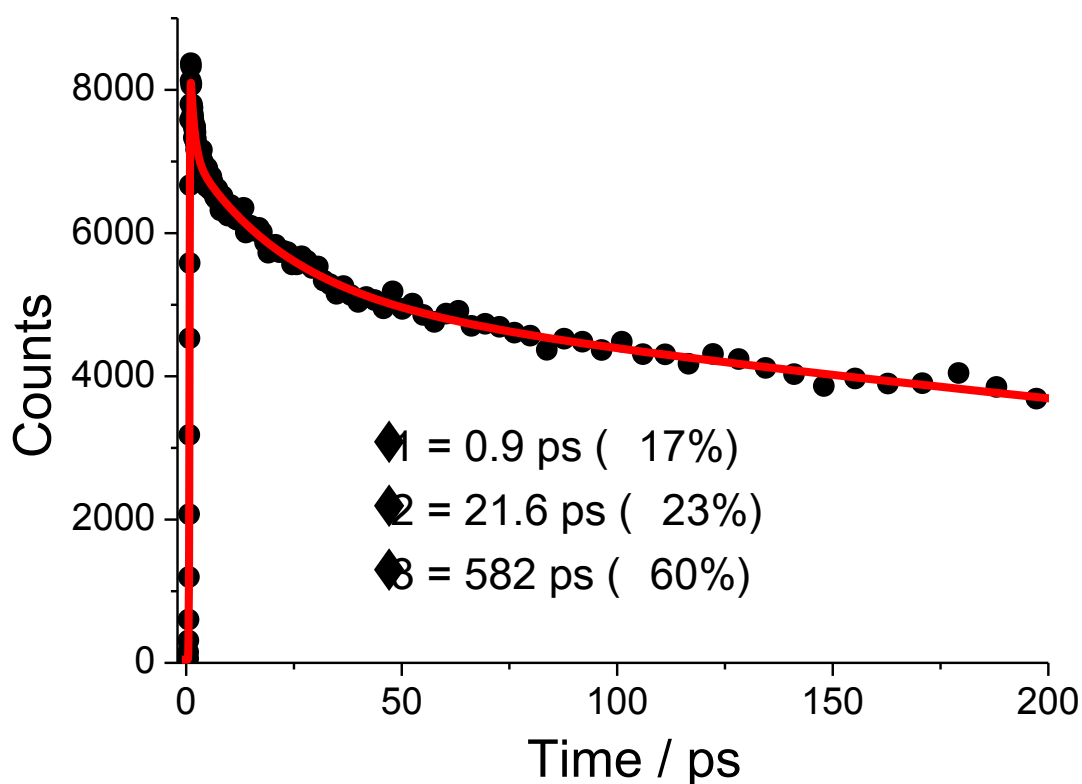


**Figure 3.26.** Differential transient absorption spectra recorded at different time delays (black - 1.1ps, red - 1.8 ps, blue - 3.8 ps, green – 35 ps, cyano – 1ns) following excitation of **ROBD1** in OctOH with a 70 fs laser pulse at 395 nm. Insert shows kinetic traces measured at two wavelengths and the least-squares fit to the data points.

Steady-state fluorescence experiments are fully supportive of intramolecular energy transfer between the two Bodipy units in **ROBD1**. A more complete picture of the temporal events was collected using up-conversion spectroscopy and femtosecond pump-probe spectroscopy. Only three solvent systems were studied, and they denote different points on the  $\phi_{\text{FLU}}$  correlation curve (Figure 3.25). The extreme case is for OctOH which represents the most viscous solvent tested. Excitation of **ROBD1** in OctOH with a 70 fs laser pulse delivered at 395 nm resulted in a bleach effect as shown in Figure 3.26. At the excitation wavelength ca. 30% of photons are absorbed by the **BOD** unit in the dyad. At the very early time delay the profile appears to be dominated by bleaching from the rotor Bodipy (502 nm). A closer inspection reveals

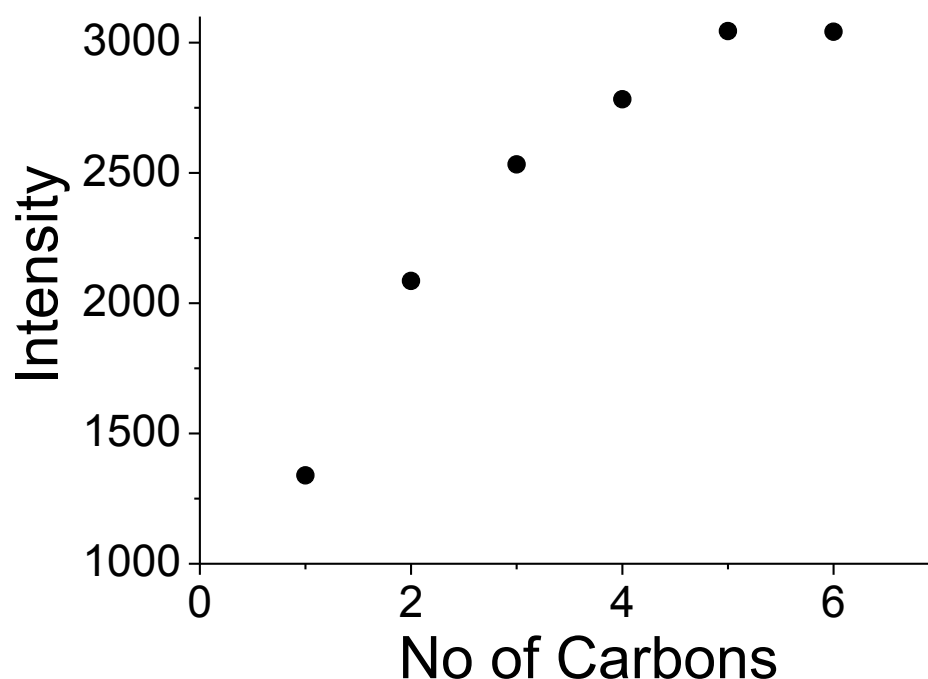
that there is also a contribution from the **BD** unit in the dyad. With increasing time delays this contribution increases to the expense of reduction in the bleach signal for the rotor Bodipy. At around 1 ns the transient profile appears to be only associated with **BOD** from **ROBD1**. However, there is considerable absorption overlap for **BOD** and **ROT** in the region around 500 nm. Decay kinetics monitored at two disparate wavelengths (Figure 3.26) required three exponentials to obtain a meaningful fit. The increase in bleaching at 531 nm matches well with the decrease at 502 nm, and comprises of two short lifetimes. A more comprehensive temporal picture is obtained by a global fit over the entire spectra region and timescale. The lifetimes for the two fast components are  $\tau_{TA1} = 6$  ps and  $\tau_{TA2} = 64$  ps.

The up-conversion lifetime data collected for **ROBD1** in OctOH are shown in Figure 3.27. The monitoring wavelength was set at 500 nm in attempt to selectively collect emission from **BD** within the dyad. There is an extremely fast decay process ( $\tau_{uc1} = 0.9$  ps), which is taken as structural relaxation of the excited state. Two further lifetime components are required to fit the decay profile. The contribution from the long lifetime ( $\tau_{uc3}$ ) component is around 60% of the total decay profile. It is noticeable that there is a discrepancy in lifetimes measured by the two fast techniques. We believe a complication is due to reverse energy transfer from **BOD** to **ROT** and a more in-depth analysis of the data is required.



**Figure 3.27.** Lifetime data collected for **ROBD1** in OctOH using up-conversion spectroscopy following excitation at 395 nm with a 70 fs laser pulse. Monitoring wavelength = 500 nm. Three exponential fit (red line) to the data points is shown.

The dyad **ROBD2** contains a slightly longer spacer but overall we might expect it to behave in a similar manner to **ROBD1**. The only main difference would be the maximum separation distance possible between the two Bodipy groups. Basic fluorescence steady-state measurements carried out for **ROBD2** in solvents of different viscosity were very similar to **ROBD1**. As shown in Figure 3.28 with increasing number of carbon atoms in alkanol solvents the emission intensity increases and reaches a plateau at around hexanol.



**Figure 3.28.** Fluorescence intensity versus no of carbon atoms in alkanol solvents for **ROBD2**.

### 3.3 Remarks and Conclusions

In this chapter we have shown that the “click” reaction can be used to produce a wide range of molecular systems containing metal-based units and secondary Bodipy groups. The use of the ligand, TBTA, is highly beneficial in promoting the reaction and ensures that the yield of the final triazole-based product is reasonable. Spectroscopic measurements detail elucidated the occurring event following excitation of the molecular systems, although the initial idea of producing dual responsive assemblies to perhaps sense viscosity and temperature simultaneously did not work as planned. A more comprehensive analysis of data for the **ROBD1** & **ROBD2** dyad system is required since there is the possibility that reverse Förster energy transfer is also happening.

### 3.4 References

1. A E. Nikolaev, G. Myszkiewicz, G. Berden, W L. Meerts, J F. Pfanstiel and D W. Pratt. (2005) Twisted intramolecular charge transfer states: Rotationally resolved fluorescence excitation spectra of 4,4'-dimethylaminobenzo-nitrile in a molecular beam. *J. Chem. Phys.* **122**, 084309.
2. A .C. Benniston and A. Harriman. (2006) Charge on the move: how electron-transfer dynamics depend on molecular conformation. *Chem. Soc. Rev.*, **35**, 169-179.
3. Z. R. Grabowski, W. Rettig and K. Rotkiewicz. (2003) Structural Changes Accompanying Intramolecular Electron Transfer: Focus on Twisted Intramolecular Charge-Transfer States and Structures. *Chem. Rev.*, 103 (**10**): 3899–3932.
4. (a) A C. Benniston, A. Harriman, P Y. Li, C A. Sams and M D. Ward. (2004) Orientational control of electronic coupling in mixed-valence, binuclear ruthenium(II)-bis(2,2':6',2''-terpyridine) complexes. *J. Am. Chem. Soc.*, **126**, 13630; (b) A C. Benniston, A Harriman, D J. Lawrie and A Mayeuxa (2004) The photophysical properties of a pyrene–thiophene–terpyridine conjugate and of its zinc(II) and ruthenium(II) complexes. *Phys. Chem. Chem. Phys.*, **6**: 51-57
5. M. A. Haidekker and E. A. Theodorakis. (2010) Environment-sensitive behavior of fluorescent molecular rotors. *J. Biol. Engin.* **4**:11
6. J. F. Qi and C. Guo. (1993) Viscosity Effects on TICT Excited State in Mixed Solvents. *J. Beijing Institute of Technology (Natural Science)* **2**, 152-156.
7. Th. Förster and G. Z. Hoffman. (1971) Die Viskositätsabhängigkeit der Fluoreszenzquantenausbeuten einiger Farbstoffsysteme (Viscosity dependence of fluorescent quantum yields of some dye systems). *Zeitschrift für Physikalische Chemie.* **75**:63-76.
8. D. S. Bulgarevich, O. Kajimoto and K. Hara. (1995) High-pressure studies of the viscosity effects on the formation of the twisted intramolecular charge-transfer (TICT) state in 4,4'-diaminodiphenyl sulfone (DAPS). *J. Phys. Chem.*, **99** (36): 13356–13361.
9. G. S. Kottas, L. I. Clarke, D. Horinek, and J. Michl, (2005) Artificial Molecular Rotors. *Chem. Rev.*, **105**, 1281–1376.
10. M. E. Nipper, S. Majd, M. Mayer, J. C. Lee, E. A. Theodorakis, M. A. Haidekker.

(2008) Characterization of changes in the viscosity of lipid membranes with the molecular rotor FCFV. *Biochim. Biophys. Acta* 1778(4): 1148–53.

11. A. Hawe, V. Filipe and W. Jiskoot. (2010) Fluorescent Molecular Rotors as Dyes to Characterize Polysorbate-Containing IgG Formulations. *Pharm. Res.* 27(2): 314–326.

12. C. Torigoe, T. Iwaki, M. Noji, M. Nakanishi. (1993) Antibodies for fluorescent molecular rotors. *Biochemistry*, 32(29):7589-92.

13. N. Boens, V. Leen and W. Dehaen. (2012) Fluorescent Indicators based on BODIPY. *Chem. Soc. Rev.*, 41, 1130–72

14. M. A. H. Alamiry, A. C. Benniston, G. Copley, K. J. Elliott, A. Harriman, B. Stewart and Y-G Zhi. (2008) A Molecular Rotor Based on an Unhindered Boron Dipyrromethene (Bodipy) Dye. *Chem. Mater.* 20 (12): 4024–32.

15. J. A. Levitt, P.-H. Chung, M. K. Kuimova, G. Yahiloglu, Y. Wang, J. Qu, K. Suhling. (2011) Fluorescence Anisotropy of Molecular Rotors. *ChemPhysChem.* 25; 12(3): 662-72.

16. Theilheimer's Synthetic Methods of Organic Chemistry. (2009) 74: 146-147.

17. H. C. Kolb and K. B. Sharpless. (2004) The growing impact of click chemistry on drug discovery. *Drug Discov. Today.* 9(8): 348-9.

18. V. Rostovtsev, L. Green, V. Fokin and K. B. Sharpless. (2004) A Stepwise Huisgen Cycloaddition Process: Copper(I)-Catalyzed Regioselective Ligation of Azides and Terminal Alkynes. *Angew. Chem. Int. Ed.* 41(14) 2596-99.

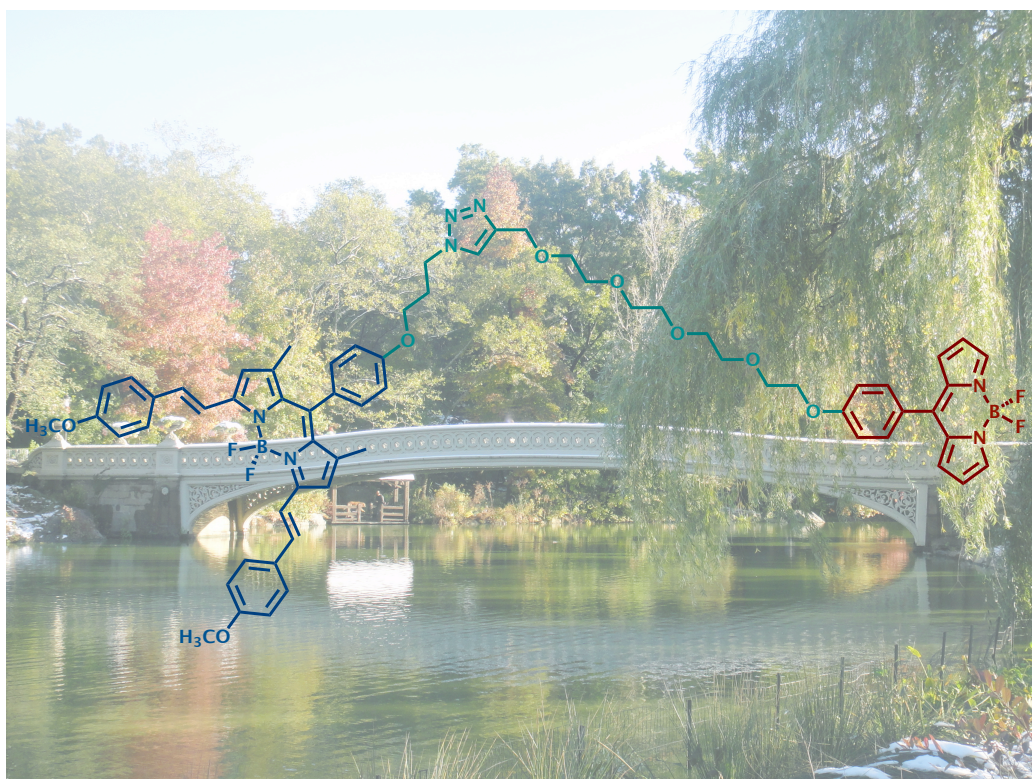
19. A. Harriman, A. Mayeux, C. Stroh and R. Ziessel. (2005) Photophysical properties of binuclear ruthenium(ii) bis(2,2':6',2''-terpyridine) complexes built around a central 2,2'-bipyrimidine receptor. *Dalton Trans.* 7 (17):2925-32.

20. O Filevich, B García-Acosta and R Etchenique. (2012) Energy transfer from a rhodamine antenna to a ruthenium–bipyridine center. *Photochem. Photobiol. Sci.*, 11, 843-47.

16. A. C. Benniston, V. Grossshenny, A. Harriman and R. Ziessel (1994) Electron Delocalization in Ethynyl-Bridged Binuclear Ruthenium(II) Polypyridine Complexes. *Angew. Chem. Int. Edit.* 33 (18) :1884-85.

# Chapter 4

## Modulated Multichromophoric Systems





## 4.1 Background and Molecular Design Principle

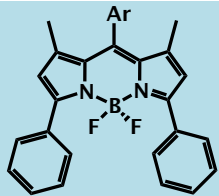

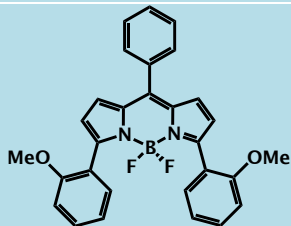
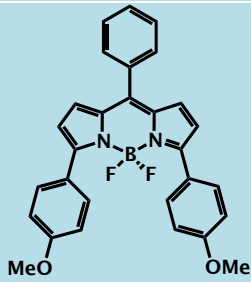
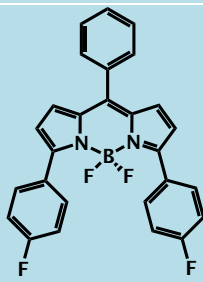
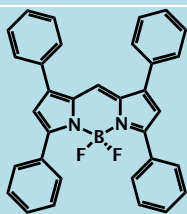
### 4.1.1 Versatility of Bodipy Compounds

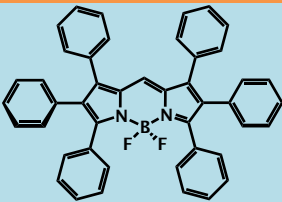
The intrinsic spectroscopic properties of a molecular system can be modulated via alterations in the overall chromophore architecture. Both the fluorescence intensity (e.g., redox-active switchable molecular systems<sup>1-2</sup>) and the wavelength of the fluorophore (e.g., red-emitting dyes<sup>3-4</sup>) are readily adjustable, courtesy to meet their application requirements. This chapter is a sequel of the previous chapter and is mainly concerned with tuning the properties of Bodipy derivatives via introducing electron-donating moieties and extending  $\pi$ -conjugation. Part of the motivation behind the work was to try and improve on the Bodipy derivatives discussed in Chapter 3 and develop new applications in areas such as neural imaging.

#### 4.1.1.1 Literature Methods

A typical parent F-Bodipy dye displays a major absorption band at around 500-520 nm, which is sharp and is attributed to the  $\pi$ - $\pi^*$  transition. A much broader band at is observed at around 400 nm. To increase electron conjugation a common method is to condense aromatic aldehyde at one or both the 3- and 5- positions of the parent Bodipy core, thus creating an alkenyl linkage to generate mono or di-substituted aryl- and styryl groups. Tetra-extended and hexa-extended (fully, including the meso- position) Bodipy systems have also been reported. The peripherally expanded  $\pi$ -electronic conjugation can then act to accelerate the folding and unfolding motions of the molecule, which can tune the optical properties by creating bathochromic shifts. Many researchers have reported 3,5-diaryl  $\pi$ -extended Bodipys with wavelengths shifted to lower energy (550-600 nm). Some system even have red and near-IR absorption (600–800 nm), which is a region more suitable for good quality imaging in medical applications. The tunable-platform parent F-Bodipy is also good for establishing a quantified experimental approach to study electronic energy transfer process, attribute to

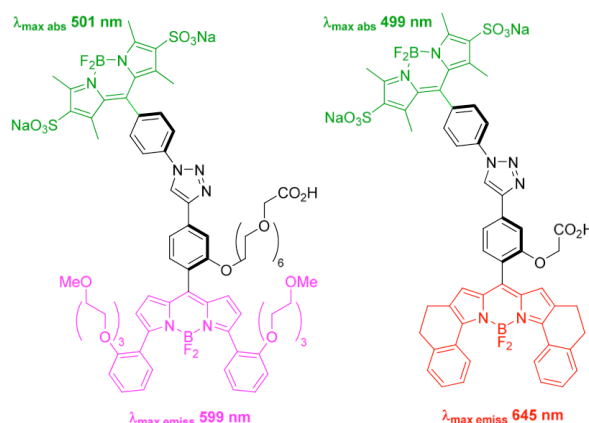
their increased Stoke's shift. Presented in Table 4.1 are collected literature reported derivatives.<sup>5-6</sup>

	$\lambda_{\text{abs}} / \lambda_{\text{em}}$	$\Phi_f$
 Ar = phenyl iodine	555/588 nm (CHCl <sub>3</sub> )	0.20
	542/607 nm (CHCl <sub>3</sub> )	0.38
	545/598 nm (CHCl <sub>3</sub> )	0.08
	582/626 nm (CHCl <sub>3</sub> )	0.42
	555/590 nm (CHCl <sub>3</sub> )	0.22
	564/593 nm (CH <sub>2</sub> Cl <sub>2</sub> )	1.00

	576/608 nm (CH <sub>2</sub> Cl <sub>2</sub> )	0.96
---	--	------

**Table 4.1:** Literature recorded Bodipy systems and their structure alteration plus their optical data.

Although spectroscopic properties fluorescent dyes could be readily tuned, to apply as fluorescent imaging sensitizer require adequate solubility of the compound within cellular environment.<sup>7</sup> Water-soluble energy transfer cassettes were reported by Burgess *et al.*, the solubility was achieved via sulfonation at Bodipy core and adding polyethylene glycol (PEG) chain. The  $\pi$ -extended Bodipy core and the sulfonated Bodipy were connected to form dyad system via click chemistry. On the phenyl bridge the side chain of carboxylic acid functionalized polyethylene glycol can then undergo Staudinger-Bertozzi ligation transform to NH<sub>2</sub> group, which are readily to form amide bond for protein labeling. (Figure 4.1) The two dyad systems can act as a FRET pair monitoring dynamics of protein-protein interactions within living cells and *in vitro* via fluorescence microscopy combined with the differential interference contrast (DIC) technique.<sup>8</sup>

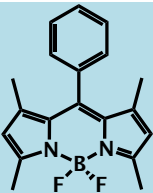
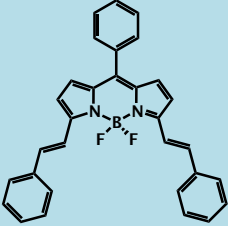
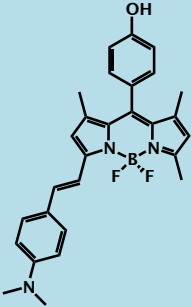


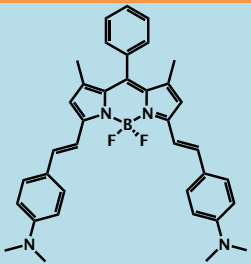
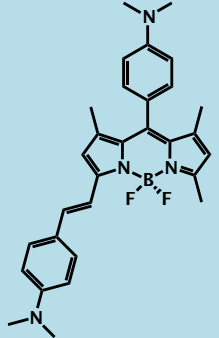
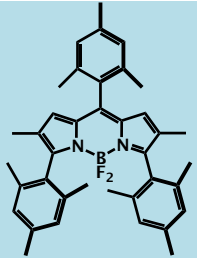
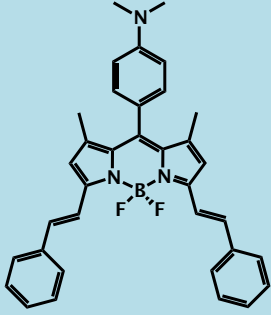
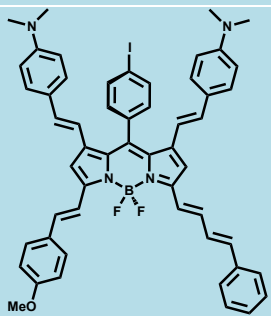
**Figure 4.1.** Water-soluble  $\pi$ -extended energy transfer cassette systems; image courtesy of Burgess *et al.*

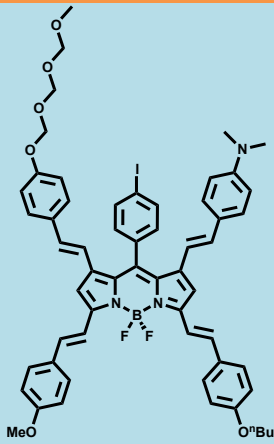
To attach electron-donating styryl groups to the parent F-Bodipy core is often performed by a Knoevenagel-type condensation. The method introduces

increased  $\pi$ -conjugation which results in a bathochromic shift, and can tune the absorbance and fluorescence spectra towards the red or even near infra-red (NIR) region. In the Knoevenagel reaction the selected  $\pi$ -electron rich aromatic units (e.g., *p*-hydroxyl-, *p*-dimethylamino- and *p*-dialkylamino-, benzaldehyde- and 4-*tert*-butylbenzaldehyde-) are condensed at the methyl positions in Bodipy core. Note that electron-deficient aldehydes such as the 3,5-dinitrosalicylaldehyde can also be attached to the methyl units of an 8-pentafluorophenyl Bodipy platform according to the works of Clavier *et al.*<sup>9</sup> Ziessel *et al.* reported the asymmetrically tetra-substituted dye bearing four vinyl functions produced with three different benzaldehyde derivatives. The highly substituted core created possible buckling, which reflected on the several transitions of the absorption profile.<sup>10</sup>

The literature reported Bodipy systems comprising styryl units are shown in Table 4.2.<sup>5-6</sup>

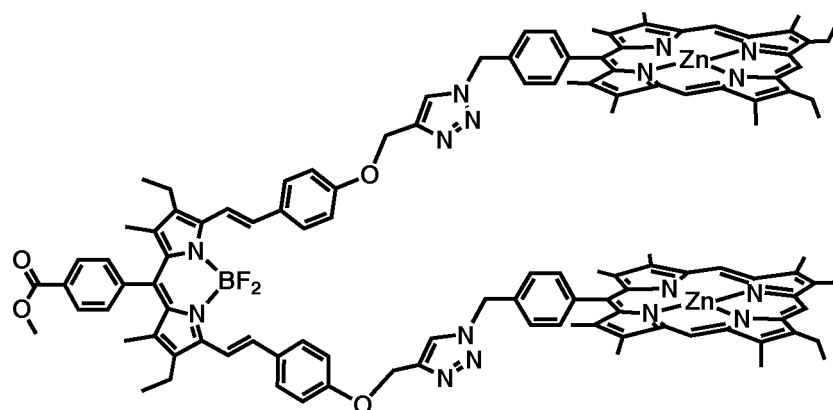
	$\lambda_{\text{abs}} / \lambda_{\text{em}}$	$\Phi_f$
	500/510 nm (CHCl <sub>3</sub> )	0.64
	628/642 nm (CH <sub>3</sub> CN)	0.84
	565/660 nm (THF)	0.25

	700/753 nm (CHCl <sub>3</sub> ) $\lambda_{em}$ = 630 nm (CHCl <sub>3</sub> + 2H <sup>+</sup> )	
	578/758 nm (H <sub>2</sub> O)  557/565 nm (H <sub>2</sub> O + 2H <sup>+</sup> )  594/699 nm (MeOH)	9×10 <sup>-4</sup> (H <sub>2</sub> O)  0.55 (H <sub>2</sub> O + 2H <sup>+</sup> )  0.10 (MeOH)
	543/559 nm (CH <sub>2</sub> Cl <sub>2</sub> )	0.95
	620/636 nm (CH <sub>3</sub> CN)  634/652 nm (CH <sub>3</sub> CN + H <sup>+</sup> )	4×10 <sup>-4</sup> (CH <sub>3</sub> CN)  0.75 (CH <sub>3</sub> CN + H <sup>+</sup> )
	718/778 nm (CH <sub>2</sub> Cl <sub>2</sub> )  707/725 nm (CH <sub>2</sub> Cl <sub>2</sub> + H <sup>+</sup> )	0.06 (680 nm)  0.03 (670 nm)

	700/714 nm (dioxane)	0.13 (610 nm)
	695/713 nm dioxane/HCl(M+H <sup>+</sup> )	0.13 (610 nm)

**Table 4.2:** Literature reported styryl-substituted Bodipy systems.

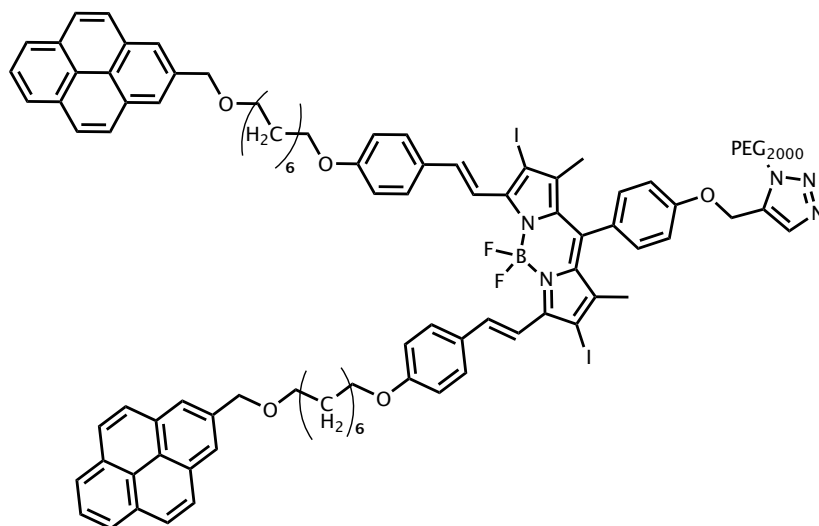
Knoevenagel condensation carried on 2,6-diethyl-1,3,5,7-tetramethyl-8-(*p*-methylbenzoyl)-Bodipy core with 4-(prop-2-yn-1-yloxy)-benzaldehyde was reported by Fukuzumi *et. al*; a click reaction was then carried on the phenyl acetylene with an azide activated zinc porphyrin. The porphyrinoid assembly was constrained via the coordination of nitrogen atom of the triazole ring to the zinc ion within the porphyrin units, also via  $\pi$ – $\pi$  interaction between the zinc porphyrins. The chemoselective role of aromatic aldehydes in Knoevenagel condensation reaction: *p*-dialkylaminobenzaldehyde results only in mono-substituted derivative, 4-alkoxybenzaldehydes results in mixture of mono- and distyryl derivatives.<sup>11</sup> (Figure 4.2)



**Figure 4.2.** Porphyrin comprised distyryl Bodipy tweezer compound.

Reverse singlet–singlet energy transfer from the zinc porphyrin to the  $\pi$ -conjugated Bodipy core was observed, attribute to the coordination reduced fluctuations on the  $\pi$ -electron overlap conformation. There also speculation on temperature induced conformational change but was not yet verified.

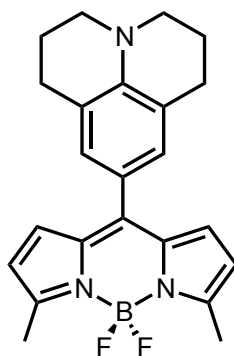
Another tweezer-like distyryl-Bodipy system was reported by Akkaya *et. al.*, with the aid of solubilizing group PEG<sub>2000</sub> group at the meso position (Figure 4.3) the compound could act at photodynamic therapy (PDT) agent when attached to the carrier of single-walled carbon nanotube via non-covalent  $\pi$ -stacking interaction between the terminal perylene units and the carbon wall.<sup>12</sup>



**Figure 4.3.** Example of a pyrenyl distyryl-Bodipy photodynamic therapy sensitizer.

#### 4.1.1.2 Molecular Design Principle

The main part of this chapter focuses on a basic Bodipy chromophore that displays strong ground-state charge transfer (CT). The dyad, **MJULBD**, comprises a julolidine donor and the Bodipy unit acts as the acceptor (Figure 4.4). The CT interaction results in the appearance of a broad long-wavelength absorption band. Emission from **MJULBD** is highly solvent dependent, but more significantly the fluorescence response is sensitive to the electric field of neurons.

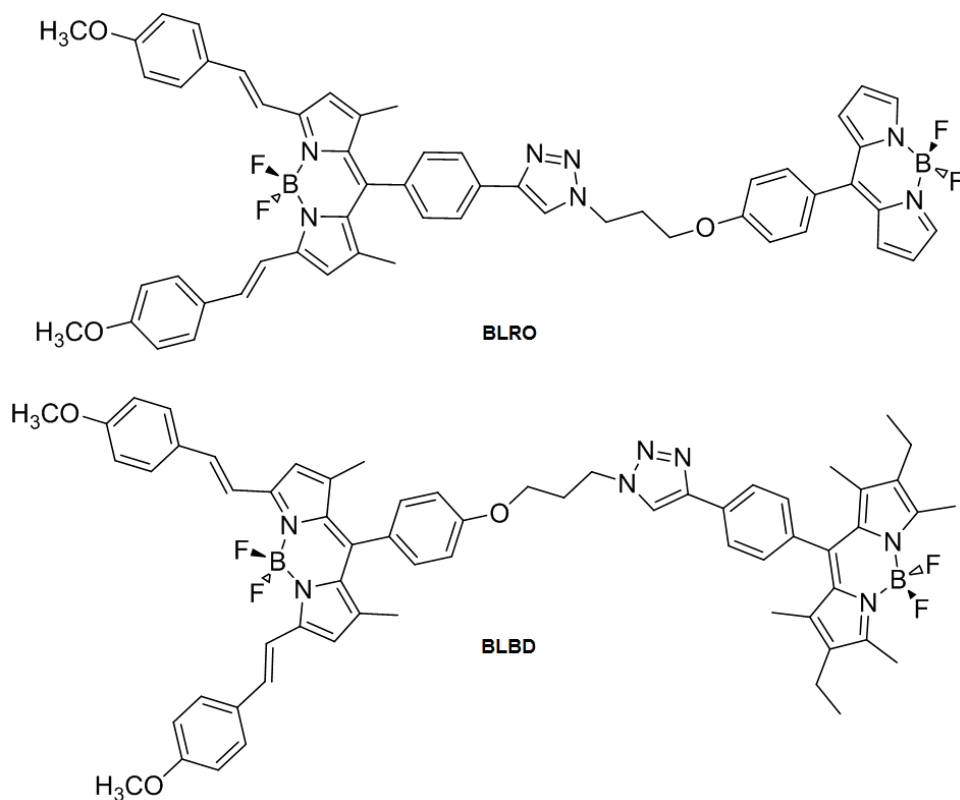


**MJULBD**

**Figure 4.4.** Illustration of the donor-acceptor Bodipy **MJULBD**.

In the previous chapter we discussed the possibility of producing dual mode systems, especially those containing two Bodipy groups. One problem was the very close overlap of the emission from the two units, which precluded any chance of observing two independent signals and developing a ratiometric probe. In an attempt to circumvent this problem the two dyads **BLRO** and **BLBD** were designed (Figure 4.5). The main idea was extend  $\pi$ -conjugation and switch their absorption/emission profile to longer wavelength region to test inter-molecular energy transfer.



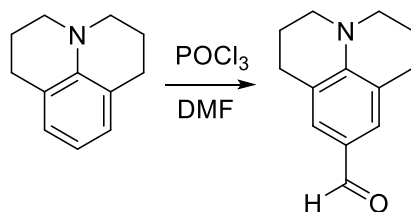


**Figure 4.5.** Examples of Bodipy dyads containing a long-wavelength emitting chromophore.

## 4.2 Results and Discussion

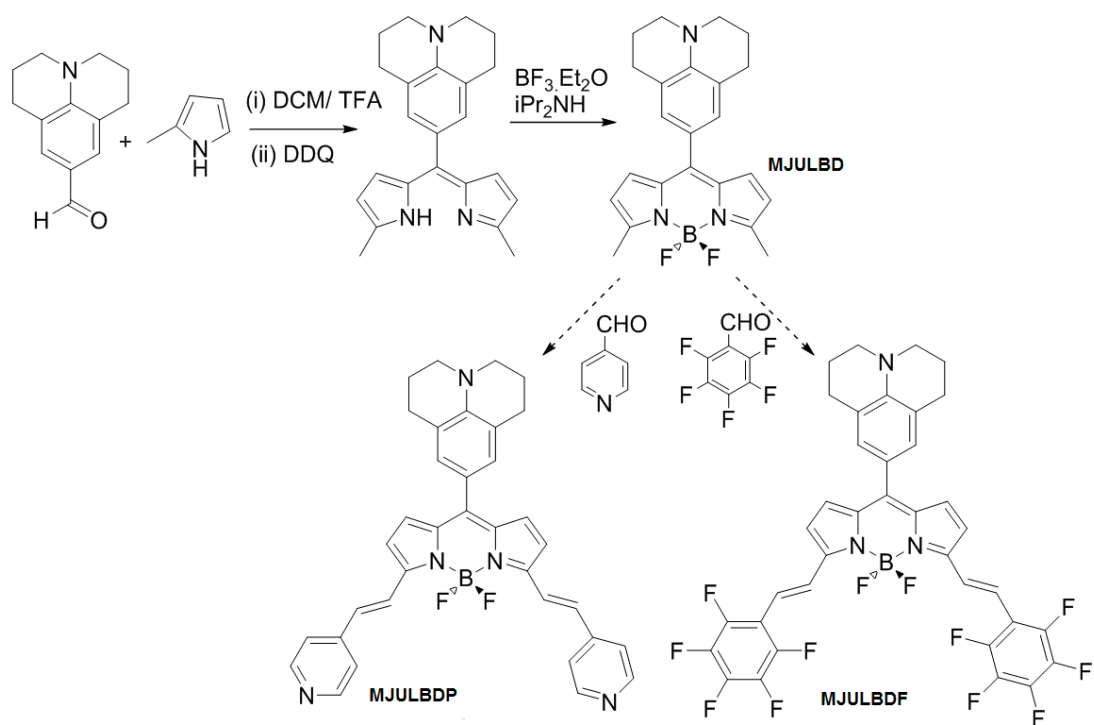
### 4.2.1 Synthesis of Julolidine Donor Acceptor Probes

By disconnection of **MULBD** the two required compounds are 2-methylpyrrole and *p*-julolidinecarboxaldehyde. The incorporation of an aldehyde into julolidine is relatively straightforward and is carried out using the well known Vilsmeier–Haack reaction as shown in Scheme 4.1. The yield of the aldehyde was around 40% from the commercially available julolidine starting material.



**Scheme 4.1.** Preparation of julolidinecarboxaldehyde via the Vilsmeier–Haack reaction.

The starting material 2-methyl pyrrole was commercially available and when coupled with julolidinecarboxaldehyde in the presence of acid and oxidation produced the intermediate dipyrromethene in 40% yield. The reaction of intermediate compound with  $\text{BF}_3 \cdot \text{Et}_2\text{O}$  in the presence of base afforded **MJULBD** in 62% yield as a purple solid (Scheme 4.2).



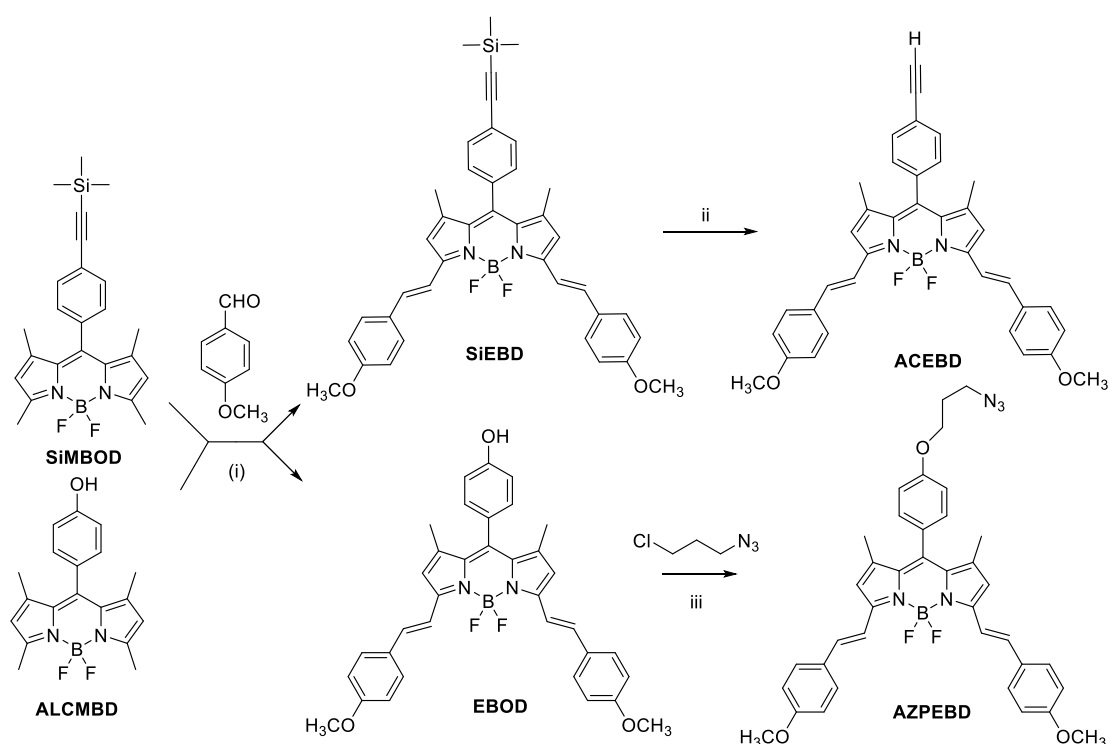
**Scheme 4.2.** Preparation of **MJULBD** and the attempted increase in  $\pi$ -conjugation via Knoevenagel condensation .

## 4.2.2 Synthesis of Multichromophoric Systems

### 4.2.2.1 Preparation of Activated Distyryl Bodipy Precursors

In order to prepare the dual-chromophoric dyad systems **BLRO** and **BLBD**, via the azide-alkyne click reaction, precursor Bodipy compounds were required as shown in Scheme 4.3. The two starting materials **SiMBOD** and **ALCMBD** were prepared stepwise via general protocols (described in previous Chapter). Both were treated to Knoevenagel condensation by reacting with *p*-methoxybenzaldehyde. The water formed during the reaction was removed azeotropically in a Dean-Stark apparatus using silica gel in the run-off tube to ensure completion of the reaction. Purification of the crude

reaction mixture was troublesome since one of the side products is the mono-styryl derivative. After repeated purifications the desired compounds **SiEBD** and **EBOD** were isolated in 35% and 38% yield, respectively. The silyl protecting group from **SiEBD** was removed using KF to afford **ACEBD** in 90% yield. The acetylene proton for **ACEBD** was observed at 3.12 ppm. The azide functionality was introduced onto **EBOD** by in-situ deprotonation of the phenol and reaction with chloropropylazide. As discussed in the previous chapter the reaction proceeded selectively at the chloro site to afford **AZPEBD** as a blue solid.

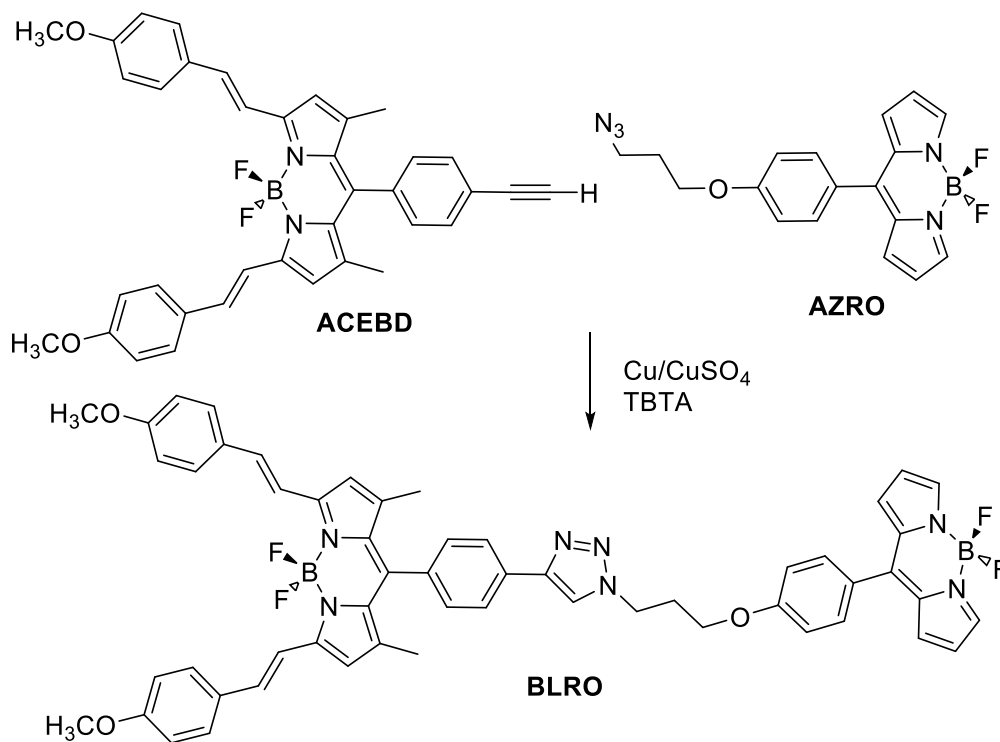


**Scheme 4.3.** Preparation of the precursor compounds with extended  $\pi$ -conjugation. Reaction conditions: (i) Glacial AcOH, piperidine, in anhydrous toluene reflux at 140°C, 50-96 hr. (ii) KF in  $\text{CH}_2\text{Cl}_2$ . (iii)  $\text{K}_2\text{CO}_3$  in DMF.

#### 4.2.2.2 Synthesis of Alkyl Linked Dyad Systems

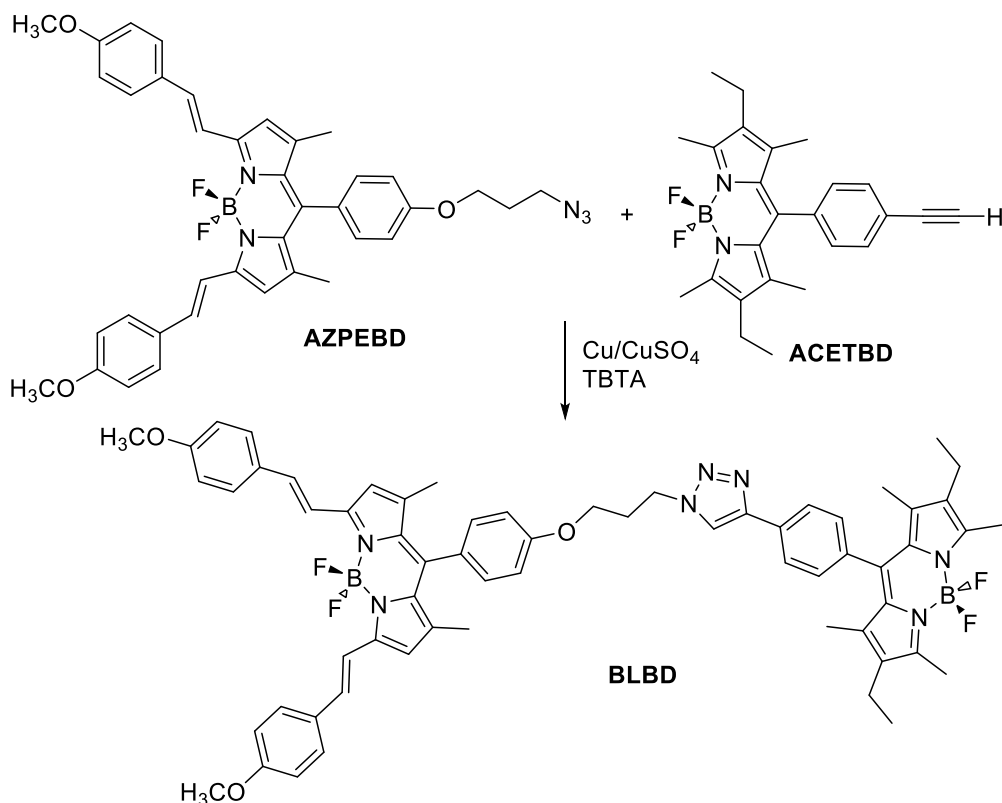
The alkyne containing long-wavelength emitter **ACEBD** was tethered to the rotor moiety as shown in Scheme 4.4. The reaction involved use of the rotor Bodipy **AZRO** and again the “click” conditions worked well, and **BLRO** was eventually isolated as a blue solid after careful column chromatography. The

multiple overlapping aromatic resonances for the  $^1\text{H}$  NMR spectrum of **BLRO** hindered full interpretation, but the MALDI mass spectrum displayed a clear peak at  $m/z = 952.39$  consistent with the structure. In addition the absorption spectrum displayed bands (see later) that confirmed presence of the two Bodipy chromophores.



**Scheme 4.4.** Preparation of **BLRO** via the “Click” Reaction.

In order to make a control compound the derivative **BLBD** was also prepared (Scheme 4.5). Instead of simply using the fully alkylated version of compound **AZRO** we decided to modify the synthetic method slightly and do the “click” reaction the other way around. Thus, the alkyl azide containing spacer was connected to the long-wavelength emitting Bodipy and the acetylene group was part of the fully alkylated Bodipy. The triazole attachment site is reversed but this is unimportant. Once again the aromatic region of the  $^1\text{H}$  NMR spectrum for **BLBD** was complicated because of overlapping peaks. The MALDI mass spectrum confirmed the dimer structure.



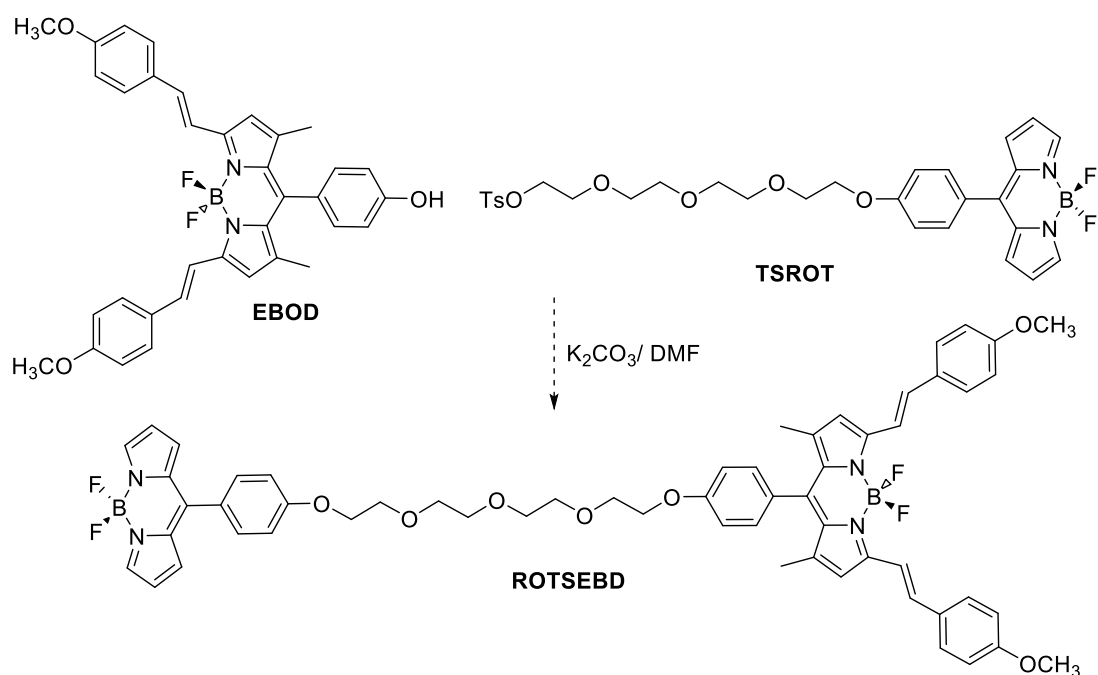
**Scheme 4.5.** Preparation of **BLBD** using “click” chemistry.

#### 4.2.2.3 Towards Polyether-linked Dyad Systems

The previous two examples showed that the “click” reaction is beneficial for coupling together specifically designed molecular components. As apart of the project other coupling methods were tried but in most cases with limited success. As shown in Chapter 3 the alkyl group can act as spacer/linker. Presented in the following are attempts to use a polyether spacer (Scheme 4.6). One reason for incorporating such a group is its good permeability in cellular environments, which would be beneficial for applications as fluorescence tracers to examine muscular dystrophy. The mono-tosylation of the glycol derivative **GLY** was carried out by using it in excess with respect to tosyl chloride. The excess reagent is far more water soluble than **TSETH** which facilitates work up and purification. The identity of **TSETH** as the mono-tosylated product was easily confirmed by  $^1\text{H}$  NMR spectroscopy, by comparing the integrals for the two tosyl doublets to one of the characteristic

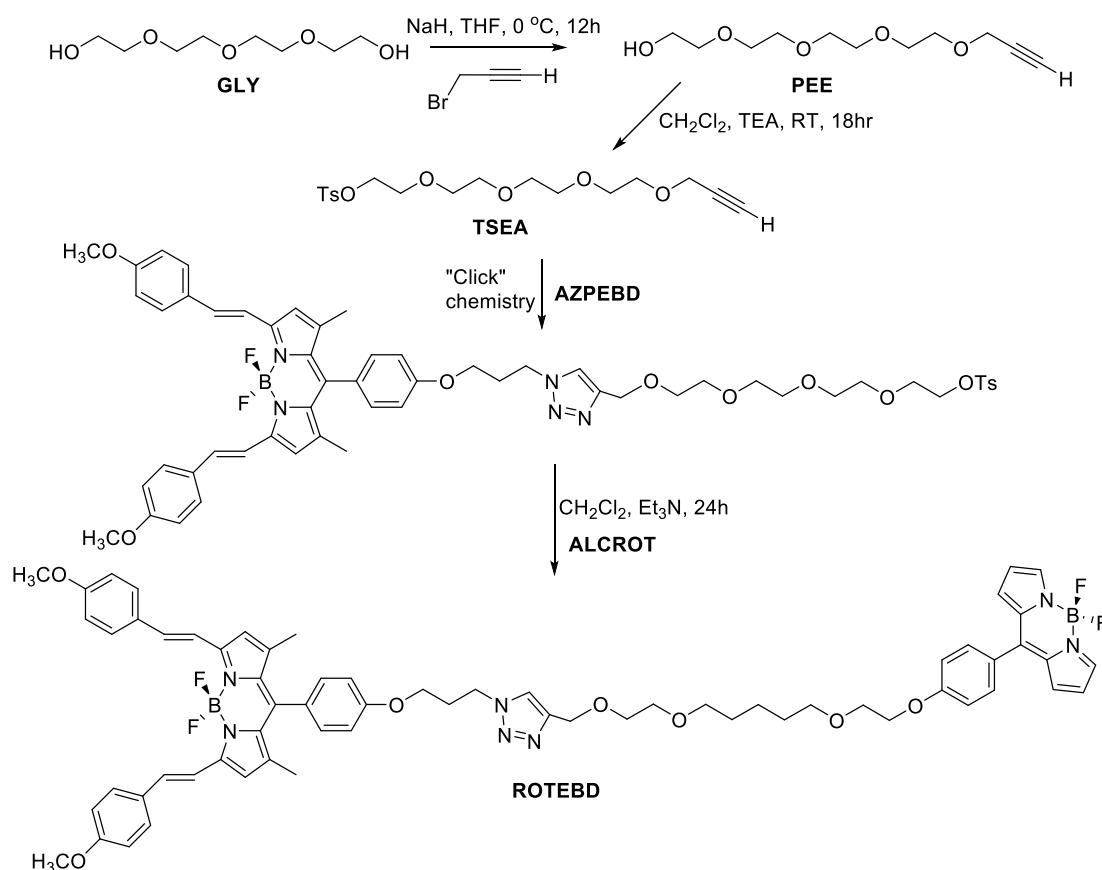
OCH<sub>2</sub> signals. The coupling of **TSETH** with **ALCROT** proceeded smoothly to create the rotor glycol derivative **ETROT** as a red solid in 40% yield. The terminal hydroxyl group in **ETROT** is a poor leaving group. In an attempt to facilitate nucleophilic reactions at the site, the hydroxy group was converted to the OTs derivative by the reaction of **ETROT** with TsCl in the presence of Et<sub>3</sub>N. The <sup>1</sup>H NMR for **TSROT** seemed to show resonances associated with the tosyl group, but the attempted reaction of **TSROT** with **EBOD** (Scheme 4.7) did not yield the desired compound. After prep-TLC purification of starting materials the reaction was carried several times each on a 80 mg scale with slight alterations in the stoichiometry. Again there was no success in obtaining the desired product. The reason for the reaction failures is unclear since deprotonation of **EBOD** generates a good nucleophile.

**Scheme 4.6.** Synthetic route of the polyether-based spacer derivative **TSROT**.



**Scheme 4.7.** Attempted synthesis of the polyether-based dyad **ROTSEBD**.

Retrosynthetic analysis was used and it was decided to start the reaction again, attaching ethylene glycol to the low-energy side of Bodipy dyad (Scheme 4.8). In this case the acetylene group was attached to **GLY** to produce the derivative **PEE**. The free alcohol group was then made into the tosylate using standard conditions. The ditopic **TSEA** was then reacted with the azide derivative **AZPEBD** under standard “click” chemistry conditions to produce the intermediate containing the expanded Bodipy and the tosylate at the other end. The final reaction worked to produce a deep green solid in 16% yield. The  $^1H$  NMR spectrum of the crude compound revealed the existence of target compound but after purification and preparative TLC there was not enough of the collected compound to run full characterization analysis.

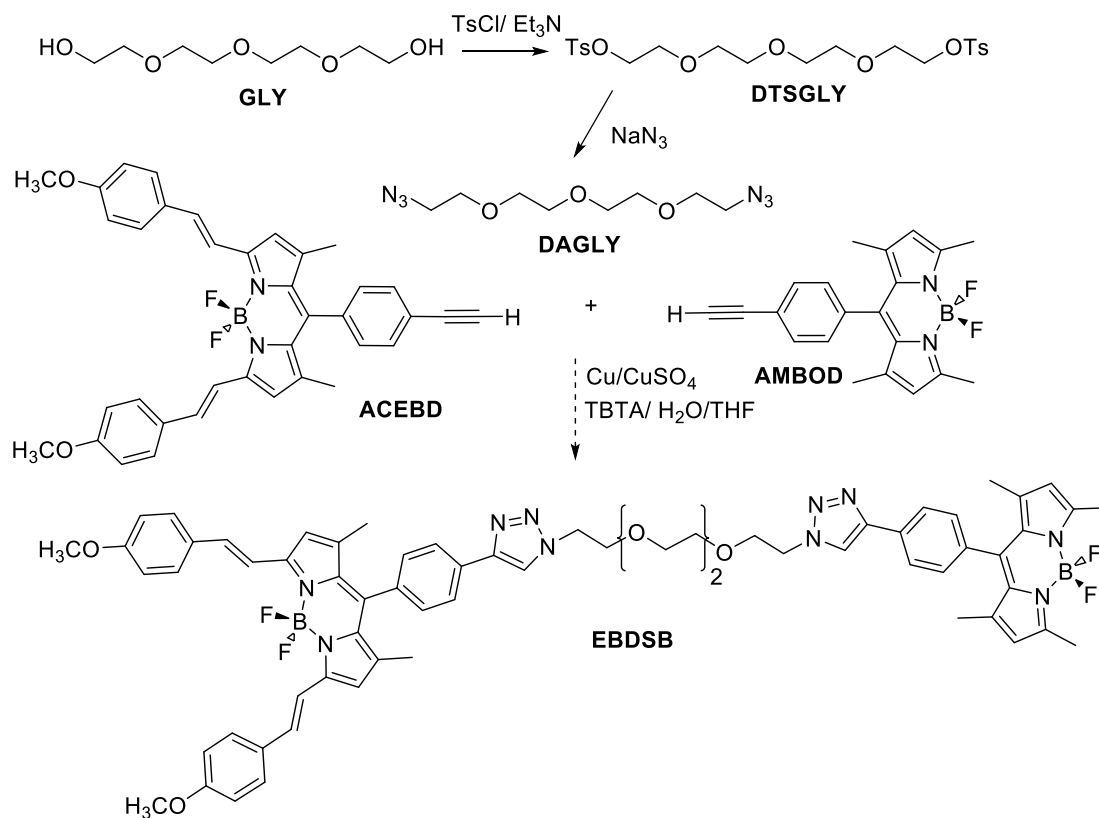


**Scheme 4.8.** Attempted synthetic route of polyether connected dyad compound of Bodipy rotor and distyryl condensed Bodipy.

Inspired by the multi-component assembly process (MCAP) methodology, one attempted synthesis was based on a "double click" reaction as illustrated in Scheme 4.9. Based on a literature method **GLY** was converted into the ditosylate **DTSGLY** which was reacted with excess NaN<sub>3</sub> to produce **DAZGLY**. The I.R. spectrum for **DAZGLY** confirmed the presence of the azide moieties. The attempted "double click" reaction of **DAGLY** with **ACEBD** and deprotected **SiMBOD** was again inconclusive. The actual reaction was only carried out on a 20 mg scale, and upon purification a deep olive-green coloured band appeared on the silica column. The colour is in contrast to the blue and red coloured starting compounds. The olive-green portion was separated and a preliminary <sup>1</sup>H NMR spectrum of the collected material suggested the presence of the target compound **EBDSB**. After preparative TLC purification the amount of the product was not enough to collect a good <sup>1</sup>H NMR spectrum. Because the preparation time of the starting materials was



quite time consuming the reaction was not carried again. Although this attempt of “double click” reaction could not be called an “orchestrated cascade reaction”, since it suffers the side reaction of homo-dimerisation, the method is still worth attempting on a larger scale so that target products could be properly identified.

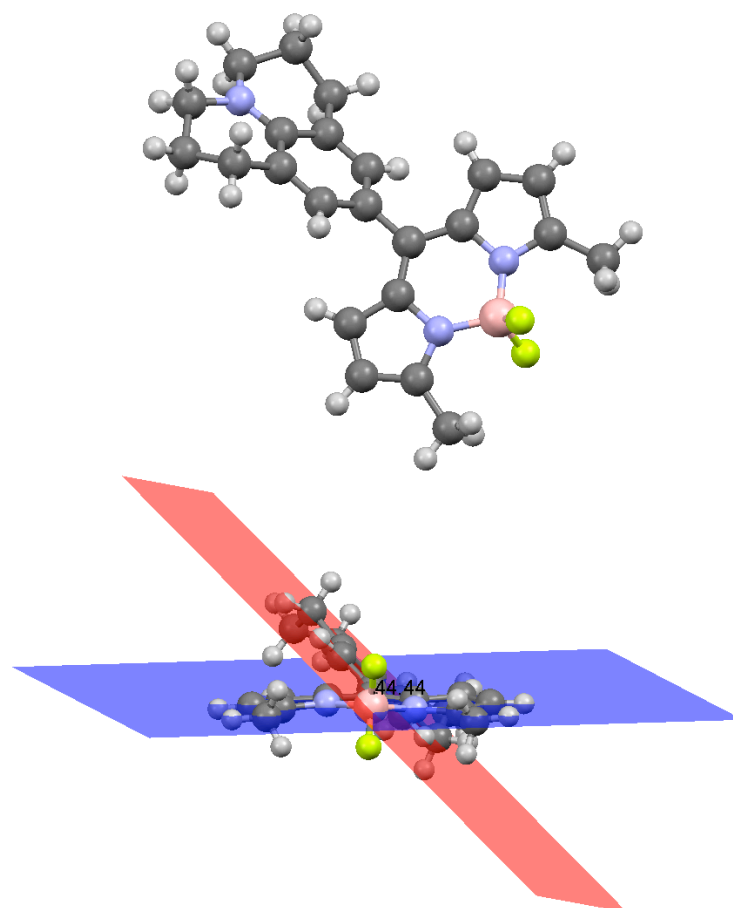


**Scheme 4.9.** Attempted double “click” reaction to produce **EBDSB**.

## 4.2.3 Molecular Structure and Orbital Calculations

### 4.2.3.1 Crystal Structure of MJULBD

Good quality single crystals of **MJULBD** was collected and the structure was proven by X-ray crystallography (Figure 4.6). The julolidine group is twisted with respect to the Bodipy by  $44^\circ$  because of unfavourable H-H steric interactions.

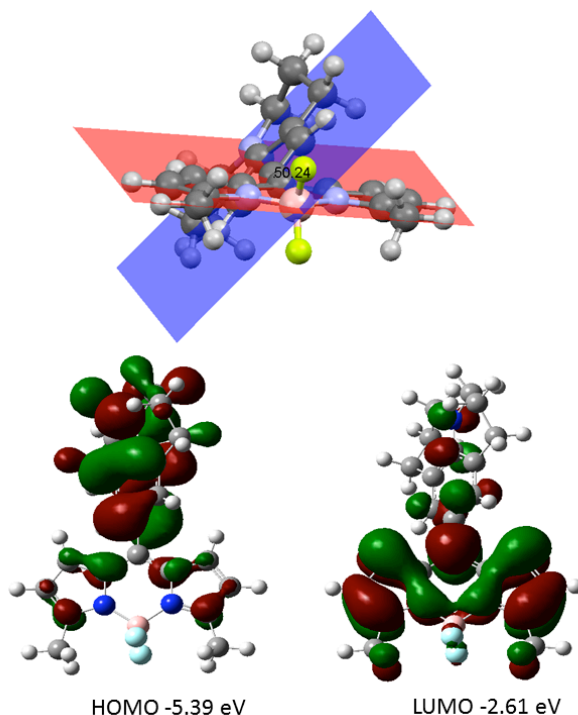


**Figure 4.6.** X-ray determined molecular structure for MJULBD (top) and the angle between planes created using the Bodipy unit and julolidine group (bottom).

A noticeable feature of **MJULBD** is the presence of two methyl groups adjacent to the  $\text{BF}_2$  unit. Considering the previous success in performing Knoevenagel condensations we attempted to react **MJULBD** with aryl-aldehyde groups. Two were chosen specifically to be highly electron withdrawing (pentafluorobenzaldehyde) and be quaternerised (4-pyridinecarboxaldehyde). The attempted condensation reactions were inconclusive since purification of the products was problematic, and  $^1\text{H}$  NMR spectra of collected products were difficult to interpret. It is possible that the two methyl groups are not as active towards the condensation reaction.

The overall computer calculated structure for **MJULBD** is very similar to the X-ray determined structure (Figure 4.7). The small difference is the angle between the julolidine and Bodipy groups which is increased to ca.  $50^\circ$ . It is

possible that packing effects reduce the angle for the X-ray structure. The HOMO is localized on the julolidine segment as would be expected since this is the electron donor. The LUMO is based on the dipyrromethene subunit and is typical for a Bodipy group. We can speculate that the HOMO-LUMO gap is representative of charge transfer.



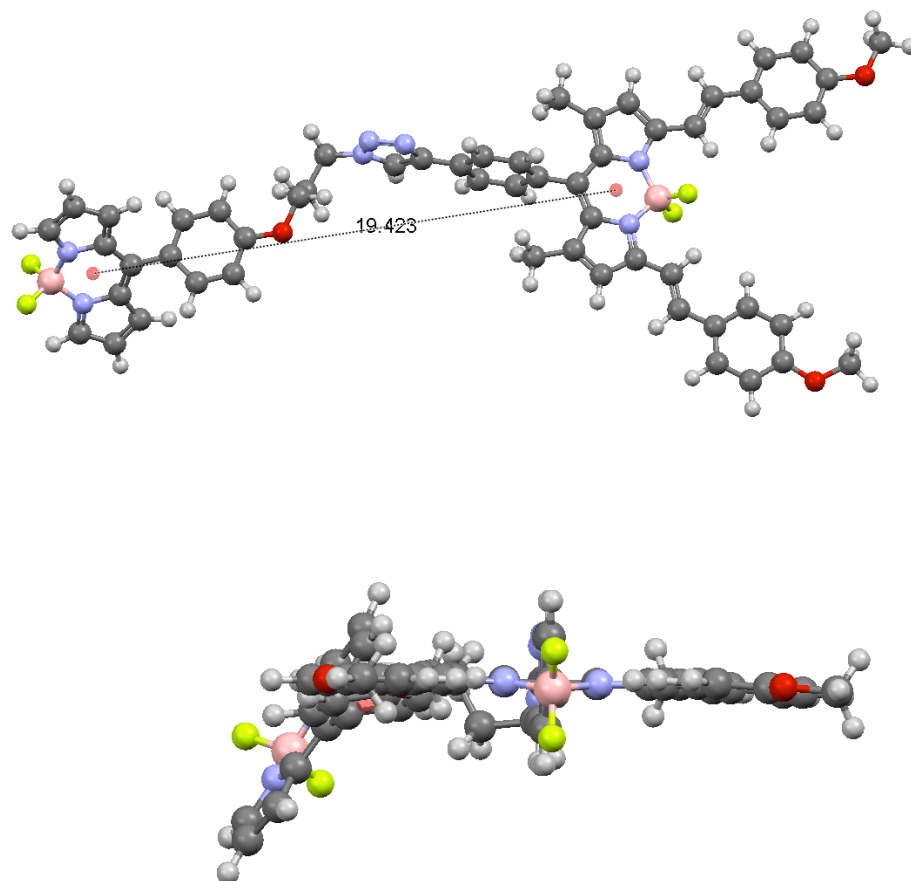
**Figure 4.7.** Top: Computed structure for MJULBD showing the twisted julolidine unit. Bottom: The HOMO and LUMO for the dyad as calculated by DFT (B3LYP) 6-311G.

#### 4.2.3.2 Red & Blue **BLRO**

Computational calculations at DFT level were performed on selected compounds using Gaussian 03. To minimise run-time the B3LYP level and 6-31G basis set was used without a solvent continuum model.

The computer calculated energy minimized structure for **BLRO** is shown in Figure 4.8, and likely represents one possible low-energy conformation because of the flexibility of the propyl spacer. The separation distance between the two Bodipy groups is around 19 Å. It is noted that the aryl-vinylene groups are almost completely co-planar with the dipyrromethene unit

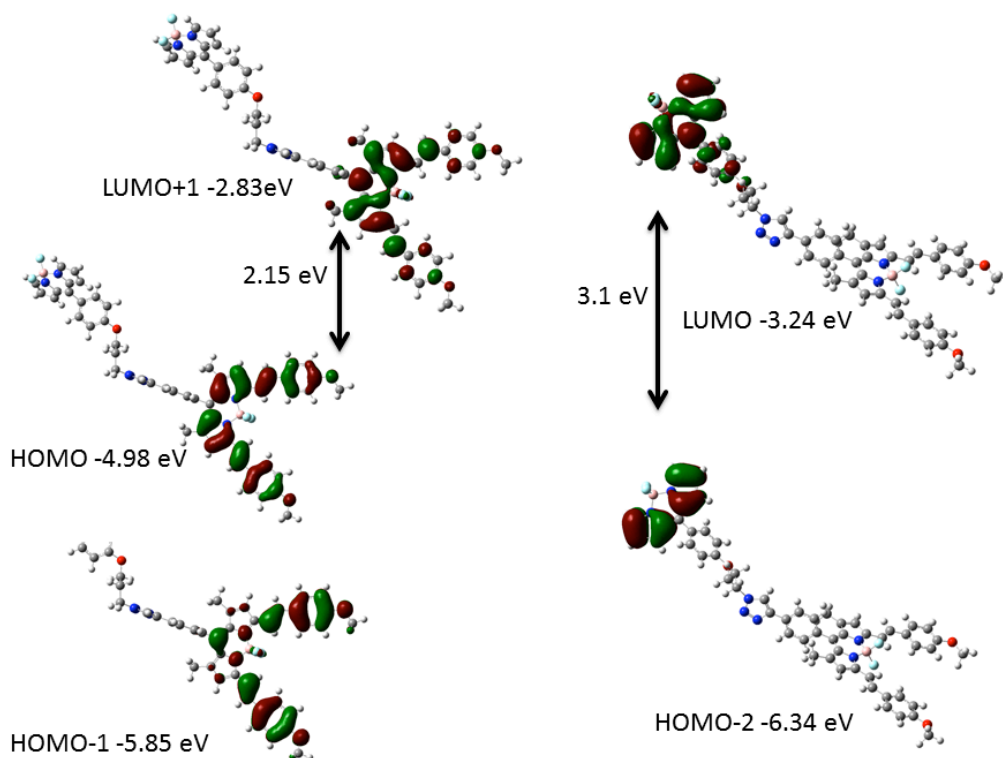
for the extended Bodipy (Figure 4.8 bottom). There is no twist in the two units which might be caused by steric interaction with the BF<sub>2</sub> group.



**Figure 4.8.** Top: Computer calculated energy minimized structure for **BLRO**. Bottom: View of **BLRO** along the extended Bodipy unit showing the planarity of the aryl-vinylene groups.

A selection of the molecular orbitals for **BLRO** are shown in Figure 4.9. The HOMO as might be expected is associated with the expanded Bodipy and extends onto the two aryl-vinylene groups. The HOMO-1 is again distributed on the expanded Bodipy and it is the HOMO-2 which is located on the rotor Bodipy. The LUMO is situated on the rotor Bodipy and it is the LUMO+1 that resides on the expanded Bodipy. We can see at a simple level that the HOMO-2 to LUMO is the electronic absorption for the rotor, and the HOMO to LUMO+1 is the electronic absorption for the expanded Bodipy. The difference in energy associated with each electronic transition is at least qualitatively in

line with the difference in colour of the two Bodipy groups (i.e., the expanded Bodipy absorbs at longer wavelength).



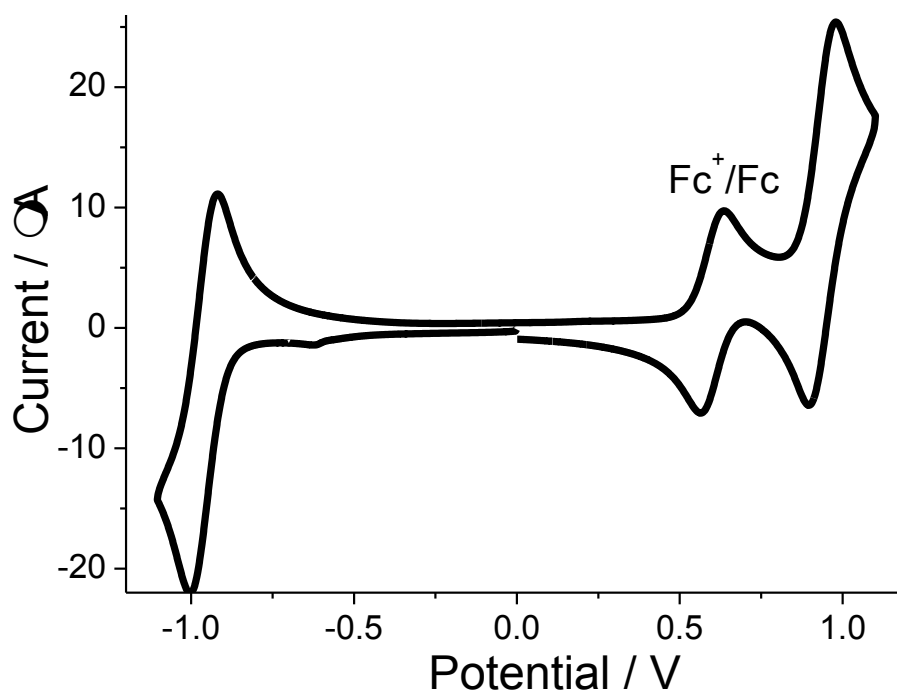
**Figure 4.9.** Selected HOMO/LUMOs for **BLRO** with arrows showing electronic transitions associated with Bodipy-based absorption.

## 4.2.4 Results and Analysis of Photophysics Measurements

### 4.2.4.1 Electrochemical and Absorption/Fluorescence Properties of MJULBD

The redox behavior for **MJULBD** was measured by cyclic voltammetry in dry DCM using 0.2 M tetrabutylammonium tetrafluoroborate (TBATFB) as background electrolyte. The cyclic voltammogram recorded using ferrocene as internal standard is shown in Figure 4.10. To the right of the ferrocene redox couple is seen a quasi-reversible wave at  $E_{1/2} = 0.33$  V ( $\Delta E = 90$  mV) vs  $\text{Fc}^+/\text{Fc}$  and is associated with redox at the julolidine site. To the left of the ferrocene redox couple is observed a quasi-reversible wave at  $E_{1/2} = -1.57$  V

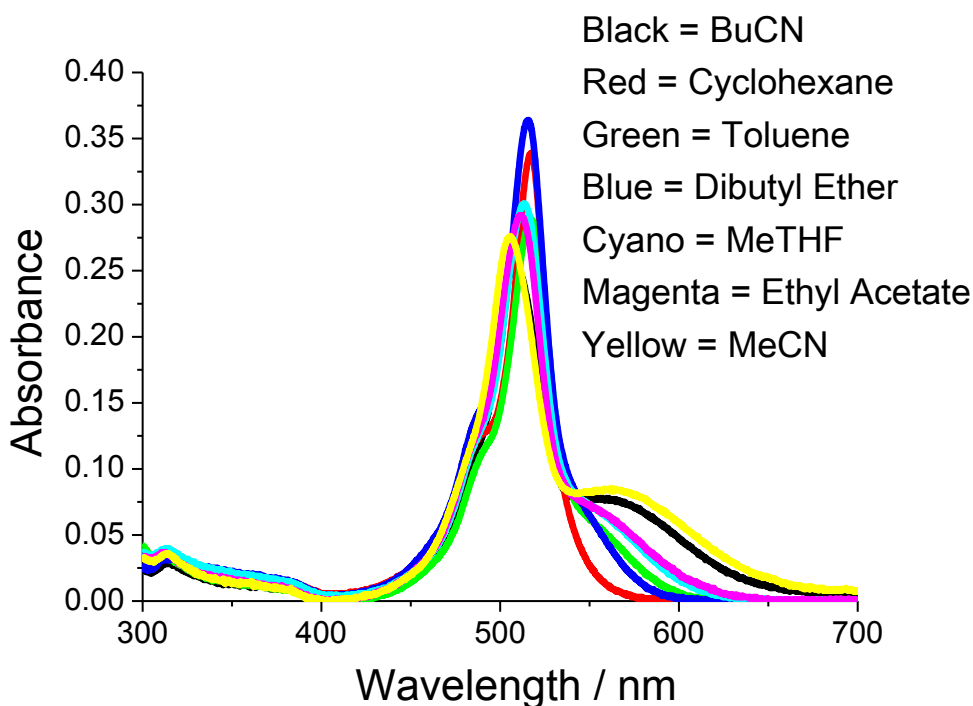
( $\Delta E = 80$  mV) vs  $\text{Fc}^+/\text{Fc}$ . This wave is Bodipy-based redox behaviour. The energy difference ( $\Delta E$ ) between the two waves corresponds to 1.90 V and can be thought of as the energy gap for charge transfer. It is noted that 1.90 V corresponds to  $15,324\text{ cm}^{-1}$  (652 nm).



**Figure 4.10.** Cyclic voltammogram for **MJULBD** in dry DCM (0.2 M TBATFB) at a glassy carbon working electrode and a platinum wire counter electrode. Scan rate =  $50\text{ mV s}^{-1}$ .

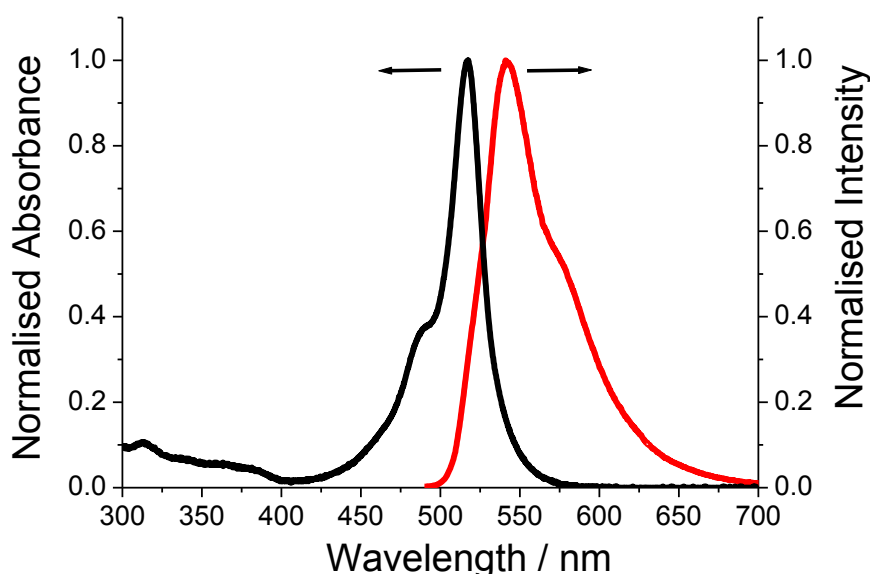
Absorption spectra for **MJULBD** collected in a range of solvents are shown in Figure 4.11. The typical  $S_0$ - $S_1$  Bodipy-based electronic absorption profile is seen at around 515 nm. Unlike a classic Bodipy there is an additional broad absorption profile at low energy. In a polar solvent such as MeCN this band is clearly visible and centred at ca. 563 nm. In the non-polar solvent cyclohexane the profile is barely seen in the spectrum. The shift in absorption maximum with solvent polarity is typical for a charge transfer band, and has been seen previously for the unmethylated version of **MJULBD**. We can see that the wavelength maximum for charge transfer ( $\lambda_{\text{CT}}$ ) does not correspond completely to the energy gap ( $\Delta E$ ) measured by cyclic voltammetry. The reason for this difference is the reorganisation energy ( $\lambda$ ) since  $\lambda_{\text{CT}} = \Delta E +$

$\lambda$ . If we assume that  $\Delta E$  does not vary greatly between DCM and MeCN then  $\lambda \sim 0.3$  eV for the latter solvent. A major contribution to  $\lambda$  is from solvent reorganisation which will be modest for a polar solvent like MeCN, but will be larger for less polar solvents which need to readjust to support the generated charges.



**Figure 4.11.** Absorption spectra for MJULBD recorded in a range of solvents of different polarity.

Strong emission is observed from **MJULBD** in non-polar solvents such as cyclohexane (Figure 4.12), but is extinguished when the polarity of the solvent is increased. The actual fluorescence spectrum shown in red is a poor mirror image of the absorption profile shown in black in Figure 4.12. The profile is considerably broader and the shoulder to the low-energy side is far more pronounced than seen for a basic Bodipy. Emission from **MJULBD** is more complicated than anticipated and more detailed studies are required to understand fully the excited state deactivation process.



**Figure 4.12.** Absorption (black) and fluorescence (red) spectra for MJULBD in dilute cyclohexane.

#### 4.2.4.2 Neural Imaging with **MJULBD**

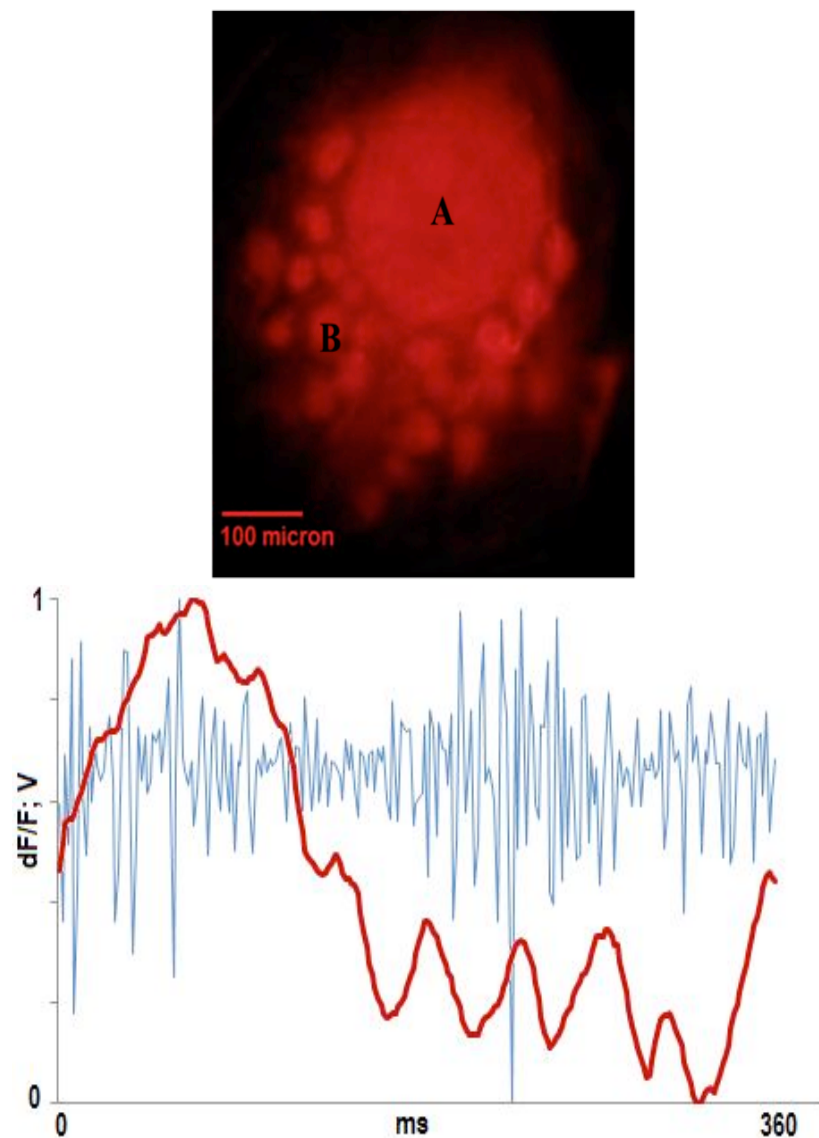
Neural imaging is widespread in diagnostics science for evaluating response of neurons towards an external electrical stimulus. Application of voltage sensitive dyes (VSDs) is universally applied as the imaging agent, with zwitterionic dyes such as di-4-ANEPPS dominating the technology. The fluorescence response of VSDs relies on the electrochromic mechanism in which charge distribution shifts within the dye upon visible light excitation. The intrinsic polar end group of a VSD acts as the electron acceptor, and the in-built amphiphilicity of the dye is believed to anchor it in the cell membrane perpendicular to the surface. This means that the molecule's electric dipole moment is parallel to the electric field vector across the membrane. The ground- and excited-state are stabilised to different extents by the intramolecular electric field, causing a shift in the fluorescence spectrum and its intensity when the membrane potential changes. The strong ground-state charge transfer and polarity dependent emission for **MJULBD** led us to believe that the dye may act as a VSD. The effectiveness of **MJULBD** for neural imaging was demonstrated using the stomatogastric nervous system of brown crabs (*C. pagarus*). *The crab STG is the preeminent model system for all motor ganglia, including human motor ganglia, and is a highly robust*



neural system, which makes it ideal for identification and characterisation of new VSDs. To record a set of experiments a stock solution was made up by dissolving around 5 mg of Bodipy dye in DMSO (1 mL) containing 20% pluronic acid. A 20  $\mu$ L sample of the stock solution was then dissolved in appropriate amount of crab saline to obtain ca.  $10^{-5}$  M,  $10^{-4}$  M and  $10^{-3}$  M dye solutions (e.g. 27 mL saline was used in the case of the **MJULBD** dye to obtain a ca.  $10^{-5}$  M dye solution). To ensure complete uptake of the dye by the neurons the stomatogastric ganglion (STG) was bathed with the Bodipy dye solution for 20 minutes. Any dye which remained unbound to the cell membranes, or did not get absorbed into the cells, was removed by washing the STG with a flowing saline solution for around 20 minutes. It is clear that following the dyeing procedure the Bodipy dye is localised mostly in the cell membrane and the inside of the STG neurons as illustrated in Figure 4.13 (top). The localisation of the lipophilic Bodipy dye in the cell membrane is not too surprising. The large dark central area (**A**) is the neuropil of the ganglion (i.e., the location of dendrites and part of axons of the neurons), whereas the smaller dark circular areas (**B**) represent the neurons of the ganglion. The darkness of the images indicates the strength of the fluorescence of the dye at the pixel's location. It is worth noting that the neurons of the crab STG are large and arranged in a crescent shape with no or little overlap between the cell bodies of the neurons.

Under normal conditions the STG produces spontaneously the pyloric neural activity rhythms, which involves 11 neurons in the crab (one AB, IC, VD and LP neuron, two PD neurons and 5 PY neurons). The overall rhythm for the STG was recorded from the lateral ventricular nerve (*lvn*). For completeness and comparison purposes a PY neuron was also recorded using an intracellular glass micro-electrode. Fluorescence imaging of the STG under pyloric neural activity rhythms was performed and the imaging data were processed using event-triggered temporal averaging. That is data corresponding to full cycles of the pyloric rhythm were averaged by matching the start times of the full cycles. The full set of results were collected by averaging imaging data extracted for several imaged neurons. The results

clearly demonstrate (Figures 4.13 bottom) that the imaging recordings match the activity of the neuron which was recorded using the intracellular electrode. In addition, the imaging data collected by optically recorded activities of several neurons match well with the cycles of the pyloric rhythm. The results show that **MJULBD** can be used to record the activity of neurons, represented by the variation of its membrane potential difference.

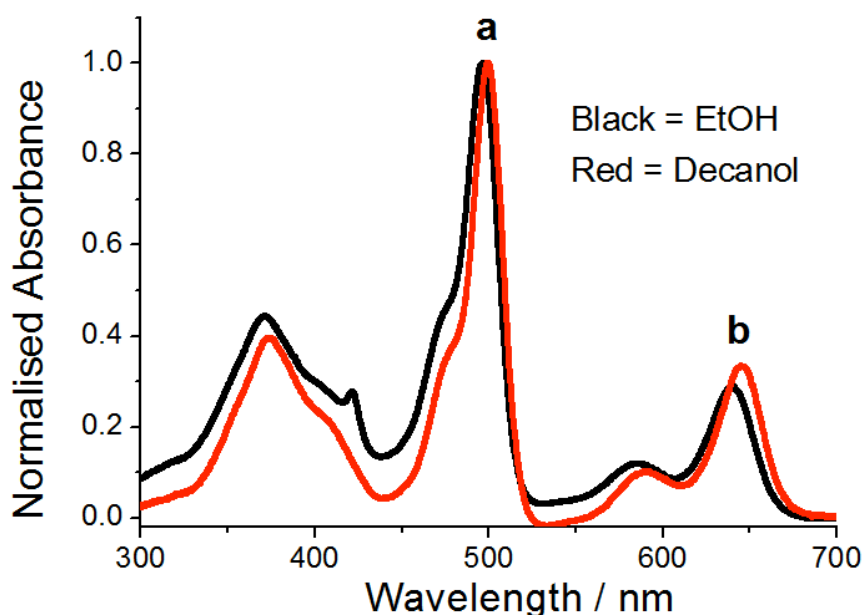


**Figure 4.13.** Top: Fluorescence image of the stomatogastric ganglion (STG) of *C. pagarus* after bathing with a **MJULBD** saline solution. A – neuropil, B – an STG neuron. Bottom: Extracellular and optical VSD recording using **MJULBD** of neural activities in the crab STG. The blue traces in the panel shows the extracellular recording of full pyloric cycle from the *lvn*. The red traces in the panel shows the VSD imaging recording of an STG neuron. All

shown recording data were calculated using event-triggered averaging as described in the paper. The units on the vertical axes are arbitrary scaled units.

#### 4.2.4.3 Absorption/Fluorescence Properties of BLRO

There are two different chromophores in the dyad **BLRO** and as expected its absorption spectrum in EtOH (Figure 4.14) displays two distinct regions marked **a** and **b**. By comparison to control compounds the region **a** is easily assigned to the electronic absorption for the rotor Bodipy. Because of the increased conjugation the region **b** is associated with the expanded Bodipy and is noticeably much less intense when compared to the main band. The other significant difference in the absorption spectrum is in the region between 300-420 nm. This region is usually devoid of a strong absorption profile but is not in the case as shown in Figure 4.15.

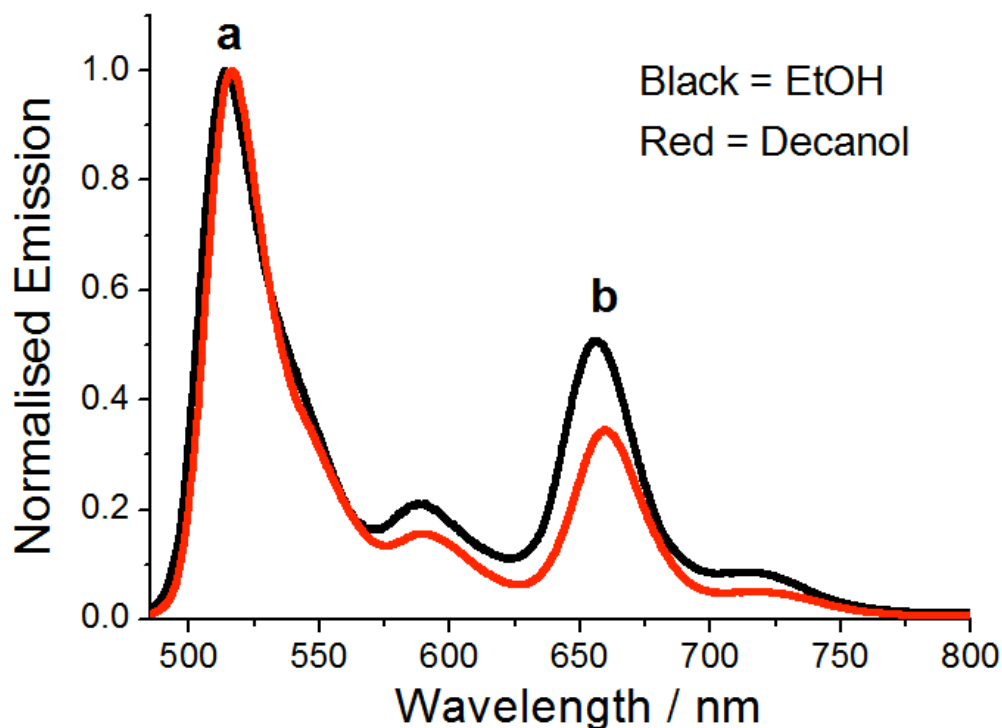


**Figure 4.14.** Room temperature absorption spectra for **BLRO** recorded in two alkanol solvents.

There is a very clear alteration in the absorption spectrum, especially region **b**, in changing the solvent to the more viscous decanol; the two bands shift to longer wavelength by about 7 nm. The small shift in wavelength maximum for region **a** is normally observed for Bodipy derivatives because of the change in

polarizability of the solvent. There is evidently more of a solvent effect on the electronic transitions for the expanded Bodipy.

Excitation of a sample of **BLRO** in EtOH at 475 nm results in emission from both the chromophores as shown in Figure 4.15. The fluorescence profile marked **a** is associated with the rotor Bodipy while region **b** is assigned to the expanded Bodipy. At the excitation wavelength it is evident from Figure 4.15 that most of the photons are absorbed by the rotor Bodipy. The dual emission would suggest that energy transfer takes place between the two chromophores in solution probably via a Förster-type mechanism. The overlap integral is reasonable since emission from the rotor does correspond to a region where the expanded Bodipy absorbs. In addition the flexible linker will allow the two chromophores to come within close proximity. The same experiment performed in the viscous solvent decanol results in dual emission but the relative height of the peaks for regions **a** and **b** is different (Figure 4.16). Less emission is seen from the expanded Bodipy. It is known that the fluorescence quantum yield for the rotor Bodipy increases with solvent viscosity. We therefore might expect to see more emission from the rotor Bodipy in decanol. The other matter to consider is the change in probability of Förster energy transfer with solvent. More detailed studies are required but the main point to note is the possibility of using ratiometric sensing of solvent properties. Considering that the chromophores in the dyad are flexibly linked the sensing of solvent flow may be conceivable. For example, if the dyad becomes more stretched out then the probability for Förster energy transfer will decrease and the ratio of **a** to **b** should change.



**Figure 4.15.** Room temperature fluorescence spectra for **BLRO** recorded in two alkanol solvents.

### 4.3 Conclusion

In this chapter the development of more complex chromophoric systems was discussed focussing mainly on expanded Bodipy derivatives. Although some of the synthetic procedures did not work as expected there is still scope to develop the chemistry using the click approach. One especially important result is the neural imaging displayed by the julolidine-based Bodipy derivative. Although several voltage sensitive dyes are known generally they are zwitterionic and sometimes require counter ions. The julolidine-Bodipy dyad is among one of the *ab initio* generations of low molecular weight neutral dyes developed for neural imaging and opens up a new sensing field for Bodipy dyes.

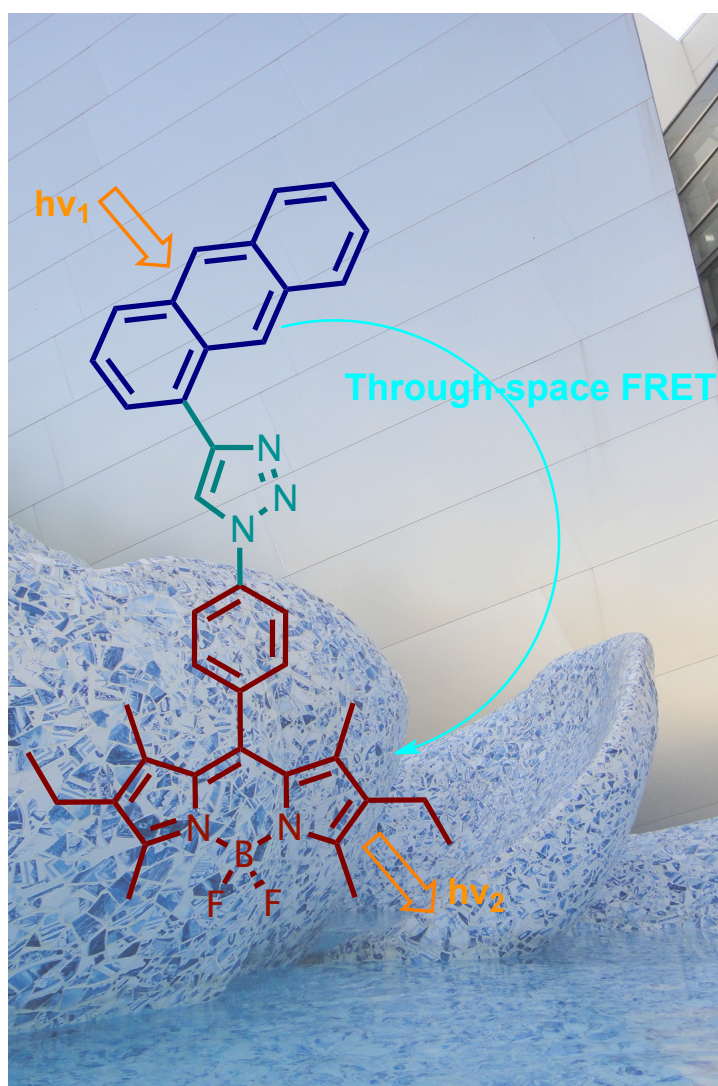
## 4.4 References

1. A. C. Benniston, G. Copley, K. J. Elliott, R. W. Harrington, W. Clegg (2008) Redox-controlled fluorescence modulation in a BODIPY-quinone dyad. *Eur. J. Org. Chem.* **16**, 2705.
2. A. Kaloudi-Chantzea, N. Karakostas, C. P. Raptopoulou, V. Psycharis, E. Saridakis, J. Griebel, R. Hermann and G. Pistolis. (2010) Coordination-driven self assembly of a brilliantly fluorescent rhomboid cavitand composed of Bodipy-dye subunits. *J. Am. Chem. Soc.*, 132 (**46**) : 16327–329.
3. M. Grossi , A. Palma , S. O. McDonnell , M. J. Hall , D. K. Rai , J. Muldoon, and D. F. O'Shea. (2012) Mechanistic insight into the formation of tetra-arylazadipyrromethenes. *J. Org. Chem.*, 77 (**20**), pp 9304–12.
4. A. Martin, C. Long, R. J. Forster and T. E. Keyes. (2012) Near IR emitting BODIPY fluorophores with mega-stokes shifts. *Chem. Commun.*, 2012, **48**, 5617-19.
5. J.-S. Lee, H. K. Kim, S. Feng, M. Vendrell and Y.-T. Chang (2011). Accelerating fluorescent sensor discovery: unbiased screening of a diversity-oriented BODIPY library. *Chem. Commun.*, **47**, 2339-41.
6. BODIPY Dye Series. Invitrogen Molecular Probes Product List.
7. S. Niu (2011) Advanced water soluble BODIPY dyes: synthesis and application. Dissertation. University of Strasbourg.
8. L. Wu, A. Loudet, R. Barhoumi, R. C. Burghardt, and K. Burgess. (2009) Fluorescent cassettes for monitoring three-component interactions in vitro and in living cells. *J. Am. Chem. Soc.* 131(**26**): 9156–57.
9. O. Galangau, C. Dumas-Verdes, R. Méallet-Renault and G. Clavier. (2010) Rational design of visible and NIR distyryl-BODIPY dyes from a novel fluorinated platform. *Org Biomol Chem.* 8(**20**): 4546-53.
10. T. Bura, P. Retailleau, G. Ulrich and R. Ziessel. (2011) Highly substituted Bodipy dyes with spectroscopic features sensitive to the environment. *J Org Chem.* 76(**4**):1109-17..
11. A. Eggenspillier, A. Takai, M. E. El-Khouly. (2012) Synthesis and photodynamics of fluorescent blue BODIPY-porphyrin tweezers linked by triazole rings. *J. Phys. Chem. A.*, 116 (**15**): 889–98.
12. S. Erbas, A. Gorgulub, M. Kocakusakogullaric and E. U. Akkaya (2009) Non-covalent functionalized SWNTs as delivery agents for novel Bodipy-based potential PDT sensitizers. *Chem. Commun.*, 4956-58.

13. D. Tuncel, Ö. Ünal and M. Artar (2011) Supramolecular Assemblies Constructed by Cucurbituril-Catalyzed Click Reaction. *Isr. J. Chem.* 51:(**5-6**) 525–32.
14. M. Munteanu (2009) Supramolecular Chemistry with Cyclodextrin Containing Polymers: Click Chemistry, Structures and Properties. Dissertation. Heinrich-Heine-Universität, Düsseldorf.

## Chapter 5

### Energy Transfer in Closely Spaced Dyads

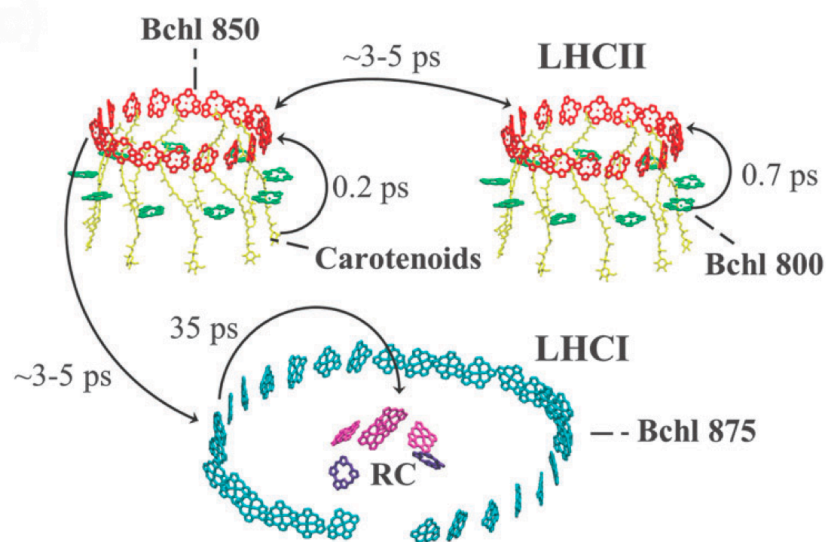




## 5.1 Background and Molecular Design Principle

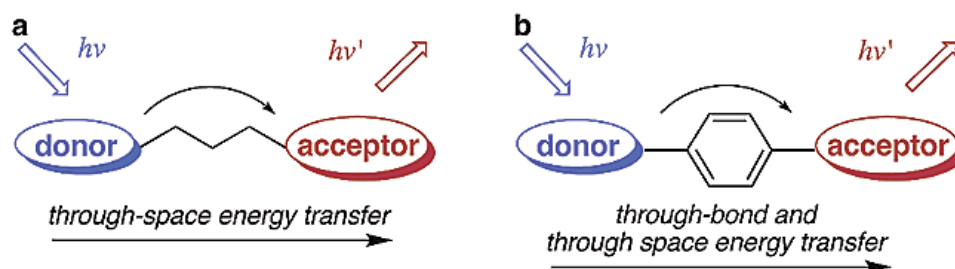
### 5.1.1 Through-Bond & Through-Space Energy Transfer

Nature accomplishes the essential task of photosynthesis using light-harvesting complexes (LHC) to collect incident photons, move them over large distances and direct them to a light harvesting reaction centre (LH1-RC) - a site the chemistry take place, where charge separation happens and the in-situ generation of a proton gradient across the membrane takes place. Nature opted to transfer excitation energy between weakly coupled chromophores via the mechanism of Förster resonance energy transfer (FRET), which involves through-space interactions between the antennae and the reaction centre. Both intra- and inter-complex FRET from the LHCII to the LHCI site takes place, complementary to the through-bond electron exchange interactions that occur within the reaction centre (i.e., excitonic coupling between the affiliated proteins within the LHCI). The proton gradient is then collected to accomplish the synthesis of adenosine-5'-triphosphate (ATP) in order to complete the photosynthetic conversion of solar energy into chemically stored energy.<sup>1</sup>



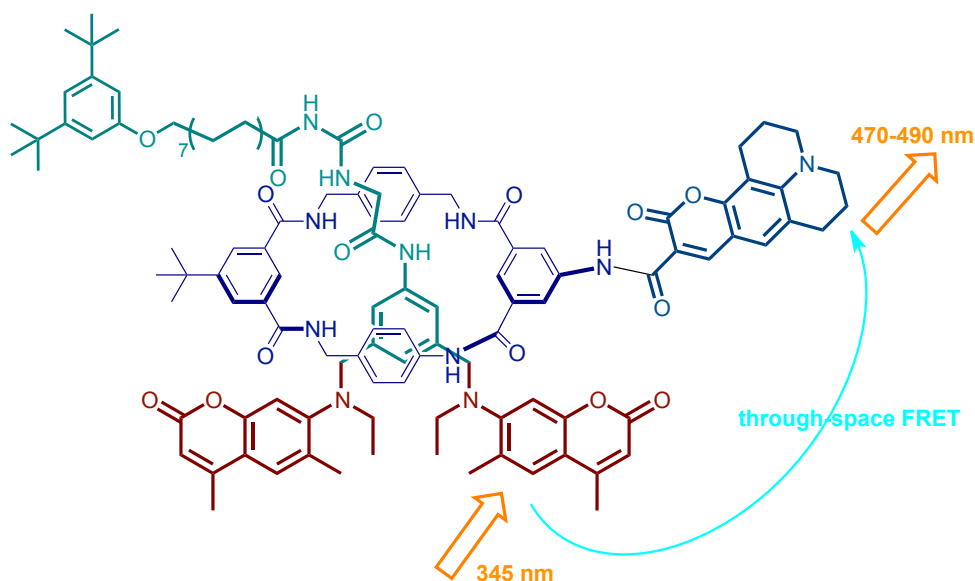
**Figure 5.1 .** Summary of the energy transfer dynamics and time scales within the photosynthetic purple non-sulfur bacteria LHC II and the reaction center (green = Bchl 800, red = Bchl 850, yellow = carotenoids, cyan = Bchl 875, purple = reaction center Bchl 870, violet = reaction center BPheo).<sup>2</sup>

The pathways of excitation energy redistribution can be investigated via an artificial assembly (Figure 5.2).

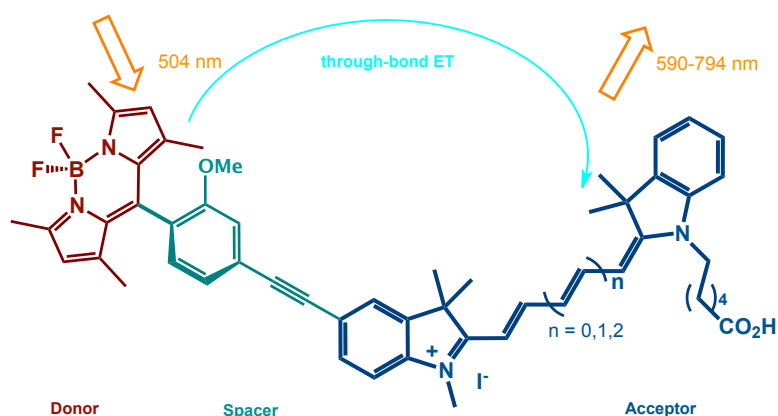


**Figure 5.2.** Cartoon representation of a donor-acceptor assembly. Image Courtesy of K Burgess<sup>3</sup>

In order to achieve efficient FRET within molecular systems a sufficiently large spectral overlap is necessary between the donor emission and the acceptor absorption. For practical purposes this can limit the resolution of double-channel images in microscopy. No such problem is seen for a through-bond energy transfer (TBET) system, since energy transfer does not need spectral overlap between the donor and acceptor. The two examples shown in Figure 5.3 and Figure 5.4 represent molecular systems designed and built to study energy transfer. In the rotaxane-based assembly shown in Figure 3 the donor and acceptor are separated. In this case FRET operates via through-space Coulombic interactions. For the Bodipy-cyanine conjugate shown in Figure 5.4 the two units are connected via a conjugated bridge. Excitation energy collected at the Bodipy unit is transferred to the cyanine via orbitals of the aryl group and triple bond.<sup>4-5</sup>



**Figure 5.3.** A molecular rotaxane-based assembly where FRET is the mechanism for energy transfer.

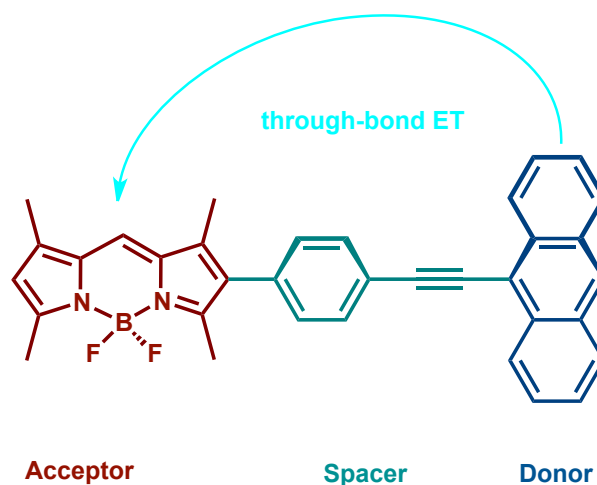


**Figure 5.4.** A molecular system for which through-bond energy transfer is the mechanism.

### 5.1.2 The Alignment of Dipole Moments and FRET Efficiency

A detailed discussion of Förster energy transfer was given in the Introduction, but one key factor is the alignment of the dipoles on the donor and acceptor. In the molecular system shown in Figure 5.5 the anthracene is connected to the Bodipy group via a conjugated spacer. The transition dipoles on both the Bodipy and anthracene units are long-axis polarised. Hence the two dipoles

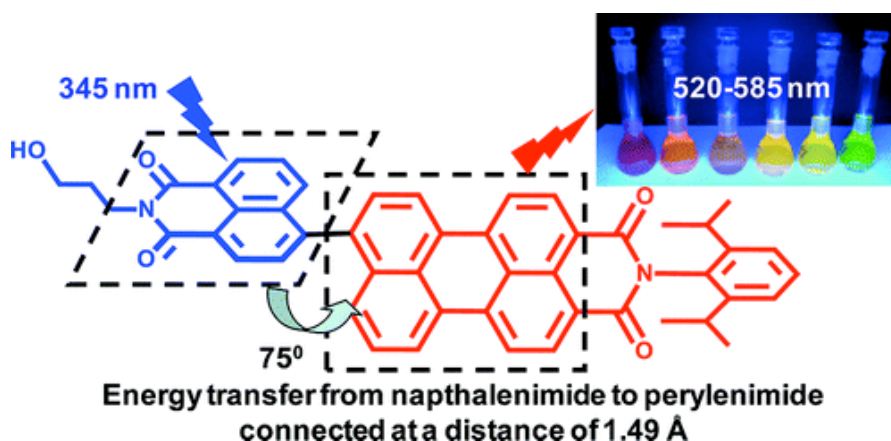
are orthogonal and not conducive for efficient Förster-type energy transfer.<sup>1</sup> The conjugation between the donor and acceptor is adequate to promote through-bond energy transfer. Clearly, an ideal system to study purely Förster energy transfer would not contain  $\pi$ -conjugation.



**Figure 5.5.** Example of a donor-acceptor Bodipy-anthracene dyad.<sup>6</sup>

It should be noted that dual electron transfer can also take place between connected groups via non-covalent bonds, such as metal-ligand coordinate bonds, a hydrogen bond interface and between components which were linked because of hydrophobic or aromatic stacking interactions.<sup>7</sup>

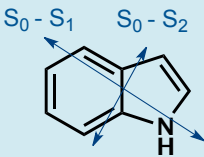
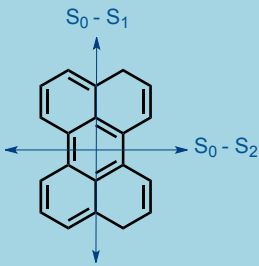
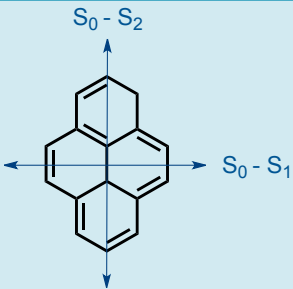
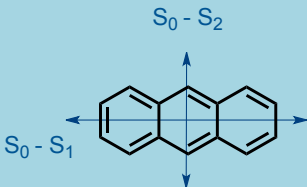
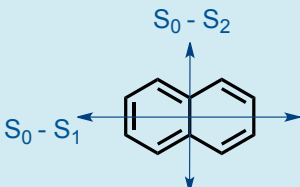
The molecular dyad shown in Figure 5.6 is an interesting example where energy transfer does not occur in the planar and fully conjugated state. Within the conjugated system only when the donor-acceptor fragments are in an orthogonal geometry can the system act as an energy-transfer cassette.



**Figure 5.6.** A near orthogonally arranged donor-acceptor dyad.<sup>8</sup>

Prior knowledge of the electronic transition dipoles for chromophores can be extremely important in the design of molecular systems for studying energy transfer. Listed in Table 1 are a selection of organic chromophores showing both the  $S_0$ - $S_1$  and  $S_0$ - $S_2$  transition directions. Generally emission is observed from the lowest vibrational level of the  $S_1$  state in line with Kasha's rule. However, depending on the chromophore it is possible that the Förster overlap may involve higher singlet excited states such as  $S_2$ . For example, in Bodipy the  $S_0$ - $S_2$  electronic transition is situated between 350-400 nm and the absorption profile is broad and not as intense as the  $S_0$ - $S_1$  band. A donor chromophore which emits in the 350-400 nm range will likely overlap better with the  $S_0$ - $S_2$  state. This is not a problem since the collapse of  $S_2$  to  $S_1$  is extremely fast ( $\sim 100$  fs) and so emission is still observed from the Bodipy unit.

<b>Rhodamine 6G</b>	
<b>Coumarin 500</b>	

<b>Indole</b>	
<b>Perylene</b>	
<b>Pyrene</b>	
<b>Anthracene</b>	
<b>Naphthalene</b>	

**Table 5.1** Polycyclic aromatic hydrocarbons (PAH) compounds and their transition dipole moments (indicated with a blue arrow).<sup>9</sup>

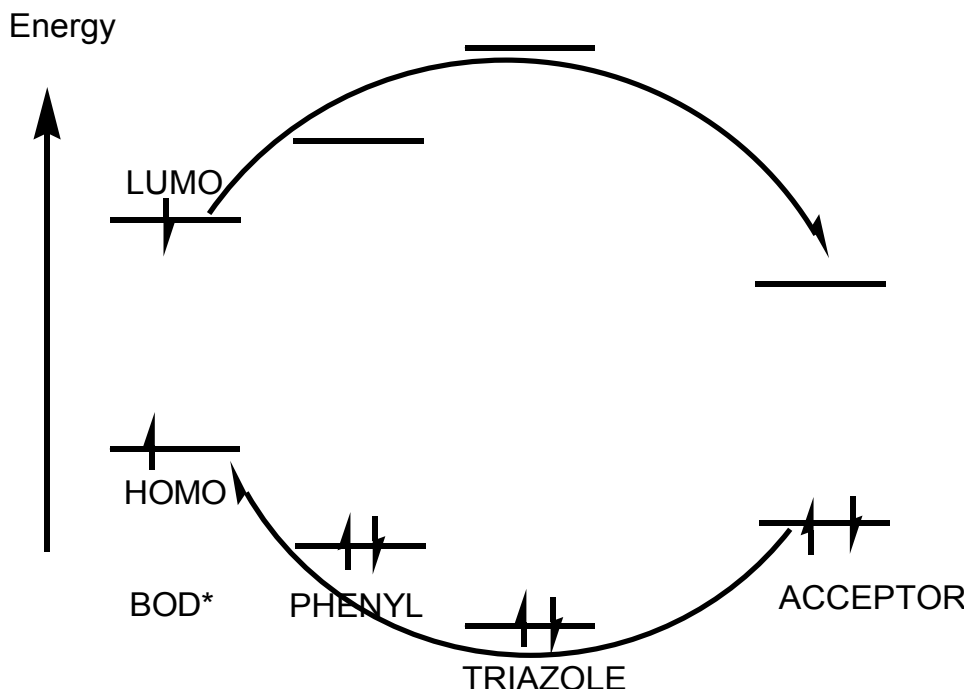
The basic photophysical properties of chromophores are important and listed in Table 2 are a few examples, focusing mainly on compounds used in our studies. With increasing the number of aromatic rings moving from naphthalene to pyrene the absorption spectrum changes and shifts more to the red end of the visible spectrum. In addition the fluorescence profile is red shifted. Therefore, we can expect the Förster overlap with the Bodipy chromophore to change significantly.

Compound	Solvent (temperature)	$\Phi_F$	$\Phi_{ISC}$	$\tau_s$ (ns)	$\tau_T$ (s)
Naphthalene	Ethanol (293 K)	0.21	0.79	2.7	
	Cyclohexane (293 K)	0.19		96	
	EPA (77 K)			0.06	2.6
Anthracene	Ethanol (293 K)	0.30	0.72		
	Cyclohexane (293 K)	0.30			0.09
	EPA (77 K)				
Pyrene	Ethanol (293 K)	0.65	0.38	475	
	Cyclohexane (293 K)	0.65		450	

**Table 5.2.** Selected photophysical properties of some key chromophores used in studies. Note: EPA is a mixture of ethanol, isopentane, diethyl ether<sup>9</sup>

We can expect Förster energy transfer from naphthalene, anthracene and pyrene to Bodipy, and there are literature examples where this has been observed. As discussed previously one problem often encountered is through-bond energy transfer and separating its contribution from an overall process can be problematic. We attempted to solve the problem by trying to identify an appropriate inert “linker” to separate the two chromophore units. Structural rigidity was still required in the final molecular dyad, since a flexible system would allow the two groups to come into close contact. For these two reasons we chose the triazole group. The main argument for its inclusion was the poor availability of orbitals on the unit to promote through-bond electron exchange as illustrated in Figure 7. The triazole absorbs in the UV-region and so the HOMO-LUMO gap is relatively large making electron transfer via the LUMO energetically unfavourable. The same argument can be used for

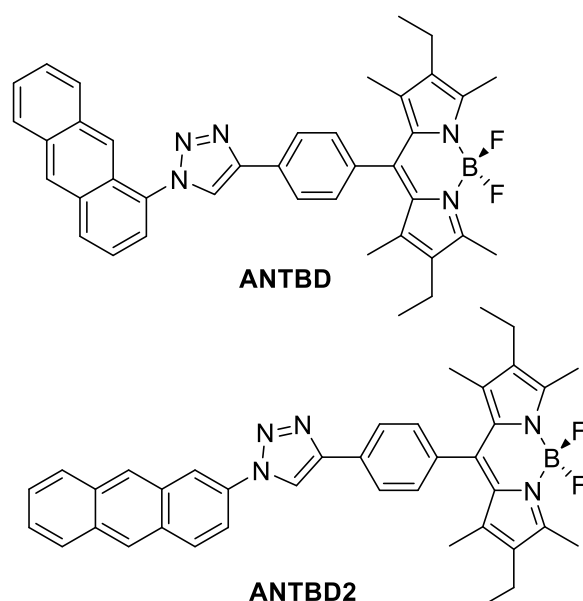
involvement of the HOMOs.



**Figure 5.7.** Picture showing the dual electron exchange mechanism and the role of the bridging orbitals in promoting the process.

Combining all the design features afforded the two dyads **ANTBD** and **ANTBD2** as shown in Figure 5.8. By using anthracene the added advantage was it allowed alteration of the attachment site to the Bodipy framework. There is a change in the orientation of the transition dipoles by moving the connection point.





**Figure 5.8.** The two anthracene-Bodipy dyads designed to study Förster energy transfer.

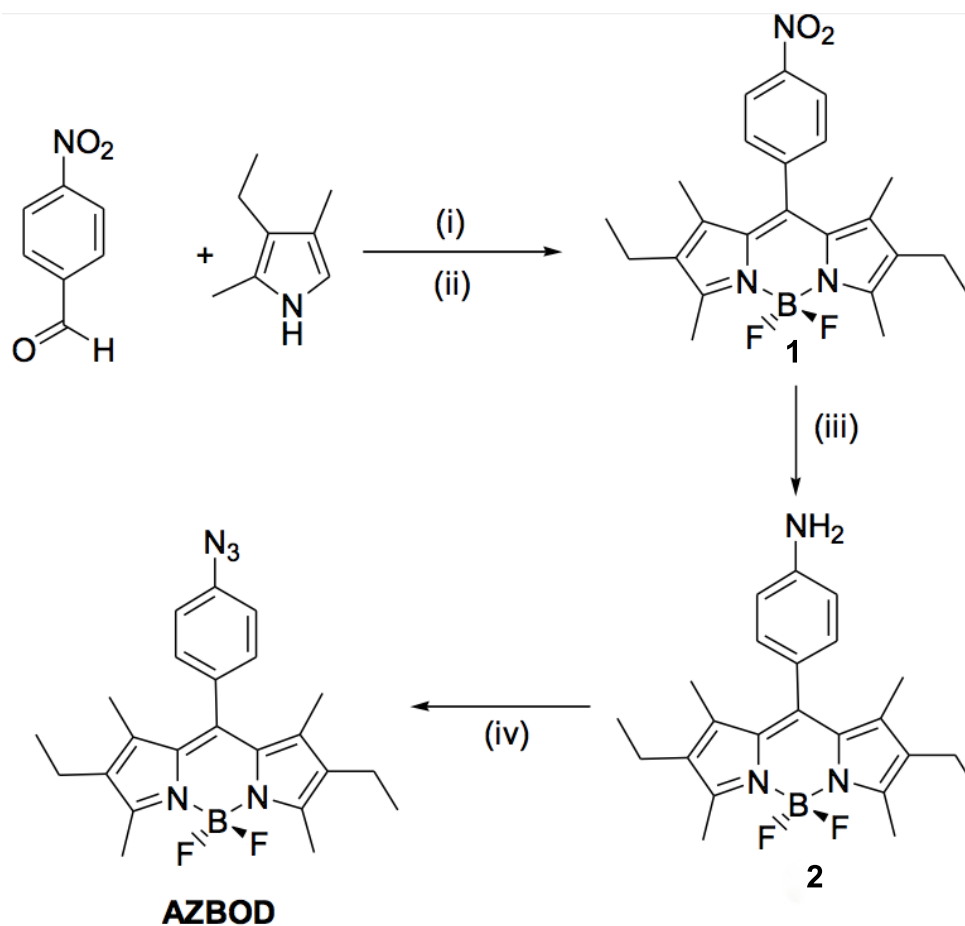
## 5.2 Results and Discussion

### 5.2.1 Synthesis of Precursor Compounds

#### 5.2.1.1 Preparation of 8(4-Azidephenyl)-Bodipy (AZBOD)

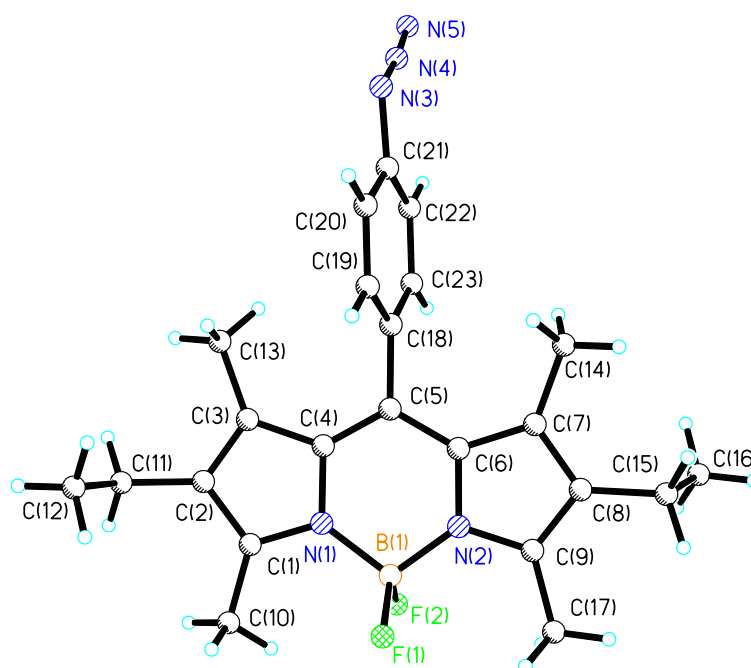
Synthetic methods for preparation of Bodipy-based compounds are well established, and many examples can be found in the literature and several reviews. The basic approach relies on the condensation of an appropriate aldehyde with a suitable pyrrole derivative to form the intermediate dipyrromethane (Scheme 1), which is oxidized and chelated to the  $\text{BF}_2$  moiety. The  $\text{BF}_2$  unit acts to stop any rotation of the dipyrromethene unit and maintain planarity of the molecule. This is particularly important since this structural rigidity means that the molecule is highly fluorescent. The basic procedure mentioned to prepare the starting material are shown in Scheme 1. A key point to note is that a substituted pyrrole was specifically chosen since the methyl substituents restrict rotation of the aromatic groups attached at the 8-position,

and the resultant orthogonal geometry serves to minimize electronic coupling between the dye and the meso-substituent. The first target molecule was the azide functionalised Bodipy compound, **AZBOD**, since this would be the precursor for carrying out 'click' reactions. The initial part of the synthesis involved the preparation of the compound 8-(4-nitrophenyl)Bodipy by condensation of 4-nitrobenzaldehyde with commercially available 3-ethyl-2,4-dimethyl-1*H*-pyrrole, oxidation and chelation to the BF<sub>2</sub> group. This reaction proceeded smoothly to afford 8-(4-nitrophenyl)Bodipy **1** in 32% yield. Reduction of the nitro group via hydrogen gas flow over a Pd/C catalyst afforded the compound 8-(4-aminophenyl)Bodipy **2** in an average yield (57%). Conversion of the aromatic-amino group to the azide moiety was rarely reported in literature at the time when this reaction was conceived; most literature reported the method of diazotization and reaction with sodium azide in water which usually gave very low yields of the target compound. The low yield in the case may be due to the rather poor solubility of 8-(4-aminophenyl)Bodipy in water at low temperature. The alternative procedure was to carry out the reaction in anhydrous CH<sub>3</sub>CN and use <sup>t</sup>BuNO<sub>2</sub> with TMSN<sub>3</sub>. This procedure which worked in a better yield (28%) to afford **AZBOD** as a red with green tint crystalline solid which was analysed by <sup>1</sup>H, <sup>13</sup>C, <sup>19</sup>B and <sup>11</sup>F NMR spectroscopy.



**Scheme 5.1.** Reagents and Conditions: (i) DCM, TFA, RT, (ii) DDQ, N.N-diisopropylethylamine,  $\text{BF}_3 \cdot \text{Et}_2\text{O}$ , (iii)  $\text{H}_2$  Pd/C, RT, (iv)  $\text{CH}_3\text{CN}$ ,  $-20^\circ\text{C}$ ,  $^t\text{BuNO}_2$ ,  $\text{TMSN}_3$  ( $-20^\circ\text{C}$  for 18 hr then  $0^\circ\text{C}$  24 hr).

Crystals of **AZBOD** were of suitably good quality to collect X-ray data and solve the structure as shown in Figure 9. A selection of bond lengths and angles are collected in Table 3. The phenyl ring connected at the 8-position of the Bodipy is almost orthogonal because of steric interactions with carbons C13 and C14. The azide unit is as expected linear; the N3-N4-N5 bond angle is  $172.5^\circ$



**Figure 5.9.** Molecular structure of **AZBOD** showing the azide moiety labelled in blue (N3 to N5) (structure determined by Dr Ross Harrington).

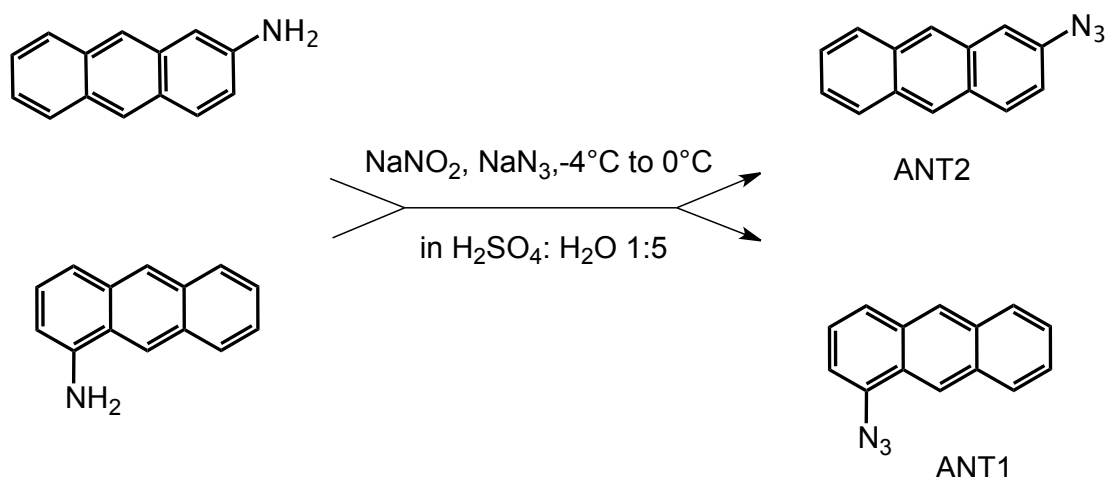
Bond Length / Å		Bond Length / Å	
<b>B1-N1</b>	1.542	<b>B1-N2</b>	1.530
<b>B1-F1</b>	1.387	<b>B1-F2</b>	1.392
<b>N3-N4</b>	1.233	<b>N4-N5</b>	1.145
<b>N1-C1</b>	1.357	<b>N1-C4</b>	1.396
<b>N2-C6</b>	1.395	<b>N2-C9</b>	1.369
<b>N3-C21</b>	1.427		
Bond Length / °		Bond Length / °	
<b>N1-B1-N2</b>	106.4	<b>N2-B1-F1</b>	110.8
<b>N2-B1-F2</b>	110.9	<b>N1-B1-F1</b>	110.3
<b>N1-B1-F2</b>	109.7	<b>F1-B1-F2</b>	108.7
<b>N3-N4-N5</b>	172.5		

**Table 5.3.** Selected bond lengths and angles for AZBOD.

#### 5.2.1.2 Preparation of azide activated anthracene compounds

The azide-activated anthracene compounds were prepared from 1-amino and 2-amino anthracene and the reactions were quite straightforward (Scheme 2)

Note that the reaction was kept between 0-4°C at all time and the saturated NaN<sub>3</sub> aqueous solution was added dropwise slowly to minimize the appearance of a foam which indicated occurrence of a side reaction. The ochre coloured crystals were collected in yields of 27% (**ANT1**) and 73% (**ANT2**) The FT-IR (solid) confirmed presence of the azide moiety by appearance of moderately strong bands at 2112 cm<sup>-1</sup> and 2110 cm<sup>-1</sup> respectively.

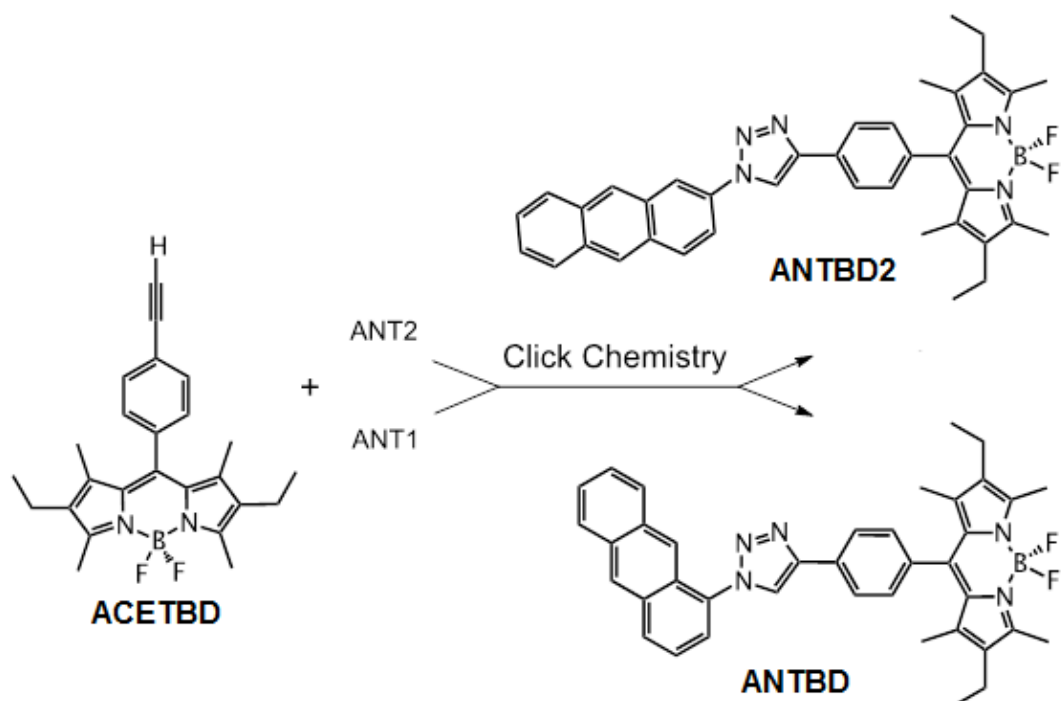


**Scheme 5.2.** Method used in the preparation of the azide derivatives of anthracene from the amino derivatives.

## 5.2.2 Synthesis and Characterisation of Electronically

### Decoupled Dyad Systems

The procedure used in the preparation of the two anthracene-based molecular dyads is shown in Scheme 3. The triazole unit is used to couple together the Bodipy and anthracene groups using “click” chemistry. The acetylene derived Bodipy derivative **ACETBD** was prepared according to the literature method by firstly palladium catalysed cross-coupling of 8-(4-bromophenyl)-Bodipy with ethynyltrimethylsilane. Deprotection of the silyl group produced the desired compound in 91% yield as a red crystalline material. The compounds **ANTBD** and **ANTBD2** were synthesised via the standard protocol of “click chemistry” as red solids in 73% and 56% yields, respectively.



**Scheme 5.3.** Synthetic route to the anthracene-based dyads using click chemistry to introduce the triazole group.

The two dyads could be crystallised and single crystals for **ANTBD** were of good enough quality to collect X-ray data. The fully refined structure is shown in Figure 10 along with the atomic numbering scheme. In the crystalline phase the main long-axis for the anthracenyl subunit lies almost parallel to the similar axis for the Bodipy unit. The separation of the anthracenyl and Bodipy groups as measured by the centroid-to-centroid distance along the connector axis is 11.96Å. In accord with similar structures the phenylene ring connected is nearly orthogonal to the Bodipy (dihedral angle = 87.6°). The triazole ring is slightly askew with respect to the phenylene ring; the dihedral angle is 22.8° as defined by the planes constructed using the two rings. Viewed side-on the overall structure is slightly bowed mainly because of constraints imposed by the five-membered triazole ring. It is of course conceivable that crystal-packing effects contribute to structural features, and indeed the crystal packing diagram (Figure 11) does show close contact between two asymmetric units

via an athracenyl hydrogen and a BF<sub>2</sub> subunit.

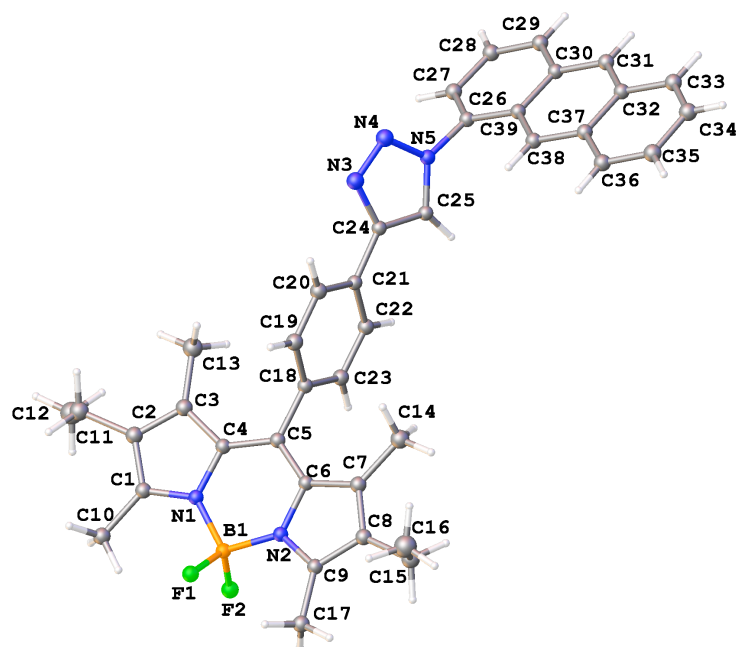
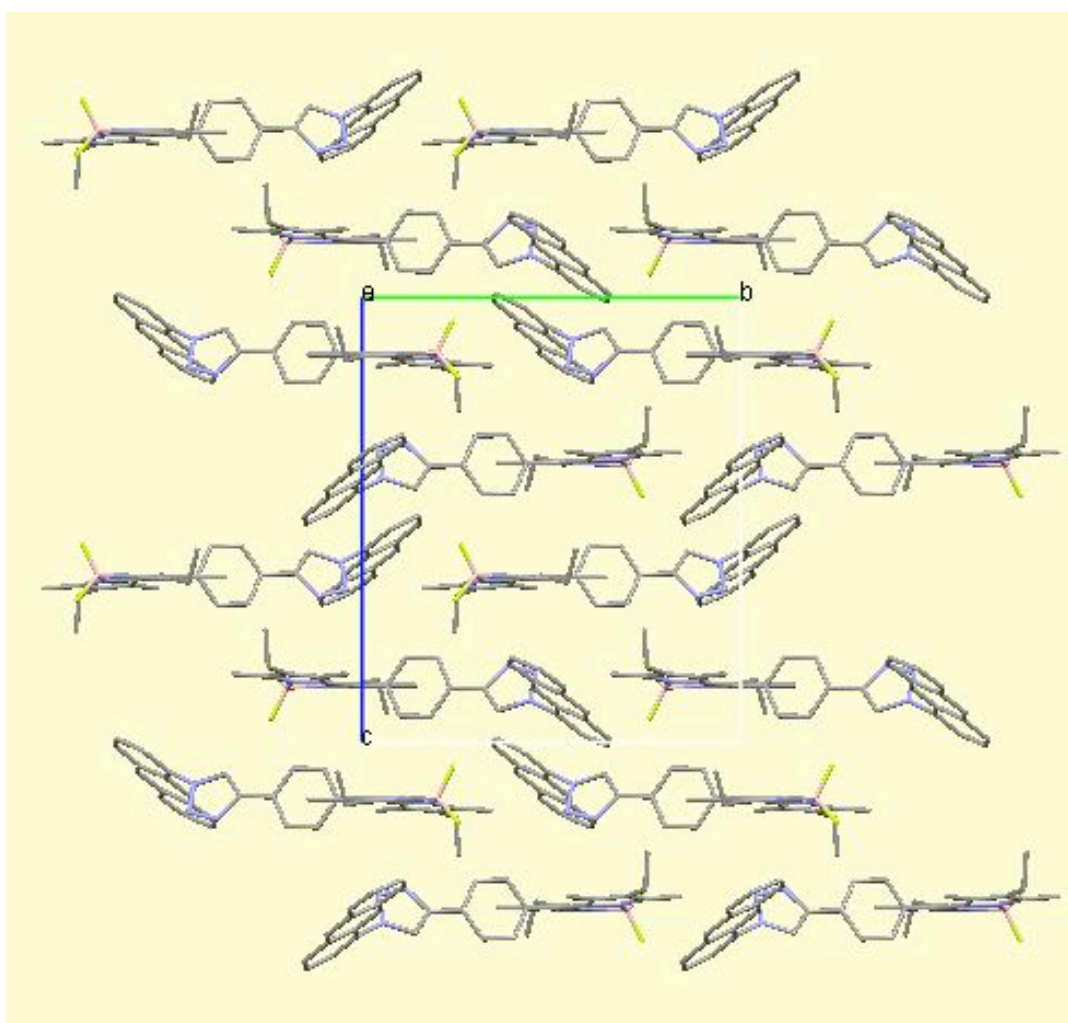


Figure 5.10. X-ray determined molecular structure for ANTBD showing the atomic numbering scheme.

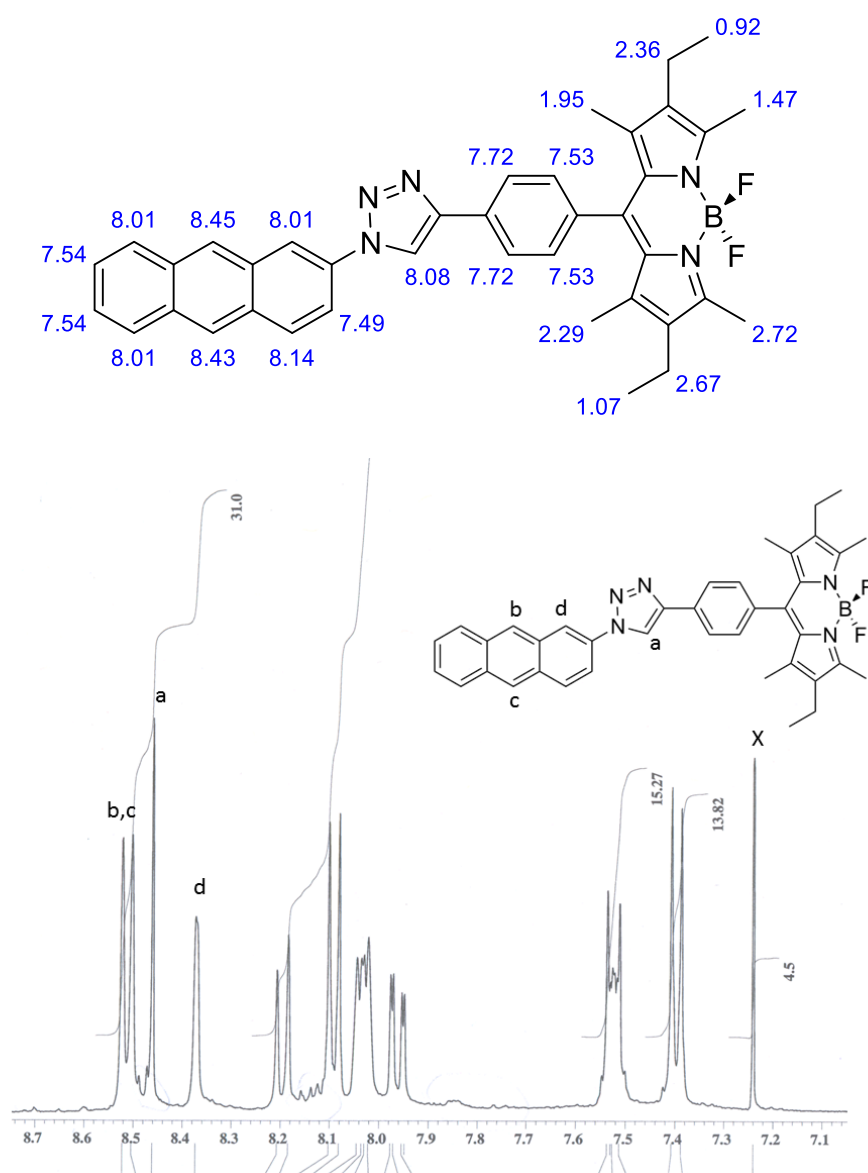


**Figure 5.11.** Crystal packing diagram for **ANTBD** in which pairwise stacking of anthracene units and a close approach of triazole CH to an F atom can be seen. H atoms are omitted for clarity; the view is down the a axis.

Unfortunately crystals for **ANTBD2** were not of suitable quality for X-ray studies. The  $^1\text{H}$  NMR spectrum for the compound (Figure 12) in the aromatic region confirmed the presence of the anthracene, triazole and phenyl ring attached to the Bodipy. Using a  $^1\text{H}$  NMR chemical shift prediction it is possible to make partial assignments for aromatic protons in the spectrum. For example,



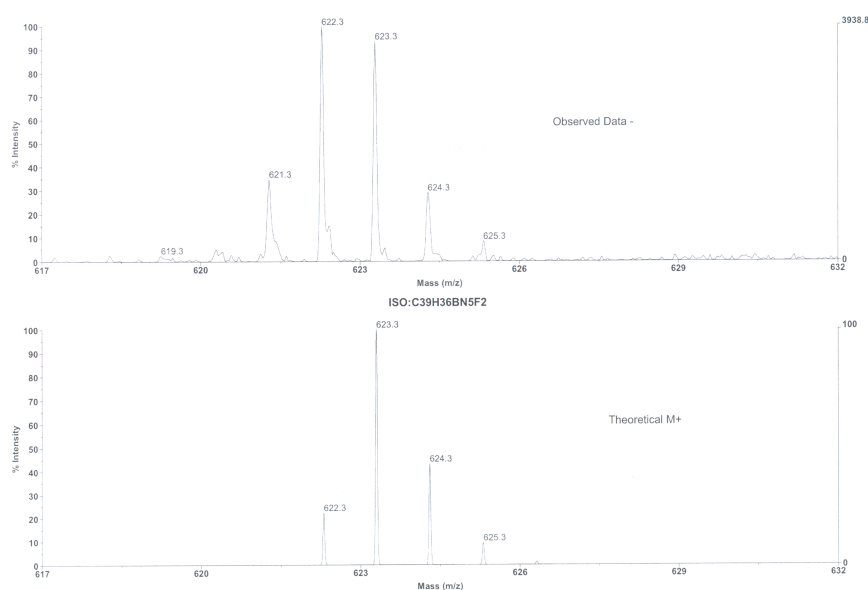
the singlet resonance observed at  $\delta = 8.46$  is typical for the single hydrogen of the triazole group. The two most downfield resonances are two singlets for protons *b* and *c*. The other singlet is likely to be for proton *d*. Proton resonances corresponding to the methyl and ethyl groups attached to the Bodipy were also observed more upfield. The  $^{11}\text{B}$  NMR spectrum consisted of a triplet at  $\delta = -0.1326$  ppm because of coupling to the two identical fluorine atoms.



**Figure 5.12.** Top: Prediction of proton chemical shifts for **ANTBD2** using ChemDraw Ultra. Bottom: Room temperature  $^1\text{H}$  NMR spectrum for **ANTBD2** in  $\text{CDCl}_3$ , showing the aromatic region only and partial assignments. X =

solvent.

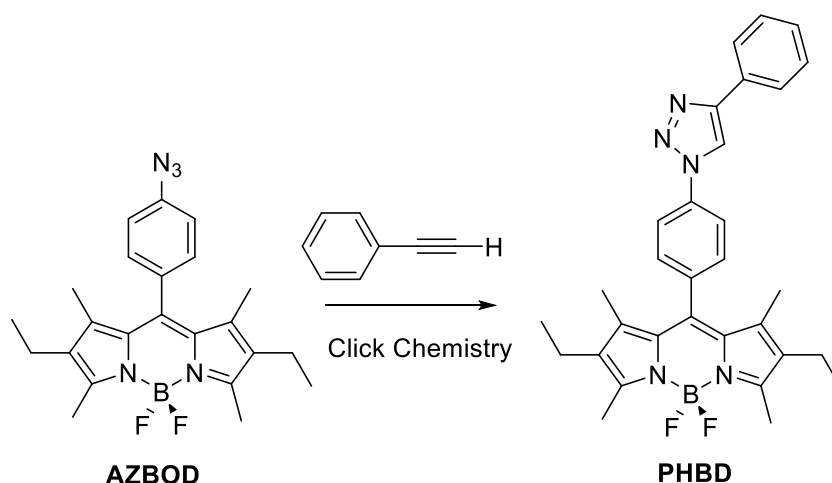
A slightly peculiar result was the mass spectrum of **ANTBD2** which consisted of a cluster of peaks at  $m/z = 622$  (Figure 13). From the molecular formula the molecular mass is 623 and the isotope pattern is somewhat similar to the observed data. It would appear that the  $[M-H]^+$  ion is observed.



**Figure 5.13.** Observed and theoretical mass spectrum for **ANTBD2** revealing the  $[M-H]^+$  molecular ion.

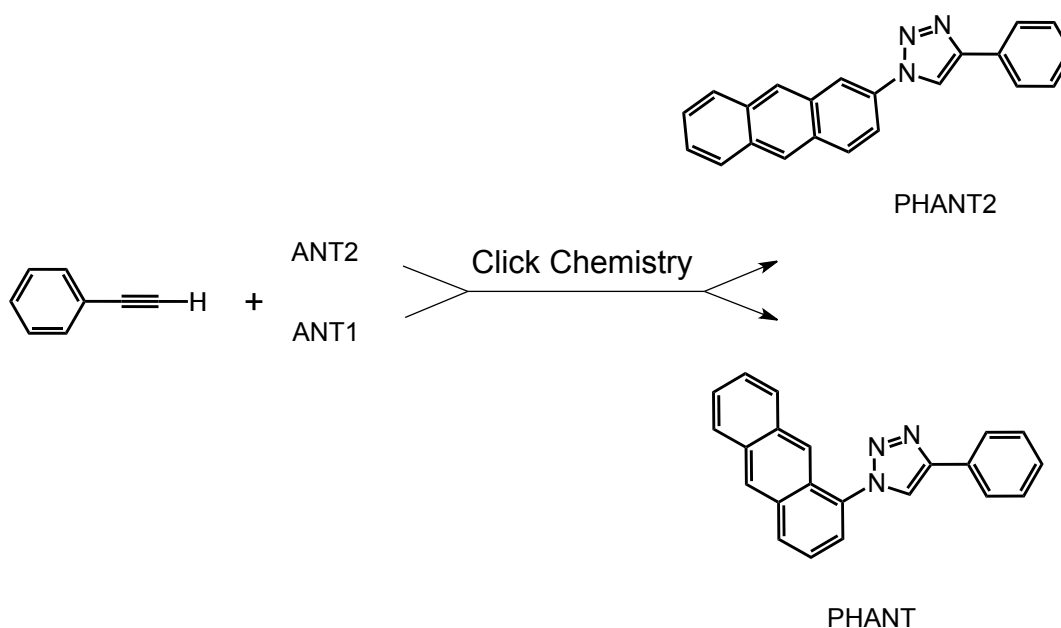
### 5.2.3 Preparation of reference compounds

The reference compound **PHBD** was prepared incorporating the triazole unit by reaction of **AZBOD** and 1-phenylacetylene (Scheme 4). The reaction worked well to afford **PHBD** as a red crystalline solid in 94% yield.



**Scheme 5.4.** Preparation of the control compound **PHBD**.

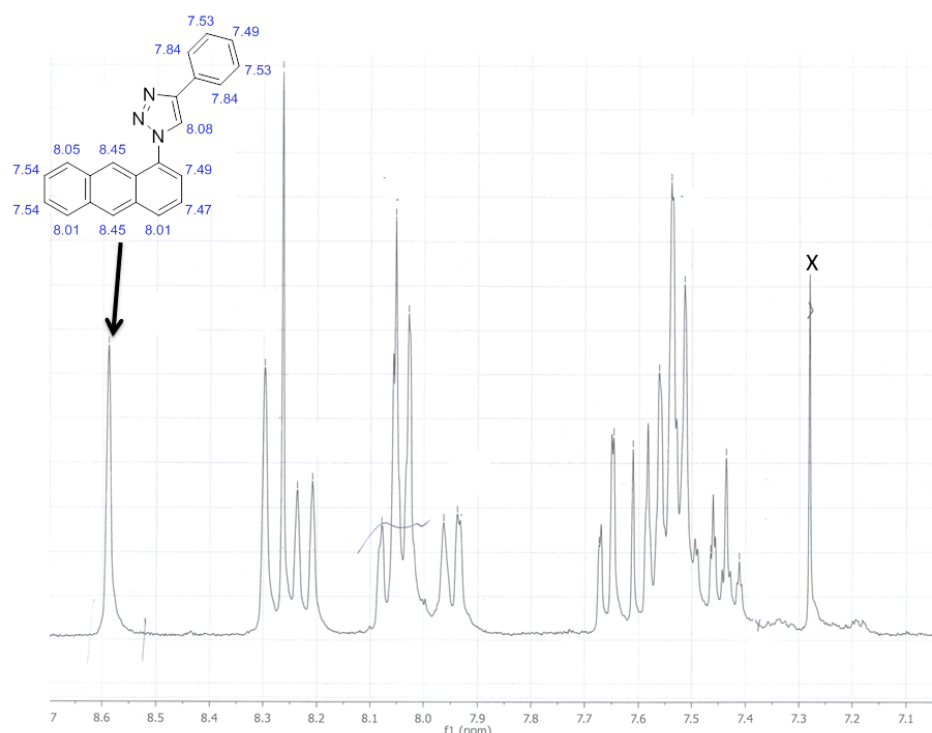
Even though in the control compound **PHBD** the triazole attachment point is reversed, this did not effect its photophysical properties to any great extent as discussed in the photophysics section.



**Scheme 5.5.** Preparation of the control compounds **PHANT** and **PHANT2**.

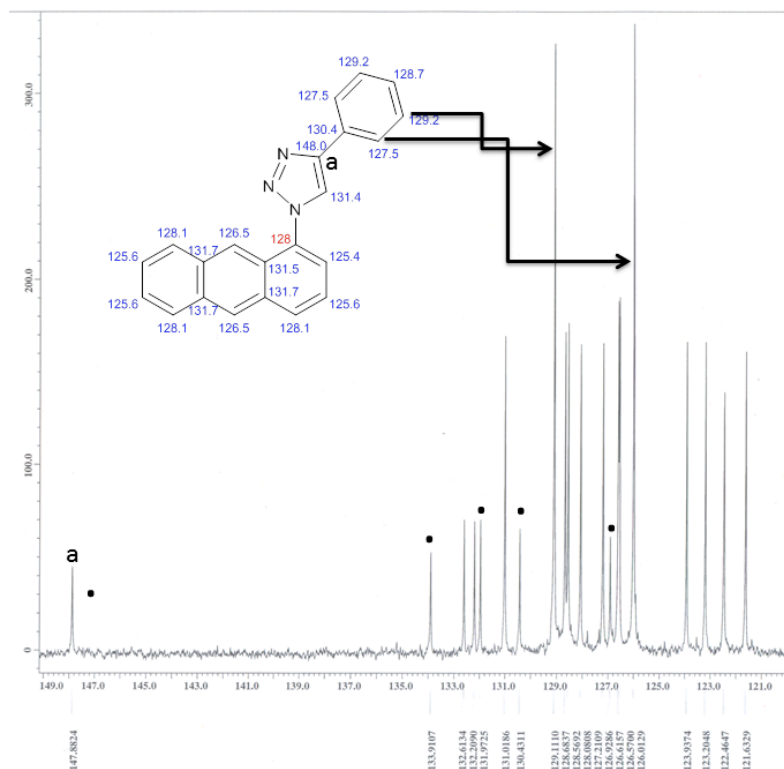
To complete the reference compounds the two derivatives based on anthracene were prepared as shown in Scheme 5. Compounds **PHANT** and **PHANT2** were prepared by condensation of 1-phenylacetylene to the azide activated anthracene compounds **ANT1** and **ANT2** in 93% and 54% yield, respectively, as a pale yellow solid and brown crystals.

The aromatic region for the  $^1\text{H}$  NMR spectrum of **PHANT** is shown in Figure 14. Again a predicted spectrum helped in partial assignment of the resonances. The most downfield resonance is assigned to the singlet for the anthracene group. There is multiple overlap of signals around 7.5 ppm from the phenyl group and the anthracene moiety.



**Figure 5.14.** Room temperature  $^1\text{H}$  NMR spectrum for **PHANT** in  $\text{CDCl}_3$ . X = solvent.

The  $^{13}\text{C}$  NMR spectrum for **PHANT** (Figure 15) was a little more easier to interpret in terms of the total number of resonances. The total number of expected signals is 20, and is made up of 14 signals for the anthracene, 2 for the triazole and 4 for the phenyl group. As seen in Figure 15 there are exactly 20 signals in the aromatic region. The two larger signals at 129.1 and 126.0 ppm are for the phenyl group and each peak is worth two carbons. The 7 small peaks are assigned to the quaternary carbons.



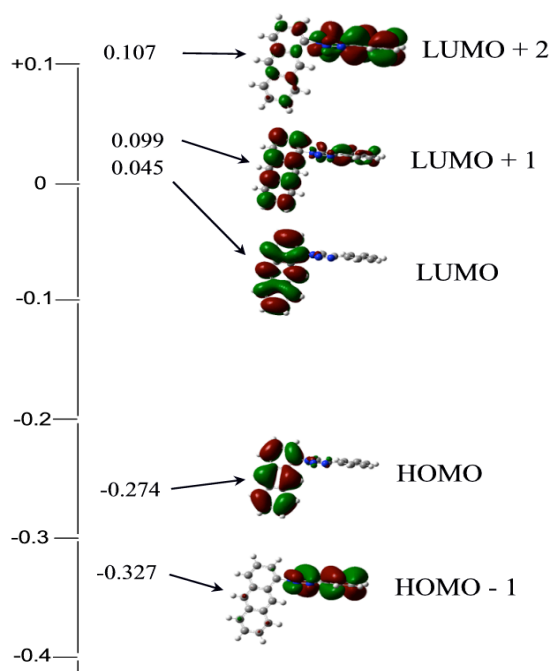
**Figure 5.15.** Room temperature  $^{13}\text{C}$  NMR spectrum for **PHANT** in  $\text{CDCl}_3$ . • = quaternary carbons.

<sup>1</sup>H NMR spectra for the other compounds are collected in the Appendix. Analysis of the NMR spectra for the other compounds were consistent with their molecular structures.

### 5.2.4 Molecular Orbital Calculations & Electrochemistry

To acquire a more complete picture of the molecular orbital framework for **ANTBD**, *ab-initio* computer calculations were carried out *in-vacuo* using Guassian 03 on both the dyad and **PHANT**. Basic Hartree-Fock level calculations were sufficient to firstly obtain a ground-state molecular structure for the two compounds. The structure calculated for **ANTBD** compared well to that obtained by X-ray crystallography. These low-level calculations, in the first instance, afforded a fairly good representation of the HOMO/LUMOs, and their spatial localisation. For **PHANT**, the HOMO is localised on the anthracenyl unit,

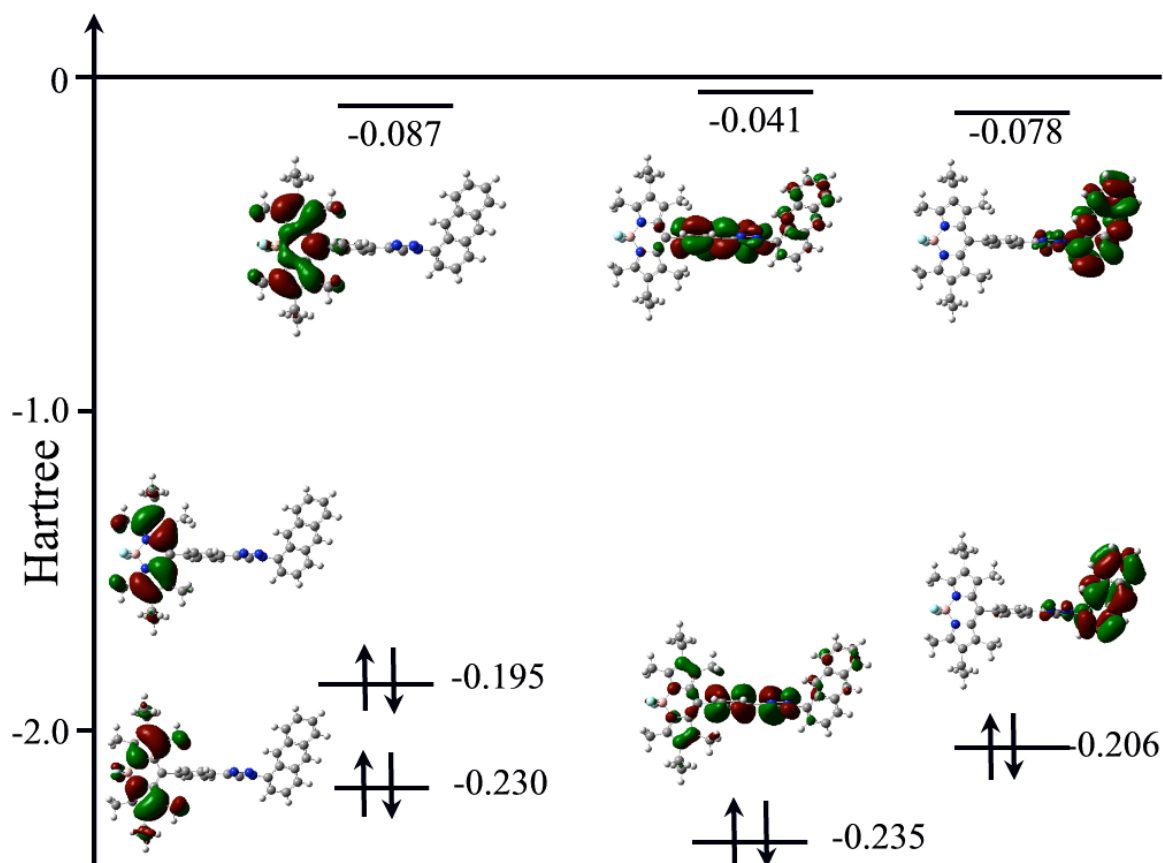
whereas the HOMO-1 is associated with the triazole and phenylene units (Figure 16). The LUMO is exclusively localised on the anthracenyl group and it is the LUMO+2 that dominates the phenylene-triazole group.



**Figure 5.16.** HOMO and LUMO molecular orbitals calculated for **PHANT** using Gaussian-03 at the Hartree-Fock level and using a 6-311G basis set. Energies are given in Hartrees.

The addition of the Bodipy group only perturbs slightly the molecular orbitals on the phenylene-triazole unit as evidenced by calculations performed on **ANTBD** (Figure 17). As seen for other Bodipy derivatives the HOMO is localised on the two pyrrole-like groups with very little orbital contribution at the meso carbon atom. The LUMO, by contrast, is more spread over the entire dipyrromethene backbone. Calculations performed by DFT at a higher-level of sophistication (B3LYP 6-31G/6-311G) did lead to slight modifications in the general molecular orbital picture for both **PHANT** and **ANTBD**. In particular, for **ANTBD** the HOMO-1 for the Bodipy unit is introduced into the overall picture, and it is closer in energy to the HOMO on the bridge (Figure 17). A more

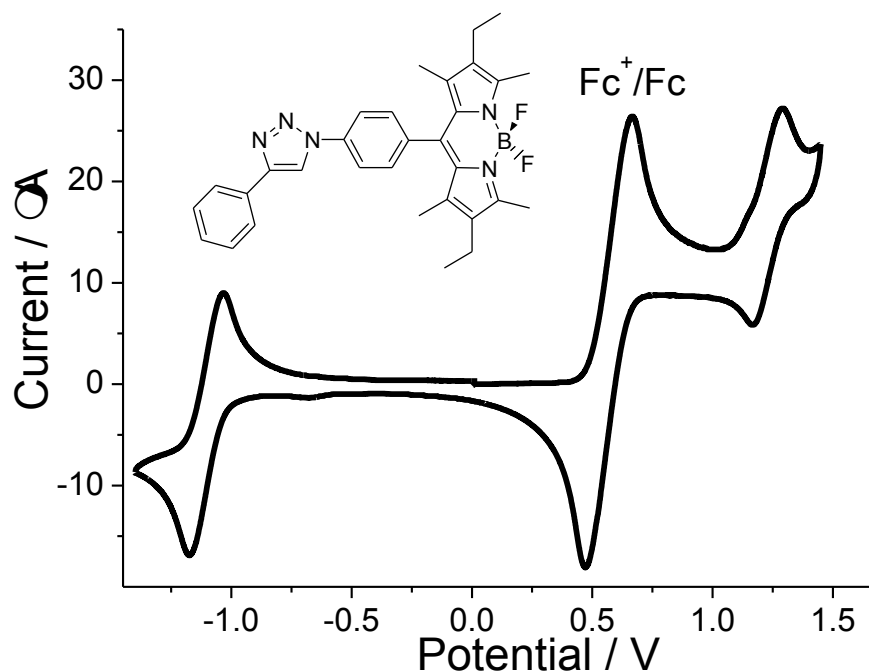
general improvement was a reduction in the HOMO-LUMO energy gaps). For example, the HOMO-LUMO energy gap for the Bodipy is  $23,700\text{ cm}^{-1}$  (422 nm).



**Figure 5.17.** Representation of the HOMO and LUMO molecular orbitals for **ANTBD** and their corresponding energies calculated using DFT (B3LYP) level using the 6-311G basis set.

Another indication of the orbital energies was measured electrochemically using the technique of cyclic voltammetry. The CV for **PHBD** was measured in dry  $\text{CH}_2\text{Cl}_2$  at a glassy carbon electrode (Figure 18). Upon oxidative scanning a quasi-reversible wave is seen at  $E_{1/2} = 1.23\text{ V}$  (vs Ag/AgCl) and is assigned to oxidation at the Bodipy site. No wave is seen corresponding to oxidation of the triazole. In the reductive portion of the CV a quasi-reversible wave is seen at  $E_{1/2} = -1.11\text{ V}$  (vs Ag/AgCl) and is again associated with reduction at the Bodipy site. The difference in energy between the oxidation wave and

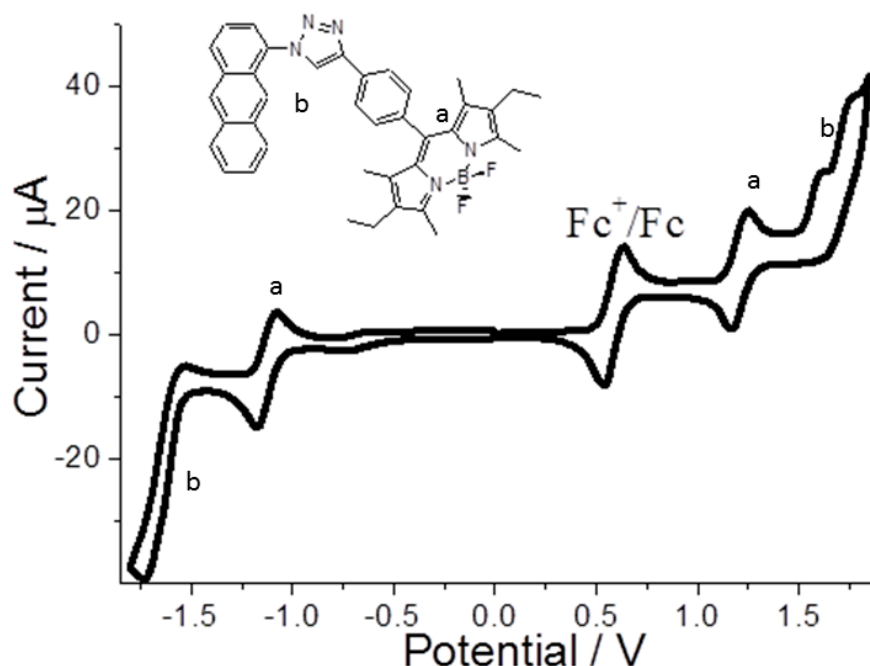
reduction wave ( $\Delta E = 2.34$  V) is the HOMO-LUMO energy gap.



**Figure 5.18.** Cyclic voltammogram recorded for **PHBD** in dry  $\text{CH}_2\text{Cl}_2$  (0.2 M TBATFB) at a glassy carbon electrode.

The electrochemical behaviour for **ANTBD** is readily understood as a near perfect overlap of the cyclic voltammograms collected for **PHANT** and **PHBD**. The oxidative segment is dominated by a quasi-reversible one electron wave at  $E_{1/2} = +1.21$  V (vs Ag/AgCl) followed by irreversible waves at +1.62 V and +1.78 V (vs Ag/AgCl). In the reduction side once again is seen a wave at  $E_{1/2} = -1.13$  V (vs Ag/AgCl) and an irreversible wave at  $-1.73$  V (vs Ag/AgCl). From these results it is inferred that the anthracenyl unit and Bodipy group are isolated and minor, if any, electronic communication takes place through the bridge in the ground state.





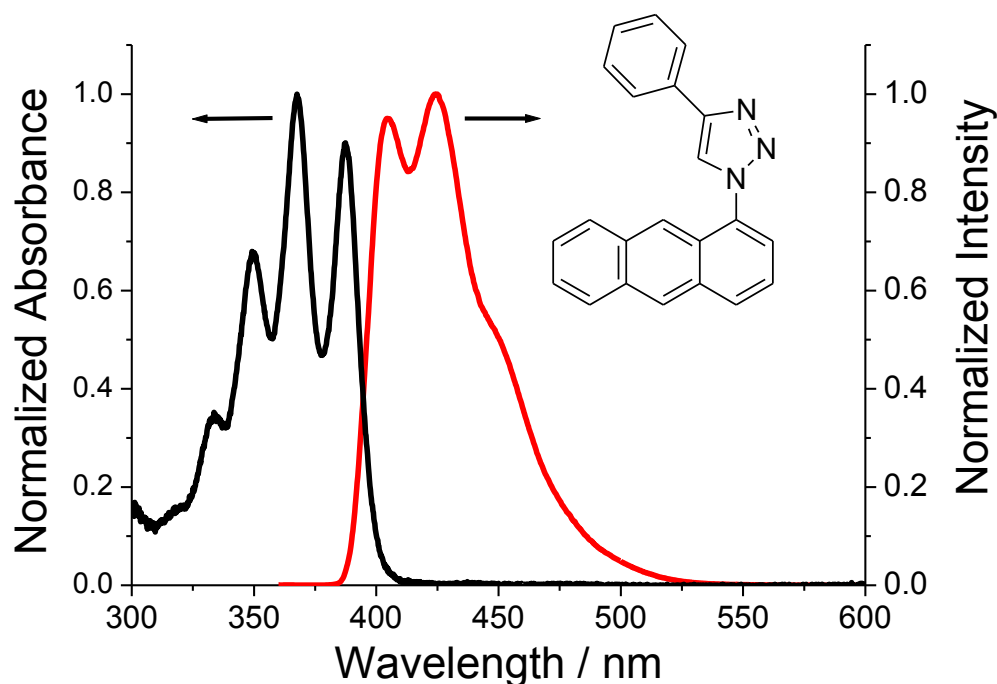
**Figure 5.19.** Cyclic voltammogram recorded for **ANTBD** in dry  $\text{CH}_2\text{Cl}_2$  (0.2 M TBATFB) at a glassy carbon electrode. a = Bodipy waves, b = anthracenyl waves.

## 5.2.5 Photophysical Measurements

### 5.2.5.1 Absorption and Fluorescence

In the first instance the basic properties of the two control compounds were examined in toluene solution. The electronic absorption spectrum for **PHANT** is dominated by four sharp vibronically resolved bands in the 300-400 nm region, typical for anthracene-based compounds, and are ascribed to  $^1\text{A} \rightarrow ^1\text{L}_\text{a}$  category. The molar absorption coefficient ( $\epsilon_{\text{MAX}}$ ) of  $9700 \text{ M}^{-1} \text{ cm}^{-1}$  at the peak maximum ( $\lambda_{\text{ABS}} = 367 \text{ nm}$ ) is as expected for anthracene derivatives. Excitation at 350 nm results in fluorescence ( $\lambda_{\text{FLU}} = 424 \text{ nm}$ ) and a spectrum that is a poor mirror image of the absorption spectrum (Figure 20), but a good

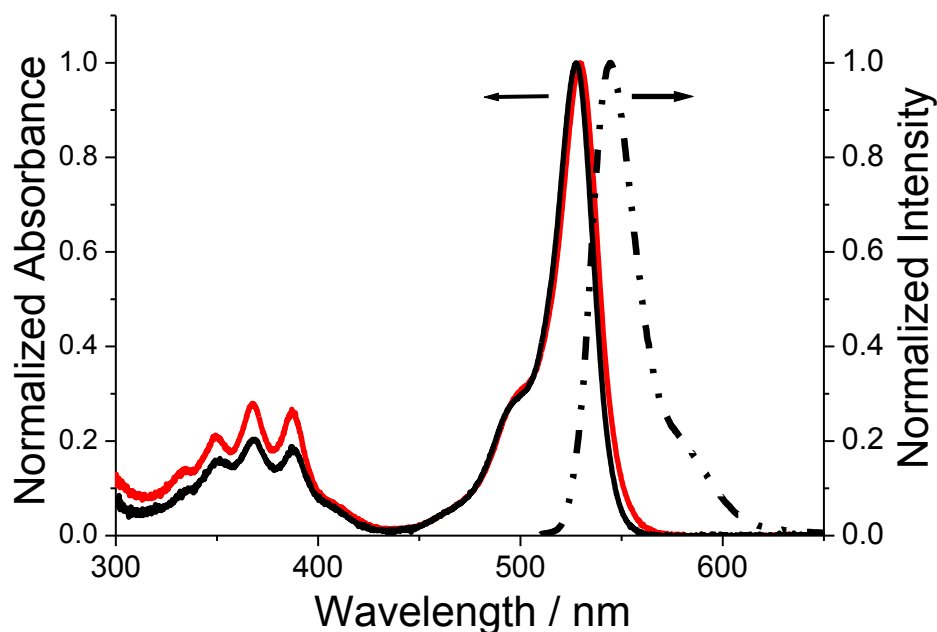
match is observed over all wavelengths between the fluorescence excitation spectrum and the absorption profile .



**Figure 5.20.** Absorption (black) and emission (red) spectra for **PHANT** in dilute toluene.

We infer from observation of the partial vibronic structure and broadening of the fluorescence band that electronic excitation takes place from a planar ground state to a non-planar excited state. The quantum yield of fluorescence ( $\phi_{\text{FLU}}$ ) is 0.34, which is remarkably similar to basic anthracene. Fluorescence decay, as measured by single-photon-counting, was strictly mono-exponential and independent of monitoring wavelength. The fluorescence lifetime ( $\tau_{\text{S}}$ ) is 2.96 ns. Both results point to the fact that no additional non-radiative deactivation pathway from the first-excited singlet state is imparted by the appended triazole unit. The absorption profile for **PHBD** in toluene displays the typical series of vibrationally resolved transitions at  $\lambda_{\text{ABS}} = 530$  nm, for which  $\epsilon_{\text{MAX}}$  was measured as  $78,500 \text{ M}^{-1} \text{ cm}^{-1}$ . The basic fluorescene spectrum ( $\lambda_{\text{FLU}}$

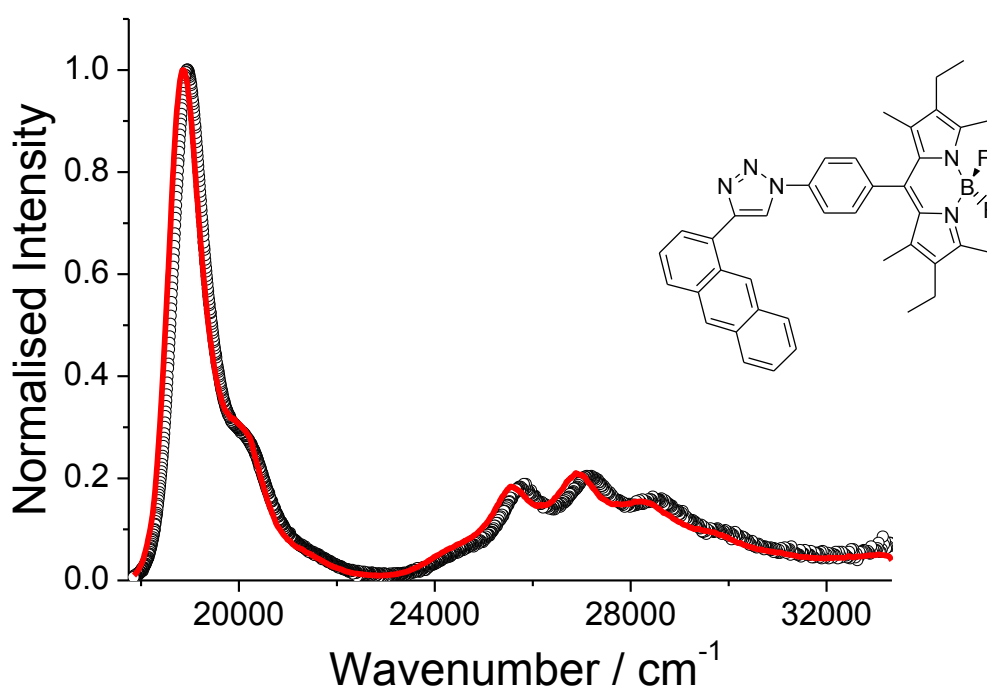
= 547 nm) at room temperature is again on par with the simple Bodipy derivative, along with values for  $\phi_{\text{FLU}} = 0.62$  and  $\tau_{\text{S}} = 4.5$  ns. The radiative rate constant ( $k_{\text{RAD}} = \phi_{\text{FLU}}/\tau_{\text{S}}$  of  $1.4 \times 10^8 \text{ s}^{-1}$ ) is as expected by comparison with the literature, and there is good agreement with the value found using the Strickler-Berg expression.



**Figure 5.21.** Absorption/fluorescence spectra for **ANTBD** (black) and the absorption spectrum for an equimolar mixture of **PHANT** and **PHBD** (red) in toluene.

The room temperature electronic absorption spectrum for **ANTBD** is shown in Figure 21, along with the spectrum for a 1:1 mixture of **PHBD** and **PHANT** under identical conditions. Evidently, the two spectra are remarkably similar and the near perfect coincidence of line shape and  $\lambda_{\text{ABS}}$  for the Bodipy segment is good indication that electronic coupling is negligible between the two subunits in the ground state. Excitation at 350 nm leads only to fluorescence from the Bodipy unit, and the measured  $\phi_{\text{FLU}} = 0.67$  and  $\tau_{\text{S}} = 4.6$  ns are good indicators that first-excited singlet state of the Bodipy is not quenched by any additional internal non-radiative processes. The fully corrected fluorescence

excitation spectrum for **ANTBD** matches extremely well over a wide wavelength range with its absorption spectrum in toluene. We infer from this result that photons collected at the anthracenyl group are transferred to the Bodipy subunit at near unit quantum efficiency.

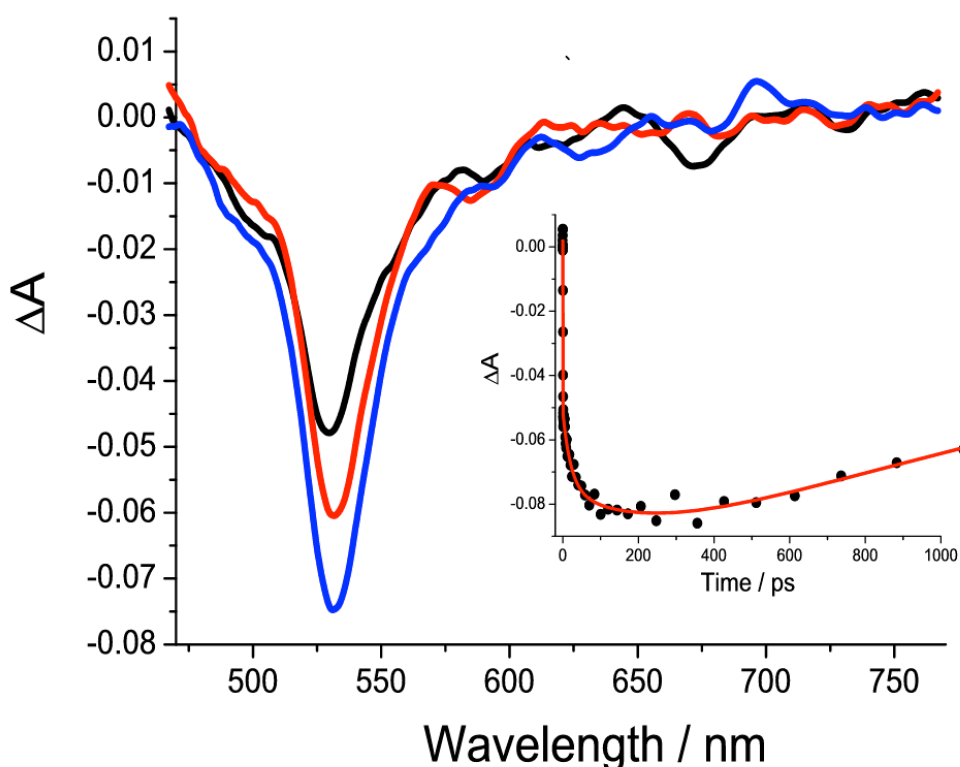


**Figure 5.22.** Comparison of the corrected fluorescence excitation spectrum (red) with the absorption spectrum (black) for **ANTBD** in dry toluene.

#### 5.2.5.2 Time-Resolved Studies

A more comprehensive conception of excited-state behaviour for **ANTBD** was obtained by femtosecond up-conversion fluorescence lifetime measurements and femtosecond transient absorption spectroscopy. For the latter measurements, the excitation wavelength ( $\lambda_{\text{ex}}$ ) was 400 nm. At this wavelength ca. 50% of the photons are absorbed by the anthracene, as determined by comparison of the absorption spectra for **ANTBD** and **PHBD**. The remaining photon balance is taken up by excitation into the  $S_2$  state of the

Bodipy group. The photon balance for the femtosecond up-conversion fluorescence lifetime measurements ( $\lambda_{\text{ex}} = 380 \text{ nm}$ ) is ca. 65% (anthracene) and 35% ( $S_2$ -Bodipy). It is worth noting that internal conversion of  $S_2$  to  $S_1$  states in phenyl-Bodipy takes place in 100-230 fs depending on the solvent. In this case the instrument response for transient absorption (or up-conversion) spectroscopy is not sufficient to resolve this fast process, but we may expect to observe vibrational relaxation as the molecule cools.



**Figure 5.23.** Differential transient absorption profiles recorded at 1.9 ps (black), 14.6 ps (red) and 206 ps (blue) after excitation of a sample of **ANTBD** in toluene at 400 nm with a 70 fs laser pulse. Insert shows the kinetics recorded at 530 nm (●) and the least-squares fit (red line) to the data points.

Excitation of a solution of **ANTBD** in toluene with a 70fs laser pulse delivered at 400 nm affords differential transient absorption profiles as depicted in Figure 5. There is a strong bleach centered around 530 nm after ca. 2ps corresponding to depletion of the ground state. The bleach region continues to grow-in over some 200 ps or so, followed by a slow decay and a non

restoration of the pre-pulse baseline. The transient records show no obvious sign of radical cations/anions associated with either the Bodipy or anthracenyl subunits. The temporal alterations in bleach profile can be adequately fit to two basic models. The first case is a single exponential grow-in of the signal at 530 nm with a lifetime of 35.2 ps, followed by a slow decay component of around 4 ns. For the second case, a bi-exponential fit to the increase in bleach is used ( $\tau_1 = 12.6$  ps,  $\tau_2 = 65$  ps), again followed by a slow decay component ( $\tau_3 \sim 4$  ns). A global analysis of the transient profiles afforded similar results.

Femtosecond up-conversion experiments were performed on **ANTBD** in toluene, monitoring at two different wavelengths as shown in Figure 24. At 545 nm, the photons collected are exclusively associated with the  $S_1$ - $S_0$  electronic transition for the Bodipy segment. The second monitoring wavelength of 460 nm was chosen, by inspection of the fluorescence spectrum for **PHANT**, to detect photons emitted exclusively from the anthracenyl group. It should be noted that no emission from the anthracenyl moiety is seen in the steady-state fluorescence records because of efficient excited-state quenching. The up-conversion profile monitored at 545 nm shows a rise in signal over some 40 ps, and is fitted to a single exponential with a lifetime  $\tau_1 = 10.8$  ps. The fluorescence decay kinetics as monitored at 460 nm is very similar ( $\tau_2 = 15.3$  ps).

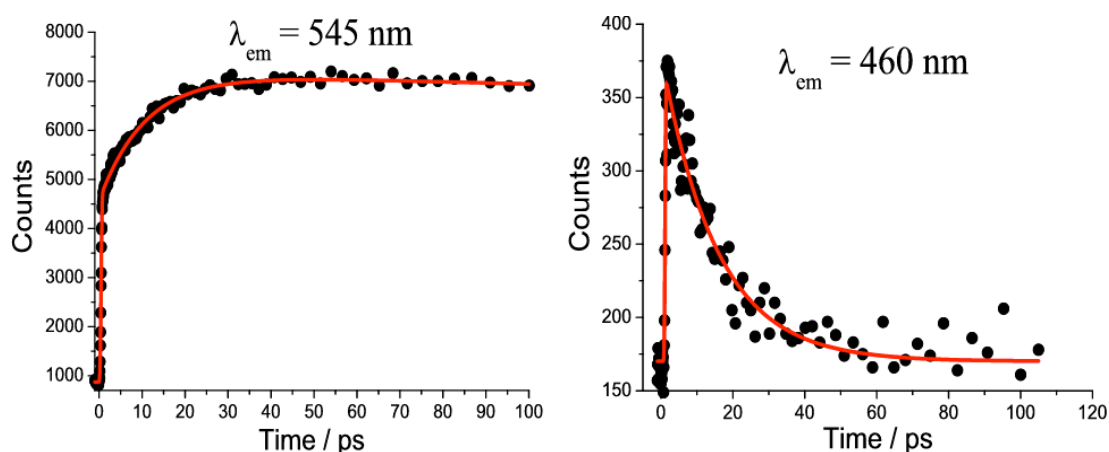
**Table 5.4.** Comparison of lifetime data for **ANTBD** in various solvents.

Solvent (refractive index)	$\tau$ (TA) <sup>a</sup> ps	$\tau$ (UC) <sup>b</sup> ps
TOL <sup>c</sup> (1.493)	$\tau_{\text{mono}} = 35.2$ $\tau_{\text{bi}} = 12.6, 65$	$\tau_{545} = 10.8$ $\tau_{460} = 15.3$
DCE <sup>d</sup> (1.442)	$\tau = 6.4^e$	$\tau_{545} = 7.7$ $\tau_{460} = 7.3$
MeTHF <sup>f</sup> (1.403)	$\tau = 4.5^e$	$\tau_{545} = 5.7$ $\tau_{460} = 8.5$

<sup>a</sup>Transient absorption pump-probe, <sup>b</sup>Femtosecond up-conversion, <sup>c</sup>Toluene, <sup>d</sup>1,2-dichloroethane, <sup>e</sup>only single exponential fit possible, <sup>f</sup>

Methyltetrahydrofuran.

Both types of fast spectroscopic measurements were also performed on **ANTBD** in 1,2-dichloroethane (DCE) and methyltetrahydrofuran (MeTHF). The collected spectra are very similar to the above case of toluene. In Table 4 are collected the lifetime data for the other two solvents. One point to note is the slight decrease in lifetimes with the decrease in the refractive index of the solvent.



**Figure 5.24.** Femtosecond up-conversion profiles recorded at two different wavelengths following excitation of **ANTBD** in toluene at 380 nm with a 70 fs laser pulse. Least-squares fit to data points (●) is shown by red line.

### 5.2.5.3 Interpretation of Fast Spectroscopy Data

To proceed, we firstly discount any Bodipy-based (or anthracenyl-based) excited-state driven electron transfer, to establish a charge transfer state (CTS), on a number of spectroscopic and theoretical grounds. First, the Bodipy-based emission is not quenched in **ANTBD** in any of the solvents, and calculations show that CTS formation by excited-state electron transfer either to or from the anthracenyl subunit is thermodynamically uphill (e.g.,  $\Delta G^0 \sim + 0.45$

eV and + 0.25 eV toluene). Second, similar Gibbs free energy calculations for excited-state quenching of the anthracenyl unit are again endothermic ( $\Delta G^\circ \sim + 0.36$  eV and + 0.16 eV toluene). In addition, there is no spectroscopic evidence from the transient absorption records to support CTS formation. Furthermore, we can discount the formation of an exciplex, as seen in closely-coupled anthracenyl-Bodipy dyads, since no broad featureless emission is observed in the steady-state records. The conclusion is that quenching of the anthracenyl singlet state is via energy transfer to the Bodipy segment of the dyad. The only conundrums left are to which electronic state(s) on the Bodipy does energy transfer occur and which mechanism (Förster or Dexter) dominates?

From the up-conversion experiments, especially in DCE, it is seen that decay of the anthracenyl first-excited singlet state coincides fairly well with formation of the Bodipy  $S_1$  state. Hence, we infer that inverse of the lifetimes, especially  $\tau_{460}$ , (Table 1) correspond to the rates of electronic energy transfer (EET). There is, of course, one slight problem in that the timescales are very close to vibrational relaxation times. In terms of a basic energetic consideration the  $S_1$  vibrational manifold for the anthracenyl group matches well with the  $S_2$  state for the Bodipy moiety. Thus, we can expect energy transfer into the  $S_2$  state of the Bodipy followed by ultrafast internal conversion to the  $S_1$  state and vibrational relaxation. It is noticeable, especially for the toluene case, that the single exponential rise time for the transient absorption bleach does not match that well with the up-conversion lifetime data. However, a somewhat better agreement is obtained using a bi-exponential rise. For the other two solvents  $\tau_{TA}$  values match more closely to the up-conversion lifetimes. The excitation wavelength for transient absorption experiments was chosen specifically since we might expect to observe Bodipy  $S_1$  vibrational cooling regardless of any EET process. We infer that the transient absorption spectroscopic records are



indicating that EET and vibrational cooling are occurring on similar timescales.

#### 5.2.5.4 Electronic Energy Transfer (EET) Mechanism

One of our initial design criteria was to try and eliminate the Dexter-type dual electron energy transfer mechanism by incorporating into the dyad the insulating triazole group. Certainly ground-state electrochemical and absorption data are supportive of very weak interaction between the anthracenyl and Bodipy moieties. The molecular orbital calculations also reveal that the HOMO associated with the bridge is lower in energy than HOMOs associated with both the Bodipy and anthracenyl centres. Conversely, the LUMO energy lies above the LUMOs for the two terminal groups. Considering that a Dexter-type mechanism requires excited-state electron injection into the LUMO and hole-transfer via the HOMO on the phenylene-triazole, there appears even at this basic level of calculation, two energetically unfavourable processes.

#### 5.2.5.5 Comparison with Förster Theory in Toluene

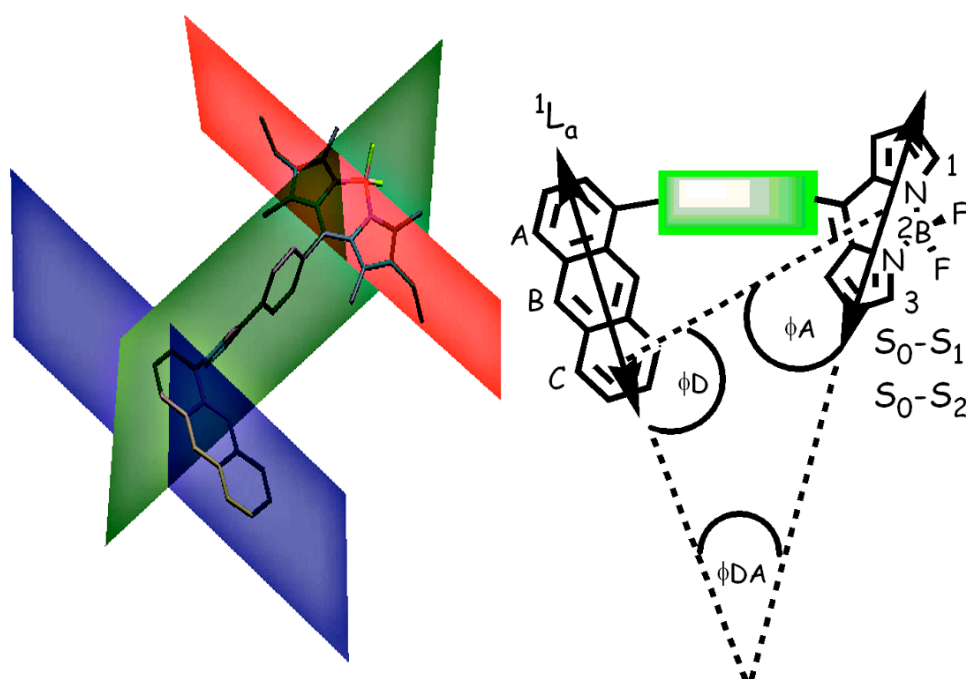
As discussed in the Introduction according to Förster theory the rate of EET ( $k_{\text{EET}}$ ) is related to several spectroscopically determined and calculated parameters by equation 1:

$$k_{\text{EET}} = \frac{8.8 \times 10^{-25} \kappa^2 \phi_D}{n^4 \tau_D R^6} \frac{\int F(\nu) \epsilon(\nu) \nu^{-4} d\nu}{\int F(\nu) d\nu} \quad (\text{Eq. 1})$$

It is fairly evident to be able to compare observed  $k_{\text{EET}}$  values with those calculated via the Förster equation one has to be sure of several factors. First, and the most obvious, is  $k_{\text{EET}}$  as determined by some spectroscopic technique must relate solely to Förster EET and not inevitably contain some secondary contribution. Second,  $\kappa^2$  is calculated using the appropriate angles

between the two electronic transition dipoles; the average value of  $2/3$  is generally used for flexible systems to take into account the randomised angles. In this case, because of the bridge rigidity in **ANTBD** it does allow a more comprehensive analysis for  $\kappa^2$ .

Instead of a relying solely on a single-point calculation a more global analysis was chosen, but this is not as detailed as the density cube method developed by Fleming *et al.*. The three aryl rings of the anthracene and three rings of the Bodipy were used as reference points (Figure 25). Values for  $\kappa^2$  were determined using Eq.2 and angles subtended between planes generated from the molecular structure of **ANTBD**. Likewise, separation distances  $R$  were calculated in a similar manner using centroids created on each ring of the anthracene and the Bodipy group.



**Figure 5.25.** Left: calculated planes for the long-axis of the anthracenyl group (blue), Bodipy unit (red), and intramolecular axis (green) using the X-ray determined molecular structure for **ANTBD**. Right: cartoon representation of the bond angles and numbering/lettering scheme used in the discussion of Förster theory.

$$\kappa = \cos\phi_{DA} - 3\cos\phi_D\cos\phi_A \quad (\text{Eq. 2})$$

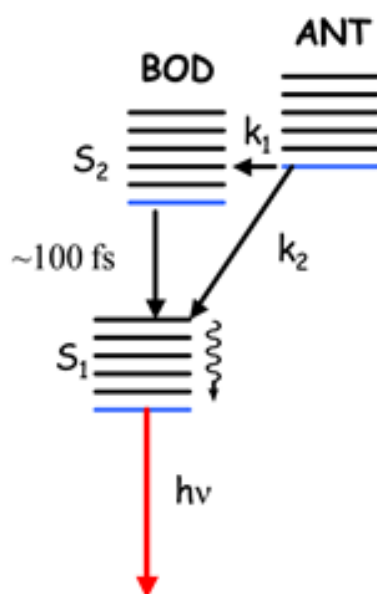
To elucidate the overlap integral the spectroscopic properties of **PHANT** and **PHBD** were used to model the complete dyad. This assumption seems reasonable since very little perturbation is seen by connecting to the two groups together to construct **ANTBD**. The calculated value for  $J_F$  ( $1.6 \times 10^{-14}$  mmol cm<sup>6</sup>) takes into account the noticeable overlap between emission from **PHANT** and both the S<sub>0</sub>-S<sub>1</sub> and S<sub>0</sub>-S<sub>2</sub> electronic transitions for **PHBD**. Close inspection reveals, in fact, that the distribution in the overlap integral is almost 50:50 between these two transitions. Both theoretical calculations and experimental results are in agreement with the notion that the S<sub>0</sub>-S<sub>1</sub> electronic transition dipole for Bodipy is long-axis polarised. Whereas calculations for a simple C<sub>2v</sub> symmetric Bodipy seem to show that the S<sub>0</sub>-S<sub>2</sub> transition is short-axis polarised, work by Glasbeek et al. assigned the transition almost parallel to the S<sub>0</sub>-S<sub>1</sub> electronic transition. Using this later interpretation, both the S<sub>0</sub>-S<sub>1</sub> and S<sub>0</sub>-S<sub>2</sub> electronic transition dipoles for the Bodipy are almost parallel to the dipole moment for the anthracenyl group (Figure 25); the calculated dihedral angle  $\phi_{DA} = 7.1^\circ$ . In Table 5 are parameters associated with the global analysis method (Figure 25), and the corresponding values for  $k_{EET}$  obtained using Eq.1.

**Table 5.5.** Selected parameters and rates of Förster EET calculated using Eq.1, for energy transfer from anthracene into the S<sub>2</sub> state of the Bodipy in **ANTBD** in toluene.

Pairing	R / Å	$\kappa^2$	$k_{EET} / 10^{10} \text{ s}^{-1}$
A-1	12.2	0.76	3.7
A-2	11.9	0.98	5.6
A-3	12.1	0.81	4.2
B-1	12.8	0.34	1.2
B-2	12.2	0.83	4.1
B-3	11.9	0.98	5.6
C-1	13.9	0.096	0.2
C-2	12.9	0.52	1.8
C-3	12.2	0.90	4.5
	Average	0.69	3.4

It is noticeable that the average of  $k^2$  is remarkably similar to the value used for randomised angles. For most of the permutations  $k_{\text{EET}}$  values are in agreement with fast energy transfer from the anthracene to the Bodipy unit. Moreover, the average value for the calculated  $k_{\text{EET}}$  ( $3.4 \times 10^{10} \text{ s}^{-1}$ ) is nearly half the rate for EET by taking the average of the two up-conversion lifetimes ( $7.7 \times 10^{10} \text{ s}^{-1}$ ). Evidently, when the overlap between the  $S_0$ - $S_1$  transition is taken into account, the summation of calculated  $k_{\text{EET}}$  values ( $2 \times 3.4 \times 10^{10} \text{ s}^{-1}$ ) is similar to the measured  $k_{\text{EET}}$  value; this could, of course, be purely coincidental. In fact, it is noticeable that the fastest calculated  $k_{\text{EET}}$  is around 70% of the measured rate. In Figure 26 is depicted a simple illustration of the feasible pathways for EET and vibrational relaxation.

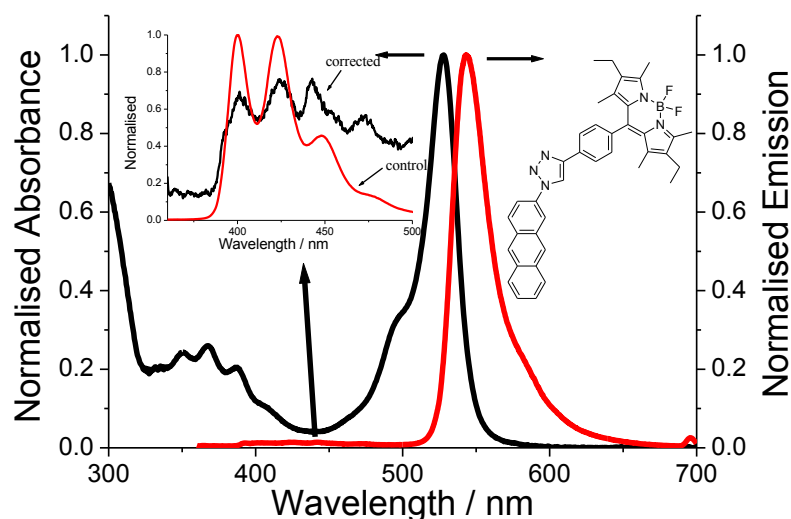
The first scenario is that EET occurs exclusively into the  $S_2$  state ( $k_1 = 7.7 \times 10^{10} \text{ s}^{-1}$ ,  $k_2 = 0$ ) and this is followed by ultrafast internal conversion and vibrational relaxation. The second case is that EET occurs with equal rates ( $k_1 + k_2 = 7.7 \times 10^{10} \text{ s}^{-1}$ ) into both  $S_2$  and  $S_1$ , with the  $S_2$  to  $S_1$  conversion being too fast to contribute to the kinetic profile. It is difficult to distinguish between these two cases, but the first is possibly more favourable owing to better vibrational overlap between the potential energy surfaces.

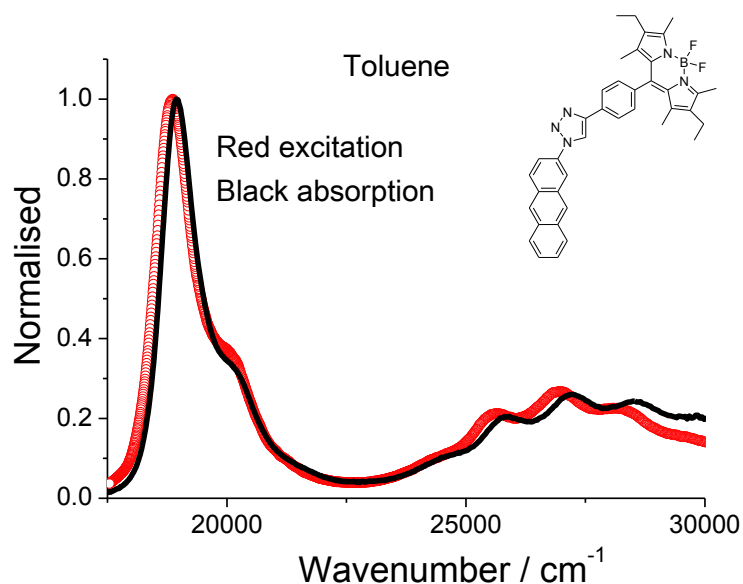


**Figure 5.26.** Pictorial representation of pathways for EET and vibrational cooling. Note:  $k_1$  and  $k_2$  represent rates of EET into the  $S_2$  and  $S_1$  states from anthracene.

### 5.2.5.6 Comparison to ANTBD2

For comparison purposes the absorption and fluorescence spectra for **ANTBD2** were recorded in toluene. The absorption spectrum (Figure 27) comprises peaks which fit for both anthracene and Bodipy units. There is a good match between the absorption spectrum and the corrected fluorescence excitation spectrum (Figure 27). At first there appeared to be good evidence that energy transfer from the anthracene to the Bodipy was not as efficient as in case for **ANTBD**. A very weak structured signal was observed at around 420 nm which matched well with the fluorescence profile for **PHANT2**. Such a profile would be expected if the probability for Förster energy within **ANTBD2** had decreased. Unfortunately after careful purification of the sample the structured emission signal disappeared. The result is spurious and emphasises the need for pure samples when collecting fluorescence data as wrong interpretations can be made.





**Figure 5.27.** Top: Absorption (black) and emission (red) spectra for **ANTBD2** in dilute toluene. Bottom: Comparison of absorption and corrected fluorescence excitation spectra for **ANTBD2**.

Once again fast time-resolved spectroscopic studies performed on **ANTBD2** in a range of solvents were consistent with very fast energy transfer from the anthracene to the Bodipy group. We did not undertake such any detailed analysis of the results in term of Förster theory. We chose instead to alter the donor to pyrene and naphthalene as discussed in the following chapter.

### 5.3 Remarks and Conclusions

In this Chapter we have shown that basic molecular dyads can be constructed using a “click chemistry” approach. It would appear that Förster theory adequately predicts the rate for electronic energy transfer in the molecular dyad, **ANTBD**. One possible reason for the goodness of fit between experiment and theory is the role of the triazole unit. The group acting as the linker between an anthracenyl unit and a Bodipy group effectively decouples

the two components. It is interesting to note that recent work by Guldi *et al.* has shown that in zinc porphyrin-C60 adducts triazole is discussed as an excellent bridge for electron transfer.<sup>10</sup> Furthermore, Vauzeolles and co-workers concluded that efficient electron transfer occurs through the triazole unit in ruthenium(II) polypyridine dyads.<sup>11</sup> Both these pieces of work are in contrast to previous studies where the evidence was supportive of the poor conduit nature for the triazole group. Probably one matter to consider is the spin state of the photosensitizer, and the fact that for ruthenium complexes it is the triplet state that participates in electron transfer. The molecular orbitals residing on the triazole may be more energetically conducive to promote electron transfer. In this case the singlet-singlet Dexter-type exchange is not favoured. In conclusion, triazole could be best viewed as an 'ambivalent' group for promoting electron exchange.

It is very noticeable that  $k_{\text{EET}}$  appears to increase in the solvent order TOL < DCE < MeTHF. From Förster theory the measured  $k_{\text{EET}}$  should vary with  $1/n^4$  (Eq. 1), but because of the limited number of solvents the linearity should be viewed with some scepticism. In the following Chapter 6 we attempt to look at the  $1/n^4$  prediction in a little more detail using a pyrene-based molecular dyad.

## 5.4 References

1. A. C. Benniston and A. Harriman (2006) Charge on the move: how electron-transfer dynamics depend on molecular conformation. *Chem. Soc. Rev.*, **35**, 169-79.
2. (a) P. D. Frischmann, K. Mahata, F. Würthner. (2012) Powering the future of molecular artificial photosynthesis with light-harvesting metallosupramolecular dye assemblies. *Chem Soc Rev.* **42**(4):1847-70. (b) J. S. Yang, M.-C. Yoon, H. J. Yoo, P. S. Kim and D. H. Kim (2012) Excitation energy transfer in multiporphyrin arrays with cyclic architectures: towards artificial light-harvesting antenna complexes. *Chem. Soc. Rev.*, **41**, 4808-26.

3. A Loudet, et. al. World Scientific, (2011) BODIPY® Dyes and Their Derivatives: Syntheses and Spectroscopic Properties, in "Handbook of Porphyrin Science: With Applications to Chemistry, Physics, Materials Science, Engineering, Biology and Medicine" World Scientific. pp 203.
4. (a) H. Onagi and J. Rebek, Jr. (2005) Fluorescence resonance energy transfer across a mechanical bond of a rotaxane. *Chem. Commun.*, 4604-06.  
(b) T. Ogoshi, D. Yamafuji, T. Yamagishia and A. M. Brouwer (2013) Förster resonance energy transfer by formation of a mechanically interlocked [2]rotaxane. *Chem. Commun.*, **49**, 5468-70.
5. J. Jose, Y. Ueno, J. C. Castro, L. L. Li and K. Burgess (2009) Energy transfer dyads based on Nile Red. *Tetrahedron Lett.*, **50**, 6442–45.
6. Al. Nierth, A. Yu. K. G. U. Nienhaus and A. Jäschke (2010) Anthracene-BODIPY Dyads as fluorescent sensors for biocatalytic Diels-Alder reactions. *J. Am. Chem. Soc.* **132**, 2646–54.
7. M D. Ward (1997) Photo-induced electron and energy transfer in non-covalently bonded supramolecular assemblies. *Chem. Soc. Rev.*, **26**, 365-75.
8. R T. Cheriya, J. Joy, A. P. Alex, A. Shaji, and M. Hariharan (2012) Energy transfer in near-orthogonally arranged chromophores separated through a single bond. *J. Phys. Chem. C*, **116** (**23**), pp 12489–98.
9. J B. Birks (1970) Photophysics of Aromatic Molecules. Wiley-Interscience, London. pp 125-129
10. D M. Guldi, et al. (2011) *J. Am. Chem. Soc.* **133**, 13036.
11. B.Vauzeilles et al. (2011) *Chem. Commun.* 2011, **47**, 11011.



## Chapter 6

# Tuning Förster Resonance Energy Transfer Efficiency

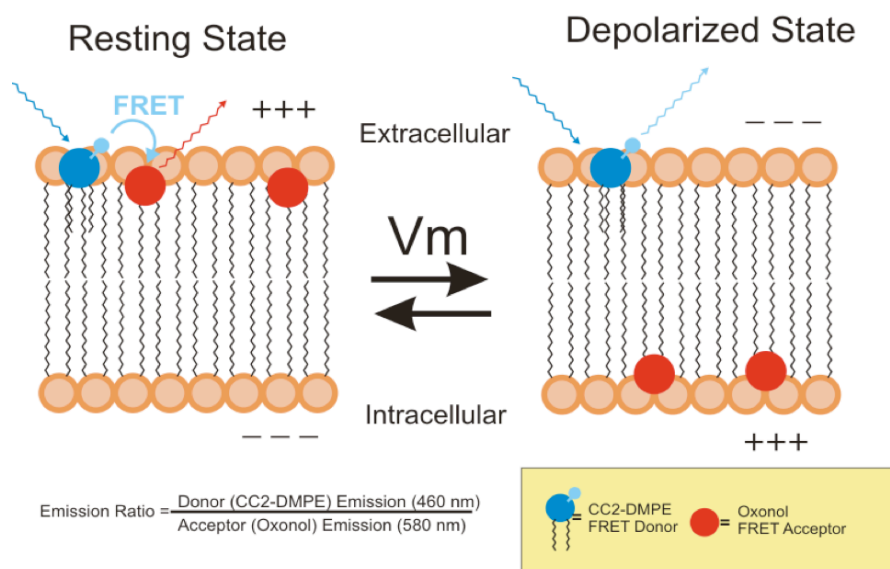


## 6.1 Background and Molecular Design Principles

In the previous chapter the concept of measuring Förster energy transfer was introduced and studied in a simple molecular dyad. This concept is carried on in this chapter but mainly focus on controlling the overlap integral and at the same time evaluating the solvent dependency of electronic energy transfer over a relatively short distance.

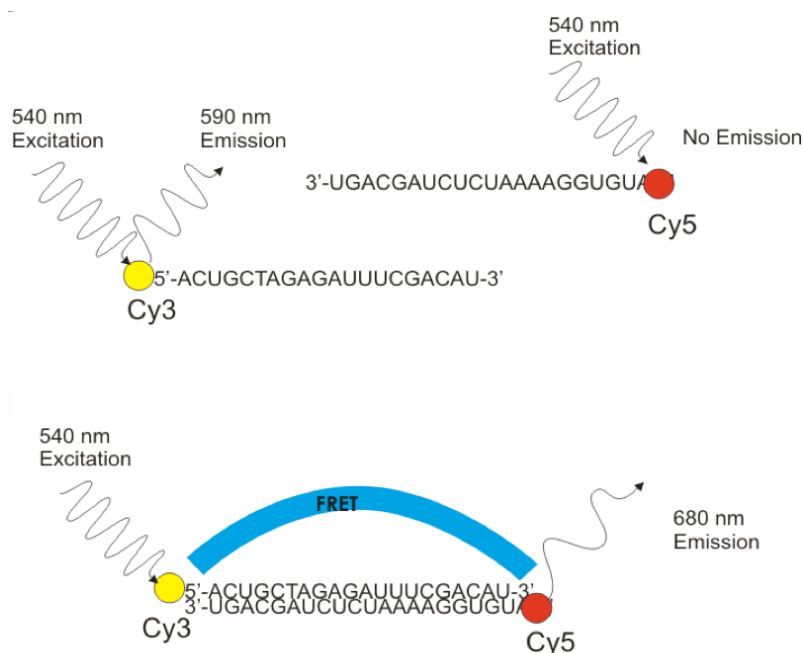
### 6.1.1 Parameters for FRET Efficiency

The parameters which contribute to understanding the rate of electronic energy transfer were discussed previously. Efficiency of Förster energy transfer within molecular systems could be tuned *couture* to suit application requirements. As discussed in Chapter 4 voltage sensitive probes (VSPs) are highly useful in imaging the electric response of membranes. In the example shown in Figure 6.1 the control of FRET is used as a means to image the membrane potential. The primary use for such technology is high-throughput ion channel drug discovery. Two components are used: coumarin-phospholipid (CC2-DMPE) and bis-(1,3-diethylthiobarbituric acid)trimethine oxonol (DiSBAC<sub>2</sub>). The CC2-DMPE is the FRET donor and DiSBAC<sub>2</sub> is the acceptor. In the resting state the two molecular components are in close proximity within the membrane and so FRET efficiency is high and emission is observed from the oxonol acceptor. In the depolarized state the direction of charge across the membrane is altered and the oxonol migrates to the positive side of the membrane and away from the donor. Even though the overlap integral probably remains the same the increase in distance between the two components results in a decrease in FRET efficiency. The output is read by a ratiometric manner by looking at emission at 460 nm (donor) and 580 nm (acceptor).<sup>1-2</sup>



**Figure 6.1.** Example of using the change in FRET efficiency to produce a voltage sensitive probe system. Images in Fig.6.1 and Fig.6.2 are courtesy of R. Hoffman and P. Held, BioTek Application Note.

The theme of biological FRET is shown in the example of Figure 6.2, in which two dyes are functionalised with complementary oligonucleotides. When separate and excited at 540 nm only emission is observed from Cy3 at 590 nm. At the excitation wavelength photons are not absorbed by Cy5 and so no emission is observed. When mixed together the two oligonucleotide strands combine via hydrogen bonding recognising that G-C and A-U pairing is highly favourable. FRET is turned on because of the favourable overlap between emission from the donor and absorption from the acceptor. Emission at 680 nm is the signal that informs the reader of molecular association. Potential application of this technique includes multi-candidate genotyping for clinical diagnosis<sup>3-4</sup>



**Figure 6.2.** Use of FRET to demonstrate the association of the two oligonucleotide chains.

### 6.1.2 Aim of Research and Molecular Design Principle

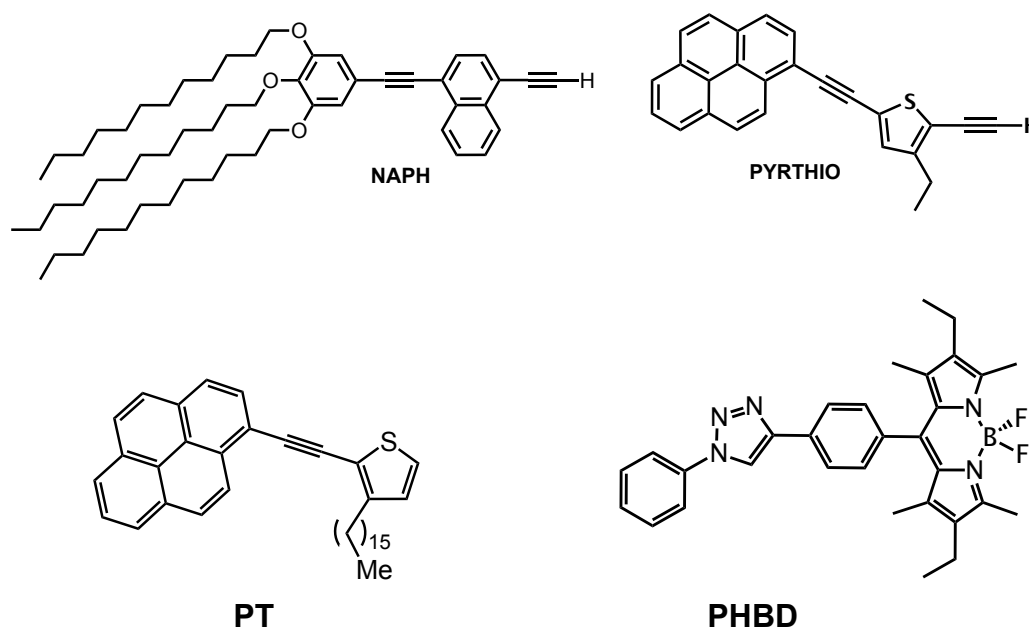
In designing the molecular systems it was aware that in order to achieve efficient Förster energy transfer the overlap integral between emission from the donor and absorption from the Bodipy had to be significant. Furthermore, since we intended to test the refractive index ( $n$ ) dependency in Förster theory the compounds needed to be soluble in organic solvents.<sup>5-7</sup> With these two criteria in mind several donor molecules were considered including polyaromatic hydrocarbon compounds including perylene, pyrene and naphthalene. Regarding the latter compound alkyl substitution into the naphthalene is needed, since emission from the donor is too high in energy to overlap with the  $S_0$ - $S_1$  electronic transition of the Bodipy group. Also perylene is rather insoluble in most organic solvents and needs alkyl groups attached to aid in solubility.

## 6.2 Results and Discussion

### 6.2.1 Synthesis of Bodipy Tethered Dyad Systems

#### 6.2.1.1 Preparation of precursors and control compounds

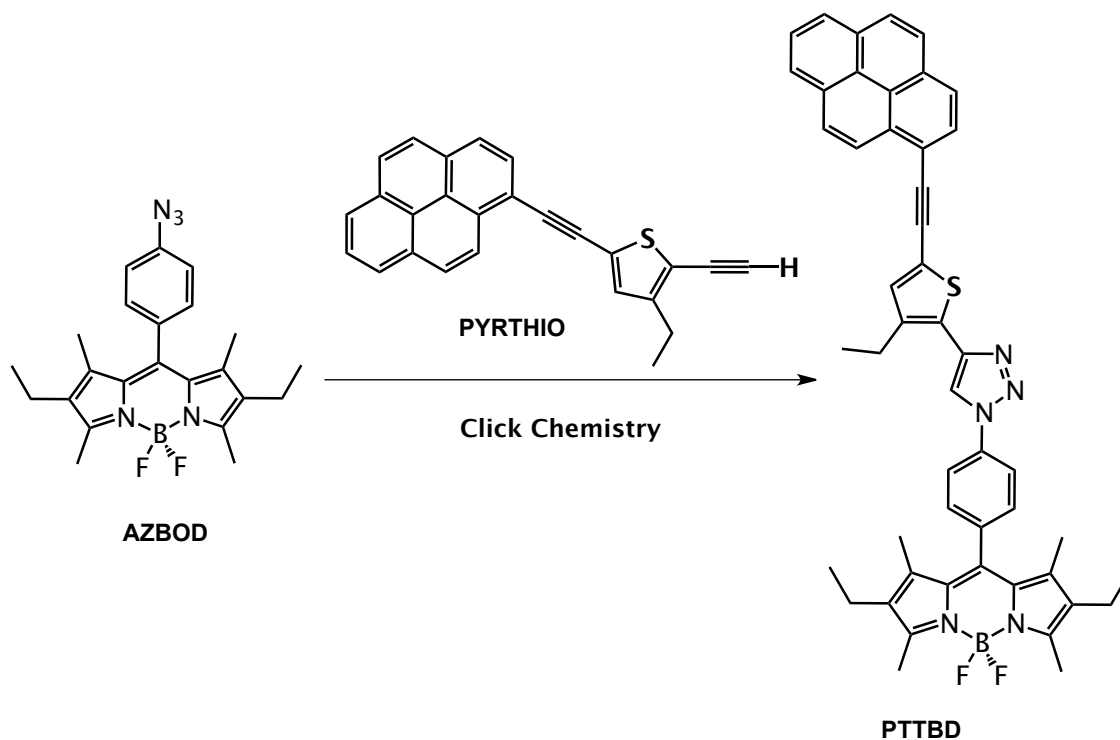
The compounds **PTTBD** and **NAPBD** were prepared in a similar manner via standard 'click' chemistry conditions. For brevity the synthesis of compound **PTTBD** is discussed as shown in Scheme 1. The starting material **PYRTHIO** was given courtesy to a previous member of the MPL. The precursor **PYRTHIO** contains the pyrene-thiophene chromophore which is emissive from an intramolecular charge transfer state. This should give the opportunity to tune the Förster overlap integral with change in solvent polarity. The long alkyl groups in compound **NAPH** aid in its solubility and the acetylene unit moves the absorption profile more to the red region. The reference control compound **PT** were also available from previous projects. The compound **PHBD** is again implemented as the reference compound for electrochemical and photophysical measurements.



**Figure 6.3.** Acetylene activated precursor compounds for carrying out 'click' reactions, alongside their reference control compounds.

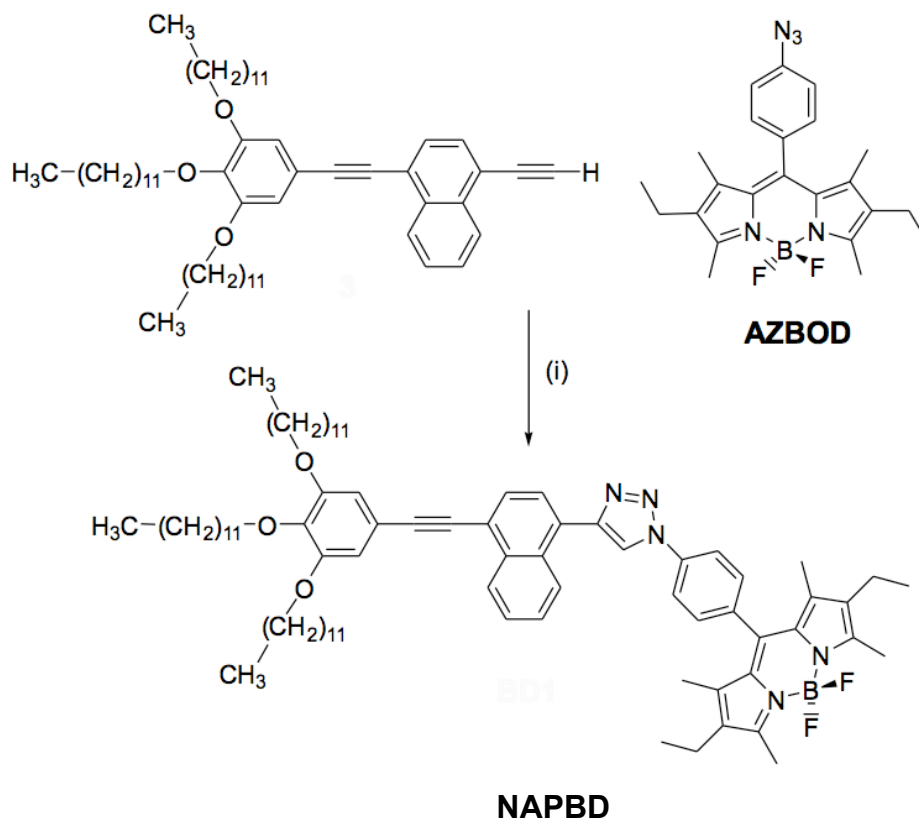
### 6.2.1.2 Preparation of Dyad Systems PTTBD and NAPBD

A click reaction of acetylene activated precursor compounds with azide activated **AZBOD** in THF: H<sub>2</sub>O containing copper/copper sulfate and the ligand tris-[(1-benzyl-1H-1,2,3-triazol-4-yl)methyl]amine afforded after purification the molecular array **PTTBD** and **NAPBD** in 72% and 24 % yields, respectively.



**Scheme 6.1.** Preparation of **PTTBD**. Reagents: (i) TBTA, Cu/CuSO<sub>4</sub>, 1:1 THF/H<sub>2</sub>O, 25 °C for 18 hour then reflux at 80 °C for 18 hours.

The preparation of the naphthalene-based dyad is shown in Scheme 2, starting again from **AZBOD** and the acetylene derivative **TNAP**. Click chemistry was employed under conditions worked out for previous reactions.



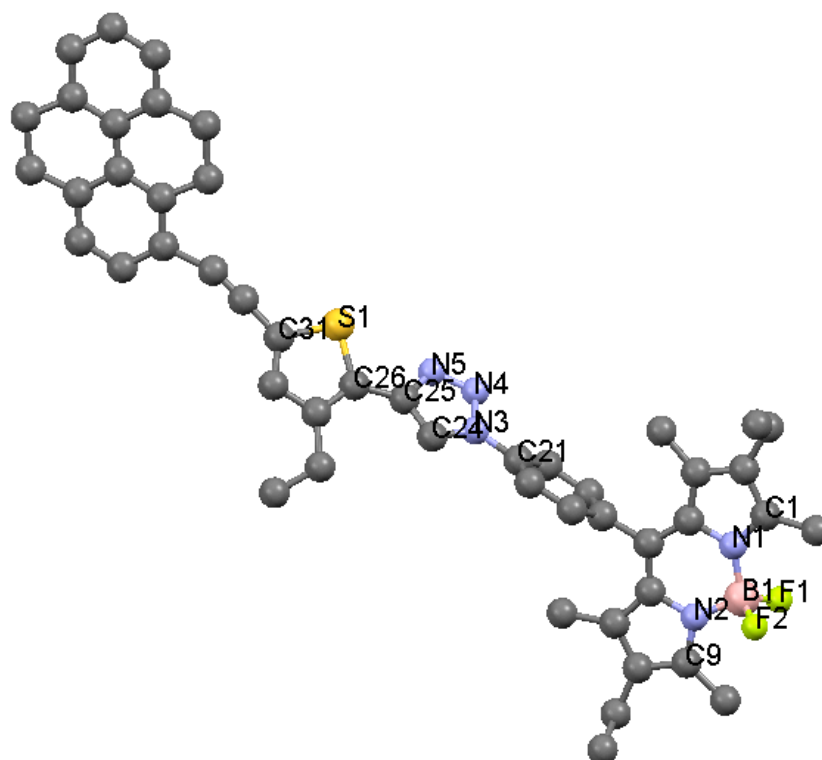
**Scheme 6.2.** Reagents and Conditions (i) TBTA, Cu/CuSO<sub>4</sub>, 1:1 THF/H<sub>2</sub>O, 25 °C for 18 hour then reflux at 80 °C for 18 hours.

## 6.2.2 Characterisation of of PTTBD and NAPBD

The dyads arrays were identified via <sup>1</sup>H, <sup>13</sup>C, <sup>19</sup>F, <sup>11</sup>B NMR spectroscopy, melting points and FT-IR and mass spectrometry

### 6.2.2.1 Crystal structure of PTTBD

Crystals for **PTTBD** were grown and were of suitable quality for an X-ray crystal analysis. The molecular structure for **PTTBD** is shown in **Figure 6.4** and selected bond lengths are collated in Table 6.1.



**Figure 6.4.** Molecular structure for **PTTBD** as determined by X-ray analysis.

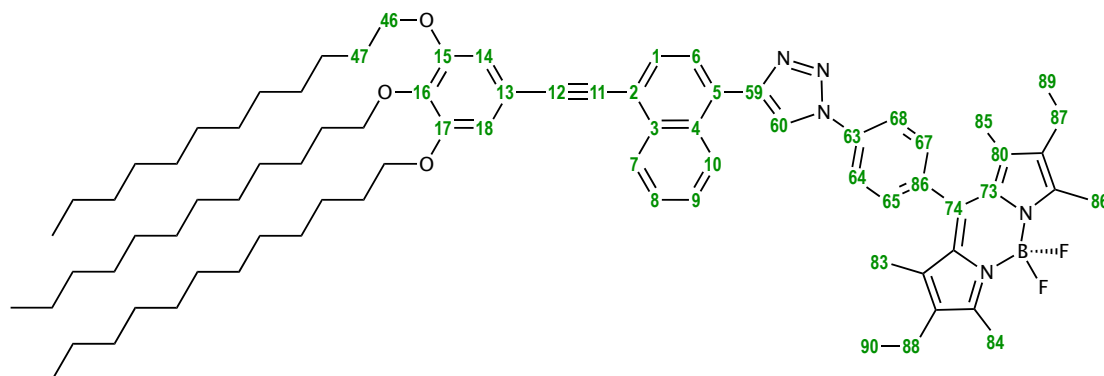
Bond Length / Å		Bond Length / Å	
N(1)–B(1)	1.546(9)	N(1)–C(1)	1.344(8)
N(1)–C(4)	1.409(7)	N(2)–B(1)	1.523(9)
N(2)–C(6)	1.412(7)	N(2)–C(9)	1.365(8)
N(3)–N(4)	1.345(7)	N(3)–C(21)	1.440(7)
S(1)–C(26)	1.733(6)	S(1)–C(31)	1.733(6)
F(2)–B(1)	1.397(7)		
Bond Length / °		Bond Length / °	
C(26)–S(1)–C(31)	91.0(3)	B(1)–N(1)–C(1)	126.7(5)
B(1)–N(1)–C(4)	124.7(5)	C(1)–N(1)–C(4)	108.5(5)
B(1)–N(2)–C(6)	126.2(5)	B(1)–N(2)–C(9)	125.9(5)
C(6)–N(2)–C(9)	107.8(5)	N(4)–N(3)–C(21)	119.9(4)
N(4)–N(3)–C(24)	111.6(4)	C(21)–N(3)–C(24)	128.5(5)
N(1)–B(1)–F(1)	109.9(5)	N(2)–B(1)–F(1)	111.3(5)
F(1)–B(1)–F(2)	108.6(5)	N3–N4–N5	106.6(4)

**Table 6.1.** Selected bond lengths and angles for **PTTBD**.



### 6.2.2.2 Characterization of NAPBD

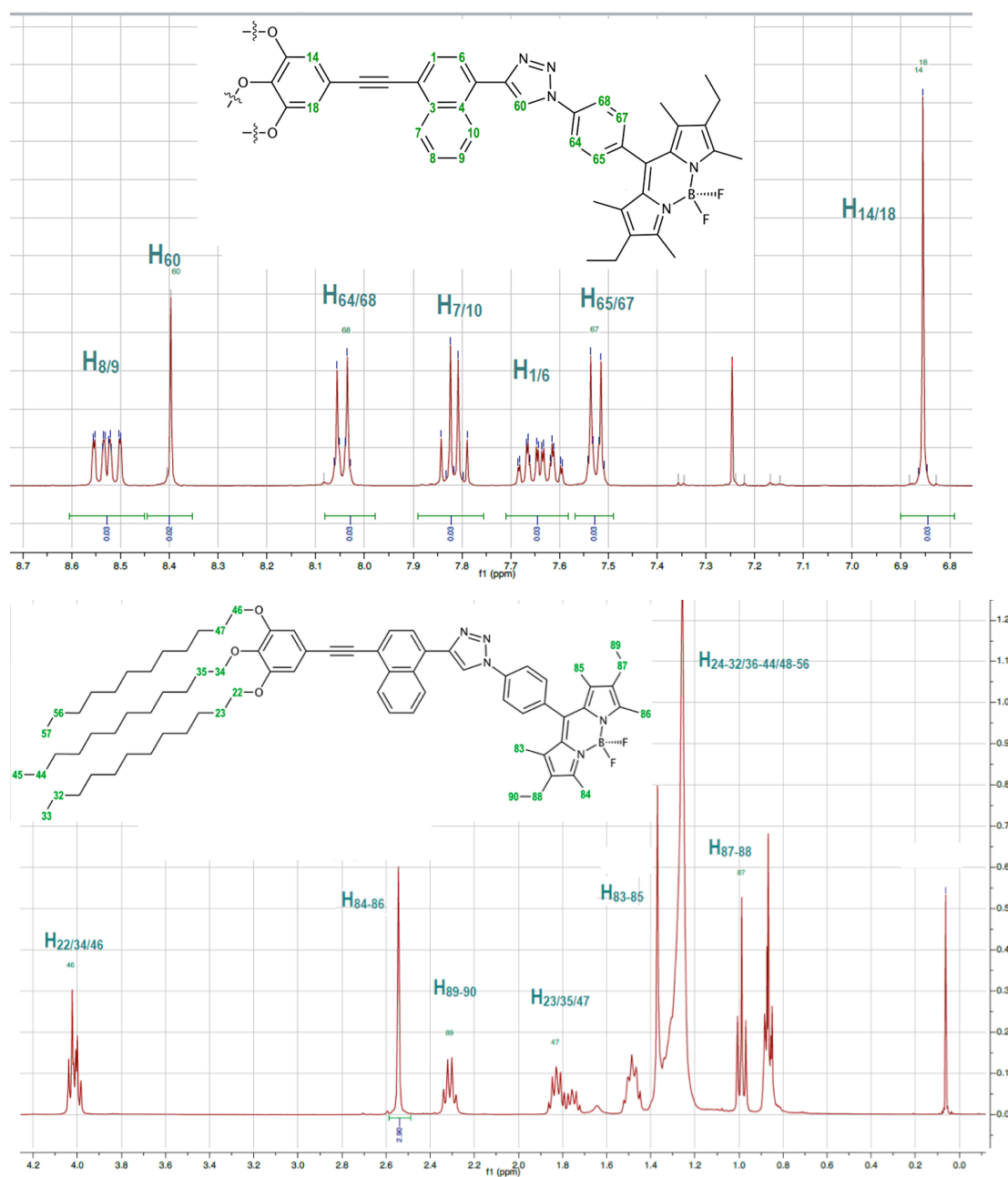
Characterization of **NAPBD** was carried via the combination of  $^1\text{H}$  NMR, COSY, HMQC and HMBC, and was analysed thoroughly. The collected data was sufficient to identify the target compound as genuine and pure. In Figure 6.5 is shown a selected numbering scheme for the compound.



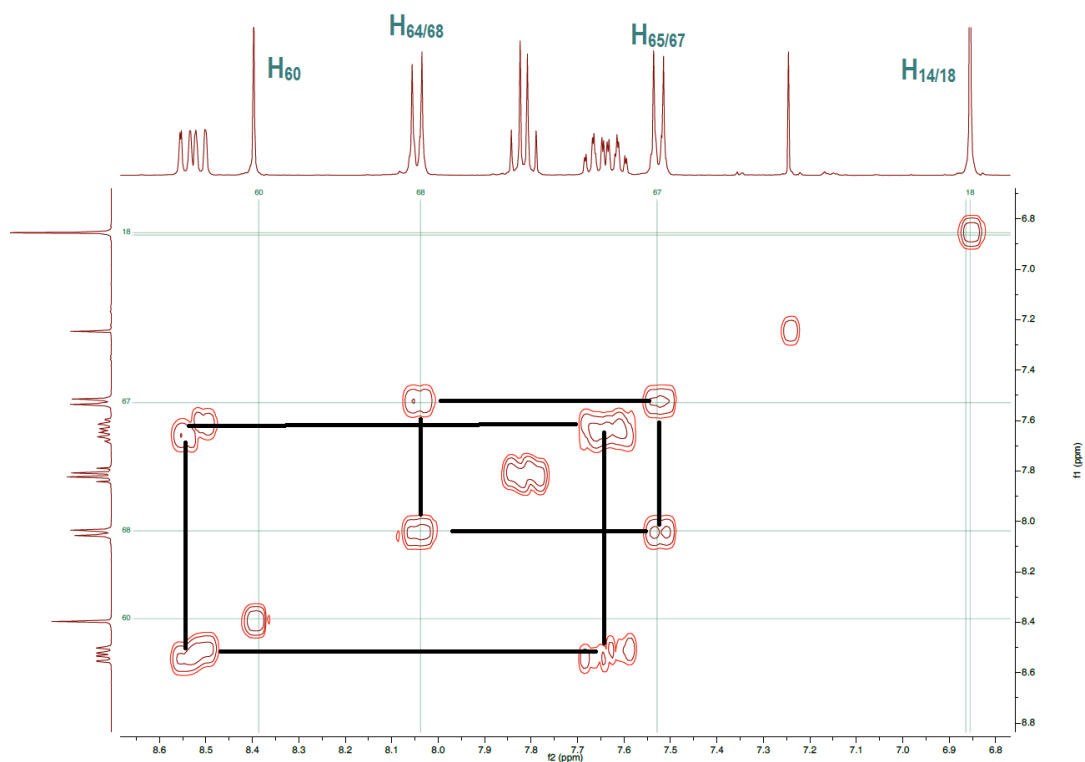
**Figure 6.5.** Partial numerical scheme of **NAPBD**, the carbon atoms were labelled in teal.

The  $^1\text{H}$  NMR spectrum for **NAPBOD** is shown in Figure 6.6, which clearly displays resonances associated with both the aromatic and aliphatic portions of the dyad structure. In assigning the resonances COSY was particularly useful and a selection of spectra are shown in Figures 6.7 and 6.8. The two doublets at 8.05 ppm and 7.5 ppm are clearly correlated. The multiplet signals at 8.55 ppm and 7.65 ppm are again spin-coupled, even though it should be noted that there are signs of signal overlap. In the aliphatic region of the COSY spectrum is a little more complex because of overlap of resonances. It is easy to see the cross correlation for the 3  $\text{OCH}_2$  groups with their neighbouring  $\text{CH}_2$  units at around 1.8 ppm. The correlation between the quartet and triplet at 2.3 ppm and 1.0 ppm, respectively, readily assigned these to the ethyl group of the Bodipy unit. The quadropolar  $^{11}\text{B}$  nucleus was revealed by its characteristic triplet at -0.1535 ppm with the  $^{11}\text{B}$ - $^{19}\text{F}$  coupling constant ( $J = 31.9$  Hz); the  $^{19}\text{F}$ -NMR spectrum of **NAPBOD** revealed a quartet at  $\delta = -145.62$  ppm, which

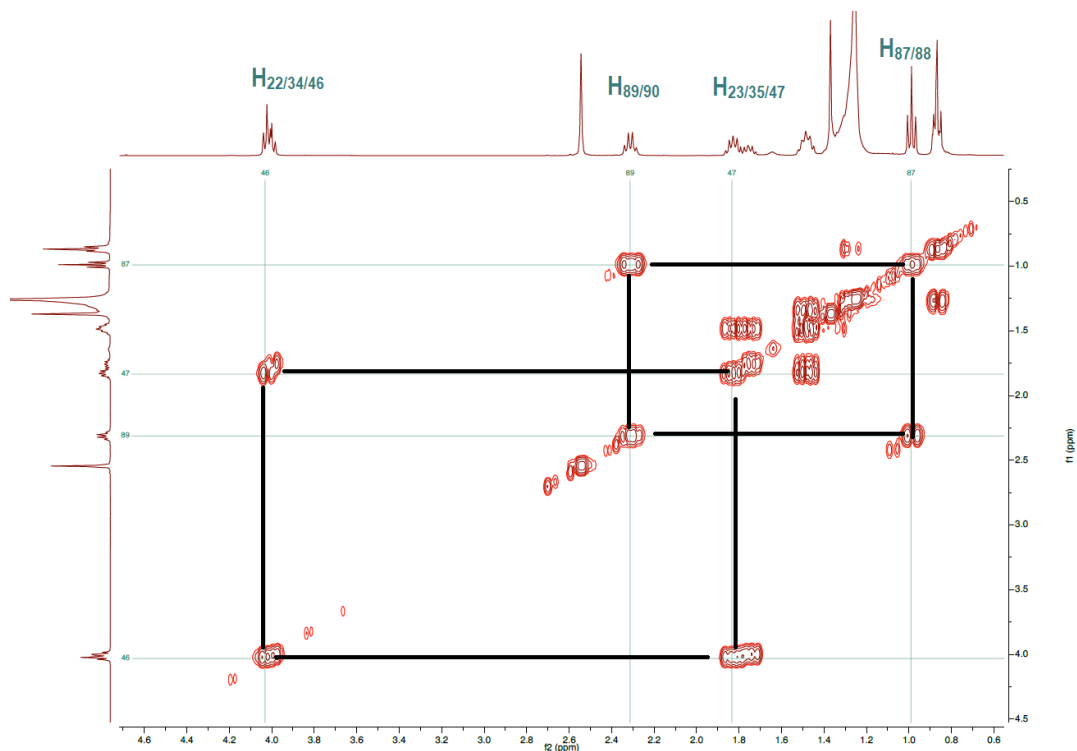
was consistent to previous values.



**Figure 6.6.**  $^1\text{H}$  NMR spectrum for **NAPBD** in  $\text{CDCl}_3$  at room temperature with assignment of peaks for the aromatic and aliphatic region.

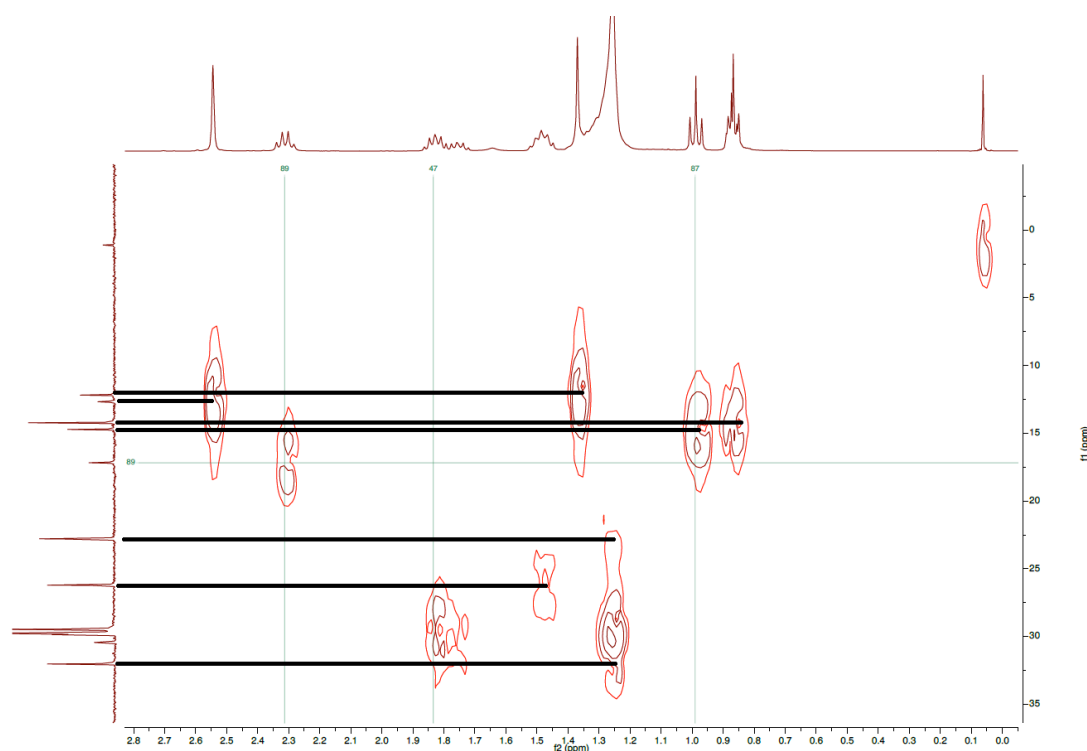


**Figure 6.7.** Partial  $^1\text{H}$ - $^1\text{H}$  COSY spectrum for **NAPBD** in  $\text{CDCl}_3$  showing selected correlations in the aromatic region.

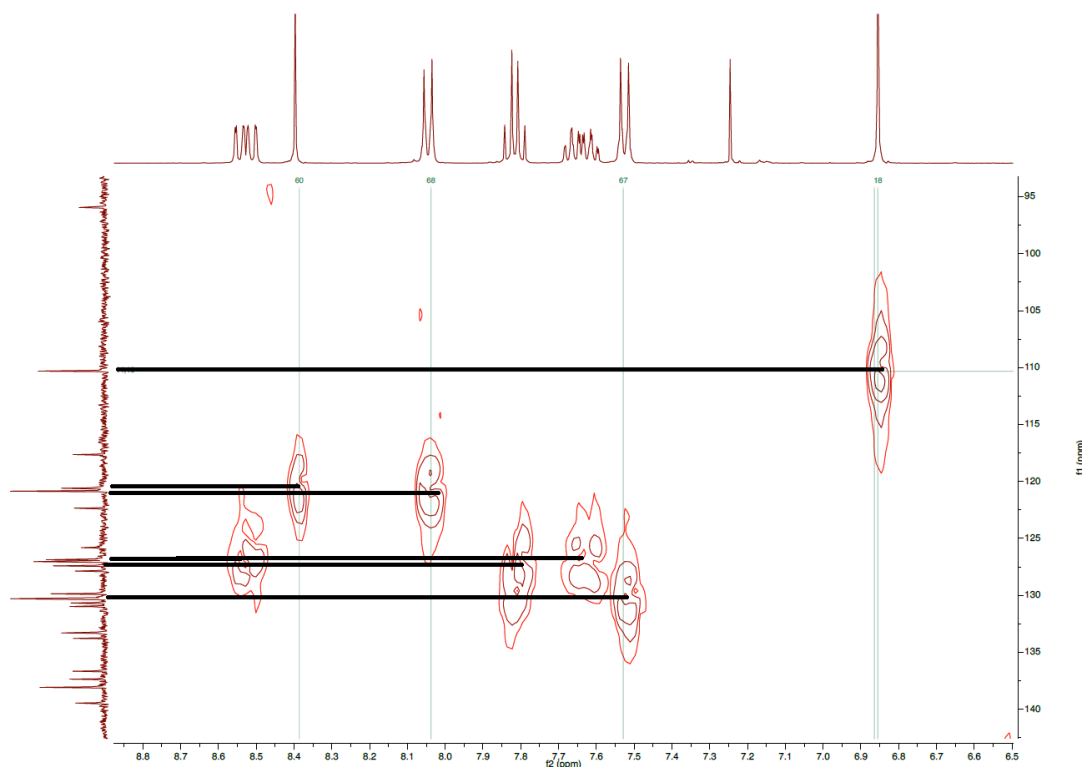


**Figure 6.8.** Partial  $^1\text{H}$ - $^1\text{H}$  COSY spectrum for **NAPBD** in  $\text{CDCl}_3$  showing selected correlations in the aliphatic region.

Peaks of the aromatic region for the  $^{13}\text{C}$  NMR spectrum appeared to be solvent dependent, two aromatic carbon resonances and several carbon resonances on the alkyl chain were missing because of accidental equivalence. To help analyze the  $^{13}\text{C}$  NMR spectrum more clearly a combination of 400 MHz heteronuclear multiple quantum coherence (HMQC) and heteronuclear multiple bond coherence (HMBC) spectra were collected. These reveal the direct C-H coupling correlation (apart from the quaternary carbons) and the remotely correlated C-H coupling. Aromatic carbons at Bodipy core, phenyl, and naphthalene were assigned alongside the alkyl moieties. It is very noticeable that the methyl groups (84/86), the most downfield in the  $^1\text{H}$  NMR spectrum, are upfield in the  $^{13}\text{C}$  NMR spectrum. Methyl groups are electron donating and move electron density onto the carbon atom. The most downfield resonance in the  $^{13}\text{C}$  NMR spectrum for the alkyl region is associated with a methylene on the long alkyl chain.

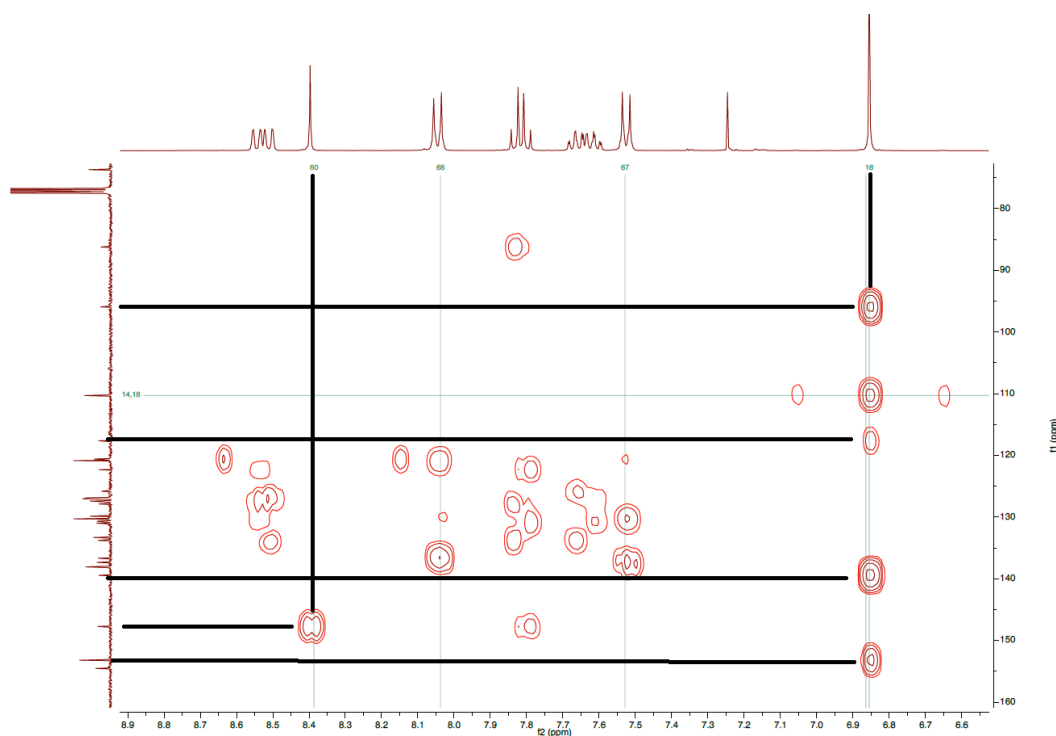


**Figure 6.9.** Selected HMQC spectrum for **NAPBD** in  $\text{CDCl}_3$  showing the alkyl region.



**Figure 6.10.** Selected HMQC spectrum for **NAPBD** in  $\text{CDCl}_3$  showing the aromatic region.

There are 16 quaternary carbons associated with aromatic groups for **NAPBD** and these can be partially identified in the HMQC spectrum of Figure 6.10; there are some peaks which are very close together and make full assignment difficult. The set of the most downfield resonances between 140-132 ppm are evidently quaternary. Using HMBC spectroscopy it is possible to delve a little more deeper into  $^{13}\text{C}$  resonance assignments. The equivalent protons 14/18 should be correlated to carbons 12, 13, 15/17 and 16. These four are marked on Figure 6.11, noting that the contour at 110 ppm is a breakthrough of the one-bond correlation. We can assign the quaternary carbon at 95 ppm to the acetylene group (carbon 12). The carbon resonance at ca. 85 ppm must be carbon 11 of the acetylene. This is confirmed by the 4-bond correlation to proton  $\text{H}_7$  of the naphthalene group. The other easy to identify carbon resonance is that of the triazole (carbon 59); there is a clear 2-bond correlation to proton  $\text{H}_{60}$ .

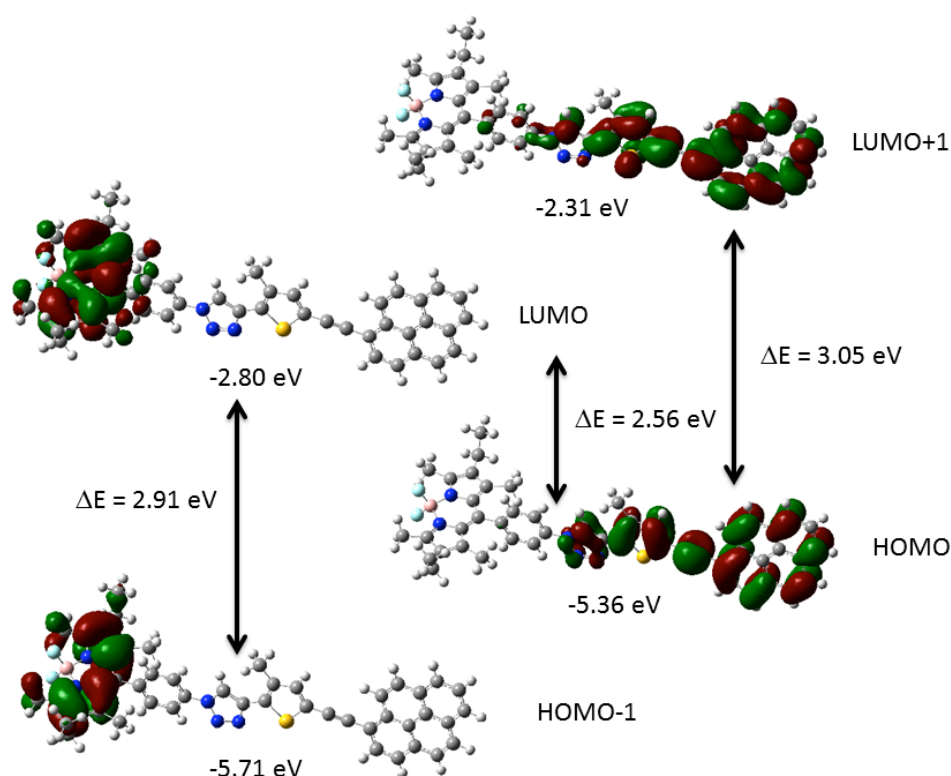


**Figure 6.11.** Partial HMBC spectrum for **NAPBD** in  $\text{CDCl}_3$  showing the aromatic region.

### 6.2.3 Molecular Orbital Calculation and Energy Diagrams

The role of the triazole unit in **PTTBD** and **NAPBD** is to principally decouple the two photoactive units. Certainly previous work by ourselves and others, suggests that the unit is a conducive for this purpose. In order to show the point more clearly molecular orbital calculations were carried out using Gaussian 03. For brevity the case for **PTTBD** is only discussed. The structure for **PTTBD** was energy-minimised *in vacuo* (Hartree-Fock) and refined using DFT (B3LYP) and using a 6-311G basis set. The fully minimised structure is very similar to the X-ray determined structure. A collection of the most significant HOMOs and LUMOs is shown in Figure 6.12. The HOMO is localised on the pyrene-thiophene unit while the HOMO-1 is associated with Bodipy. The HOMO plot is very similar to that calculated for the control compound **PT**. The LUMO is associated with the Bodipy while the LUMO+1 is localised on the pyrene-thiophene unit. It is evident that the HOMO-LUMO gap

is correlated with a possible electronic transition from the pyrene-thiophene group to the Bodipy. The *in vacuo* calculations clearly do not take into account solvent effects. They do, however, at least qualitatively predict that the Bodipy-based electronic transitions will contribute to the lowest energy absorption band. In addition, the calculations also show that the pyrene and thiophene are highly conjugated. As discussed later the coupling of the two units is especially pertinent with regard to the nature of the emissive state.



**Figure 6.12.** Selection of HOMOs and LUMOs for **PTTBD** calculated by DFT (B3LYP) 6-311G basis set.

#### 6.2.4 Photophysical Measurement and Analysis

##### **PTTBD**

The basic properties for the control compound, **PT**, were reported previously. In summary, the electronic absorption spectrum comprises a series of bands which traverse from the UV just into the visible region. The lowest energy

absorption band is centred at  $\lambda_{\text{ABS}} = 393 \text{ nm}$ , and is assigned to a  $\pi-\pi^*$  transition. Absorption spectra collected in different polarity solvents are slightly sensitive to the change. Fluorescence spectra, in comparison, alter in appearance and the emission maxima ( $\lambda_{\text{FLU}}$ ) shift with changing the solvent. Fluorescence lifetimes ( $\tau_s$ ) for **PT** were measured by time-correlated single-photon counting. In order to obtain a meaningful fit it was necessary to introduce a rise-time to the fluorescence profile ( $\tau_{\text{RIS}}$ ). Values for  $\tau_{\text{RIS}}$  were noticeably dependent on the solvent, and in particular showed a good correlation to solvent viscosity ( $\eta$ ). Fitting of the data to the Stokes-Einstein expression (Eq. 1), which assumes hydrodynamic friction, afforded a volume for the molecular rotor ( $V$ ) of ca.  $144 \text{ cm}^3 \text{ mol}^{-1}$  ( $239 \text{ \AA}^3 \text{ molecule}^{-1}$ ). The molar volume for pyrene is  $109 \text{ cm}^3 \text{ mol}^{-1}$  ( $181 \text{ \AA}^3 \text{ molecule}^{-1}$ ) whereas  $V$  for the alkyl-thiophene is  $204 \text{ cm}^3 \text{ mol}^{-1}$  ( $338 \text{ \AA}^3 \text{ molecule}^{-1}$ ). The results imply that the pyrene unit must rotate in **PT** to form the fluorescent state.

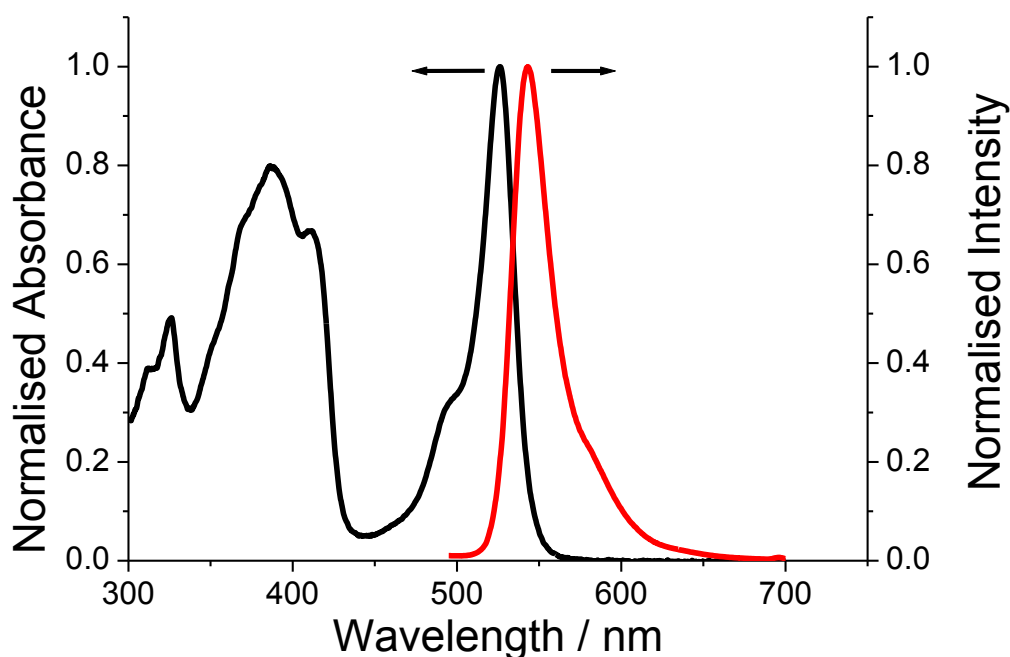
$$\tau_{\text{RIS}} = \frac{\eta V}{k_B T} \quad (\text{Eq. 1})$$

The excited state behaviour of **PT** is best described as a mixing between a  $\pi-\pi^*$  excited state and an intramolecular charge transfer state formed by partial electron migration from the pyrene to the thiophene group. The molecule must adopt a preferred geometry to support partial charge transfer in agreement with the rise-time data. The quantum yields of fluorescence ( $\phi_{\text{FLU}}$ ) and fluorescence lifetimes ( $\tau_s$ ) for **PT** are collected in Table 6.2. The rates for radiative decay ( $k_{\text{RAD}} = \phi_{\text{FLU}}/\tau_s$ ) vary slightly across the solvent series.

In Chapter 5 the absorption and fluorescence profiles for **PHBD** were discussed since again this compound is a good control. The absorption spectrum for **PTTBD** in MeTHF contains both features of **PT** and **PHBD** (Figure 6.13), with the intense band for the pyrene group masking the  $S_0-S_2$



transition at ca. 350 nm associated with the Bodipy moiety ( $\epsilon_{\text{MAX}} = 57,500 \text{ M}^{-1} \text{ cm}^{-1}$ ). The Bodipy-based  $S_0$ - $S_1$  electronic absorption maximum ( $\lambda_{\text{ABS}} = 526 \text{ nm}$ ,  $\epsilon_{\text{MAX}} = 72,000 \text{ M}^{-1} \text{ cm}^{-1}$ ) for **PTTBD** is identical to **PHBD**. We infer that ground state electronic communication between PT and BD in the dyad is negligible. Fluorescence from **PTTBD** is readily detected and is centred at  $\lambda_{\text{FLU}} = 543 \text{ nm}$ . The profile matches extremely well with the fluorescence spectrum for **PHBD**; both  $\phi_{\text{FLU}}$  and  $\tau_{\text{s}}$  are within error identical to the control. The first-excited singlet state of the Bodipy for **PTTBD** does not appear to be quenched by the appended pyrene-thiophene group. The fluorescence excitation spectrum matches, in overall appearance, very well with the absorption spectrum over a wide spectral range. Importantly, there is a good match for the region



**Figure 6.13.** Ambient temperature normalised absorption (black) and fluorescence (red) spectra for **PTTBD** in dilute MeTHF.

corresponding to the pyrene-based chromophore which suggests that all photons absorbed by the group are collected at the Bodipy unit. A similar observation is seen for cyclohexane (CHX) and other non-polar solvents. In

contrast, in polar solvents (e.g., DMSO) there is a very noticeable depletion for the pyrene-based region in the fluorescence excitation spectrum. From this observation it is inferred that another state is formed which does not result in energy transfer to the Bodipy.

Solvent	$\phi_{\text{FLU}}$	$\tau_{\text{S}}$ ns	$k_{\text{RAD}}$ $10^8 \text{ s}^{-1}$	$k_{\text{NR}}$ $10^8 \text{ s}^{-1}$	$J_{\text{F}} 10^{-14}$ $\text{cm}^6 \text{ mmol}^{-1}$
MeCN	0.73	1.37	5.3	2.0	2.75
MeTHF	0.87	1.36	6.4	0.95	2.01
DCE	0.85	1.31	6.5	1.1	2.48
CHX	0.92	1.43	6.4	0.6	1.54
TOL	0.91	1.26	7.2	0.74	2.03
DMF	0.59	1.25	4.7	3.3	2.50
DMSO	0.63	1.18	5.3	3.2	3.00
THF	0.87	1.36	6.4	0.95	2.01
MEB	0.87	1.25	6.9	1.1	2.18
DEE	0.80	1.40	5.7	1.4	1.98

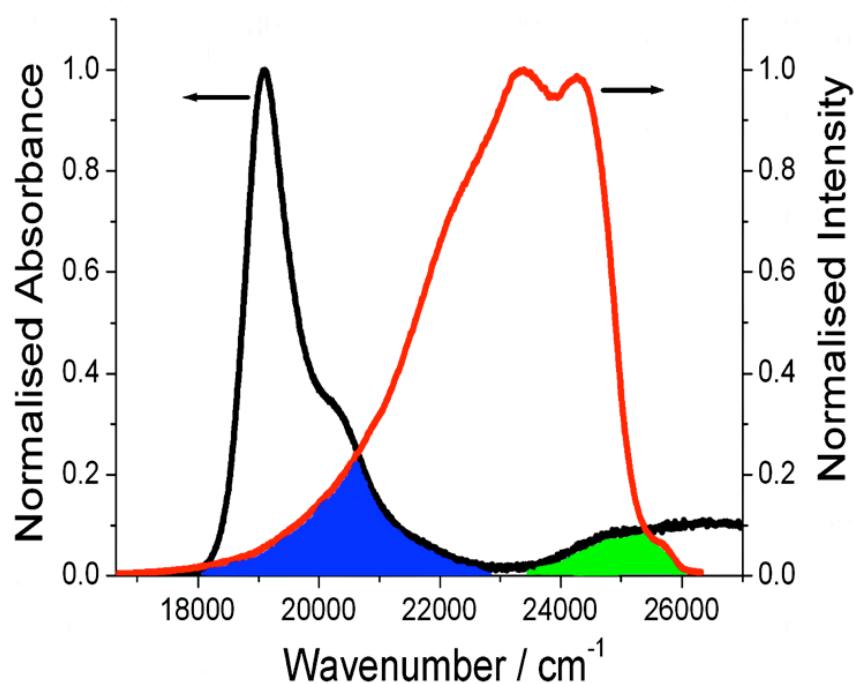
**Table 6.2.** Photophysical parameters for **PT** in a range of solvents and the calculated Förster overlap integral.

### Spectral Overlap

The normalised emission from **PT** overlaps well with the normalised absorption profile for **PHBD** for all the solvents. Illustrated in Figure 6.14 are the corresponding overlap regions for the case of MeCN. The region shown in blue is especially notable, and represents spectral overlap with the Bodipy  $S_0$ - $S_1$  electronic transition; the overlap with the  $S_0$ - $S_2$  electronic transition (green) is much smaller. In context of Förster theory the overlap integral ( $J_{\text{F}}$ ) is given by Eq. 2 where  $F$  is the fluorescence intensity of the donor at wavenumber ( $\nu$ ) and  $\epsilon$  is the molar absorption coefficient at wavenumber ( $\nu$ ). The denominator in the equation is used to normalise the fluorescence data.

$$J_{\text{F}} = \frac{\int F(\nu) \epsilon(\nu) \nu^{-4} d\nu}{\int F(\nu) d\nu} \quad (\text{Eq. 2})$$

The corresponding calculated values for  $J_F$  are collected in Table 6.2, and take into account the small shift in  $\lambda_{\text{ABS}}$  for **PHBD** with the solvent polarizability. Evidently, the overlap integral diminishes by nearly a half by changing the solvent from MeCN to CHX.

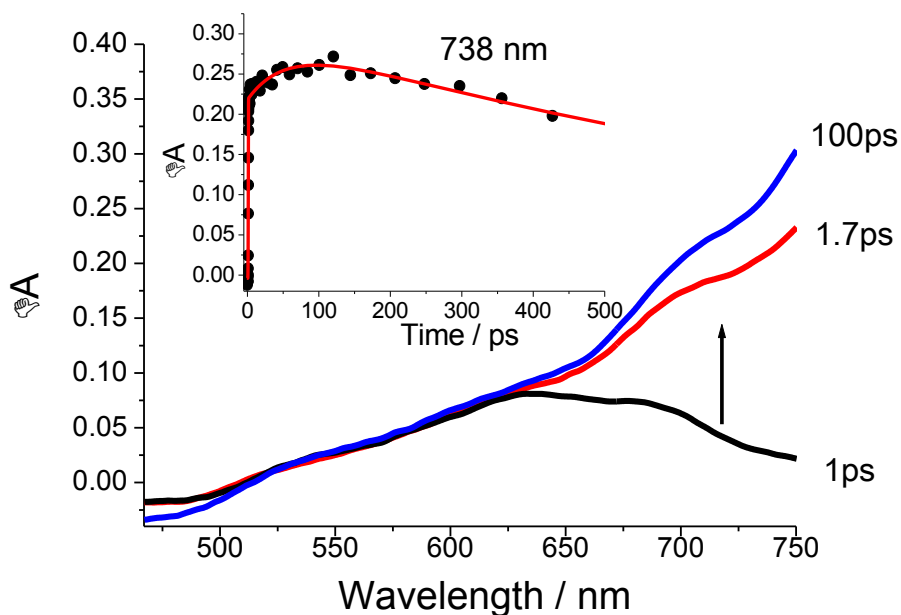


**Figure 6.14.** The spectral overlap regions from the normalised emission for **PT** and absorption for **PHBD**. The identification of the regions in blue and green are discussed in the text.

#### *Femtosecond Spectroscopic Studies*

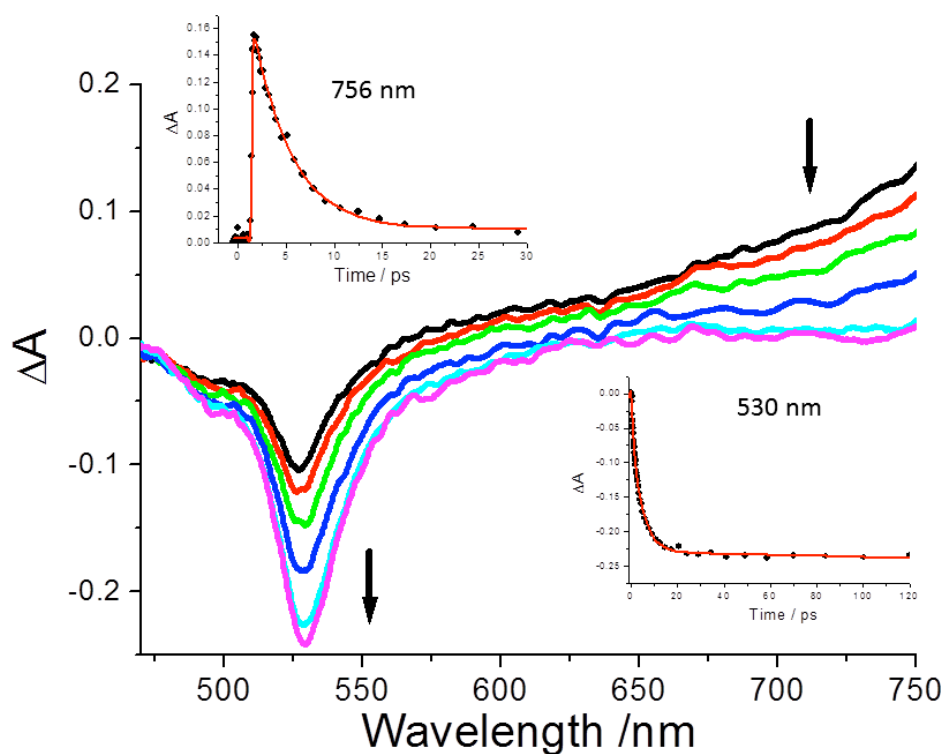
The temporal excited state behaviour for the control compound **PT** was probed by femtosecond transient absorption spectroscopy. Excitation of a solution of **PT** in toluene with a 70 fs laser pulse delivered at 400 nm afforded transient profiles as shown in Figure 6.15. After a delay time of ca. 1.7 ps there is a very distinct broad featureless absorption band that stretches well into the red region. Over a further 100 ps or so this feature continues to increase in

intensity and then decays away slowly over the nanosecond timescale. Global fitting of the transients affords a rise-time  $\tau_1$  of 38 ps which is in extremely good agreement with  $\tau_{\text{RIS}}$  measured in toluene by single-photon-counting. The slow component lifetime ( $\tau_2$ ) is around 1.4 ns. The broad transient absorption profile is taken to be indicative of a partial charge- transfer state.



**Figure 6.15.** Transient absorption profiles recorded after excitation of **PT** in toluene with a 70 fs laser pulse delivered at 400 nm. Time delays are shown. Insert shows kinetic trace measured at 738 nm and the least-squares fit (red) to the data points.

The excited state dynamics for **PTTBD** was also probed by femtosecond transient absorption spectroscopy. The temporal behaviour was slightly more solvent dependent, especially for the highly polar solvents of DMF and DMSO. The two cases for medium polarity and high polarity solvents are discussed. Excitation of the sample in MeTHF with a 70 fs laser pulse delivered at 400 nm afforded transient profiles as shown in Figure 6.16.



**Figure 6.16.** Transient absorption profiles recorded after excitation of **PTTBD** in MeTHF with a 70 fs laser pulse delivered at 400 nm. Time delays are 1.9 ps (black), 2.4 ps (red), 3.5 ps (green), 5.9 ps (blue), 14.7 ps (light blue) and 41.1 ps (pink). Insert shows kinetic traces at two different wavelengths and the least-squares fit (red) to the data points.

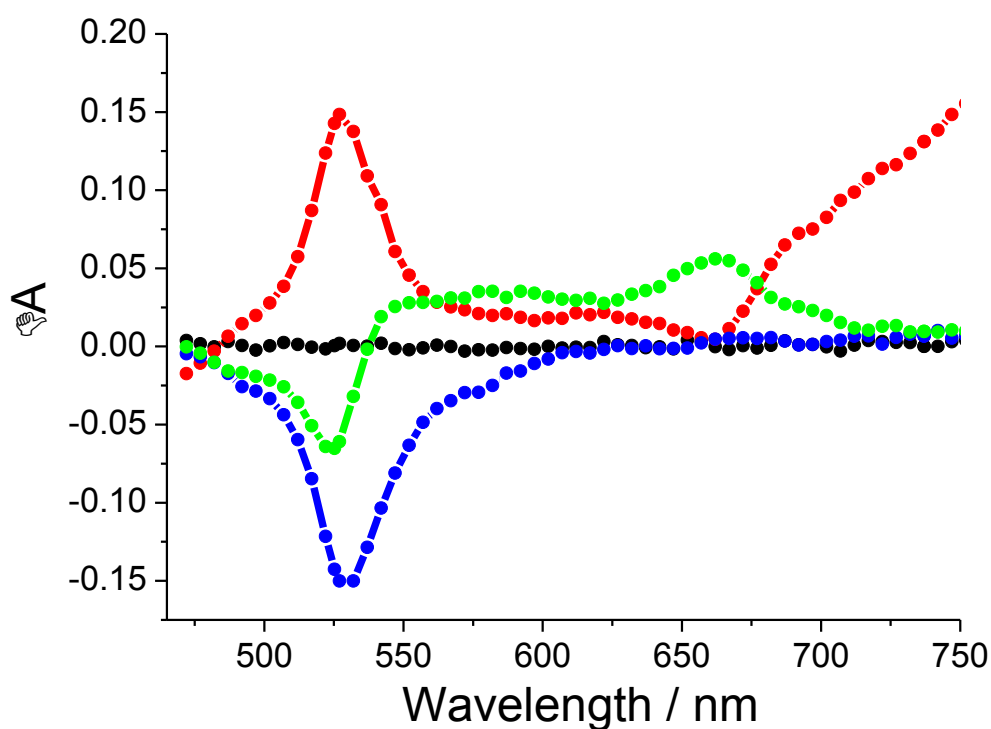
At the excitation wavelength *ca.* 90% of the photons are absorbed by the pyrene moiety. The remaining photon balance is taken up by the  $S_0$ - $S_2$  absorption for the Bodipy group. The  $S_2$  to  $S_1$  conversion is known to be rapid. At the very early time delay (1.9 ps) there is a clear bleaching at around 530 nm, which represents depletion of the ground state. In addition there is a synchronous strong absorption profile that stretches to very long wavelength. This profile cannot be assigned to either the Bodipy radical cation or anion. By comparison to the control we take the long-wavelength absorption profile to represent formation of the pyrene-based partial charge transfer state. Over some 20 ps the profile decays away to leave a level region. During the same timescale there is an increase in the bleach region. The lifetime for decay of the long-wavelength transient ( $\tau_1$ ) is 3.8 ps, which matches exceptionally well

with the increase in the bleach ( $\tau_2 = 3.7$  ps). Similar transient spectral profiles were seen for **PTTBD** in THF, TOL, DCE, DEE, MEB and CHX. Values for  $\tau_1$  and  $\tau_2$  in the range of solvents are collected in Table 6.3. A global analysis of the data for all the solvents is interesting in that a further transient profile emerges from the fit. In CHX the additional transient profile is barely discernible, but it is more prominent in, for example, DCE and THF. For all solvents, long-wavelength transient absorption bands are again evident and decay with time constants ( $\tau_{GF}$ ) that are similar to values for  $\tau_1$  and  $\tau_2$  (Table 6.3).

Solvent	n	$\tau_1$ ps	$\tau_2$ ps	$\tau_{GF}$ ps
MEB	1.517	4.7	3.6	5.8
MeTHF	1.403	3.8	3.7	3.4
DCE	1.445	2.3	2.7	3.1
CHX	1.426	6.4	5.8	7.5
TOL	1.497	5.2	4.3	5.1
THF	1.407	3.6	3.7	2.9
DEE	1.352	5.0	4.2	4.6
DMF	1.430	3.2	2.4	2.6
DMSO	1.478	2.9	2.5	2.4
MeCN	1.344	2.9	2.4	2.5

**Table 6.3.** Kinetic parameters measured for **PTTBD** in a range of solvents.

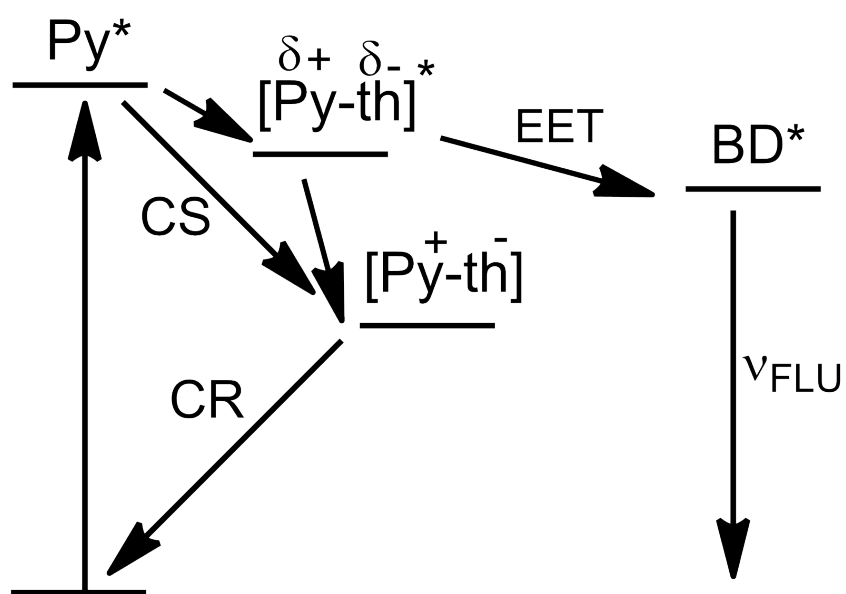
In comparison, the transient absorption profiles recorded for **PTTBD** in DMF are more supportive of the presence of another species (Figure 6.17). Following decay of the partial charge transfer state over 2.6 ps a second species is evident which decays with a lifetime of around 95 ps. As well as a bleach effect at around 524 nm there is a very noticeable broad absorption centred at *ca.* 660 nm. The feature is consistent with the radical anion of a substituted and conjugated thiophene group. The Bodipy  $S_1$  state is clearly formed as indicated by the long-lived profile (blue) in the spectral records. The cases for DMSO and MeCN are very similar .



**Figure 6.17.** Component differential transient absorption spectra recorded for **PTTBD** in DMF following excitation with a 70 fs laser pulse at 400 nm. Lifetimes are 2.6 ps (red), 95 ps (green) and  $\sim 3$  ns (blue).

### Interpretation

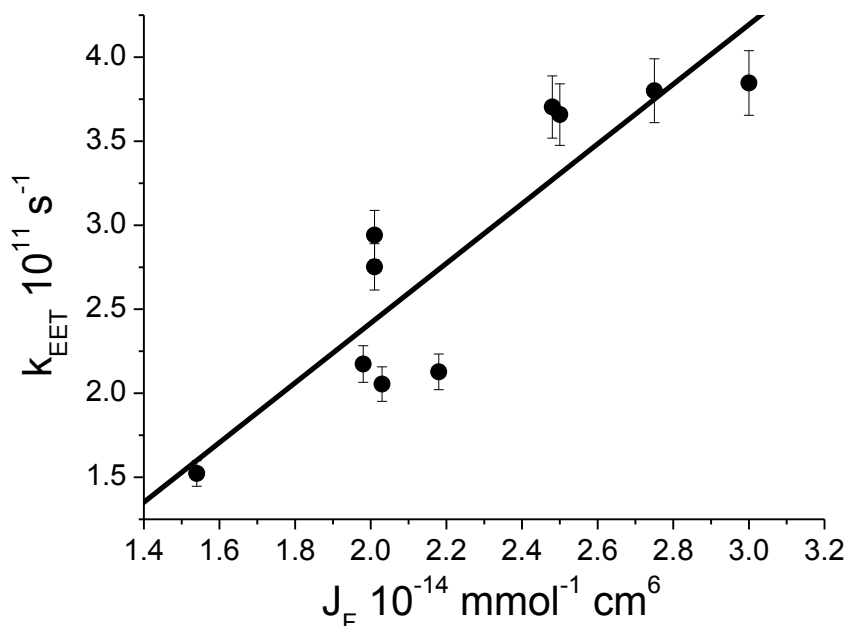
Even for the polar solvents (e.g., MeCN, DMF and DMSO) there is no compelling evidence to support the idea that the first-excited singlet state for the Bodipy group in **PTTBD** is quenched. We therefore rule out participation of electron transfer from (or to) the Bodipy  $S_1$  state involving the pyrene-thiophene (py-th) segment. There is some controversy on how effective the triazole (traz) group is at promoting electron exchange, or at facilitating electron transfer. In our own previous work in Chapter 5 we did not need to invoke any special electron conduit nature for the group. Thus, the view at this stage is that it acts to merely separate the two chromophore groups. Excitation of the pyrene-based unit results in fast formation of what resembles a partial charge-transfer state. In the low polarity solvents the time-resolved studies are consistent with the notion of energy transfer to the Bodipy unit from a pyrene-based partial charge-transfer state (Figure 6.18). The rates for electronic energy transfer ( $k_{\text{EET}}$ ) are taken as the average of the three lifetimes (Table 6.3).





**Figure 6.18.** Basic model to show deactivation pathways following excitation of the pyrene unit in **PTTBD**.

After EET the Py-th group resides in a high energy conformation, since to form the initial excited state the pyrene group must rotate. Thus, the molecular system undergoes structural relaxation accounting for the additional transient profile seen in the temporal records. In polar solvents (e.g., DMSO) the pyrene-based partial charge transfer state may also undergo full charge separation to produce  $\text{Py}^+ \text{--} \text{th}^-$ , because of solvent stabilisation of the two radicals. The charge-separated state can also be formed directly from the pyrene excited state. The fully charge separated state reforms the ground state by charge recombination (CR) (Figure 6.18). The energy of the charge separated state is too high in non-polar solvents to contribute to the deactivation pathway.

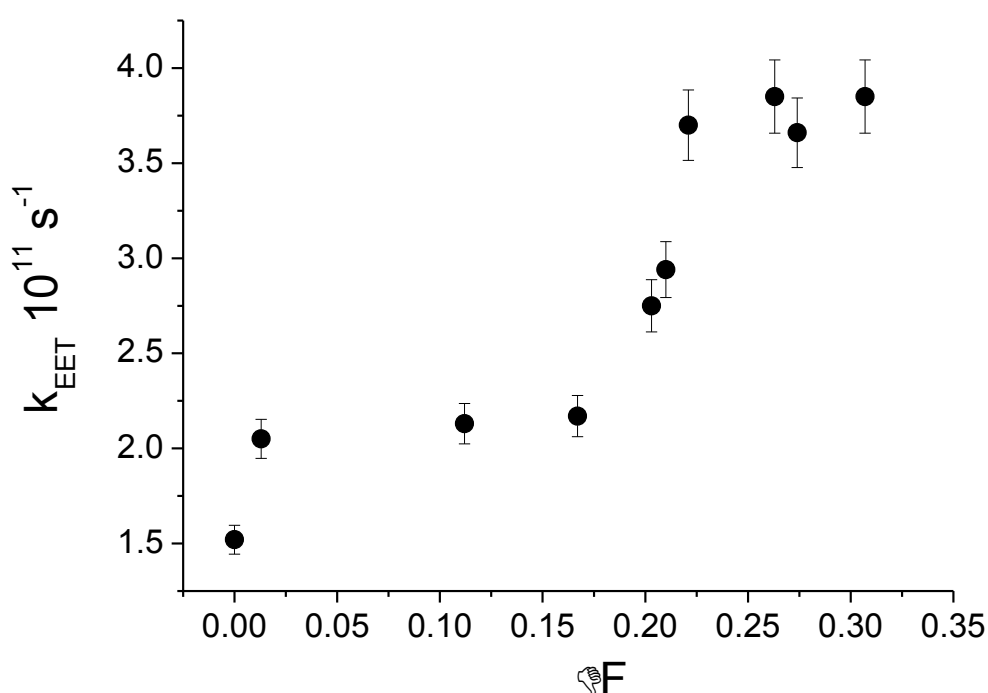


**Figure 6.19.** Relationship between the rate constant of energy transfer ( $k_{\text{EET}}$ ) and the Förster overlap integral ( $J_{\text{F}}$ ). Line represents the least-squares fit to the data points.

Armed with wealth of data collected on both **PT** and **PTTBD**, analysis in terms of the Förster equation is revealing. Remarkably, an adequate linear relationship is seen between  $k_{\text{EET}}$  and  $J_{\text{F}}$  for **PTTBD**, considering the disparity of solvents tested (6.19). In altering from one solvent to another it is assumed that both  $R$  and  $\kappa^2$  do not change greatly. This assumption may be, of course, too much of a simplification. The requirement to control  $J_{\text{F}}$  by changing the solvent polarity results in a 62% increase in  $1/n^4$  from 0.189 (MEB) to 0.306 (MeCN). Screening effects were originally assumed to be independent of donor-acceptor separation, orientation and shape. However, there is evidence that electronic coupling is unscreened at short distances and increases exponentially with increasing D-A separation. Oddly, there is an apparent inverse relationship between  $k_{\text{EET}}$  and  $1/n^4$  but it is difficult to rationalise the result. The nature of the donor and the fact that its dimensions are on par with the transition dipole moments may be a contributing factor. The solvent effect is perhaps more clearly seen by mapping  $k_{\text{EET}}$  against the solvent polarity function ( $\Delta F$ ) introduced by Lippert and Mataga (Figure 6.20). There is a very noticeable sigmoidal feature to the plot, the inflexion occurring at around  $\Delta F = 0.203$  (THF). Recent work has attempted to rationalise the solvent polarity effect on Förster energy transfer in a closely-spaced Bodipy dyad. Very subtle solvents effects operate which affect the transition dipole density and the separation distance. In this case the rate constant  $k_{\text{EET}}$  decreased with an increase in  $\Delta F$ ; roughly the opposite is witnessed in the dyad **PTTBD**. With increasing polarity the pyrene-based donor will exhibit more charge transfer character. In turn, the dipole moment will increase and the actual nature of the molecular orbital on the donor will change. One outcome from this is the likely perturbation of the transition dipole moment on the donor. It is likely that the reason for the profile shown in Figure 6.20 is a combination of several factors and it is difficult to identify the dominant aspect unequivocally.

It is noted that the data collected for **PTTBD** can be examined in term of

standard Förster theory. Although it is difficult to definitively define  $R$ , using several distances and  $\kappa^2 = 2/3$  the values for  $k_{\text{EET}}$  are very reasonable. In fact, by taking  $R_0$  values for each solvent and the corresponding fluorescence lifetimes for **PT** an average donor-acceptor separation distance of 13.8 Å is obtained. This distance is situated partially along the acetylene bond between the pyrene and thiophene groups. Such a separation distance is again in fitting with the nature of the donor excited state.

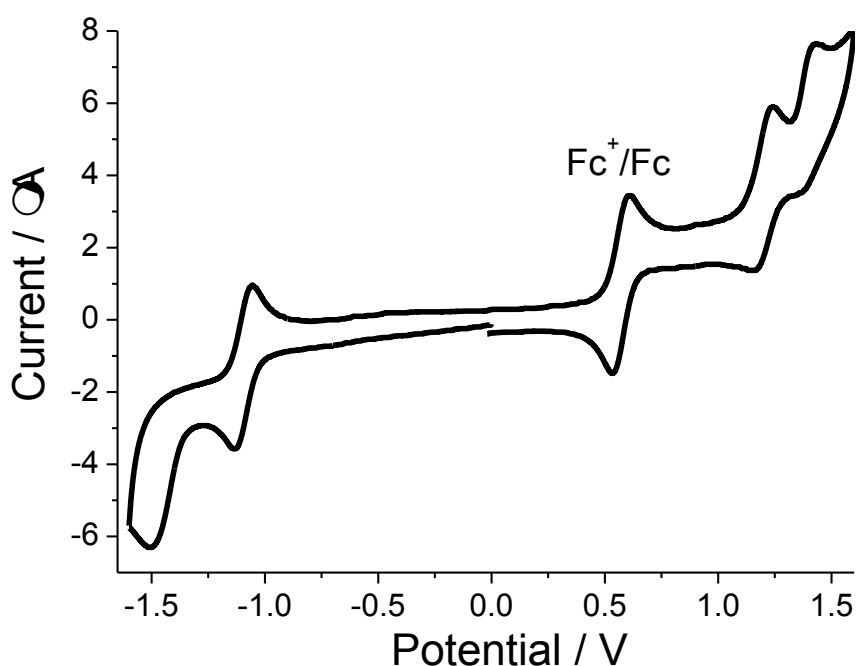


**Figure 6.20.** Relationship between the rate constant of EET for **PTTBD** and the solvent polarity function ( $\Delta F$ ).

## NAPBD

The starting point to establish for **NAPBD** was its redox chemistry to assess the likelihood for electron transfer processes following excitation of either chromophore. The cyclic voltammogram for the compound in dry DCM (0.2 M TBATFB) at a platinum electrode is shown in Figure 6.21. In the positive

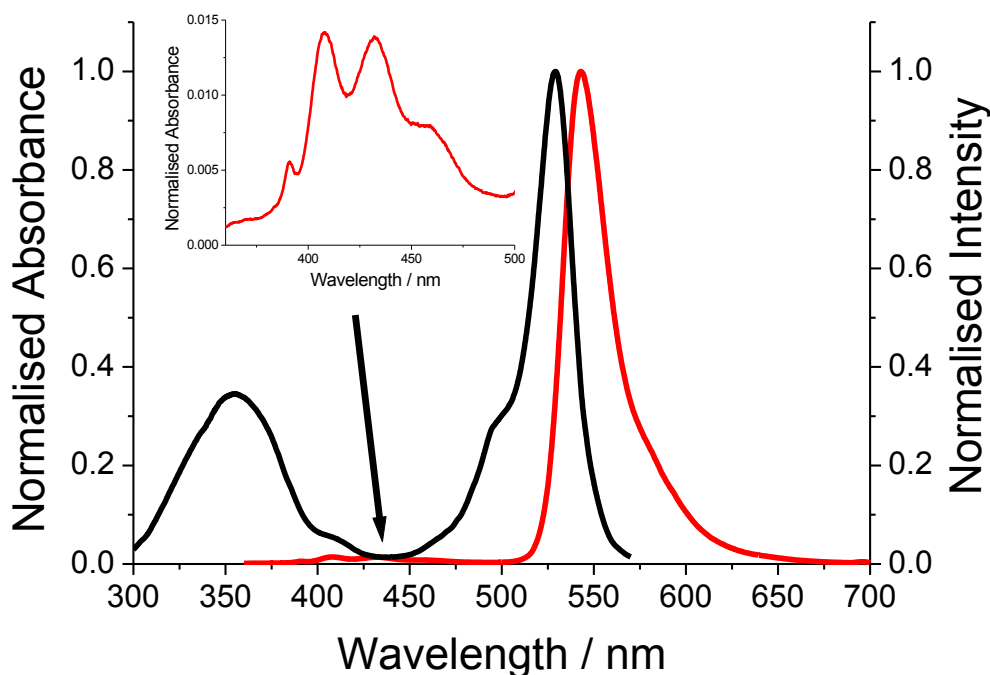
potential side of the CV is seen two reversible waves at  $E_{1/2} = +1.20$  V (70 mV)  $E_{1/2} = +1.40$  V (70 mV) vs Ag/AgCl. The first wave is oxidation of the Bodipy unit and the second is likely associated with oxidation of the trialkyloxybenzene unit. In the negative potential range a reversible wave is observed at  $E_{1/2} = -1.10$  V (70 mV) followed by an irreversible wave at  $E = -1.50$  V. The first wave is Bodipy-based redox chemistry but the second wave is a little more difficult to identify, and is possibly associated with reduction of the substituted naphthalene.



**Figure 6.21.** Cyclic voltammogram for **NAPBD** in dry DCM (0.2 M TBATFB) at a platinum working electrode. Reference electrode = Ag/AgCl.

The absorption and fluorescence profiles for **NAPBD** in MeTHF are shown in Figure 6.22. The absorption band for the naphthalene-based unit is located at around 356 nm and obscures slightly the  $S_0$ - $S_2$  absorption band for the Bodipy group. The sharp Bodipy-based absorption is located at  $\lambda_{\text{ABS}} = 528$  nm. Strong emission is observed from **NAPBD** from the Bodipy group and the quantum yield of fluorescence is very similar to the control compound **PHBD** in the same solvent. The excited state of the Bodipy is not quenched by any electron

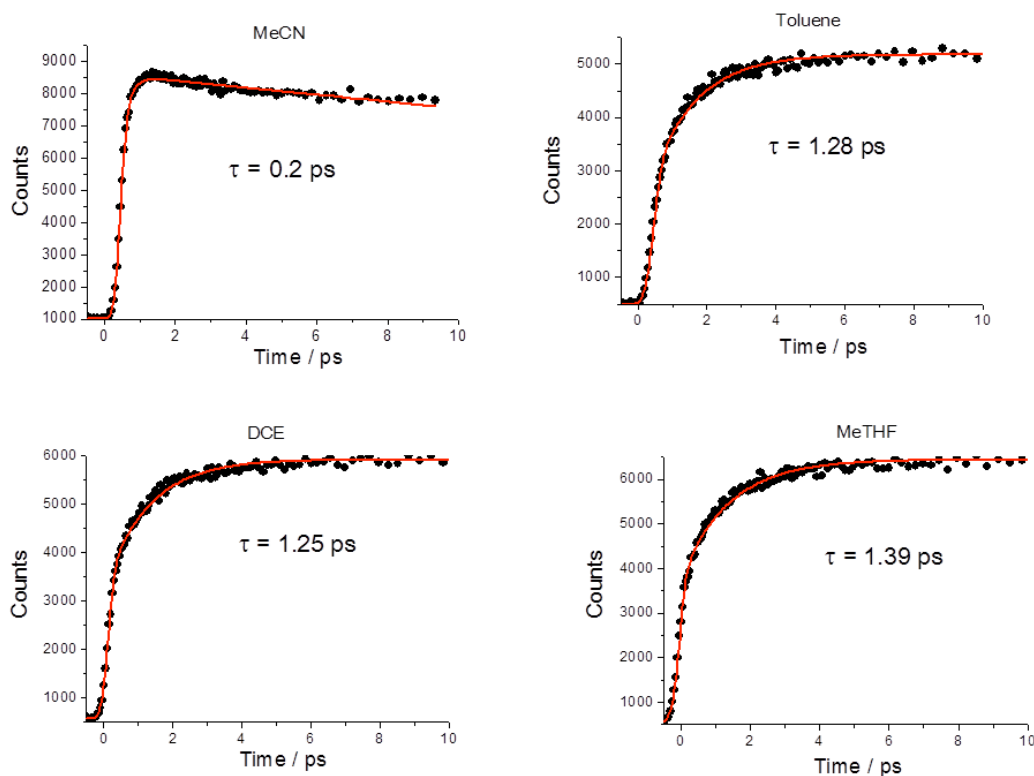
transfer process, and does agree with the electrochemistry data which would locate a charge transfer state slightly higher in energy (ca. 200 mV) than the singlet state .



**Figure 6.22.** Absorption (black) and emission (red) spectra for **NAPBD** in MeTHF. Insert shows expansion of region shown by the arrow.

To try and see if energy transfer was actually taking place in **NAPBD** the technique of fluorescence up-conversion spectroscopy was used. This spectroscopic tool is capable of measuring fast events by measuring the grow-in and decay of the Bodipy-based emission. A collection of spectra are shown in Figure 6.23. We can see that the rise times for the Bodipy-based emission are extremely fast. In fact, the timescales appear to be too fast for electronic energy transfer, considering that we see emission from the donor in the steady-state measurements. In addition, the overlap integral must be small because emission from the naphthalene-based chromophore is located in the region where there is very little Bodipy-based absorption (shown as arrow in Figure 6.22). One possible explanation for the fast rise times is they simply

mirror the internal conversion in the Bodipy chromophore as the  $S_1$  state is formed from the upper-lying  $S_2$  state. More experiments will be required to prove this point.



**Figure 6.23.** Collection of fluorescence up-conversion spectra for **NAPBD** in a range of solvents. Least-squares fits to the data points are shown in red.

### 6.3 Remarks and Conclusion

Energy transfer via a pyrene-based excited state to Bodipy appears to follow the recognised Förster overlap principle. The oddity in the results is the observed inverse Förster behaviour for the screening factor which has not been discussed in detail in the literature. This may be purely coincidental, or more indicative of energy transfer from states with high charge transfer character. Certainly this latter interpretation is more interesting. We note that once again the triazole unit appears to effectively decouple the two chromophores, so that there is no need to invoke a Dexter-like dual electron

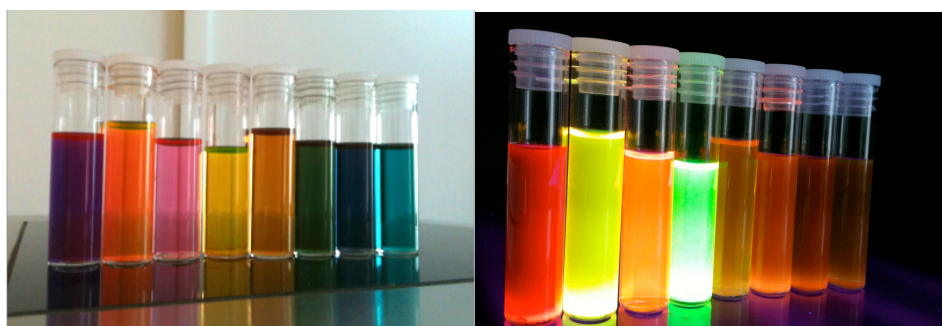
exchange mechanism. The same type of behaviour was reported for the dyad discussed in the previous chapter. Seen in the emission profile is structured fluorescence from the naphthalene-based donor, which implies that the efficiency for energy transfer in **NAPBD** is reduced when compared to **PTTBD**. Again the idea that the triazole is a poor conduit for promoting through-bond energy transfer was supported.

## 6.4 References

- 1 (a) Q. T. Nguyen and R. Y. Tsien (2013) Fluorescence-guided surgery with live molecular navigation - a new cutting edge. *Nat. Rev. Cancer* **13**(9):653-62;  
(b) R. Hoffman and P. Held (2013) An Introduction to Fluorescence Resonance Energy Transfer (FRET) Technology and its Application in Bioscience. BioTek instruments.
- 2 J. E. González and R. Y. Tsien (1995) Voltage sensing by fluorescence resonance energy transfer in single cells. *Biophys J* (**69**):1272-1280.
- 3 W. J. Greenleaf, M. T. Woodside and S. M. Block (2007) High-resolution, single-molecule measurements of biomolecular motion. *Annu Rev Biophys Biomol Struct.* (**36**): 171–190.
- 4 A. C. Krügera and V. Birkedal (2013) Single molecule FRET data analysis procedures for FRET efficiency determination: Probing the conformations of nucleic acid structures. *Methods (submitted)*.
- 5 M. V. Myakishev, Y. Khripin, S. Hu, D. H. Hamer (2001) High-throughput SNP genotyping by allele-specific PCR with universal energy-transfer-labelled primers. *Genome Res.* (**11**):163-69.
- 6 A. C. Benniston, A. Harriman A, D. J. Lawrie, S. A. Rostron. (2004) A closely-coupled pyrene dimer having unusually intense fluorescence. *Eur. J. Org. Chem.* (**10**), 2272-76.
7. A. Harriman, M. Hissler and R. Ziessel (1999) Photophysical properties of pyrene-(2,2'-bipyridine) dyads. *Phys. Chem. Chem. Phys.*, (**1**), 4203-11.

# Chapter 7

## Conclusion Remarks & Outlook





## 7.1 Concluding Remarks

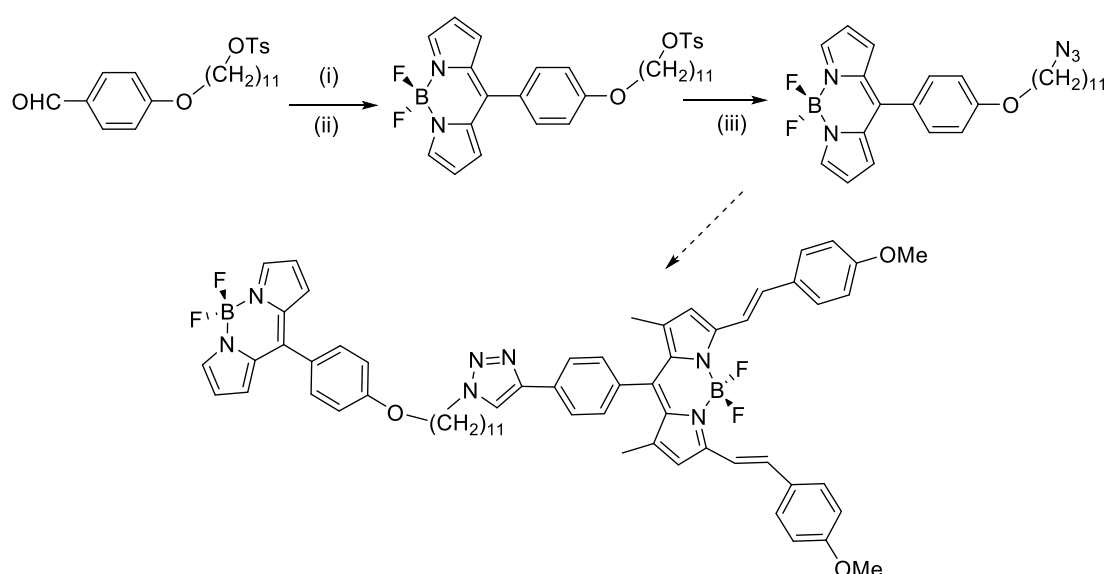
The main theme covering all the chapters discussed in the thesis is artificial photosynthesis, and the conditions for electronic energy transfer in terms of Förster resonance energy transfer have been validated. Alongside fundamental photophysical studies the molecular rotor systems and Bodipy-based dyad systems also have application as molecular environmental sensing probes. They have great potential offering opportunity to map out physical and conformational dynamics on the nanoscale, but more work will need to be carried out.

The work presented in Chapter 3 evince simple “click” chemistry can be used to produce metal-based assemblies which display interesting temperature dependent luminescence behaviour. The main problem of starting with Ru-terpy units as the photoactive group is the low quantum yield, but this could be solved by using other transition metal complexes such as highly luminescent iridium complexes. There was some attempt at trying this type of chemistry but the high temperature conditions employed to introduce, for example, Ir-terpy proved to be too harsh. The simple dual Bodipy molecular systems were easier to produce but the complication in this case is the probability of reverse energy transfer and the flexibility in the systems. Some of the problems were tried to be addressed in the dyads produced (or attempted ) in Chapter 4. The expanded Bodipy group shifted the absorption towards lower energy and reduced the possibility of reverse energy transfer. Again the dyads are flexible because of the linker groups. The rigid molecular systems introduced in Chapters 5 and 6 allowed a more detailed study of Förster energy transfer over short separation distances. In particular, we were able to show that the triazole group is a rather poor group to facilitate through-bond energy transfer via a Dexter-type mechanism. This view of the poor electron conducting nature of the triazole is still under debate as work by other groups

seem to show that electron flow through the group is good. More work is still needed to finally resolve this issue.

## 7.2 Outlook: Future Work

In attempt to produce certain molecular systems in Chapter 4 there were a few failures especially when using the polyether linker. One hypothesis was the polyethylene glycol in some way interfered with the catalytic activity of the “click” reaction. It was planned to replace the polyethylene glycol spacer with aliphatic carbon chains as outlined in Scheme 7.1. The synthetic route in this case relies on building the rotor Bodipy into the one half starting from the aldehyde precursor. It was possible to produce the azide rotor but because of time constraints, and limited materials, the final reaction was not attempted. In the future it should be possible to scale-up the reaction and see if this method will work.

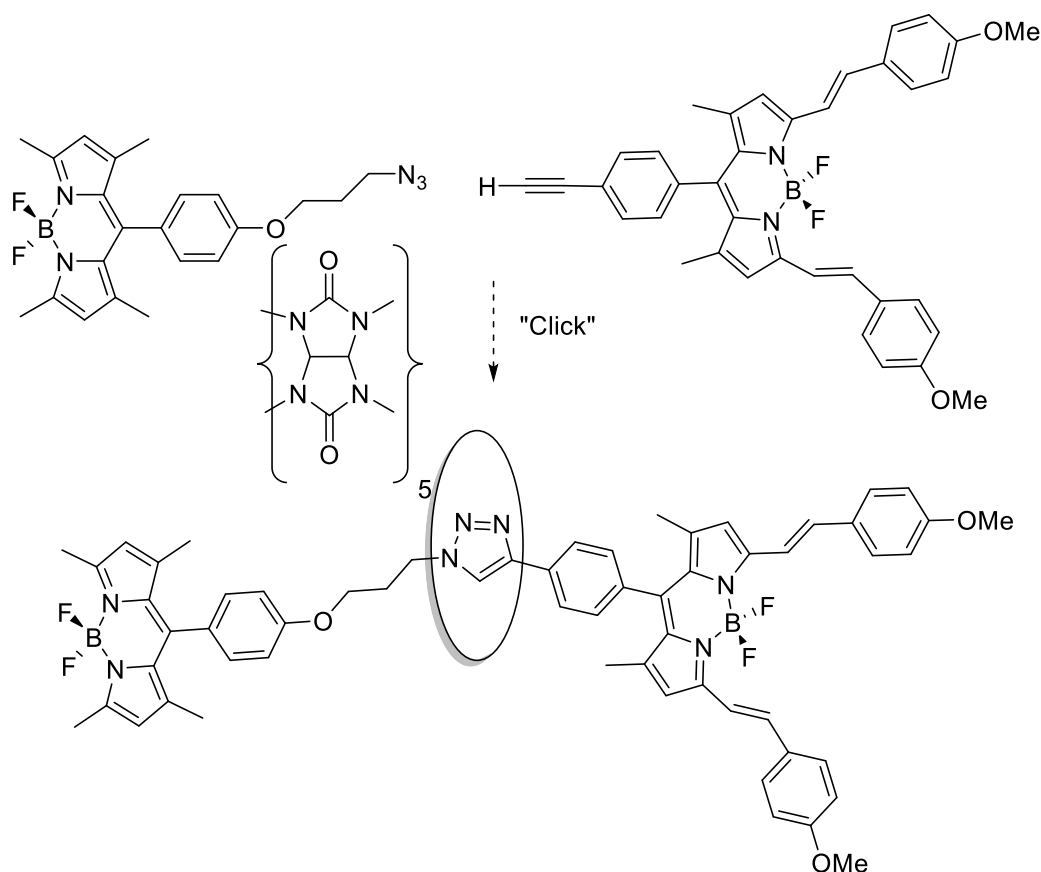


**Scheme 7.1.** Synthetic route to the undecane connected dyad system. *Reagents and Conditions:* (i) pyrrole, RT, TFA, 8h, CH<sub>2</sub>Cl<sub>2</sub>, DDQ, 8h. (ii) BF<sub>3</sub>Et<sub>2</sub>O, Et<sub>3</sub>N, CH<sub>2</sub>Cl<sub>2</sub>. (iii) NaN<sub>3</sub>, DMF/H<sub>2</sub>O, 80 °C, 1h.

### *Rotaxane formation using Cucurbituril*

In attempts to produce relatively flexible systems the reactions often failed or it was difficult to identify the final product. It is known that cucurbituril can act as

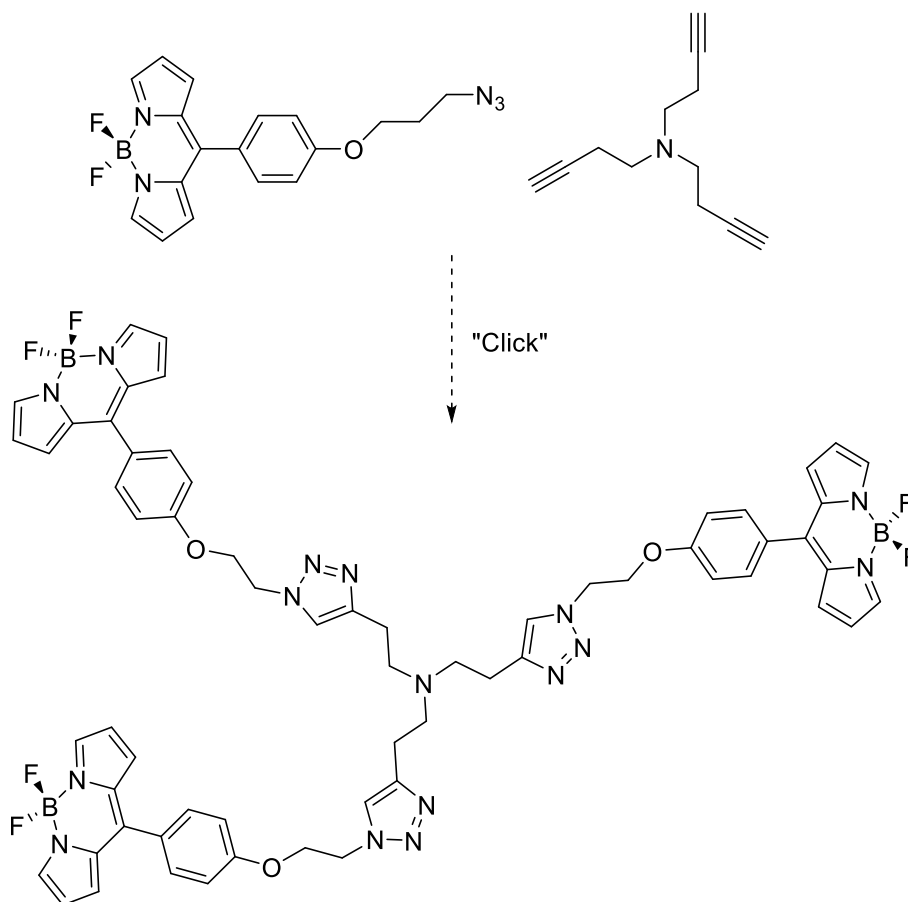
a template to facilitate “click” reactions. One interesting reaction is shown in Scheme 7.2 where the triazole forming reaction is hopefully accelerated by the presence of the cucurbituril macrocycle. A preliminary reaction under the conditions did not give us any evidence for formation of the rotaxane structure. One problem may be the size of the cucurbituril which may be too small to facilitate the triazole group. Again future work could concentrate on trying to use larger macrocyclic cavitands.



**Scheme 7.2.** Synthetic procedure for an *in-situ* click reaction in the presence of cucurbituril to form a rotaxane structure.

In order to try and make cage-like structure “click” chemistry was carried with **AZROT** in the presence of N,N-di(prop-2-yn-1-yl)but-3-yn-1-amine Scheme 7.3. The  $^1\text{H}$  NMR and  $^{13}\text{C}$  NMR spectra seemed to reveal the target compound was produced. However, sadly the mass spectrum (peak at  $m/z = 409.2$ ) only confirmed partial formation of the triazole linked Bodipy unit. It is possible that the reaction stops at some point because of steric crowding. In the future

alternative conditions could be tried using a large excess of **AZROT**. The interesting feature of the triad is the central hub which should also act as a metal ion binding site. It is easy to imagine metal ion binding pulling the three Bodipy groups closer together to permit the groups to interact. Sensing applications look possible using such a molecular array.



**Scheme 7.3.** Synthetic procedure for formation of a triad Bodipy rotor system.

Julolidine-Bodipy probe was designed via Knoevenagel condensation to make distyryl substitution with pentafluorophenylaldehyde. It was speculated that intrinsic property of pentafluorinate aldehyde would affect reactivity of piperidine catalysed amine base induced elimination reaction. However under same condition with p-dimethylaminobenzaldehyde the styryl substitution didn't work either, side product of initial starting material julolidinealdehyde was collected in crystalline on this reaction. Since the condensation condition is modified and worked well with other Bodipy core (dyad systems in Chapter

4), it could thus suspect that the methyl groups at 3,5 position of the Bodipy core in this case is not sufficiently reactive towards condensation. It is worth well to carry distyryl condensation in different condition such as microwave assistance; another method worth exploring is the Pd(II) catalyzed direct C-H arylation.

Photophysics measurements could be further conduct on the crystal of collected compounds to investigate energy transfer in molecular systems in the crystalline solid state rather than in fluid solution, that is more akin to the natural light-harvesting complex anchored by protein.